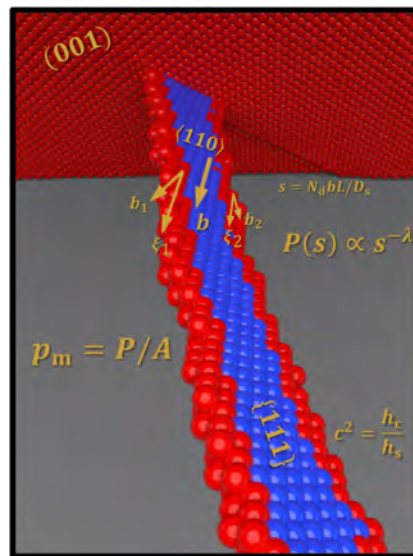# UNIVERSITAT POLITÈCNICA DE CATALUNYA

DEPARTAMENT DE CIÈNCIA DELS MATERIALS I ENGINYERIA METAL·LÚRGICA

Ph.D. Thesis

A Molecular Dynamics Study of Nanocontact Plasticity and Dislocation Avalanches in FCC and BCC Crystals

Author: **Javier Varillas Delgado**

Director: **Jorge Alcalá Cabrelles**

Barcelona, April 2019

Cover art: Glide of a screw dislocation pinned at the surface as encountered in a MD simulation of Al (001) nanoindentation. Photo by Jordi Torner.

Abstract

This study aims to investigate the underlying mechanisms which govern the development of dense defect networks in nanoscale crystal plasticity, either under contact and uniaxial loading conditions, with emphasis on the onset of intermittent avalanche phenomena. The investigation is based on a comprehensive set of massive molecular dynamics (MD) simulations performed with embedded-atom method potentials in face-centered cubic (FCC) and body-centered cubic (BCC) crystals.

The first part of the thesis concerns the combined role of elasticity and plasticity in nanocontact loadings, where attention is given to the mechanisms leading to the formation of a permanent nanoimprint as well as to the onset of material pile-up at the contact vicinity. It is found that the topographical arrangement of the slip traces emitted at the surface into specific deformation patterns is a distinctive feature of the underlying dislocation glide and twinning processes occurring in FCC and BCC crystals as a function of temperature and surface orientation. A mechanistic analysis is made on the influence of the defect nucleation events in conjunction with the development of entangled defect networks upon the material hardness and its evolution towards a plateau level with increasing indenter-tip penetration. Complementary MD simulations of the uniaxial stress-strain curve of the plastically deformed region are carried out with the purpose of establishing a direct correlation between nanoscale material responses attaining under uniaxial and contact loading conditions. The results of this comparison illustrate on the key role played by defect nucleation processes on the formation of permanent nanoimprints, which differs from the conventional view in that in micro and macroscopic scales imprint formation is essentially governed by the evolutionary character of a preexisting (entangled) defect network: the greater the dislocation density, the larger the measured hardness. In overall, this work provides a fundamental insight into the understanding of why BCC surfaces are harder than FCC surfaces at the nanoscale.

A statistical physics background is devised to investigate the influence of the dislocation mechanisms on the onset of avalanche events that are inherent to crystal plasticity. The analysis is predicated upon the notion in that the size distribution of such avalanches follows power-law scaling. To investigate the avalanche size distributions in cubic crystals, a group of novel MD simulations are performed where the computational cells containing a periodic arrangement of a preexisting dislocation network are subjected to uniaxial straining under displacement control at different strain rates and temperatures. Under sufficiently slow driving, the dislocation networks evolve through the emission of dislocation avalanches which do not overlap in time. This illustrates that the mobilized entangled dislocation arrangements exhibit quiescent periods during each plastic (dissipative) event, enabling comparison with experimental results which are also performed under strict displacement controlled conditions. The results illustrate on the attainment of a transitional slip size separating two power-law avalanche regimes as a function of the fundamental dislocation glide processes at the crossroads of self-organized and tuned criticality models. Detailed analyses of the MD simulations furnish specific mechanisms characterizing dislocation avalanche emission and propagation in FCC and BCC metals throughout a wide temperature range, which is central in supporting the onset of the aforementioned two power-law regimes.

Resumen

En este estudio se investigan los mecanismos fundamentales para el desarrollo de las densas redes de defectos que se producen durante la deformación plástica de metales mediante ensayos uniaxiales y de indentación en escalas nanométricas. Estos procesos de deformación plástica se caracterizan por la producción de eventos intermitentes o avalanchas de dislocaciones. La investigación se basa en un extenso grupo de simulaciones de dinámica molecular en las que se emplean potenciales interatómicos del tipo *embedded-atom method* en cristales cúbicos centrados en las caras (CCC) y cúbicos centrados en el cuerpo (CC).

La primera parte de esta tesis discute el papel combinado de la elasticidad y plasticidad en los nanocontactos. Se presta una especial atención a los mecanismos que llevan a la formación de nanohuellas plásticas así como al desarrollo de apilamiento de material alrededor del nanocontacto. Se encuentra que los arreglos topográficos de trazas de deslizamiento (emitidas a la superficie) muestran patrones específicos de deformación, los cuales son a su vez un rasgo distintivo de los mecanismos de deslizamiento de dislocaciones y procesos de nanomaclado que ocurren en los materiales CCC y CC en función de la temperatura y la orientación de la superficie. Se presenta un estudio mecanístico sobre la influencia de los eventos de nucleación de defectos, que llevan al desarrollo de una compleja red de defectos, sobre la nanodureza y su convergencia hacia un valor relativamente constante a medida que el indentador penetra en la superficie. La modelización del comportamiento uniaxial de la zona deformada debajo de las nanoindentaciones permite la correlación entre ambos tipos de ensayos. Los resultados de esta comparación ilustran el importante papel que juegan los procesos de nucleación de dislocaciones sobre la formación de nanohuellas plásticas, lo que difiere (en términos mecanísticos) del comportamiento plástico convencional encontrado en escales micro y macroscópicas, donde el carácter evolutivo de una red de defectos preexistente gobierna la formación de huella, cumpliéndose así que cuanto mayor es la densidad de defectos, mayores son también las macro y microdurezas. En general, este trabajo aporta un trasfondo fundamental para comprender la razón por la que las superficies CC son más duras que las CCC en la nano escala.

En la última parte de esta investigación se utilizan modelos de física estadística para investigar la influencia de los mecanismos de propagación de dislocaciones sobre la emisión de avalanchas plásticas. El análisis se basa en la noción de que la distribución del tamaño de las avalanchas sigue una ley potencial universal. Para investigar esta distribución en cristales cúbicos, se realizan un grupo de simulaciones novedosas donde las celdas computaciones, que contienen arreglos periódicos de las redes de dislocaciones, son sometidas a cargas uniaxiales a diferentes temperaturas y velocidades de deformación. A velocidades de deformación suficientemente lentas, las redes de dislocaciones evolucionan a través de la emisión de avalanchas que no se sobreponen en el tiempo, lo que ilustra que la movilización de las redes ocurre de tal manera que se garantiza una alternancia entre periodos de inactividad y cada evento plástico. La comparación entre resultados experimentales y computacionales lleva a encontrar la existencia de una magnitud de deslizamiento crítico que separa a dos regímenes de avalanchas cuya distribución de tamaños obedece leyes potenciales. Este resultado demuestra que los procesos de avalanchas son claramente dependientes de los mecanismos de deslizamiento e interacción de dislocaciones presentes en el material; aspecto que describe la transición entre el modelo de criticalidad gobernada por la tensión y el de criticalidad auto-organizada. Las simulaciones muestran los mecanismos específicos que caracterizan la emisión y propagación de avalanchas en metales CC y CCC en un amplio rango de temperatura, lo que es de gran importancia para justificar la utilización de estos modelos de criticalidad.

Glossary

ABBREVIATIONS

BCC	base-centered cubic
BTW	Bak-Tang-Weisenfeld (SOC model)
CCDF	complementary cumulative distribution function
CDF	cumulative distribution function
CNA	common neighbor analysis
DXA	dislocation extraction algorithm
EAM	embedded-atom method
EOM	equations of motion
FCC	face-centered cubic
FEA	finite element analysis
GND	geometrically necessary dislocation
HCP	hexagonal close-packed
MD	molecular dynamics
NG	Nix and Gao (model)
NPT	iso-baric iso-thermal canonical ensemble
NVE	microcanonical ensemble
NVT	canonical ensemble
PBC	periodic boundary condition
PDF	probability density function
r-RESPA	(reversible) reference system propagator algorithm
RSS	resolved shear stress
SF	stacking fault
SFE	stacking-fault energy
SFT	stacking-fault tetrahedra
SOC	self-organized criticality
STC	self-tuned criticality

LATIN ALPHABET

a	indentation contact radius
a_ϕ	circumferential contact radius
a_o	lattice constant
A	indentation contact area
A_s	area swept by a gliding dislocation
$\boldsymbol{b}$	Burgers vector
b	Burgers vector magnitude
c^2	pile-up parameter
c_max^2	pile-up parameter
c_ϕ^2	circumferential pile-up parameter
$\overline{c^2}$	mean pile-up parameter
$C(\dots)$	complementary cumulative distribution function
D	indenter diameter
D_s	representative cell width, sample width (or diameter in micropillars)

E	Young's modulus
E^*	effective Young's modulus
E_d	dislocation energy
E_q	quasi-elastic Young's modulus
$f(...)$	interatomic force (from $V(\boldsymbol{r})$)
$F(x)$	repulsive force (from the indenter)
G	shear (elastic) modulus
h	representative cell height
h_c	contact penetration
h_f	imprint penetration after indenter removal
h_{max}	maximum contact penetration
h_s	indenter-tip penetration
$\mathcal{H}(\boldsymbol{r}, \boldsymbol{p})$	Hamiltonian
K	indenter stiffness
l	representative cell length / sample height
l_0	initial computational domain length
l_x	computational domain length in the x-axis
l'	distance traveled by a gliding dislocation
l_{GND}	GND length
L	mean-free path of a gliding dislocation
L_G	distance between GNDs
M	Schmid factor
m	mass
N	number of particles/atoms in the system
N'	extended number of particles/atoms in a periodic domain
N_c	number of in-contact particles/atoms
N_d	number of dislocations (avalanche)
$\boldsymbol{p}$	particle momentum (vector)
p_m	mean pressure or contact hardness
$P(...)$	probability density function
$\boldsymbol{P}$	pressure tensor
P	applied force (indentation)
$\boldsymbol{r}$	particle position (vector)
r	radial distance in a spherical contact
S	dislocation avalanche size
s	slip size
s_{min}	minimum slip size
t	time
T	temperature
T_m	melting point temperature
$\boldsymbol{v}$	particle velocity (vector)
$\bar{v}$	dislocation mean velocity
$V(\boldsymbol{r})$	potential energy
V	volume
V_{pl}	plastic volume
x	axis
$\boldsymbol{x}$	vector defining the distance between a particle and the indenter center
y	axis
z	axis

iv

GREEK ALPHABET

α	Taylor's coefficient
β	thermodynamic temperature
$\boldsymbol{\Gamma}$	phase space
γ	shear strain
$\dot{\gamma}$	shear strain rate
γ_{usf}	unstable stacking-fault energy
γ_{sf}	(metastable) stacking-fault energy
γ_{utw}	unstable twinning energy
δ	distance between particle and indenter center
$\delta(\dots)$	Dirac function
δ_{Sh}	distance between leading and trailing partial (Shockley) dislocations
Δt	timestep
ε	strain
$\dot{\varepsilon}$	strain rate
θ	angle of conical indenter tip
κ	critical exponent (CCDF)
λ	critical exponent (PDF)
ν	Poisson's ratio
$\boldsymbol{\xi}$	dislocation line vector
$\rho(x)$	electron density function
ρ	dislocation density
ρ_{f}	dislocation forest density
ρ_{G}	GND density
σ	normal stress
σ_y	yield stress
τ	shear stress
τ_{c}	critical shear stress
φ	probability distribution function of a particle ensemble
$\phi(\boldsymbol{r})$	interatomic (pair) potential
ϕ	circumferential angle of a spherical contact
Ω	system observable

CONSTANTS

e	Euler´s number, $e \approx 2.718281828459\dots.$
π	pi, $\pi \approx 3.14159265359\dots$
k_B	Boltzmann´s constant, $k_B = 1.38064852 \times 10^{-23}$ m^2 kg s^{-2} K^{-1}

SPECIAL OPERATORS

$\langle \dots \rangle$	mean value of a statistical quantity
$\dot{\dots}$	time derivative of a variable
$i\mathcal{L}$	Liouville operator

Acknowledgments

Contents

List of figures

List of tables

CHAPTER 1.
PREFACE

CRYSTAL PLASTICITY has long been investigated by means of uniaxial and indentation testing of metallic samples [1-10], where the deviation from the early elastic response with increasing loading represents a clear indication of the onset of plastic deformation [1, 4, 9, 11]. While elasticity is prescribed by the atomic bonding [4], *dislocation glide* is the fundamental mechanism that leads to metal plasticity [3]. The presence of dislocation networks prescribes the mechanical properties and strain hardening behavior of metals [3, 4], where the *collective* glide of mobile dislocations in conjunction with the development of a dense dislocation configuration essentially govern the overall plastic response. Size effects in metallic samples [10] arise when the characteristic sample dimensions are decreased bellow 10 µm [3, 4, 12]. Under these conditions, plasticity becomes markedly affected by the finite sample size due to the advent of surface dislocation annihilation in conjunction with the activation of single-ended dislocation sources [3].

Figure 1.1 displays the stress-strain curves from uniaxial tests in pure nickel. Notice in this figure that a decrease in sample size leads to a gradual increase in crystal strength and to the attainment of markedly different strain hardening responses [13]. In accord with these observations, indented metallic samples become much harder when probed with minute tip sizes [14-16], which is along the lines of the well-established paradigm in that "smaller is stronger" [10, 12, 17]. Significant research efforts [10, 13, 17-21] have been directed to model such size effects in dislocation-mediated plasticity, which still remains as one of the most challenging problems in the field of mechanics of materials

During the past few decades, the use of mean-field models led to new insights in the understanding of crystal plasticity [10, 15, 18, 22-24]. Within this framework, the microscopic features and local activities of the dislocation networks are homogenized within a representative material volume using continuum (coarse-graining) approaches [19, 22, 23, 25]. The foundation to such continuum analyses is that the strength scales with the dislocation density under the concept of a representative material volume that contains a uniform dislocation distribution (or density) [23, 26]. Continuum crystal plasticity theories have been used to understand and to model plastic deformations under a wide range of loading configurations that involve fracture, indentation and uniaxial testing [10, 15, 19, 27-30]. These theories are taken to furnished an analytical toolbox to the assessment of macroscale (homogenized) continuum plasticity theories for polycrystalline aggregates, where each grain can be assigned a specific orientation and strain hardening characteristics [10, 24, 31-33]. Along these lines, an important topic that requires further theoretical developments concerns the onset of plastic deformations in confined material volumes (i.e. for sample dimensions < 5 µm [34]) where dislocation annihilation hinders dislocation storage [35].

Indentation testing with nanometer-sized tips provides load-penetration curves that tentatively exhibit three different contact regimes [14], see Fig. 1.2; (i) elasticity, (ii) first pop-in, marking the onset of plasticity as a function of crystal structure and surface orientation through defect nucleation processes [21, 36-40], and (iii) generalized plasticity characterized by the development of intermittent secondary pop-in events [14, 39, 41]. These pop-in phenomena (plastic bursting) are illustrative of the fundamental intermittent character of plasticity which challenges the aforementioned continuum mechanics analyses.

Intermittent crystal plasticity is also observed in micrometer-sized samples subjected to uniaxial loading [34, 42-45], where collective dislocation gliding events (or avalanches) lead to

the onset of discontinuities in the stress-strain curve (inset to Fig. 1.1). Although crystal plasticity is a fundamentally discrete process, this feature only becomes evident in small material samples which exhibit stress serrations during plastic straining (Fig. 1.1) [12, 13, 15, 16, 34, 46]. The distribution of avalanche sizes tentatively adheres to a power-law scaling, which is also a characteristic feature of many dissipative phenomena [45, 47, 48]. Thus, the intermittent development of dislocation networks can be analyzed under the analogy of an externally-driven critical system [49], where the power-law scaling of the avalanche distributions [42, 43, 45] indicates that the process is *scale-free*. This approach provides a statistical background to the understanding of intermittent plasticity, which includes the onset of a critical avalanche size [50], or cut-off value [46, 51, 52], under self-organized or stress-tuned criticality models [42-45, 53, 54].
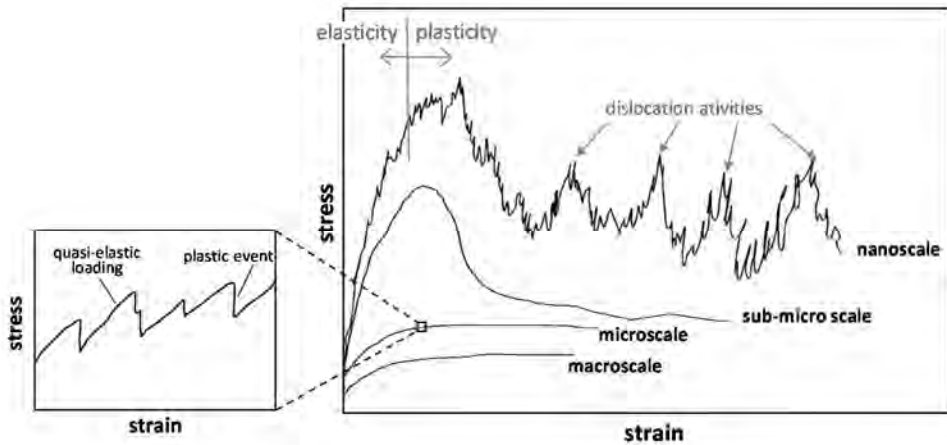
Figure 1.1. Stress–strain curves in nickel crystals at different size scales. Notice the onset of "elasticity" and "plasticity" regimes marked for reference in the nanoscale stress-strain response, as well as the intermittent features of plastic responses in small material samples. Adapted from Ref. [13].
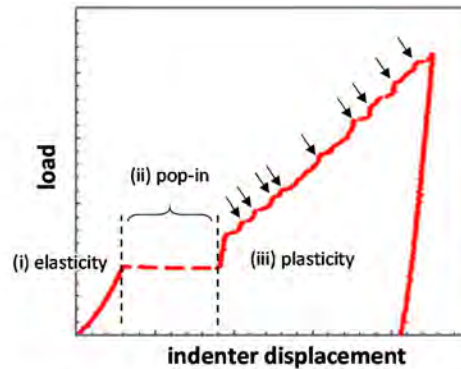
Figure.1.2. Nanoindentation experiments in BCC tantalum. The arrows denote plastic intermittencies (secondary pop-ins) in the load-displacement curve [14]. Adapted from Ref. [41].

Atomistic simulations are crucial in the understanding of crystal plasticity. These computational schemes provide a direct visualization of dislocation gliding, dislocation interaction and surface annihilation processes [55-57]. Of particular interest is the capacity to perform molecular dynamics (MD) simulations using embedded-atom method potentials that

are in principle capable of providing new insights into the understanding of the true dislocation mechanisms that govern plastic deformation in metallic materials [13, 37-39, 58-66].

Although MD simulations of nanoindentation experiments have been performed in the past [9, 16, 18, 36, 67-70], this thesis was initiated at a point where there was a lack of knowledge in the open literature with regards to the dislocation mechanisms that lead to the attainment of material pile-up patters in metal surfaces as a function of crystalline structure and orientation, and to the specific dislocation mechanisms governing imprint formation, with clear implications in the understanding of indentation size effects characterized by extreme hardness values at the nanoscale [7, 9, 36, 37, 67, 71]. Moreover, it is noted that while there appears to be a solid theoretical foundation to the statistical analysis of dislocation avalanches [43, 46, 47, 72], the use of these approaches in the characterization of dislocation-mediated plasticity has not been attempted yet. In addition, a clear description of the underlying dislocation mechanisms producing avalanche events remains to be clarified through atomistic simulations, incorporating the role of crystal structure, temperature and strain rate.

This investigation aims to shed new light on the fundamental mechanisms that govern the onset of plastic intermittencies as a main function of crystalline structure, loading rate, and temperature. It is also endeavored to provide a fresh view to the dislocation processes by which a permanent imprint is formed in nanoindentation experiments. The results are based on a comprehensive set of massive MD simulations mimicking ultra-low load nanoindentation and micropillar compression testing.

The structure of this doctoral thesis is as follows.

Chapter 2 gives a basic background of the dislocation glide theories in cubic crystals, where special attention is directed to the onset of dislocation interaction and multiplication in face-centered cubic (FCC) and body-centered cubic (BCC) metals. **Chapter 3** describes the basic scheme to run molecular dynamics simulations, including the specific procedures employed in this investigation in the context of FCC and BCC crystals subjected to uniaxial and indentation loadings. The embedded-atom method that describes interatomic interactions is also briefly reviewed.

Chapter 4 presents results concerning the MD simulations of nanoindentation. An insightful description of the fundamental crystalline phenomena that govern the development of directional patterning of the emerging dislocations at the indented surface is given in this chapter, along with the onset of specific material pile-ups around the contact as a function of crystalline structure, orientation and temperature. This is investigated through the analysis of slip trace emissions in conjunction with the evolution of the ratio between the contact depths, marking pile-up development. It is shown that the evolution of the distinct defect arrangements below the nanoimprints plays a key role in the topology of the slip trace patterning and in the morphology of the material pile-ups. In addition, the nature of defect nucleation at the inception of plasticity emerges as an important feature that governs surface morphology in both FCC and BCC metals.

Chapter 5 is devoted to study nanoimprint formation processes including the analysis of the hardness levels as a function of tip penetration attaining in FCC and BCC crystals. A discussion is given on nanocontact-induced plasticity in terms of the defect nucleation, interaction and multiplication mechanisms where, in particular, attention is given to evaluate the role of the elastic moduli of the indented surfaces upon the measured nanohardness values. The discussion provides a fundamental background to understand why BCC surfaces are harder than FCC crystals at the nanoscale.

Finally, **Chapter 6** analyzes the distributions of dislocation avalanches in micropillar compression experiments. The use of a novel MD computational procedure enables injection of a dense (entangled) dislocation network in FCC and BCC crystals in which the avalanches are emitted under subsequently applied uniaxial strains. The discussion illustrates on the onset of a transition between two different power-law regimes as a function of the fundamental dislocation glide processes during avalanche development. The analysis provides a statistical approach to the understanding of intermittent crystal plasticity in the context of the interplay of self-organized and tuned criticality models. The MD simulations furnish the fundamental features of the dislocating glide processes in each of the above power-law regimes.

CHAPTER 2.

BASICS OF PLASTICITY IN CUBIC METALS

THE ATOMIC BONDING determines the elastic properties of matter, where the stronger the bond, the harder the elastic response [4]. This feature is evidenced in ceramic materials whose elevated elastic moduli are the result of the preferentially strong covalent and/or ionic bonds [4]. Materials with such hard atomistic bondings are typically susceptible to develop brittle failure [4] as the crystals are unable to sustain further deformation. In contrast, metallic bonds enable plastic *flow* to occur when the resistance to crystal slip is exceeded [73], which leads to the formation of crystalline defects. A collective activity of such defects entails the onset of irreversible (plastic) deformation, where propagation, interaction, and multiplication of crystalline defects [3] are the underlying mechanisms that govern plasticity in metals.

The two mechanisms that are associated with single-crystal metal plasticity are dislocation glide and twinning. The geometrical features of these crystalline processes are well defined and tend to occur in specific planes and orientations of the crystal lattice [3, 73] defining the most energetically favorable paths for crystal slip [3]. In the following, dislocation glide and dislocation interaction processes are discussed in cubic crystals, including the onset of mechanical twining. The governing equations to crystal plasticity are further stated.

2.1. Dislocations and crystal plasticity

A dislocation is a *linear* defect in the crystal [73]. Dislocations can be visualized as a consequence of the termination of atomic planes inside the crystal (Fig. 2.1(a)), where in the proximity of the dislocation line (marked in blue in Fig. 2.1(b)), the surrounding planes bend to accommodate the missing atoms, which produces lattice distortions [3, 73]. A closed circuit (in red in Fig. 2.1(c)) is then constructed around the dislocation line ξ, allowing determination of the magnitude and direction of the lattice distortion characterized through the Burgers vector b (Fig. 2.1(c)) [3, 4]. This construction is referred to as the Burgers circuit [3].

Ideally, a dislocation can be of *edge* or *screw* type [3, 56]. Edge dislocations have the Burgers vector perpendicular to the dislocation line ($b \perp \xi$), while screw dislocation segments have Burgers vectors in the same direction as the dislocation line ($b \parallel \xi$). The latter geometry are created by the application of a shear strain on one side of the dislocation line so that the Burgers circuit terminates in the sheared plane, as shown in Fig. 2.1(c). Therefore, a helical configuration develops around the dislocation line, thus resembling the shape of a screw [3]. It is frequently encountered that dislocation segments exhibit a combination of screw and edge characters [3, 4, 56] as the dislocation line are neither perpendicular nor parallel to the Burgers vector. This type of dislocation is referred to as *mixed* dislocations, see Fig. 2.1(c).

According to the Schmid's law [74], dislocation mobilization occurs when a *critical* stress level attains *on* the glide plane. Such a critical stress (projected on the slip plane) is commonly referred to as resolved *shear* stress (RSS), and governs the activation (glide) of a dislocation segment.
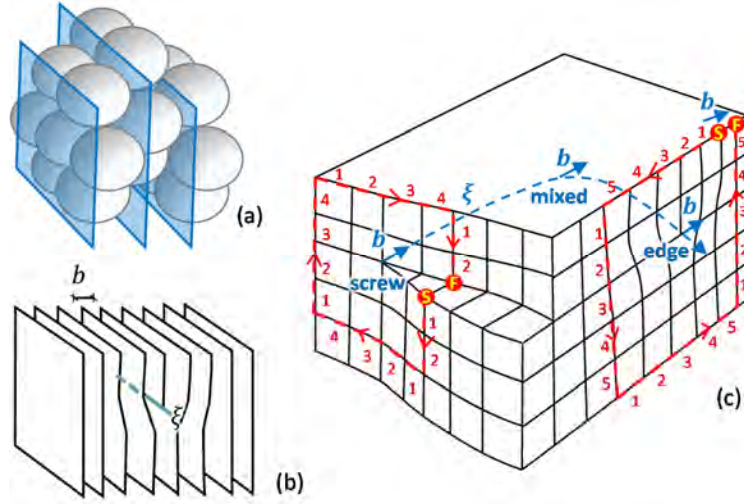
Figure 2.1. Dislocations inside a cubic crystal. (a) Representation of atoms (spheres) and closed-packed planes (in blue). (b) The stack-of-paper analogy is often employed [3] to represent an edge dislocation line (in blue), where the presence of half piece of paper illustrates the lattice distortions [3]. (c) Representation of a dislocation line ξ (dashed line) with both screw and edge character. Burgers circuit is marked in red. The Burgers vector b runs from start (S) to finish (F) points. This defines the right-hand/start-finish convention for the construction of Burgers circuits [3, 73]. Adapted from Ref. [3].

A mobile dislocation (Figs. 2.2(b)-2.2(d)) essentially induces a shear strain γ in the crystal, where in accordance with Fig. 2.2(b) $\gamma = (b/h)(l'/l)$. The sweeping of N_d dislocations in a crystal of length l then leads to a shear strain of $\gamma = N_d b/h$ (note in Fig. 2.2(d) that $l' = l$). Under this framework, the average dislocation-glide velocity $\bar{v}$ is related with γ though the Orowan's equation [73],

$$\dot{\gamma} = b\rho\bar{v}. \tag{2.1}$$

In the above equation, the dot denotes time (t) derivatives ($\dot{\gamma} = d\gamma/dt$), ρ is the dislocation defined as the length of dislocation lines per unit volume [note that $\rho \approx N_d/lh$ in Figs. 2.2(b)], and b is the magnitude of the Burgers vector $\boldsymbol{b}$.

Interaction between the mobile dislocations with an immobile dislocation forest [3] leads to a non-uniform velocity profile [73]. Under increasing straining, the mobile dislocations thus exhibit *intermittent* (discrete) arrest/remobilization stages, which are homogenized in crystal plasticity theories through the concept of a statistical mean free path length L, which is correlated with the dislocation forest density, ρ_f, through $L \propto \rho_f^{-1/2}$ [3, 26]. The forest dislocations (evenly spaced by distance L) intersecting the glide plane are the effective obstacles (pinning points) for dislocation glide [3]. This is captured in the Taylor's model [3, 75], where ρ_f acts as the coarse-grained governing parameter that determines the evolution of plastic deformation as

$$\tau = \alpha G b\sqrt{\rho_f}. \tag{2.2}$$

Here, G is the shear modulus, τ is the shear stress applied on the glide plane (Fig. 2.2(a)), and α is a coefficient measuring the strength of the dislocation junctions developing as the mobile dislocations interact with the dislocation forest (see Section 2.4) [3, 76]. Note in Fig. 2.2(a) that $\tau = \sigma M$, where M is the Schmid factor [4] that projects σ on the glide plane. Note also in Eq. (2.2) that a gradual increase in τ involves an associated increment in ρ_f. This implies the onset

of dislocation multiplication mechanisms which are usually regarded to involve the Frank-Read mechanism and the operation of glissile junctions (Section 2.4) [3, 73], see Fig. 2.2(e).
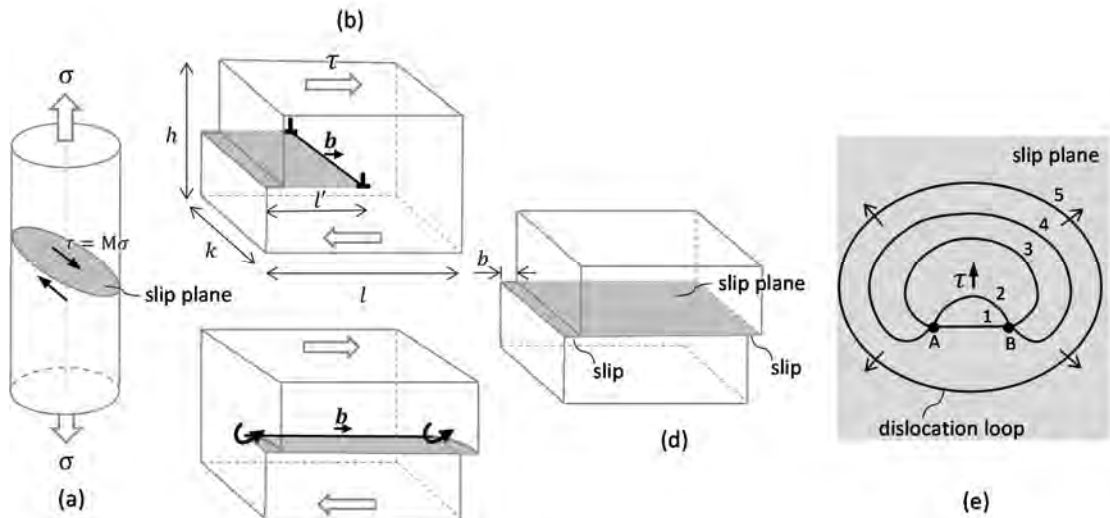
Figure 2.2. Schematic illustration of dislocation glide. (a) Representation of a slip plane in a cylindrical crystal [3]. (b) and (c): Edge and screw dislocations (respectively) producing the eventual crystal slip of size *b* illustrated in (d). The shaded planes represent the total area swept by dislocation glide. (e) Sequence of the operation of a Frank-Read source that is pinned at points "A" and "B". The process eventually leads to dislocation loop emission. Arrows denote direction of dislocation expansion.

Dislocation propagation and multiplication in metals inevitably result from the application of external stress. Dislocation nucleation and stress concentration effects at interfaces (such as grain boundaries) may also lead to the development of a dislocation structure in metals [77, 78]. Dislocation emissions through *homogeneous* nucleation arise from the rupture of atomic bonds along a lattice line so that atoms are able to move an atomic spacing. The activation energy for this process is extremely elevated (see Ref. [79]) as the associated stress levels are close to the theoretical bonding resistance of $\approx G/30$ [3]). Grain-boundaries and interfaces then provide realistic locations to the onset of *heterogeneous* dislocation nucleation due to boundary irregularities that provide a discontinuous distribution of surface tensions (that act as stress concentrators [77, 78]). Heterogeneous dislocation nucleation is produced under much lower stresses than those encountered in the above homogeneous nucleation [77]. In a similar fashion, free surfaces can also act as dislocation sources due to the natural ill-defined (atomistically rough) surface topography [3, 77].

The slip planes and directions as well as the dislocation glide mechanisms become functions of the crystalline structure. In this context, it is noted that the underlying processes of plastic deformation in cubic metals are diverse, giving rise to different plastic responses in body-centered cubic (BCC) and face-centered cubic (FCC) structures.

2.2. Dislocation glide in FCC crystals

In FCCs, dislocation slip is characterized by Burgers vectors $\boldsymbol{b}$ = 1/2<110> of magnitude $b = a_\mathrm{o}\sqrt{2}/2$ (where a_o is the lattice parameter), and occurs in the {111} close-packed planes [3]. FCC crystals exhibit a close-packed atomic structure [3] which gives rise to the emergence of a completely different set of mechanisms for dislocation glide as compared to in BCCs.

Full 1/2<110> dislocations *split* (or dissociate) into two 1/6<112> Shockley partial dislocations [3] producing a stacking fault (SF) as the splitting of vector $\boldsymbol{b}$ (Fig. 2.3(a)) changes the perfect FCC A**B**CABC… stacking sequence to the A**B**AB… sequence characteristic of hexagonal close-packed (HCP) structures [3]. Figure 2.3(a) illustrates the schematic glide of a $\boldsymbol{b}$ = 1/2<110> full dislocation lying on an A-stack whose (full) dislocation glide (A to A) exhibits an energetically more favorable path throughout an adjacent **B**-site (i.e. A to **B** to A), see Fig. 2.3(b).

According to the construction in Fig. 2.3(a), a full dislocation dissociates into two partial dislocations, i.e. the *leading* partial with Burgers vector $\boldsymbol{b}_1$ and the *trailing* partial with $\boldsymbol{b}_2$. The following reaction for the Burgers vectors therefore attains for a full 1/2[110] dislocation [3],

$$\frac{1}{2}[110] \rightarrow \frac{1}{6}[211] + \frac{1}{6}[12\bar{1}]\,. \tag{2.3}$$

This dislocation splitting essentially arises from the local energy minima of the {111} surfaces [3, 78]. Figure 2.3(b) displays the different paths that a 1/2[110] dislocation can overcome [3]. In accordance with this figure, the path A to **B** to A (reaction of Eq. (2.3)) is energetically favored.
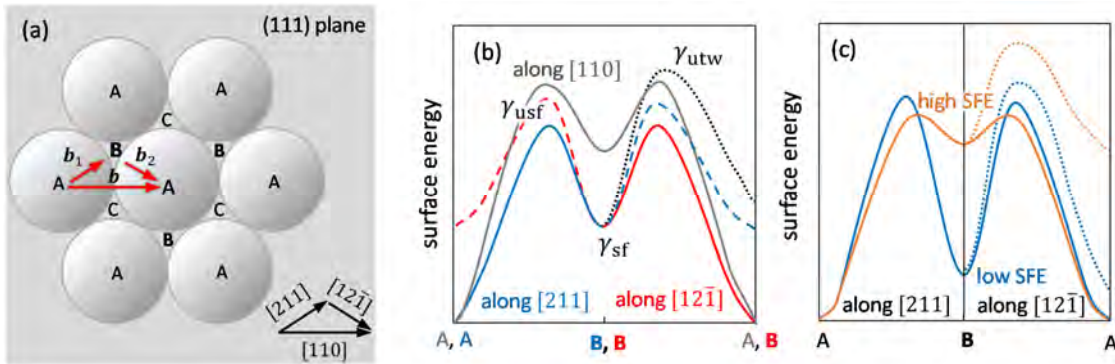
Figure 2.3 Glide of 1/2[110] dislocation in an FCC crystal. (a) Schematic illustration of dislocation gliding and SF formation, where 1/2<110>{111} full dislocations dissociate into two 1/6<112>{111} partials. Picture adapted from Ref. [3]. (b) Surface energy profiles for dislocation glide (A to A along <110> and A to B and B to A along <112> type directions). (c) Surface energy profiles for dislocation glide in high and low SFE FCC crystals. Pictures (b) and (c) are adapted from Ref. [78]. See text for full details.

The difference between surface energy maxima, γ_{usf} (unstable stacking fault), and local minima, γ_{sf} (metastable stacking fault), see Fig. 2.3(b), plays a crucial role in the above dislocation splitting as well as in the nucleation of partial dislocations in grain boundaries and in crack tips [78]. The surface energy per unit area of a SF is commonly referred to as the stacking-fault energy (SFE) of the crystal [80] (Fig. 2.3(c)). This value determines the extension

of stable SFs between partials as the SFE $\propto b^2/\delta_{Sh}$ [3], where δ_{Sh} is the distance between two partial (Shockley) dislocations [3]. Typically, low SFE FCC crystals produce extended SFs due to the large $\gamma_{usf} - \gamma_{sf}$ surface-energy barrier (Fig. 2.3(c)) that a leading partial needs to overcome to close the SF through the nucleation of the second (trailing) partial, while high SFE FCC crystals exhibit short SFs due to the low γ_{usf} - γ_{sf} barrier for the A to **B** path [3, 78], see Fig. 2.3(c).

2.2.1. Cross slip

Cross slip is the mechanism by which a screw dislocation (of Burgers vector **b**) can move from one slip system to another in such a way that b is maintained [3]. The operation of cross slip is commonly enhanced by the combination of external stress and thermal fluctuation [3, 80, 81]. The SFE of the crystal is the prime governing factor for the process [3], so that cross slip is typically hindered in low SFE FCC crystals [80].
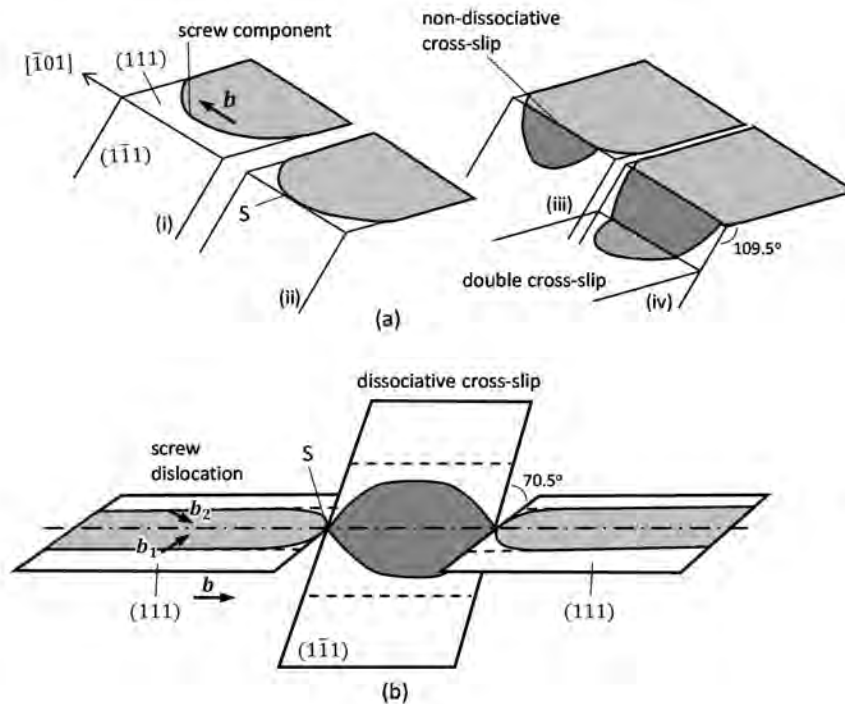
Figure 2.4. Cross-slip mechanisms in FCC crystals. (a) Sequence of events (i), (ii), (iii) of an expanding SF ribbon where the screw component undergoes non-dissociative cross-slip at "S". Shaded area denotes SF plane. Double cross-slip is shown in (iv). Adapted from Ref. [3]. (b) Illustration of the Friedel-Escaig model for dissociative cross-slip where the screw dislocation gliding on the (111) plane dissociates onto the $(1\bar{1}1)$ cross-slip plane. Double cross slip attains when the dislocation cross-slips back to the initial (111) plane. Figure adapted from Ref. [82].

Two distinct theoretical models can describe the mechanism for cross slip in FCC crystals [81]; the non-dissociative and the dissociative cross-slip. Figure 2.4(a) illustrates the non-dissociative cross-slip, where the $b = 1/2[\bar{1}01](111)$ screw component of an expanding SF ribbon cross-slips as the local stress field acting on the gliding screw enables the partial dislocation to shift towards the $(1\bar{1}1)$ slip plane [3, 81]. The dissociative cross-slip (described

by the Friedel-Escaig model [81, 82]) attains as the screw dislocation is locally constricted to a saddle point configuration (marked "S" in Fig. 2.4(b)) [22, 81], so that the screw cross-slips to a neighboring {111} plane where the dislocation returns to its dissociated ($\boldsymbol{b} = \boldsymbol{b_1} + \boldsymbol{b_2}$) configuration, see Fig. 2.4(b). This model effectively captures the influence of the SFE upon cross slip [82]. Atomistic simulations have shown that the Friedel-Escaig (dissociative) construction exhibits a lower (cross-slip) energy barrier than the non-dissociative counterpart [81]. Additionally, FCC crystals commonly exhibit double cross-slip [3] (jog-pair mechanism [81]), where a screw dislocation cross-slips back to the original glide plane, see Fig. 2.4(b). This mechanism is enhanced for high temperature and low-stresses [3, 81].

Unlike edge and mixed dislocations whose motion occurs in a unique glide plane [3], a pure screw segment is free to cross-slip towards favorable {111} slip planes. Thus, the gliding screw dislocations are able to surpass crystalline barriers by cross slip [3, 83]. This process is key in enhancing dislocation multiplication [26, 81, 83], dislocation recovery [22, 26, 81], and strain hardening [3, 22] in FCC crystals.

2.3. Dislocation glide in BCC crystals

In BCC crystals, dislocation glide occurs in the closest-packed <111> directions [3, 84] with Burgers vector $\boldsymbol{b} = 1/2$ <111>. The notation for $\boldsymbol{b}$ in a BCC crystal corresponds, in accordance with Fig. 2.5 (blue arrow), to the movement of one corner atom to the position occupied by a central atom, implying a displacement of $a_o/2$ in <111> directions. Thus, $\boldsymbol{b}$ has a magnitude of $b = a_o\sqrt{3}/2$ [3]. The (crystallographic) slip planes in BCC crystals belong to the {110}, {112} and {123} families (Fig. 2.5) where each of these planes contains at least one <111> slip direction [3, 84], see Table 2.1.
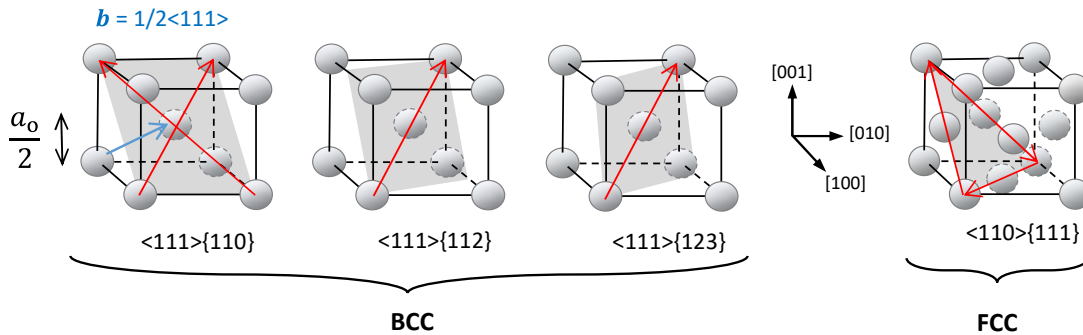
Figure 2.5. Slip systems in BCC and FCC crystals. Slip planes are shaded while slip directions are marked with red arrows. The x-axis follows the [100] direction in Miller-index notation.

Table 2.1. Slip systems in BCC and FCC crystals [3].

Crystalline structure	Slip Plane	Slip Direction	Number of non-parallel planes	Slip directions per plane	Number of Slip Systems
BCC	<110>	{111}	6	2	12 (6x2)
	<211>	{111}	12	1	12 (12x1)
	<321>	{111}	24	1	24 (24x1)
FCC	<111>	{110}	3	3	12 (4x3)

Dislocation glide in BCCs is governed by the Peierls barrier, which measures the stress that needs to be applied (at 0 K) in order to move a dislocation core to the next atomic valley in the glide plane (see the inset to Fig. 2.6) [3]. The Peierls barrier is much smaller for edge dislocations than for screw dislocations [84], a feature that stems from the *non-planar* core of the former which leads to the onset of large lattice frictions [63, 85]. This is the reason why it is generally argued that BCC plasticity is dominated by the sluggish glide of screw dislocation segments.

It is well-known that the associated critical RSS for the activation of a given BCC slip system is the lowest for the {110} planes and the highest for the anti-twinning {112} planes [84], a feature that emerges as a result of that plasticity in BCC crystals is affected by the so-called non-Schmid stresses [63, 84-87]. At this point, the discrepancies arising from whether it is the compact or the degenerated core structures that attain in a pure BCC crystals [63, 84, 88, 89] have been finally solved, where it is clear that the former is the strictly correct morphology [86]. Although the prediction of a non-degenerated core limited the understanding of the role of non-Schmid stresses on the motion of the screw dislocations (which includes the well-known twinning/anti-twinning asymmetry), a convincing explanation [86] has been put forward based on the motion of the dislocation cores from the easy to the hard to the split configurations along <111> lattice directions.

In BCCs, it is particularly significant that three {110}, three {112} and six {123} planes intersect the same <111> lattice direction (Table 2.1), which enables the mobile screw dislocations to change slip system [3]. Thus, the gliding segments attain recursively different slip systems, where erratic paths and ill-defined dislocation are a signature feature of dislocation glide in BCC crystals [3, 63, 84, 86, 88, 90].

2.3.1. Kinking

Kinking in BCCs occurs when a screw dislocation suddenly moves out to a nearby local minimum in dislocation energy, E_d [63, 90]. This non-conservative movement occurs on the same slip plane [84] as a kink *stochastically* nucleated along the dislocation line [63, 84, 88] displaces the dislocation a distance a_o (Fig. 2.6) [3]. Two distinct types of kink nucleation are encountered in BCC crystals; single kinking and kink-pair nucleation [89]. The former implies development of a single event where the segment migrates towards a neighbor energy minimum [3] overcoming one Peierls barrier, while kink-pair nucleation arises as a consequence of the appearance of two simultaneous kink nucleations at a point of the dislocation line [63, 88], see Fig. 2.6. The latter plays a key role in the dislocation mobility of BCC crystals at low temperature [63, 88, 91] as it represents an effective source for the migration of screw dislocation segments [63, 87].
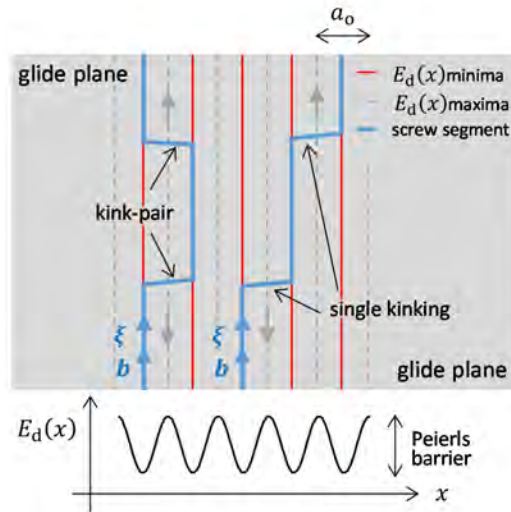
Figure 2.6. Dislocation glide in BCC crystals. Schematic representation of kinking in a 1/2<111> screw dislocation. Note that the dislocation segment migrates from one Peierls barrier to the next along subsequent minima in dislocation energy $E_d(x)$. Adapted from Ref. [3].

2.4. Interaction of dislocations

The free glide of a dislocation is interrupted due to interactions with the forest dislocation segments intersecting the glide plane [3, 73]. As plastic deformation proceeds, further mobilization of dislocation segments occurs in other slip systems, thus increasing the number of gliding (or primary) dislocations and the forest counterparts [3]. In the spirit of classical crystal plasticity (Eq. (2.2)), strain hardening ($d\tau/d\gamma > 0$) is governed by the strength of the specific interactions between mobile dislocations and the forest in conjunction with the gradual development of the dislocation network with straining [22, 25]. In the following, the onset of dislocation jogs and junctions is described with the purpose of discussing the specific roles that distinct dislocation intersections play in dislocation-mediated plasticity of BCC and FCC crystals.

2.4.1. Formation of dislocation jogs

Jog formation is the classical process that accounts for some of the elementary features of the dislocation intersection process [3, 73]. Figures 2.7(a) and 2.7(b) illustrate the intersection sequence of two orthogonal (non-dissociated) edge dislocations with parallel Burgers vectors b_1 and b_2. In this sequence, dislocation interaction leads to jog formation on both dislocation lines (Fig. 2.7(b)) where the length of "jog 1" is equal to b_2, and the length of the "jog 2" is equal to b_1 [3]. A similar construction is given in Fig. 2.7(c) where the gliding of the edge dislocation with b_2 meets the screw dislocation with b_1 (whose slip planes are also orthogonal). The interaction (Fig. 2.7(d)) leads to the formation of "jog 3" with length b_2 in the screw, and "jog 4" with length b_1 in the edge [3]. This jog construction (Figs. 2.7(b) and 2.7(d)) is referred to as *elementary* jogs [3] as the jog length is equal to the *shortest* lattice translation vector [3].

Typically, formation of elementary jogs in pure edge dislocations *do not* prevent entire dislocation segments from gliding [3, 92]. However, the type of jogs in screw segments can play an important role in the mobility of the screws. In this context, jogs lying in the same glide plane of the screw (of a similar configuration to "jog 3" in Fig. 2.7(d)) behave as kinks so that, as mentioned in previous Section 2.3.1, the mobility of such jogged screws requires stress and thermal activation [3, 63, 87]. The opposite scenario arises when the glide plane of the screw is different from that of the jog. With sufficiently high stress and/or temperature [3, 92], the screw and the jog can *jointly* move through a non-conservative (climbing) process that implies vacancy formation (see Fig. 7.7 in Ref. [3]).

Additionally, a jog larger than one atomic spacing (marked "n" in Fig. 2.7(d)) is commonly denominated *superjog* [3, 73]. The onset of superjogs along the screw dislocation segments plays an additional role during plasticity as the mobility of the overall dislocation structure is governed by the jog length [3, 92]. In this context, short jogs may become mobile, a process that leads to vacancy formation in the crystal [3, 92], while a superjog may become *immobile* passed a critical magnitude for the jog length, which thus serves as an anchor point hindering propagation of screw dislocations. With sufficiently extended jogs [3], this construction can give rise to the emergence of Frank-Read sources (Fig. 2.2(e)) that eventually lead to the emission of prismatic loops (see Fig. 7.11 in Ref. [3]).

Trails of defects and dislocation loops are common byproducts of dislocation glide [3] where, in particular, the *debris* left by the motion of dislocations typically originates from edge jogs which are connected to the screw segments that extend upon the application of external stresses [3, 73].
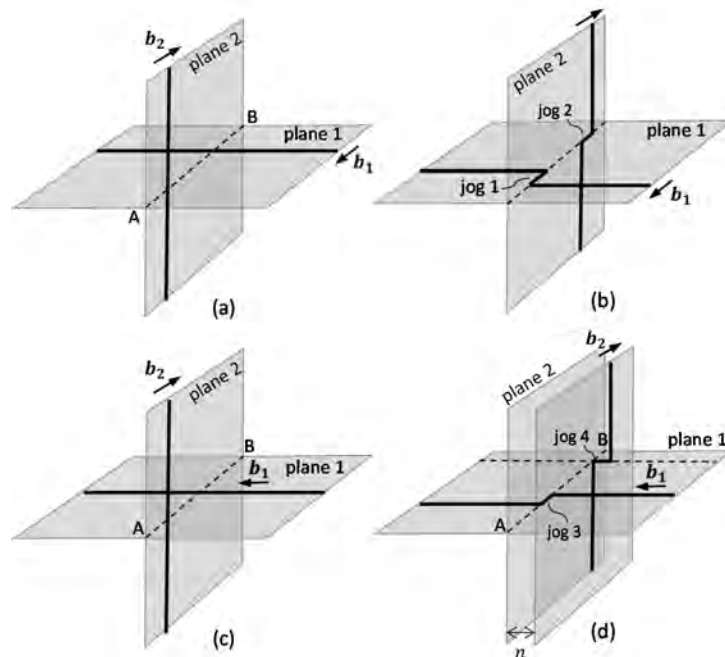
Figure 2.7. Jog formation during intersection of dislocations with parallel Burgers vectors. Intersection of two edge dislocation is represented in (a) before intersection, and (b) after intersection. (c) The glide of edge dislocation (b_2) intersects with screw dislocation (b_1) leading to the formation of "jog 3" in the screw and "jog 4" in the edge. Pictures adapted from Ref. [3].

2.4.2. Dislocation junction formations

In addition to jog formation, dislocation interaction can also lead to the onset of junction segments [3, 73]. In this context, two interacting dislocations react forming a junction segment with Burgers vector $\boldsymbol{b}_j$ equal to the sum of the two interacting Burgers vectors, i.e. $\boldsymbol{b}_j = \boldsymbol{b}_1 + \boldsymbol{b}_2$. To examine whether the configuration of two dislocations forms a stable (attractive) junction, the reaction must then reduce the overall energy of the ($\boldsymbol{b}_1 + \boldsymbol{b}_2$) interacting system. Since the energy of a dislocation is proportional to $\boldsymbol{b}^2$ [73], an attractive junction segment then satisfies $\boldsymbol{b}_j^2 < \boldsymbol{b}_1^2 + \boldsymbol{b}_2^2$ (Frank's rule) [3].

In BCC crystals, the reaction product between two dislocations is always found to be of the <100> type [25]. However, the study of the possible dislocation interactions and configurations in BCC crystals represents a difficult task [82] due to the important amount of (rarely well-defined) slip systems as well as the thermal-assisted and stress-induced mobility of screw dislocations (Section 2.3). Nonetheless, it is known that the formation of stable junctions (satisfying the above Frank's rule) gives rise to three different types of configurations in BCCs; sessile, mixed and glissile dislocation junctions [25]. For a more detailed description of the possible configurations of dislocation interactions in BCC crystals, the reader is referred to Refs. [82, 93]. Contrarily to BCCs, dislocation interactions and junction formation occurring in FCC crystals have long been studied and the configurations of all the possible reactions of two interacting {111}<110> dislocations are well established in the literature [23, 25, 29, 93-95].

Two (attractive) interacting dislocations in FCC crystals systematically lead to the onset of Lomer, Hirth, collinear, and coplanar junctions [23, 25]. Lomer and Hirth junctions are sessile (immobile) as the associated junction dislocation (with $\boldsymbol{b}_j$) lies in a non-crystallographic system [3, 73, 94]. Figure 2.8(a) illustrates a Lomer lock produced by two interacting (extended) dislocations [3], where the immobile junction is comprised by a stair-rod partial dislocation ($\boldsymbol{b}_{sr} = 1/6<110>$ [3]) and a <110> full dislocation whose glide attains on a non-crystallographic plane [3]. A similar construction to the above may lead to the formation of a Hirth lock with the peculiarity that $\boldsymbol{b}_j$ takes a <100> non-crystallographic direction [3, 73]. The (glissile) coplanar junction are mobile configurations ($\boldsymbol{b}_j$ lies in a slip system) [3]. Figure 2.8(b) depicts a *sessile* junction of two extended dislocations whose dislocation junction ($\boldsymbol{b}_j$) is pinned with the interacting dislocations [3]. Such a mobile junction may also serve as an effective dislocation source as long mobile junctions (Fig. 2.8(b)) can glide through the Frank-Read mechanism (Fig. 2.2(e)). Finally, the *collinear* interaction emerges between gliding dislocations with the same Burgers vector lying on adjacent planes in Thompson's tetrahedron [3], a construction which leads to annihilation so that in contrast to the other three junction forming interactions, a physical dislocation junction is non-existent in the collinear case [29, 93]. The sequence of the collinear interaction and eventual annihilation is given in Figs. 2.8(c) and 2.8(d).

Under the application of a sufficient stress level, unzipping of sessile dislocation junctions occurs. [29, 94]. This plays a crucial role in the strain hardening behavior of FCC metals as the zipped primary dislocations are finally remobilized at large stress levels. Computer simulations have shown that the junction strength is the highest for the collinear, followed by the Lomer, the glissile, and the Hirth (weakest) junctions [29, 93-95].

In addition, strong reactions that *fully* restrict the above junction annihilation and dislocation motion originate from the formation of multi-junctions (three- or four-fold dislocation nodes) [3, 96]. Figures 2.8(e)-(g) illustrate the sequence for a possible mechanism leading to formation of a three-node dislocation junction [96], where a two-fold junction (with sessile segment "J" –in red) formed by dislocations "1" and "2" (Fig. 2.8(g)) interacts with

dislocation "3" (Fig. 2.8(h)), producing eventually a multi-junction comprised by dislocations "1", "2" and "3" and (mobile) dislocation junction "J' " (in green), see Fig. 2.8(g). Note in this figure that nodes "A" and "B" pin the segment "J' " so the A-J'-B configuration can also act as a Frank-Read source for dislocation multiplication [3]. Computer simulations [96] have revealed that the formation of multi-junctions is a common feature in metals with dense dislocation densities, where the presence of such junctions serves as a strong obstacle to dislocation glide.
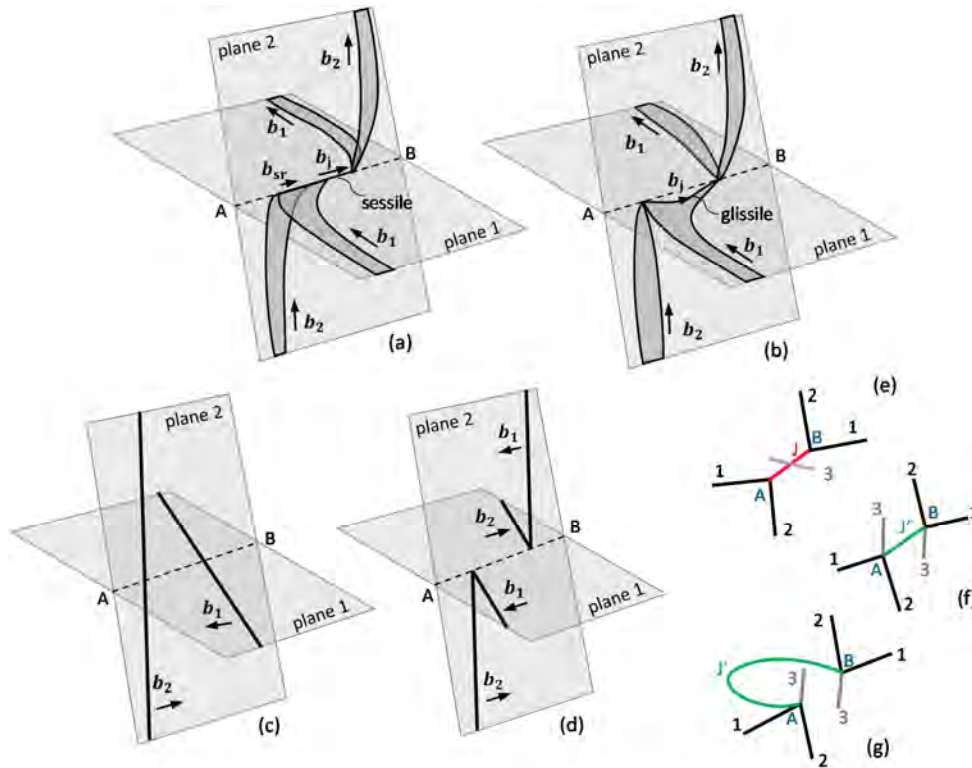
Figure 2.8. Types of dislocation junctions in FCCs. (a) Sessile Lomer lock, (b) Glissile junction, and (c) collinear interaction where junction annihilation is illustrated in (d). Line AB denotes the intersection line between plane 1 and plane 2. Figures adapted from Ref. [3]. (e)-(g): Illustration of multi-junction formation, where a third dislocation (marked "3") reacts with immobile segment junction "J" (e), converting "J" into a mobile screw dislocation "J' " [96]. Note in (g) that a multi-junction may also become an active Frank-Read source upon the application of a shear stresses. Adapted from Ref. [96].

Finally, an additional arrangement from dislocation interaction in FCC crystals involves the formation of a tetrahedron of intrinsic SFs delimited by 1/6<110> stair-rod partials. This particular configuration is commonly denominated stacking fault tetrahedra (SFT) [3, 97] and has been largely observed in metals upon quenching or when subjected to radiation damage [3]. Atomistic simulations [97] have shown that SFT arise as a consequence of a *recurrent* (and attractive) interaction of 1/6<112> partials in highly dense dislocation entanglements which may eventually lead to the formation of SFT structures (e.g., see Ref. [97] for a detailed description of the process).

2.5. Twinning

Mechanical twinning is the process by which a region of the crystal changes orientation [98] so that the atoms of the original (parent) crystal and those of the product (twinned) crystal are mirror images of each other along the twin boundary [3, 25], see Fig. 4 in Ref. [98].

In FCC crystals, mechanical twinning attains at large stresses which enhance atomistic movement through the (unstable) twinning path of the surface energy maximum (marked with a dotted line in Figs. 2.6(b) and 2.6(c)). This type of twinning is produced by the *successive* nucleation of parallel 1/6<112> twinning partials, which lead to a local change in the crystal orientation [98]. The typical twinning arrangement in an FCC crystal is defined by a twin-parent mismatch angle of 70.53º [98]. Although high strain rate and low temperature promote twinning-mediated deformation in FCCs [33], the SFE of the crystal thus become the governing parameter that dictates the formation of FCC nanotwinning. In this context, high SFE FCC crystals mainly deform by dislocation glide, while twinning deformation is typically promoted in low SFE FCCs [98], see the dashed energy path in Fig. 2.3(c).

In BCCs, mechanical twinning attains during deformation at low temperatures and/or high stain rates [3, 99]. A possible mechanism [100] that effectively describes twinning nucleation in BCC crystals implies the dissociation of a 1/2<111> screw dislocation into three 1/6<111> fractional dislocations that preferentially arrange on an {112} plane. Twin-wall growth is associated to the successive energy barriers obtained in the generalized planar fault energy curve [101] that the fractionals need to overcome to expand the {112} twin in the crystal, where the energy barrier topographies attain as a function of the BCC material, see Fig. 2 in Ref. [100]. Although crystal twinning typically contributes little (or nothing) to the overall plastic deformation in uniaxially strained BCC crystals [3], stable nanotwin formation has been extensively observed in processes of sharp-tipped crack propagation [99] and indenter-induced defect nucleations [38, 39, 102] as BCC nanotwinning seemingly plays a significant role in the inception of plasticity.

CHAPTER 3.
COMPUTATIONAL METHODS

3.1.   Statistical mechanics background

The molecular dynamics (MD) computational scheme employs statistical mechanics to determine the time evolution of N-particle systems [103]. The state of a system at time t is effectively described by the $6N$-dimensional phase space $\boldsymbol{\Gamma}$,

$$\boldsymbol{\Gamma}(t) \equiv \left\{ r_{x\ j}(t), r_{y\ j}(t), r_{z\ j}(t);\ p_{x\ j}(t), p_{y\ j}(t), p_{z\ j}(t) \right\}, \qquad j = 1,2,3,\dots,N; \qquad (3.1)$$

which is the set that contains all particle positions, $\boldsymbol{r}$, and momenta, $\boldsymbol{p} = m\boldsymbol{v}$, where m is particle mass and $\boldsymbol{v}$ particle velocity [55]. The time evolution of the phase space follows relations of the form $\dot{\boldsymbol{\Gamma}} = G(\boldsymbol{\Gamma})$, where $\dot{\boldsymbol{\Gamma}} = d\boldsymbol{\Gamma}/dt$ and $G(\boldsymbol{\Gamma})$ is a function of $\boldsymbol{\Gamma}$ that generates *unique*, non-intersecting trajectories in the $\boldsymbol{\Gamma}$-space [104].

For any given system observable Ω [104], which is a function of positions and momenta so that $\Omega = \Omega(\boldsymbol{r}, \boldsymbol{p}) = \Omega(\boldsymbol{\Gamma})$, its time evolution follows

$$\dot{\Omega} = \frac{\partial \Omega}{\partial \boldsymbol{r}} \dot{\boldsymbol{r}} + \frac{\partial \Omega}{\partial \boldsymbol{p}} \dot{\boldsymbol{p}} = \mathrm{i}\mathcal{L}\Omega\,, \qquad (3.2\mathrm{a})$$

then

$$\Omega(\boldsymbol{\Gamma}_t) = \mathrm{e}^{\mathrm{i}\mathcal{L}t}\Omega(\boldsymbol{\Gamma}_0). \qquad (3.2\mathrm{b})$$

Here, $\mathrm{i}\mathcal{L}$ is the time-reversible Liouville operator [104, 105]. Notice that $\Omega(\boldsymbol{\Gamma}_t)$ and $\Omega(\boldsymbol{\Gamma}_0)$ are the values that function $\Omega(\boldsymbol{\Gamma})$ respectively takes at time $t = t$ and $t = 0$.

Since an analytical solution that describes the motion of N-particle systems ($\boldsymbol{\Gamma}(t) = \mathrm{e}^{\mathrm{i}\mathcal{L}t}\boldsymbol{\Gamma}(0)$) is unavailable, the motion for constituent particles is integrated in the phase space at the *present* time, t, over a small time increment Δt, where $\Delta t \to 0$ [55, 103]. MD simulations need to resolve atomic-level vibrations [57] so that the timestep Δt is required to lie in the order of few femtoseconds (10^{-15} s). As the atomic frequencies are in the range of 10^{12} Hz [57], $\approx 10^2$ steps are usually sufficient to represent a full oscillation period with a reasonable numerical accuracy [57].

Along these lines, positions $\boldsymbol{r}(t)$ and momenta $\boldsymbol{p}(t)$ are successively updated throughout the simulation using *numerical stepping* [56]. Under this framework, the computation of $\boldsymbol{\Gamma}(t + \Delta t)$ at every simulation step then implies

$$\boldsymbol{\Gamma}(t + \Delta t) = \mathrm{e}^{\mathrm{i}\mathcal{L}\Delta t}\boldsymbol{\Gamma}(t). \qquad (3.3)$$

Note that $\boldsymbol{\Gamma}(t)$ evolves in time as prescribed by the time-reversible (deterministic) propagator $\mathrm{e}^{\mathrm{i}\mathcal{L}\Delta t}$ (Eq. (3.2b)) [106].

Each particle of an N-particle system at thermal equilibrium does not necessarily stay in the state of minimum energy. Instead, particles may be found in any state with an *exponential* probability function, φ_j, depending on the energy of microstate j [56, 103]. This implies that the microstates are *distributed* according to the canonical ensemble [56, 103, 104],

$$\varphi_j(\boldsymbol{r}_j, \boldsymbol{p}_j) = \frac{\mathrm{e}^{-\beta\mathcal{H}_j(\boldsymbol{r}_j, \boldsymbol{p}_j)}}{\sum_{j=1}^{N} \mathrm{e}^{-\beta\mathcal{H}_j(\boldsymbol{r}_j, \boldsymbol{p}_j)}}\,, \qquad (3.4)$$

where $\beta = (\mathrm{k_B}T)^{-1}$ ($\mathrm{k_B}$ is the Boltzmann constant and T is temperature) and $\mathcal{H}_j(\boldsymbol{r}_j, \boldsymbol{p}_j)$ is the Hamiltonian of particle j (or the energy of microstate j) [103]. The denominator of the above equation is the partition function that normalizes φ as $\sum_j \varphi_j = 1$ [104, 107].

The continuous form (large N) of the probability distribution φ provides the fundamental description of the particle system at thermodynamic equilibrium [104], where

$$\varphi(\mathbf{\Gamma}) = \frac{e^{-\beta\mathcal{H}(\mathbf{\Gamma})}}{\int d\mathbf{\Gamma}\, e^{-\beta\mathcal{H}(\mathbf{\Gamma})}}\,. \tag{3.5}$$

This equation is a powerful statement as it enables the connection of experimentally measurable (macroscopic) properties of materials with the statistical behavior of the constituent particles [103, 108]. The fraction of time that particles spend in each microstate strictly satisfies Eq. (3.4) during the evolution of a particle system [56]. Thus, macroscopic quantities of the system can be defined as a fundamental function of the statistical averages of individual-particle properties over the canonical ensemble $\varphi(\mathbf{\Gamma})$ [104]. Under this particle distribution [108], the average value ($\langle...\rangle$) of the observable $\Omega = \Omega(\mathbf{\Gamma})$ at time t is expressed as [103, 104]

$$\langle\Omega\rangle_t = \int d\mathbf{\Gamma}_t\, \varphi(\mathbf{\Gamma}_t)\, \Omega(\mathbf{\Gamma}_t). \tag{3.6}$$

3.2. The MD simulations

Present MD simulations are conducted with the LAMMPS code [109]. The simulations employ Nosé-Hoover chains [106, 110] producing *NVT* or *NPT* dynamics with the equations of motion (EOM) described respectively in Appendix A1.4 and Appendix A1.5, which systematically sample the *canonical* distribution (Eq. (3.5)). Atom positions and momenta are updated at every computational step by means of the time-reversible r-RESPA algorithm [105] which integrates Eq. (3.3), see Appendix A1.6.

3.2.1. Construction of FCC and BCC crystals

The atomic interactions between constituent particles are described through embedded-atom method (EAM) potentials [56, 111]. This model is based on concepts coming from density functional theory which stipulates that the energy of an atom is a function of the spatially-dependent electron density [58, 60]. The EAM model defines the *potential* energy of atom j [58] as

$$V_j(\mathbf{r}_j) = \sum_{j \neq k} F(\rho_j) + \frac{1}{2}\sum_{\substack{j,k \\ j \neq k}} \phi(\mathbf{r}_{jk})\,, \tag{3.7}$$

where $\rho_j = \sum_{j \neq k} \rho_j(\mathbf{r}_{jk})$ stands for the electron density contribution from atom j to atom k [112]. The total electron density ρ_j at the position of atom j is computed via a linear superposition of the electron-density contributions from neighboring atoms [55]. $F(\rho_j)$ is a functional that defines the energy required to embed atom j into the electron density ρ_j [112]. The second term of the right-hand side represents core-core repulsion between atom j and atom k [58], where $\phi(\mathbf{r}_{jk})$ is a pair-wise potential [56, 58]. Since available EAM potentials effectively reproduce the elastic and plastic features of many metallic crystals [60, 112-114], such embedding-function models have been largely used in the investigation of metal plasticity [15, 37-40, 89, 97, 98, 102, 115-117].

The simulated crystals are generated by distributing the particles (atoms) in the ideal crystallographic locations throughout the entire simulation domain [118], so as to construct a supercell with the desired dimensions. Figure 3.1 illustrates the basis atoms in FCC and BCC representative unit cells [118]. In this work, the three main [i.e. the (001), (011), and (111)] orientations are obtained (Fig. 3.2) by rotating the main axes as given in Table 3.1.
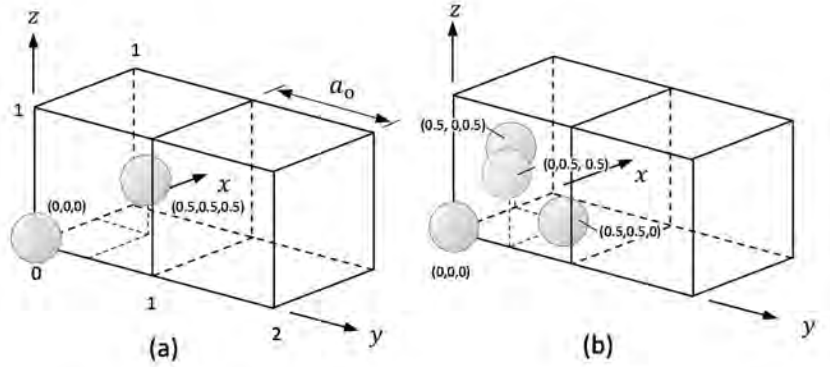
Figure 3.1. Basis atoms (in lattice coordinates) for BCC (a) and FCC (b) crystals.
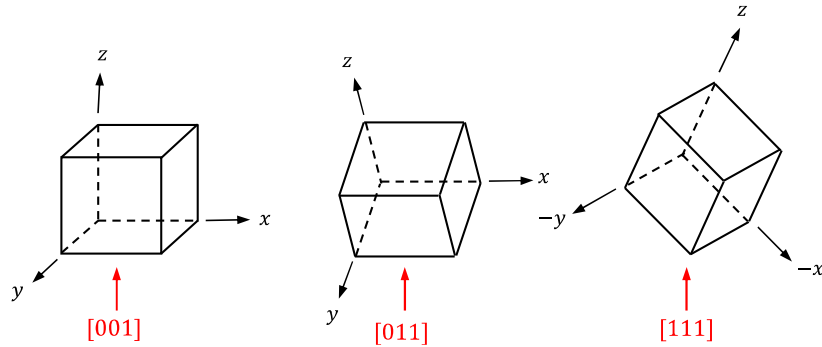
Figure 3.2. Schematic representation of the crystalline rotations applied to the representative cells in present MD simulations

Table 3.1. Axes directions for the main crystallographic orientations.

Crystalline orientation*	x-axis	y-axis	z-axis
(001)	[100]	[010]	[001]
(011)	[100]	[01$\bar{1}$]	[011]
(111)	[$\bar{1}$01]	[1$\bar{2}$1]	[111]

*Miller indices of the top (indented or uniaxially compressed) surfaces of the computational domains.

Note that the spatial atom distributions of Fig. 3.1 correspond to the ground state where atoms occupy the positions of the lowest energy state (i.e. satisfying the equilibrium lattice constant predicted by the interatomic potential at $T = 0$ K). Particle velocities distributes the energy associated with temperature $2T$ as the system's energy abruptly drops to a half during the first interactions (energy equipartition [57]). A *thermalization* run of several picoseconds [55, 103] ensures that the energies of the particles agree with the canonical distribution (Eq. (3.4)) at temperature T [55].

25

In this investigation, four different simulation volumes are employed. The computational cells are cuboidal-shaped volumes varying from ≈ 36 (length) $\times 36$ (width) $\times 18$ nm (height) to $\approx 105 \times 105 \times 40$ nm. Table 3.2 provides the nomenclature employed for the present MD cells which contain a number of atoms varying from $\approx 1 \times 10^6$ to $\approx 40 \times 10^6$, see Table 3.3. The presently employed cells are comparable to those used in the most computationally demanding (massive) MD simulations of metal plasticity from the open literature, including simulations of nanoindentation responses [15, 37-39, 60, 97, 98, 119-126].

Table 3.2. Nomenclature and dimensions of the simulation.

Box type	Box length	Box size (nm³)
Small	36 nm	$\approx 36 \times 36 \times 18$
Medium	50 nm	$\approx 50 \times 50 \times 30$
Big	70 nm	$\approx 70 \times 70 \times 40$
Large	105 nm	$\approx 105 \times 105 \times 40$

Table 3.3. Potentials and modeled crystals.

Crystal	Structure	a_o (Å)	T_m (K)[†]	Box type	Number of atoms	EAM Potential
Tantalum (Ta)	BCC	3.3026	≈ 3290	Small	$\approx 1,350,000$	Li et al [113]
				Big	$\approx 10,700,000$	
Iron (Fe)	BCC	2.855	≈ 1811	Medium	$\approx 6,500,000$	Mendelev et al. [112]
				Big	$\approx 16,850,000$	
Copper (Cu)	FCC	3.615	≈ 1358	Small	$\approx 1,820,000$	Mishin et al [114]
				Big	$\approx 16,300,000$	
				Large	$\approx 38,200,000$	
Aluminum (Al)	FCC	4.05	≈ 933	Big	11,650,000	Mishin et al. [114]

Additionally, Table 3.3 provides the crystalline structure, lattice constant (a_o), melting point (T_m) and the employed EAM potentials of the simulated metallic crystals. In particular, Tantalum (Ta) and iron (Fe) are chosen here as model BCC metals. From these two, it is noted that Ta is rather stable to oxidation [36], which is an important feature when comparing simulations with experimental results as the presence of an oxide layer is disregarded in Ta surfaces [36]. In addition, the simulations performed in FCC metals aim to probe the plasticity mechanisms developing in crystals with distinct stacking-fault energy (Section 2.2). Thus, copper (Cu) and aluminum (Al) respectively represent the behavior of moderate/low and high SFE FCC crystals.

3.2.2. The simulation of nanoindentation

Figure 3.3 illustrates the simulation domain in the present simulations of nanoindentation test, including sample and indenter. The particle system (sample) is a canonical *NVT* ensemble (Appendix A1.4) with periodic boundary conditions (PBCs) applied on the lateral sides. The indented plane corresponds with the free top surface. By imposing a $1.25a_o$ layer at the box surface of the computational cell where atoms ultimately remain fixed (in red in Fig. 3.3), the MD cell is forced to maintain its position during loading, see Fig. 3.3. The indenter is modeled as a repulsive sphere (Fig. 3.3) which exerts a force to the particle system [59] described by

$$F(x) = \begin{cases} -K\left(\dfrac{D}{2} - \delta\right)^2, & \delta < \dfrac{D}{2} \\[2mm] 0, & \delta \geq \dfrac{D}{2} \end{cases}, \tag{3.8}$$

where K is the *indenter stiffness* and $x = (D/2 - \delta)$. D is the indenter diameter (Fig. 3.3) and δ is distance between atom and indenter center. In all the simulations, K is set to 100 eV/Å^3 and D varies from 24 nm to 100 nm, see Table 3.4. The indentation process is performed under displacement control with tip penetration velocity ranging 0.2 m/s to 30 m/s (Table 3.4). The effect of the loading rate arising in such MD simulations is discussed in the Appendix A5.1. All of the indented surfaces are loaded to a maximum penetration, $h_{\max}$, which produces a contact imprint of radius a that is approximately a fourth of the total box length. The timestep Δt is set to 3 femtoseconds ($= 3 \times 10^{-15}$ s), see Appendix A3. The load applied by the indenter tip (along the vertical direction) is computed by adding each individual $F(x)$ contribution from the atoms satisfying $\delta \leq D/2$, see Appendix A3. Delaunay triangulation is employed to compute the projected contact area, $A = \pi a^2$, comprised by the atom coordinates where $F > 0$ and $\delta \leq D/2$ in Eq. (3.8), see Appendix A4.

Table 3.4. MD simulations of nanoindentation responses conducted in this investigation.

Crystal	Size*	T (K)	T/T_{m}	Indented surface	D (nm)	Indentation rate(s) (m/s)	Indentation*** stage
Tantalum (Ta)	36 nm	77	≈ 0.02	Main**	24	4	Load
	70 nm	77	≈ 0.02	Main	48	4	Load/unload
	70 nm	900	≈ 0.3	Main	48	4	Load
Iron (Fe)	50 nm	77	≈ 0.05	(001), (111)	36	4	Load
	50 nm	300	≈ 0.15	(001)	36	4	Load
	50 nm	600	≈ 0.3	(001)	36	4	Load
	50 nm	750	≈ 0.4	(001)	36	4, 30	Load
	50 nm	900	≈ 0.5	(001)	36	4, 30	Load
	70 nm	77	≈ 0.05	(001)	48	4	Load
	70 nm	900	≈ 0.5	(001)	48	4	Load
Copper (Cu)	36 nm	77	≈ 0.06	Main	48	4	Load
	70 nm	77	≈ 0.06	Main	48	4	Load/unload
	70 nm	400	≈ 0.3	(011)	48	4	Load
	105 nm	77	≈ 0.06	(001)	100	30	Load
Aluminum (Al)	70 nm	300	≈ 0.3	Main	48	4	Load/unload
	70 nm	300	≈ 0.3	Main	100	0.02, 4	Load

*Size refers to the nomenclature given in Table 3.2.
**Main indicates all the (001), (011) and (111) crystallographic orientations (of the indented surface), see Fig. 3.2.
***Load stands for a single loading cycle to $h_s = h_{\max}$, and Load/unload refers to a single load-unload cycle (which includes indentation loading to $h_s = h_{\max}$ and reverse (un)loading to $h_s = 0$), see Fig. 4.9.
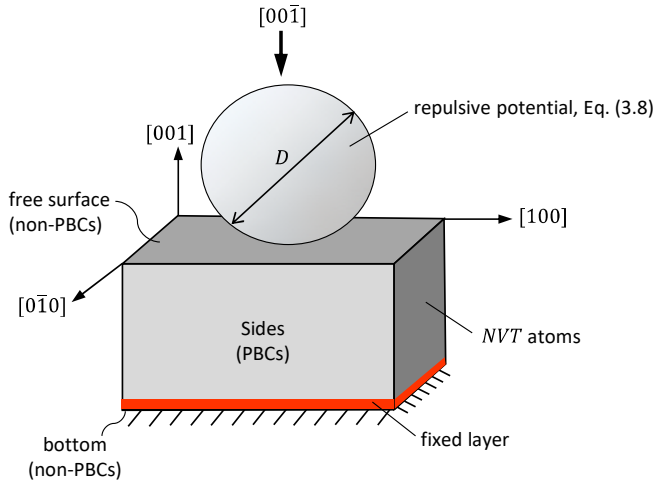
Figure 3.3. Schematic of the MD simulations of (001) indentation.

Appendix A2 provides a complementary discussion on the role that the NVE, NPT and NVT statistical ensembles play in prescribing nanocontact elasticity and plasticity in FCC and BCC crystals. In addition, Appendix A3 features a detailed analysis of the action of Eq. (3.8) reproducing contact responses with spherical tips.

3.2.3. The simulation of the uniaxial test

The simulations performed to assess the uniaxial stress-strain curve have the peculiarity that, prior to the application of uniaxial straining, the *periodic* computational domains contain a well-distributed, preexisting dislocation network. This configuration is obtained by indenting the (defect-free) crystals through the procedure described in the previous section at large indenter penetrations, leading to the attainment of dense defect networks in both FCC and BCC crystals (Fig. 3.4(a)) [119]. These computational volumes are modified by removing the indentation imprint, where particles with a vertical component $> (z_{\text{box}} - c_{\text{imp}})$ are eliminated from the simulation box, see Fig. 3.4(b). PBCs are finally imposed to the modified computational domain (Fig. 3.4(b)), which is then subjected to (i) energy minimization by means of the conjugate gradient algorithm [118, 127], and (ii) a thermalization run over ≈ 50 ps under the isothermal-isobaric canonical NPT ensemble, maintaining the diagonal components of the pressure tensor at zero (Appendix A1.5). This ensures a homogenous dissemination of the dislocation networks throughout the periodic computational domains as well as the attainment of thermal equilibrium at temperature T. The so produced computational cells represent the initial conditions ($t = 0$) employed in the modeling of the uniaxial response (Fig. 3.4(c)).

The system's pressure tensor, $\boldsymbol{P}$, is computed by the 6-by-6 symmetric stress tensor [118]

$$\boldsymbol{P} = \begin{pmatrix} P_{xx} & P_{xy} & P_{xz} \\ P_{yx} & P_{yy} & P_{yz} \\ P_{zx} & P_{zy} & P_{zz} \end{pmatrix} \tag{3.9a}$$

defined as

$$P_{IJ} = \frac{\sum_k^N m_k v_{kI} v_{kJ}}{V} + \frac{\sum_k^{N'} r_{kI} f_{kJ}}{V} , \tag{3.9b}$$

where sub-indices I, J stand for I and $J = x, y, z$; $k = 1, 2, \ldots, N$; and N' includes (apart from the N constituent particles of the system) periodic-image atoms outside the simulation box [128]. The first term in the right-hand side of Eq. (3.9b) uses components of the kinetic energy tensor K_{IJ}, while the second term employs components from the virial tensor [118, 128]. Vector $\boldsymbol{f}_k$ is an outcome from Eq. (3.7) as $\boldsymbol{f}_k = -dV(\boldsymbol{r}_k)/d\boldsymbol{r}_k$, where $V(\boldsymbol{r}_k)$ is the potential energy of atom k [118].
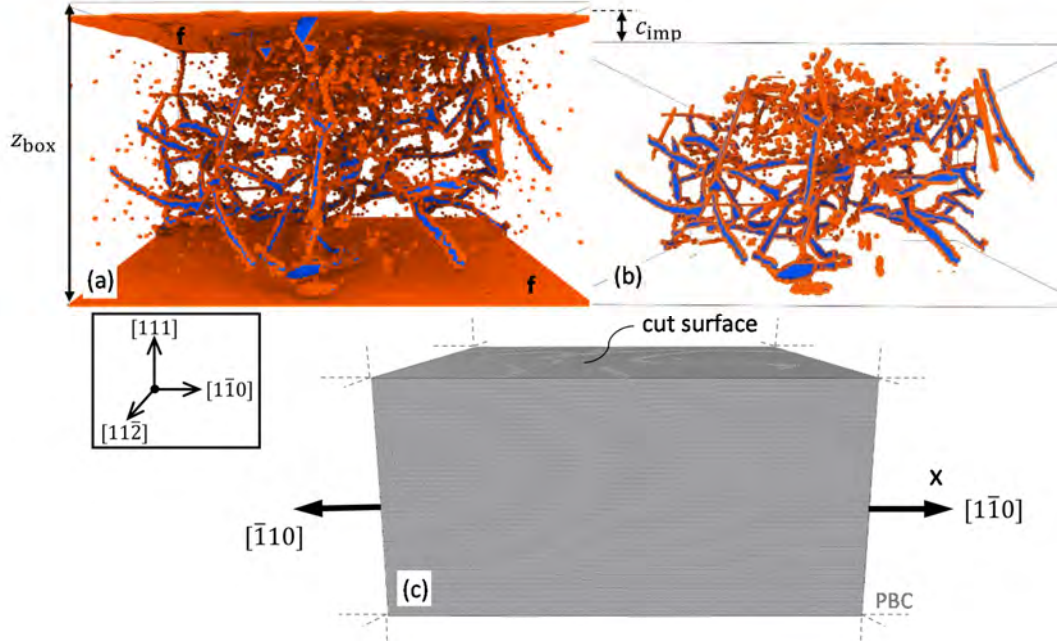
Figure 3.4. Computational procedure applied to simulate plastic responses under the uniaxial straining. (a) Representation of the MD box upon indentation preloading producing a well-distributed defect network. The snapshot corresponds to the Al (111) indentation (with $D = 48$ nm and 70-nm box) at tip penetration ≈ 36 Å. Atom coloring corresponds to the common neighbor analysis (CNA) [129], see Appendix A6. "f" denotes free surface while PBC are applied to the 4 lateral sides (see Appendix A6). (b) Computational domain with the dense defect network developing upon removal of the surface layer containing the permanent imprint (marked c_{imp} in picture (a)). (c) Particle system with $\approx$10M atoms (in grey) prior to uniaxial straining along $[\bar{1}10]$ and $[1\bar{1}0]$ directions (x-axis), where energy minimization and thermalization have been already applied.

The simulations involve *uniaxial stretching* of the periodic computational domains (Table 3.5) in such a way that the particle system deforms under a *constant* strain rate ($\dot{\varepsilon}$). The constituent particles are then *remapped* to the instantaneous dimensions of the simulation box in *each* computational step [118]. These conditions ensure strict displacement-controlled straining of the cuboidal computational cells along the stretching direction, while the barostat acts in the other two principal directions. According to Ref. [130], this computational framework provides the most accurate statistical definition for a particle system subjected to uniaxial stretching.

The applied stress σ is directly obtained from the quantity P_{xx} in Eq. (3.9a) and computed by Eq. (3.9b). The imposed strain ε is calculated as $\varepsilon = (l_x - l)/l_0$, where l_0 and l_x are the initial (at time $t = 0$) and instantaneous (at time t) simulation box lengths in the x-direction [118], see Fig. 3.4(c). The timestep is set to 2 fs (= 2×10^{-15} s). The details of the simulations that are carried out to mimic uniaxial test are given in Table 3.5.

Appendix A5.3 provides a discussion on the influence of the strain rate on the onset of a generalized plastic behavior in uniaxially deformed (periodic) MD crystals, where the fundamental intermittent character of crystal plasticity is observed when $\dot{\varepsilon} < 1.5 \times 10^8$ s^{-1}.

Table 3.5. MD simulations of uniaxial straining performed in this investigation.

Crystal	Size*	T (K)	T/T_m	Indentation**	Stretching direction†	stretching rate (m/s)††	$\dot{\varepsilon}$ (s^{-1})
Ta	70 nm	300	≈ 0.1	$D = 48$nm (011) at 900 K	[100]	≈ 0.8	1.2×10^7
	70 nm	300	≈ 0.1	$D = 48$nm (011) at 900 K	[100]	≈ 0.1	1.5×10^6
	70 nm	900	≈ 0.3	$D = 48$nm (011) at 900 K	[100]	≈ 0.1	1.5×10^6
Cu	36 nm	150	≈ 0.1	$D = 24$nm (001) at 77 K	[100]	≈ 1	1.5×10^7
	36 nm	150	≈ 0.1	$D = 24$nm (001) at 77 K	[100]	≈ 0.1	1.5×10^6
	70 nm	400	≈ 0.3	$D = 48$nm (001) at 77 K	[100]	≈ 0.8	1.2×10^7
	70 nm	400	≈ 0.3	$D = 48$nm (111) at 77 K	[1$\bar{1}$0]	≈ 0.1	1.5×10^6
	70 nm	650	≈ 0.45	$D = 48$nm (111) at 77 K	[1$\bar{1}$0]	≈ 0.1	1.5×10^6
Al	36 nm	300	≈ 0.3	$D = 24$nm (111) at 300 K	[1$\bar{1}$0]	≈ 30	4.5×10^8
	70 nm	300	≈ 0.3	$D = 48$nm (111) at 300 K	[1$\bar{1}$0]	≈ 100	1.5×10^9
	70 nm	300	≈ 0.3	$D = 48$nm (111) at 300 K	[1$\bar{1}$0]	≈ 4	8×10^7
	70 nm	300	≈ 0.3	$D = 48$nm (111) at 300 K	[1$\bar{1}$0]	≈ 0.8	1.2×10^7
	70 nm	300	≈ 0.3	$D = 48$nm (111) at 300 K	[1$\bar{1}$0]	≈ 0.1	1.5×10^6

*Box sizes described in Table 3.2. Note that the box height in these MD simulations is reduced by the removal of layer marked c_imp in Fig. 3.4(b).

** *Indentation* refers to the nanoindentation simulation that produced the dislocation network prior to the tensile (uniaxial) test. The MD simulations of the nanoindentation pre-straining stage are in accord with Table 3.4.

† *Stretching direction* is referred to the positive x-axis direction (see Fig. 3.4(c)).

†† The stress-strain curves obtained at ≈ 0.1 m/s are for an MD cell that has been pre-strained to $\varepsilon \approx 0.03$ at ≈ 0.8 m/s to ensure defect homogenization (see Section 6.4).

CHAPTER 4.

SURFACE PILE-UP AND SLIP-TRACE PATTERNING AROUND NANOINDENTATIONS

4.1. Slip trace patterning in microindentation experiments

The emission of slip traces at free surfaces is a fundamental manifestation from crystal plasticity. This is particularly evident in nanoindentation testing where these traces are indicative of the underlying dislocation glide processes occurring in the subsurface [69, 70, 131]. With increasing indenter-tip penetrations, the collective emission of slip traces leads to the onset of nanoscopic terraces at the imprint's vicinity [67]. The interaction of terraces results in the development of plastic hillocks whose morphologies then exhibit a marked directionality as a function of crystalline orientation [68-70]; this directional patterning is referred to as dislocation *rosettes* in early indentation literature [132]). Figure 4.1 provides an illustration of the plastic phenomena which are concomitant with the formation of material pile-ups in single crystals.
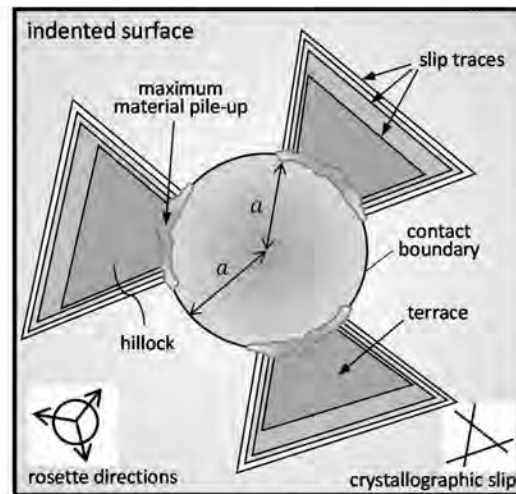
Figure 4.1. Schematic representation of slip trace patterning and material pile-up. Slip traces emerge as dislocations reach the surface. Terraces and hillocks are comprised by enclosed groups of slip traces. The indentation rosette involves the entire surface topography, which incorporates all terraces/hillocks around the imprint. Note that the maximum material pile-up are most likely located at some point close to the contact boundary.

The onset of the indentation rosettes (Fig. 4.1) marking the locations of plastic hillocks have been largely investigated in FCC [9, 133, 134] and BCC [36, 39] metals as well as in ionic crystals [9]. In these works, it is systematically investigated the strong role that the surface orientation plays in dictating the development of specific rosette morphologies. In particular, the experimental works by Wang et al. [133] and by Liu et al. [134] show that FCC crystals exhibit four-fold rosettes when indented along the (001) and (011) orientations, as well as a six-fold patterning in (111)-oriented surfaces, see Figs. 4.2(a)-(f). In addition, the experimental results by Renner et al. [131] evidence that surface patterning in indented FCC surfaces [135] essentially originates from the *collective* emergence of straight slip traces (Fig. 4.2(g)) in the <110> and <112> crystallographic directions (Figs. 4.2(h)-(j)). On the other hand, wavy slip traces are largely encountered around BCC nanoimprints (Fig. 4.3), indicating that the ill-defined glide of screw dislocations governs the inception of hillock morphologies in the nano-

indented Ta crystals from Ref. [36]. According to this investigation, a four-fold symmetry patterning appears in (001)-oriented BCC surfaces (Figs. 4.3(a)-(b)), while the (111) orientation is distinguished by the onset of three-fold symmetry rosettes (Fig. 4.3(d)) [36].
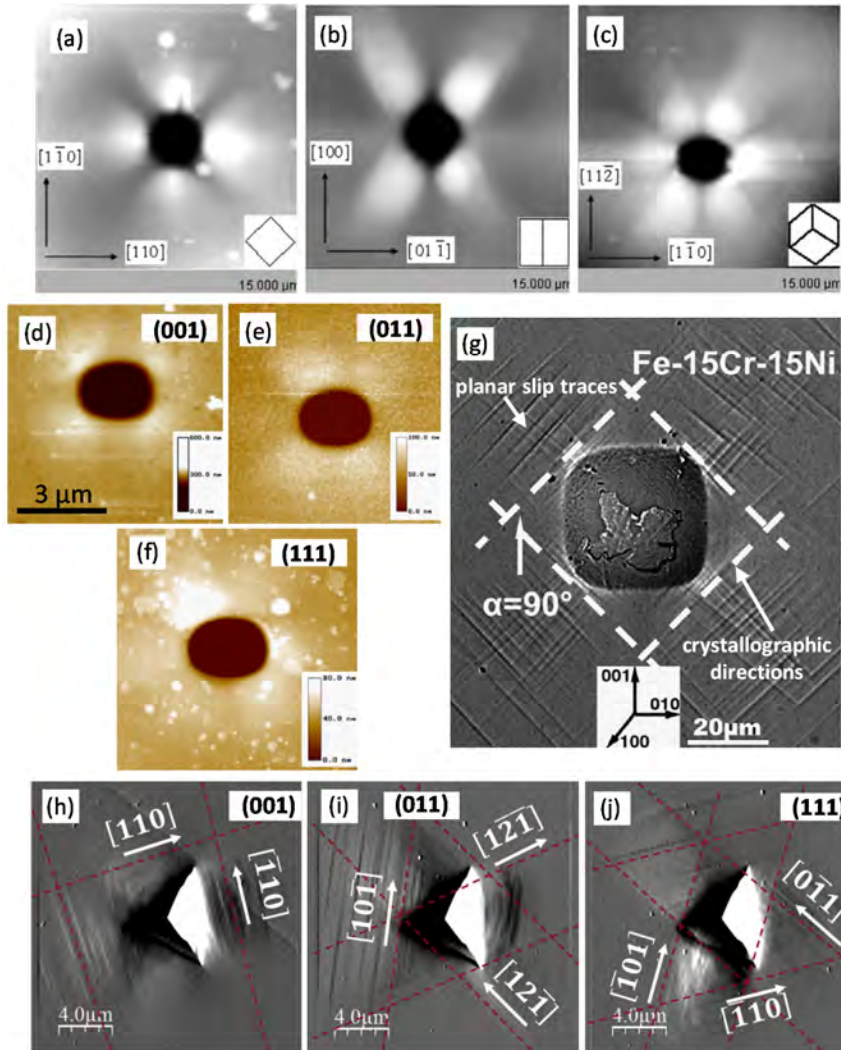
Figure 4.2. Microindentation experiments in FCC surfaces. (a)-(c) summarize the results from Ref. [133] and (d)-(f) summarize the results from Ref. [134] regarding the development of plastic rosettes at particular orientations in Cu surfaces. (g) Emergence of crystallographic slip traces in (001)-oriented FCC surfaces [135]. (h)-(j): Attainment of crystallographic slip directions as a function of surface orientation [131].
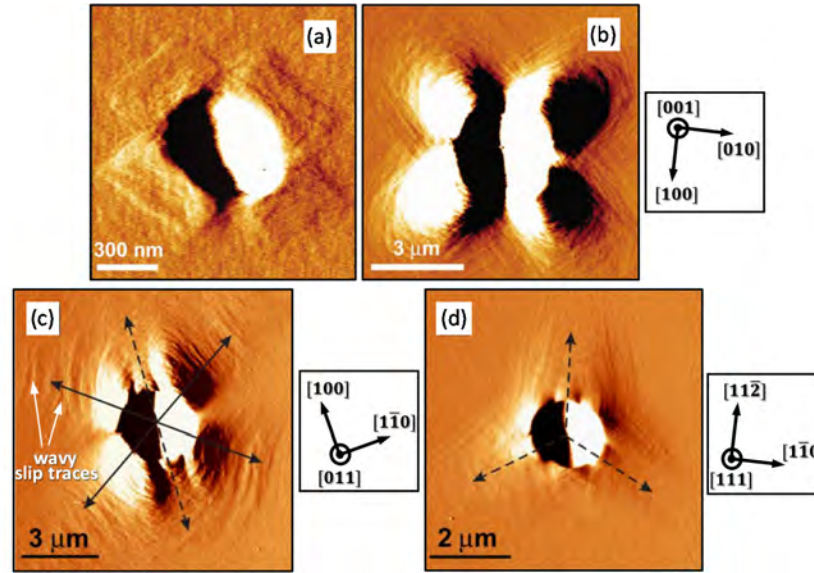
Figure 4.3. Experimental results of nanoindentations in Ta. (a)-(c): Four-fold rosettes develop in (001)-oriented surfaces as well as (tentatively) in the (011) orientation [36]. (d) Emergence of a three-fold rosette in (111)-oriented Ta [36]. Wavy traces are marked with white arrows in (c), while the additional black arrows in (c) and (d) denote rosette directions.

Although the onset of specific rosettes in FCC and BCC surfaces indented with nanometer- and micrometer-sized tips has been illustrated in the above investigations [9, 36, 39, 133, 134], the collective dislocation glide processes that lead to the development of the hillock morphologies remains unclear in the open literature. It is important to emphasize that surface patterning from micro-indentation testing fundamentally differs from that obtained with nanoindenters, as the latter develops under a preexisting dislocation network [69, 70] while the emission of slip traces in ultra-low load nanoindentation originates from nucleated defects [14, 38]. Moreover, in nanoindentation, twinning becomes an important plasticity mechanism owing to the large applied stresses as compared to in micro- and macro-indentation testing [38, 98, 102]. In this context, there is a lack of knowledge about the role that the distinct defect propagation mechanisms (i.e. dislocation glide vs. nanotwinning) play in the emission and patterning of slip traces at the surface, which lead to the inception of characteristic material pile-ups around FCC and BCC nanoimprints. This lack of knowledge on surface slip patterning is extended to (i) the role of the thermally-activated mobility of the screw dislocations in BCC crystals along with the hindrance of cross slip in low stacking fault energy FCC crystals; as well as to (ii) the role of the nucleation of distinct FCC and BCC defect structures. This chapter provides a detailed discussion on these issues as elucidated in the MD simulations performed for a wide range of temperatures, surface orientations and nanoindenter tip sizes (see Table 3.4).

4.2. Mechanisms for slip trace formation

4.2.1. FCC nanocontacts

In FCC crystals, slip trace formation results from {111} crystallographic slip of two partnering Shockley dislocations (Section 2.2), where the leading partial sweeps across the surface and the trailing dislocation closes the stacking fault ribbon leaving a trace at the surface. Figures 4.4(a) and 4.4(b) illustrate the formation of a slip trace by a screw dislocation ($\boldsymbol{b} \parallel \boldsymbol{\xi}$) and by an edge dislocation ($\boldsymbol{b} \perp \boldsymbol{\xi}$), respectively. The slip trace height matches the net vertical component of the dislocation Burgers vector $\boldsymbol{b} = \boldsymbol{b}_1 + \boldsymbol{b}_2$ (Fig. 4.4(a)), where $\boldsymbol{b}_1$ and $\boldsymbol{b}_2$ are the respective Burgers vectors of the leading and trailing partial dislocations. Note that the corresponding height of the slip trace takes a maximum value when vector $\boldsymbol{b}$ lies perpendicular to the surface. According to Fig. 4.4(b), the glide of the surfaced edge dislocations tends to produce slip traces of smaller heights than those produced by the gliding of the surfaced screws (Fig. 4.4(a)). This is so as the burgers vectors of the former edge dislocations are approximately parallel to the surface normal. The simulations show that while such edge dislocation lines emerge at the surface, the largest dislocation population has the predominantly screw character shown in Fig. 4.4(a) which leads to large trace heights.

Figure 4.5 shows specific slip trace emissions in the indented FCC surfaces, where the yellow arrows denote crystallographic directions. The emission of a slip trace is associated with the interception of the indented plane and the corresponding {111} slip systems (Section 2.2). This leads to the inception of 4 <110> slip directions in the (001) orientation (Fig. 4.5(a)) whose glide plane forms 54.7 ° with the indented surface, and 6 directions in the (011)- and (111)-oriented surfaces. It is noted that the (011) orientation exhibits preferentially <110> crystallographic slip $\approx$35º apart from the surface and <112> slip directions perpendicular (90º) to the indented plane (Fig. 4.5(b)). In (111) oriented surfaces (Figs. 4.5(c)-(d)), the <110> slip traces form an angle of 70.5 ° with the surface.

The slip traces detected in the indented FCC surfaces (Fig. 4.5) originate from the following mechanisms. (i) Outwards gliding of truncated prismatic loops pinned at the surface. Figure 4.4(c) shows the early arrangement of these loops in (001)-oriented Cu. Similar dislocation configurations are found in the (011) and (111) orientations during the incipient development of plasticity [37]. (ii) Annihilation of SF ribbons (Fig. 4.4(e)) leading to the emission of expanding dislocation loops producing antiparallel slip traces at the surface (Fig. 4.4(f)). This mechanism is an effective source for the injection of mobile surface dislocations. (iii) Slip of dislocation arrangements (predominantly with edge character) which remain pinned at the indented surface. See the W-shaped defect configuration marked "w" in Fig. 4.4(d). (iv) Detachment of dislocations from multi-segment junctions that leads to the emergence of dislocation segments at the surface. Figs. 4.4(h)-(j) show activation of an intricate four-fold junction node during the indentation of the (111) plane in Cu. According to the simulations, the mechanism (i) is characteristic of early plasticity while the mechanisms (ii)-(iv) produce slip traces at greater indenter tip penetrations under a fully-developed (dense) defect structure, where a gradual development of material pile-ups attains at the contact boundary in conjunction with slip patterning.
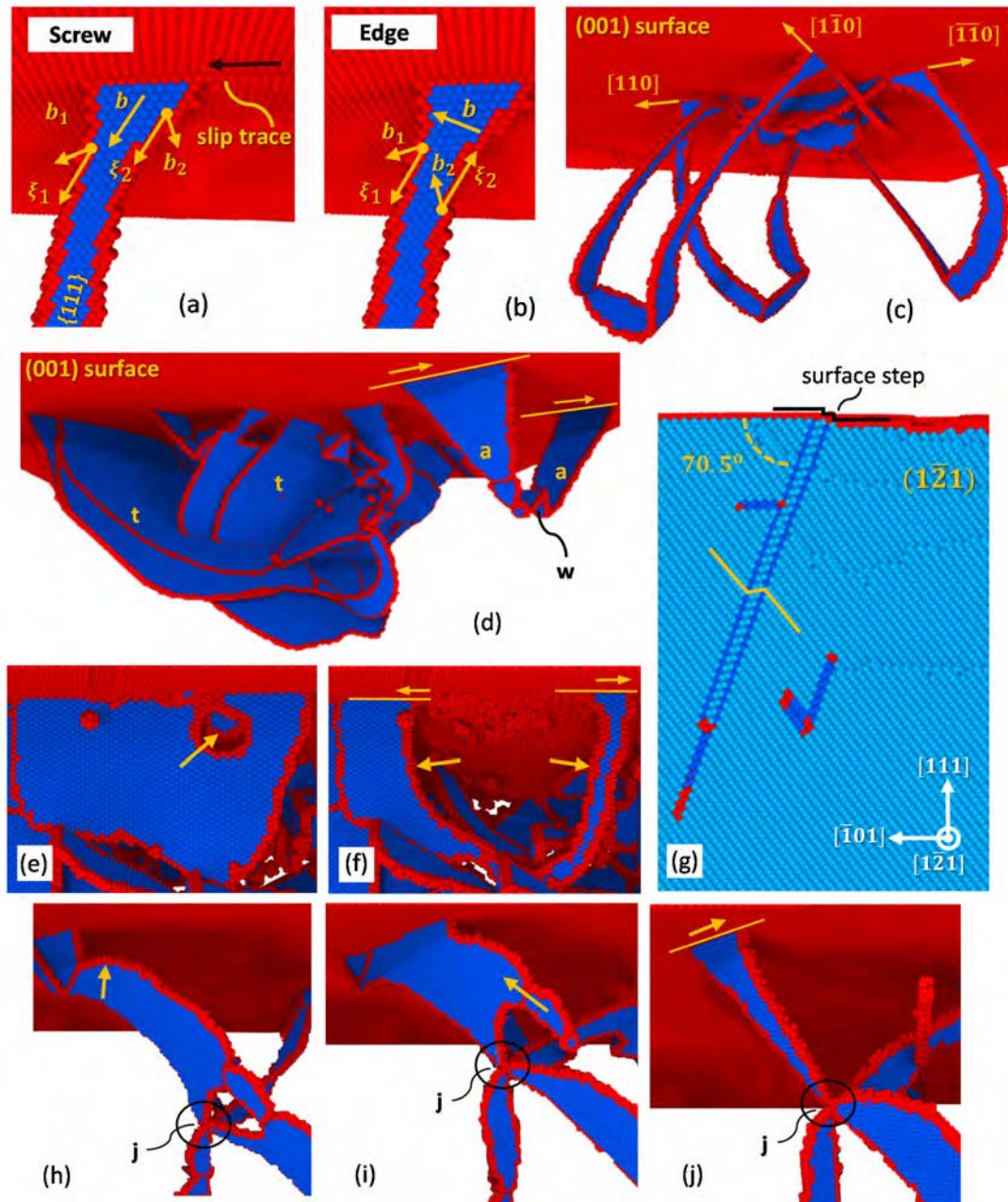
Figure 4.4. Mechanisms of slip trace emission in Cu nanoindentations. The simulations are performed with $D = 48$ **nm at 4 m/s. (a) and (b): Formation of a slip trace through the passage of a screw and an edge dislocation (respectively) dissociated into leading (1) and trailing (2) partials separated by SF ribbons (blue). (c) Prismatic loops producing early traces in the (001) indentation at** $T = 77$ **K. (d) Interception of nanotwins ("t") forming** $\approx 55^0$ **with the (001)-oriented surface and the attainment of an arrangement of edge dislocations ("a"), where yellow lines indicate glide direction and "w" marks the serrated features of the dislocation configuration. (e) and (f): Dissociation (arrow in (e)) of a large SF ribbon into a loop. (g) Cross-sectional** $(1\bar{2}1)$ **view of a nanotwin originated in the (111) indentation at** $T = 77$ **K. Yellow lines denote crystal orientation. (h)-(j): Sequence of dislocation emission from unzipping multi-junction "j". The emitted trace is marked in yellow in (j). Atomistic visualization is performed with the software OVITO, see Appendix A6.**

The Cu simulations reveal that the appearance of indentation nanotwinning (marked "t" in Figs. 4.5(a)-(c)) becomes manifest by the onset of a parallel array of slip traces associated with the shearing of {111} planes that produces a set of SF ribbons [98]. In particular, such nanotwin inception involves the emission of successive leading partial dislocations at the contact vicinity ($r \approx a$), where the indenter-induced shear strains are extremely large [20]. The Burgers vector of each leading partial dislocation is characterized by the same net vertical component, which results in the emission of a group of parallel steps of equal height separated by one atomic spacing at the indented surface, see Fig. 4.4(g). Present simulations also indicate that FCC nanotwinning attains normal to the surface in (011) indentations, or inclined at 54.7º or at 70.5º for (001) and (111) indentations, respectively (cf. Figs. 4.4(d) and 4.4(g)). It is important to remark that the majority of the emitted nanotwins remain under the residual imprint upon indenter unloading, which is indicative of the stability of the defects provided that a critical thickness of 5 atomic spacings is surpassed. In this regard, although the emission of nanotwins comprised by two or three single SF ribbons are commonly detected underneath the indenters, the SF planes annihilate passed a critical size (as shown in Figs. 4.4(e)-(f)). This mechanism promotes the dissociation of *unstable* (generally monatomic) twins and, thus, this leads to the emergence of further slip traces at the indented surface (Fig. 4.4(f)).
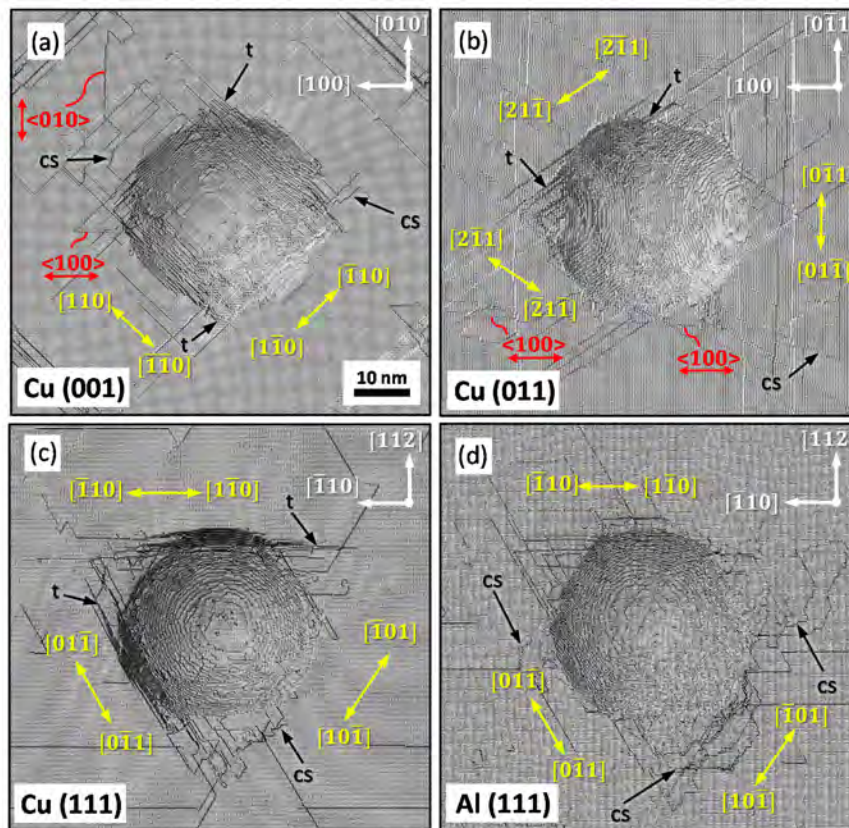
Figure 4.5. Slip traces in indented FCC surfaces at maximum penetration. The nanoindentations are performed with $D = 48$ nm at 4 m/s. The Cu and Al nanoimprints are incepted at $T = 77$ K and $T = 300$ K, respectively. Yellow arrows mark crystallographic slip directions, twinning is marked "t", and "cs" denotes cross-slip. Red directions indicate apparent non-crystallographic slip traces.

4.2.2. The role of the stacking fault energy and cross slip

Present simulations are consistent with the fact that twinning is promoted in low SFE metals, such as Cu, while twins are seldom found in such high SFE crystals as Al. It is for this reason that the onset of slip traces associated with twinning phenomena underneath the indenter tip are exclusively observed in the simulated Cu surfaces, see "t" traces in Fig. 4.5. Moreover, the role of the SFE in the development of a dislocation structure becomes evident in the extension of the SF ribbons between partials. In this context, nanoindentation in Cu crystals leads to the injection of dislocations with longer SFs (or, equivalently, greater δ_{Sh}, see Section 2.2) than those encountered in the indentation of Al counterparts. The simulations show that large values of δ_{Sh} reduce the mean traveled distance of the dislocations within the incepted network, which eventually becomes stagnant at deep penetration levels. Figure 4.6 illustrates the defect networks arising in indented Al and Cu crystals, where the yellow arrows in Figs. 4.6(a) and 4.6(b) mark δ_{Sh}.
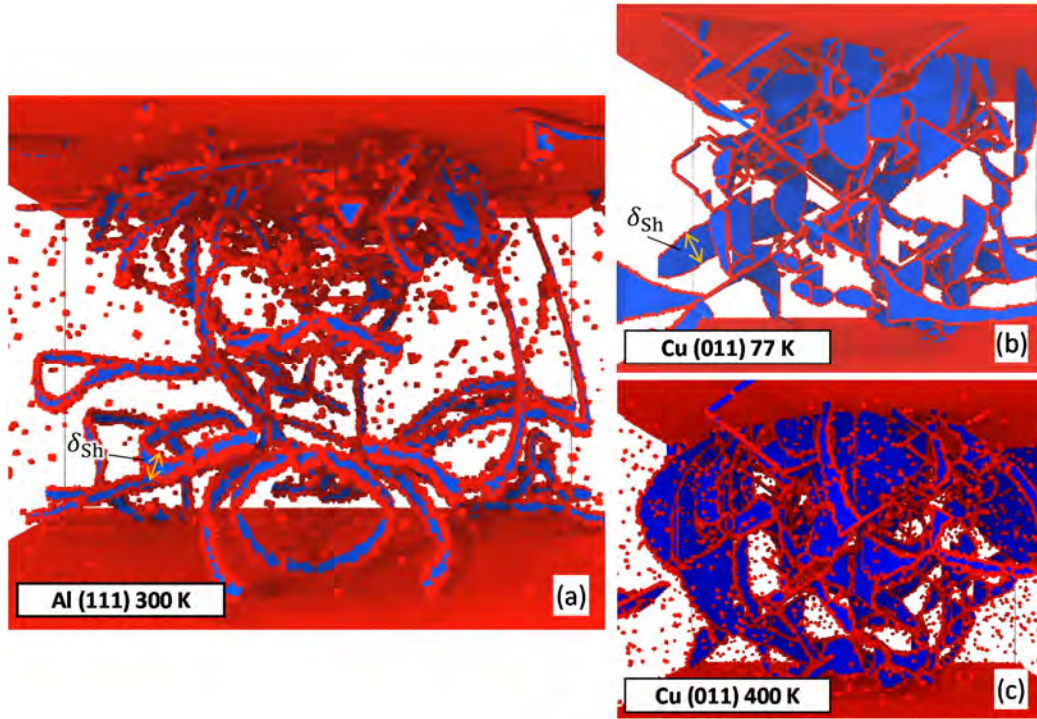
Figure 4.6. Defect networks in the Cu and Al nanoindentations. The nanoindentations are performed with $D = 48$ nm at 4 m/s. The snapshots show the loaded state at a large penetration ($h_s \approx 50$ Å). (a) Defect entanglement predominantly comprised by Shockley dislocations with small δ_{Sh} is shown for an Al (111) surface indented at $T = 300$ K. (b) and (c): Defect structures attained at 77 K and 400 K (respectively) following indentation of a Cu (011) surface. Notice the long SF ribbons (large δ_{Sh}) resulting from the simulations in Cu crystals. The atom clusters in red stem from the thermal vibrations affecting the CNA computations at elevated temperatures (pictures (a) and (c)), see Appendix A6.

The onset of straight traces is indicative of indentations performed in high SFE crystals whereas, by contrast, the attainment of zigzagged traces indicates cross slip see "cs" in Fig. 4.5 [136]. Figure 4.7(a) illustrates the operation of cross slip in a screw dislocation gliding at the indented Al (001) surface. The black arrow in Fig. 4.7(b) marks the associated change in the

<110> slip direction during the process (Fig. 4.7(a)). Cross slip (Section 2.2.1) is enhanced in the simulations of Al crystals (large SFE), where serrated traces clearly evidence the glide of the surfaced screw dislocation segments [136], see Fig. 4.5(d). Although the indentations in (011)-oriented Cu at 77 K and 400 K (Figs. 4.6(b) and 4.6(c) respectively) indicate that elongated and straight SF ribbons essentially attain irrespective of temperature, it is clear that the amount of cross slipped traces is increased at elevated temperatures which promote the onset of more entangled dislocation networks.
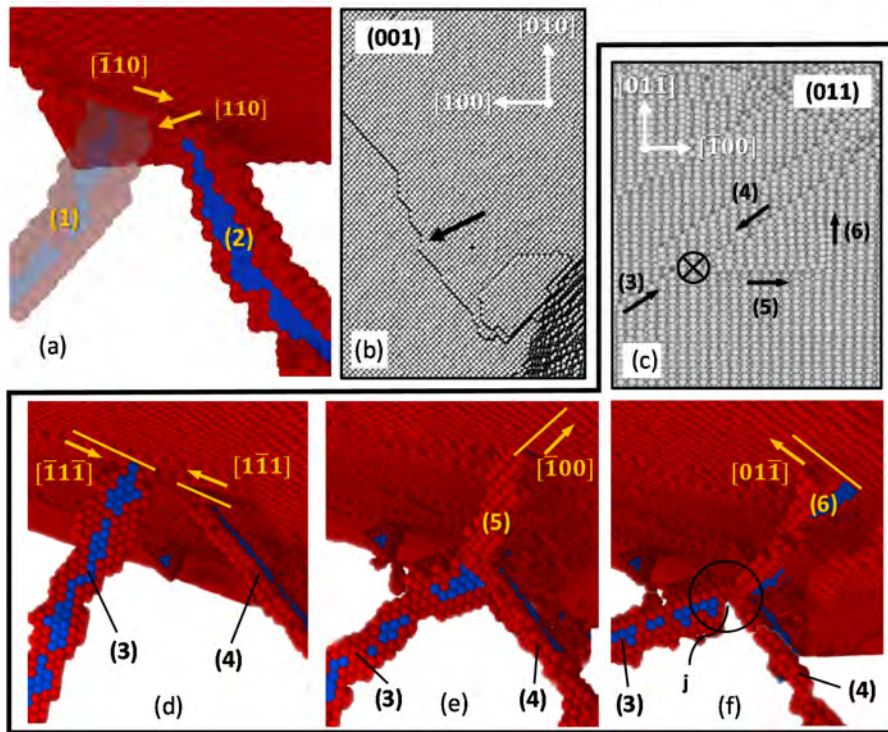
Figure 4.7. Dislocation glide at the subsurface in Al indentations. The nanoindentations are performed with $D = 48$ **nm at 4 m/s. (a) Screw (fainting) dislocation "(1)" gliding along the** $[\bar{1}10]$ **direction cross-slips to the** $[110]$ **direction (segment "(2)"). The corresponding cross-slipped trace from (a) is marked with a black arrow in (b). (d)-(f): Onset of an apparent (global) non-crystallographic slip trace in the (011)-oriented surface. Interaction of dislocation segments "(3)" and "(4)" produces non-dissociated segment "(5)" pinned with "(3)" and "(4)" at "j". Segment "(5)" is a constricted (sessile) dislocation whose glide produces a (non-crystallographic)** $[\bar{1}00]$ **trace at the surface. Dissociation of segment "(5)" into Shockley partials "(6)" (gliding in the** $[0\bar{1}1]$ **crystallographic direction) suppresses apparent non-crystallographic glide. The associated slip traces are marked with black arrows in (c), where the interaction point between dislocations "(3)" and "(4)" is highlighted with a cross.**

A mechanism that hinders cross-slip in FCCs is the straightening of surfaced dislocation segments either by the pinning action exerted by the dislocation forest in the subsurface or by the development of dislocation arrangements similar to that marked "w" in Fig. 4.4(d).

The simulations illustrate that crystallographic slip in FCCs may acquire a straight appearance along *non-crystallographic* <100> directions (marked in red in Fig. 4.5), which originate from the occasional interplay of two interacting dislocations (Fig. 4.7(d)) leading to the formation of a sessile (non-dissociated) junction truncated with the surface (Fig. 4.7(e)). The sweeping of the full dislocation produces a straight slip trace over several atomic spacings

along the non-crystallographic apparent <100> direction through multiple cross slip processes (see the trace produced by full dislocation "(5)" in Fig. 4.7(c)). Non-crystallographic slip is interrupted at a point where the full dislocation dissociates into leading and trailing partials (Fig. 4.7(f)), which restores the preferential <110> or <112> crystallographic glide at the surface (cf. Fig. 4.7(c)).

4.2.3. BCC nanocontacts

At low temperatures, nanocontact plasticity in BCC crystals is governed by a planar-to-linear evolution of the defect network [38]. In accordance with the Ta and Fe simulations, nanotwin nucleation dominates the inception of plasticity (Fig. 4.8(a)), whereas subsequent dislocation activity leads to network development at deeper penetrations as precursory twins gradually annihilate across the {112} twin boundaries [38]. The detwinning process results in the emission of dislocation semi-loops comprised by two lateral screw segments at the twin side and one frontal edge dislocation (lateral and frontal parts are marked "lat." and "fr." respectively in Figs. 4.8(a) and 4.8(b)). Although a significant number of the total dislocation segments is emitted as a result of the detwinning process, present simulations indicate that the greatest amount of slip traces at the surface are due to the emergence of heterogeneously-nucleated dislocation loops (Figs. 4.8(c) and 4.8(d)).

The screw vs. edge glide character of the dislocation loops at the surface (Fig. 4.8(c)) leads to two distinguishable patterns in terms of slip trace formation. Straight traces are associated with the emergence of mobile edge segments at the surface (Fig. 4.8(e)). Since climbing is essentially hindered in the edges (Section 2.3.1), the loops can only reach the surface when the associated <111> dislocation glide direction is conveniently directed towards the surface. Slip traces generated by screw segments are wavy and ill-defined (Fig. 4.8(e)), which readily suggest the attainment of kinking processes (Section 2.3.1). At low temperatures, propagation of screw segments involves nucleation of a leading kink that spreads along the screw line, followed by a secondary kink nucleation that trails behind [63], producing a stochastic motion of the segment by one Peierls barrier [63]. At elevated temperatures, the screws glide by the conventional thermally-assisted kink-pair nucleation mechanism (Fig. 2.6) [63, 91] stochastically occurring along the dislocation line. Since the majority of the observed slip traces in the BCC simulations are characterized by meandering lines, it becomes evident that the limited mobility of the screw dislocation segments is key to the development of the defect network and to the onset of surface slip traces.

At elevated temperatures, the simulations show that an enhanced dislocation mobility essentially leads to recurrent dislocation loop emissions without detwinning mediation [39]. The simulations in Ta at $T = 900$ K ($T/T_\mathrm{m} \approx 0.3$) already exhibit defect networks that are fully comprised by dislocation segments (Fig. 4.8(f)), where the occasional nucleated nanotwins fully annihilate [38]. Further emissions of dislocation loops produce a great amount of closed slip traces at the surface, which originate from two attractive screw segments gliding to a point where they mutually annihilate (Fig. 4.8(g)). The process then produces a dislocation loop that propagates towards the subsurface and a closed trace at the indented plane (Fig. 4.8(h)).
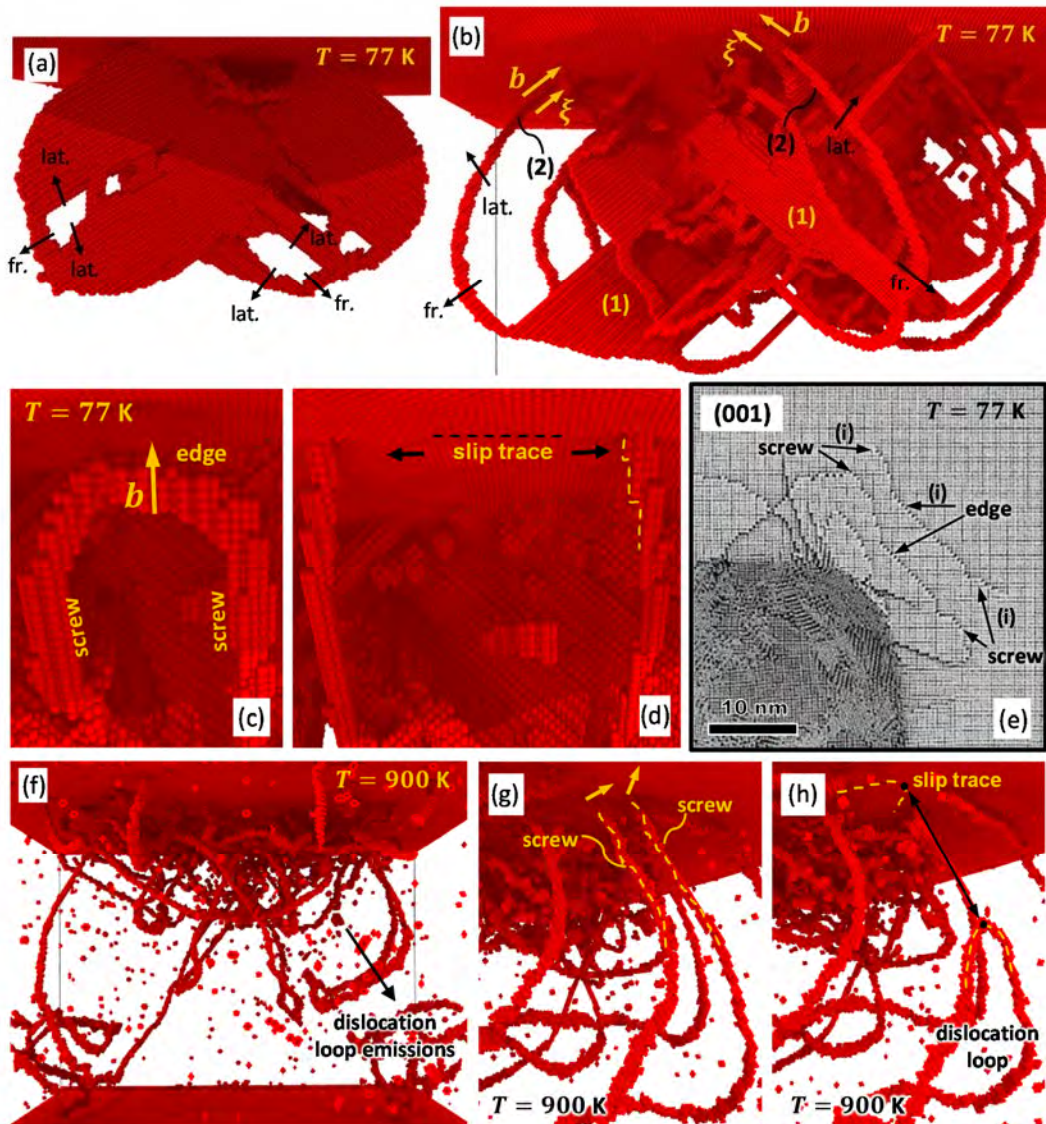
Figure 4.8. Slip trace emissions in Ta indentations. The nanoindentations are performed with $D = 48$ nm at 4 m/s. (a) Planar nucleation and twin-mediated emission of dislocation semi-loops (comprised by frontal "fr." edge and lateral "lat." screw dislocations) in (001)-oriented surfaces indented at 77 K. With increasing penetrations (b), the defect network is characterized by a predominantly planar core with dislocation loops expanding sideways ("(1)" marks twin boundaries and "(2)" marks detwinning dislocations). (c) and (d): Emergence of a heterogeneously-nucleated dislocation loop at the surface producing the slip trace "(i)" in (e). (f) Linear defect network in (011)-oriented Ta at 900 K. (g) and (h): Interplay of mobile screw segments that leads to the production of a closed slip trace at the surface and emission of a full dislocation loop.

4.3. Mechanisms for surface patterning

4.3.1. Onset of plastic bulging

The MD simulations indicate that the gradual development of material bulging (commonly denominated *material pile-up* in the indentation literature [6, 7, 9, 30, 134, 137]) at the indented surface stems from the collective attainment of the abovementioned defect mechanisms (Section 4.2) during nanoimprint formation. The use of the contact parameter c^2 defined as the ratio between the contact and indenter-tip depths [9] (Fig. 4.9),

$$c^2 = \frac{h_c}{h_s}, \tag{4.1}$$

enables the quantification of material bulging around the imprint boundary $(r \approx a)$ [9].

In this investigation, the following definitions for c^2 are employed. (i) The mean $\overline{c^2}$ refers to the vertical location of the effective contact radius, a, where $h_c = D/2 - \sqrt{D^2/4 - a^2}$ and $a = \sqrt{A/\pi}$, see Appendix A4. (ii) The circumferential c_ϕ^2 corresponds to a point of the contact boundary characterized by ϕ (along the circumferential ϕ-axis, see Fig. 4.9). (iii) The maximum pile-up, c_{max}^2, represents the c^2 value at the location of the maximum material bulging, $h_{c, max}$, so that $c_{max}^2 = h_{c, max}/h_s$.
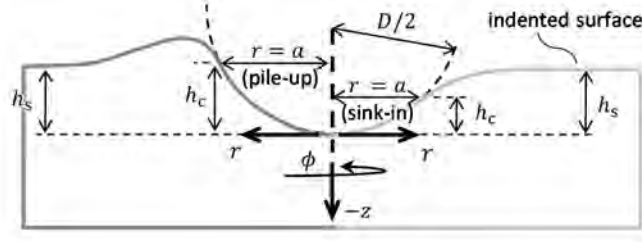
Figure 4.9. Contact variables at the onset of pure sink-in (right hand) and pile-up (left hand). Adapted from Ref. [9].

In accordance with linear elastic contact mechanics [138], a spherical contact is distinguished by the marked attainment of *material sink-in*, leading to $c^2 = 0.5$ as the material only comes into contact with the tip at one half of the penetrated depth [9] (see right-hand part of Fig. 4.9). In this regard, the MD simulations reproduce the formation of elastic sink-ins at the contact periphery as $\overline{c^2} \approx 0.5$ holds true in all of the indented FCC and BCC surfaces during early elasticity, see Fig. 4.10 where dashed lines denote $\overline{c^2} = 0.5$.

With increasing penetrations, the evolution of $\overline{c^2}$ with h_s/D from Fig. 4.10 effectively capture the inception of plasticity as the onset of material pile-ups at the contact boundary is essentially characterized by $\overline{c^2} > 0.5$ [9]. Notice that a fully plastic contact would then result in $\overline{c^2} > 1$ [9] (see left-hand side of Fig. 4.9). Present nanoindentations show that the formation of the plastic imprints is an intermittent process associated to the onset of plastic bursts (pop-in events) detected in the applied load (P)−penetration depth (h_s) curves, see inset to Fig. 4.10(a). Thus, sudden increases in parameter $\overline{c^2}$ indicate a major encasing of the indenter into the surface

caused by the inception of localized material bulging at the surface. Any given abrupt raise in $\overline{c^2}$ is directly linked with the occurrence of individual pop-ins (load drops) in the $P - h_s$ curves (see the arrows in Fig. 4.10(a)), where in overall, the marked the load drop the greater the increment in $\overline{c^2}$. At larger indentation depths, the mild positive slopes in the $\overline{c^2} - h_s/D$ curves (Fig. 4.10) suggests that material pile-up $(\overline{c^2} \geq 1$ [9]) shall finally develop with further increasing penetration.
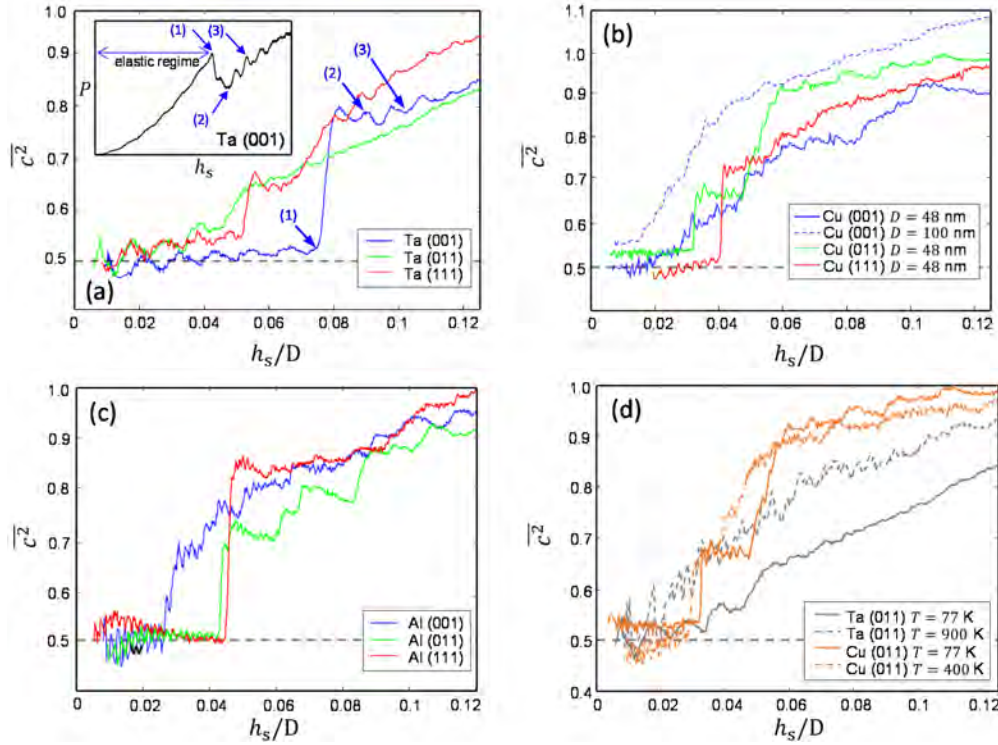
Figure 4.10. Onset of material sink-in and pile-up in FCC and BCC nanoindentations. (a)-(c): Evolutions of $\overline{c^2} - h_s/D$ **in Ta ($T = 77$ K), Cu ($T = 77$ K) and Al ($T = 300$ K) surfaces indented with $D = 48$ nm at 4 m/s. Inset to (a) provides the $P - h_s$ curve of the (001) indentation, where individual load drops mark plastic bursts leading to abrupt increments in $\overline{c^2}$. Results from a massive MD simulation (with $\approx$40 million atoms) performed with $D = 100$ nm in the (001)-oriented Cu surface (at 30 m/s) are given in (b). (d) Evolution of $\overline{c^2}$ with h_s/D in (011)-oriented Ta and Cu surfaces as a function of temperature.**

Figures 4.11(a) and 4.11(b) respectively show the atomic-displacement fields that lead to material sink-in and pile-up features in nano-indented surfaces. These representations illustrate that the atomic positions displace downward during the development of elastic sink-in (Fig. 4.11(a)), while the trajectory of surface atoms eventually changes to one with net upward component resulting in the onset of material bulging ($c^2 > 0.5$) in Fig. 4.11(b). The simulations indicate that the latter is a fundamental characteristic of the development of material pile-ups around the contact boundary ($r \approx a$).
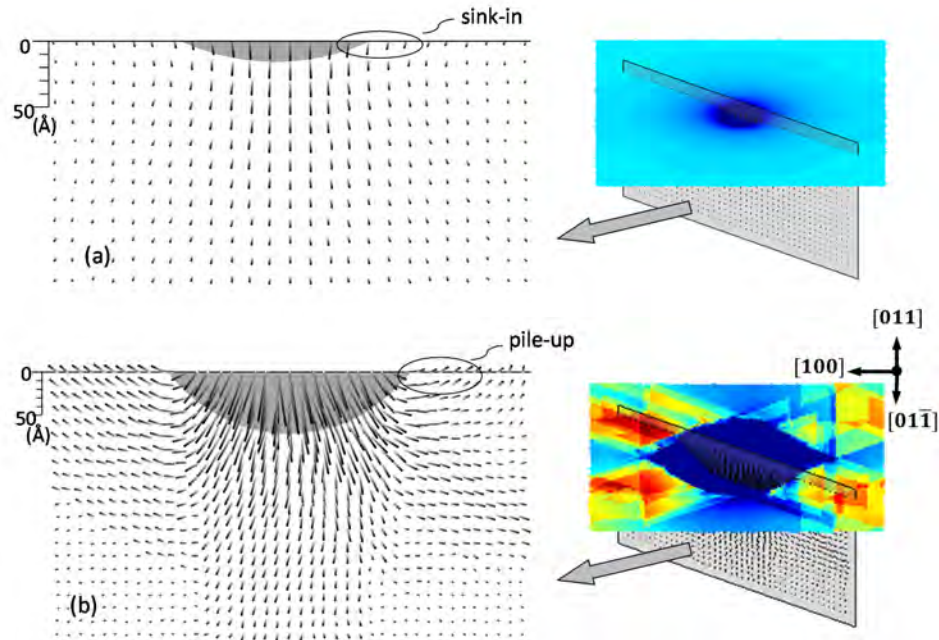
Figure 4.11. Atomic displacement fields during nanoindentation. The nanoindentation shows the (011)-oriented Cu surface at 77 K for $D = 48$ nm and penetration rate of 4 m/s. (a) Early elastic response with material sink-in ($\overline{c^2} \approx 0.5$). (b) Change in the atomic trajectories at maximum imposed penetration ($h_s/D \approx 0.12$), where plastic bulging becomes significant at the vicinity of the contact surface ($\overline{c^2} \approx 1.0$). Line lengths are proportional to the atomic displacements from the initial positions prior indentation. The associated cross-sectional cuts are shown in the right-hand insets. Colors in the insets indicate surface elevations (red) and depressions (dark blue).

4.3.2. The role of nanotwin formation

Although the advent of stable nanotwins is a common feature in the indented Cu surfaces (Section 4.2.2), the location of the plastic hillocks around the imprint is arguably unaffected by the presence of nanotwins. The FCC nanoindentations indicate that the topography of the surface decorations at $r > a$ stems from slip patterning attaining as a main function of temperature and orientation (see following Section 4.3.4). By contrast, nanotwinning favors the encasing of the indenter tip by the surface at the imprint vicinity ($r \approx a$), which leads to the development of sharp contact profiles with marked pinnacles and depressions. This is analyzed through the parameter c_ϕ^2, where peaks in the $c_\phi^2 - \phi$ curve effectively mark the locations of nanotwins in the indented Cu surfaces, see Fig. 4.12(b). The white points in Fig. 4.5(c) denote the location of the nanotwins in the (011)-oriented Cu surfaces, which are coincidental with the maximum c_ϕ^2 values ("t" arrows) in Fig. 4.12(b). While nanotwinning in Cu surfaces enhances the onset of markedly localized pile-ups characterized by $c_\phi^2 \approx 1.1 - 1.0$ (Fig. 4.12(b)), a general absence of nanotwins below the indented Al surfaces is distinguished by pinnacles having relatively smaller values of c_ϕ^2 ($\approx 0.95 - 0.9$), see Fig. 4.12(c).
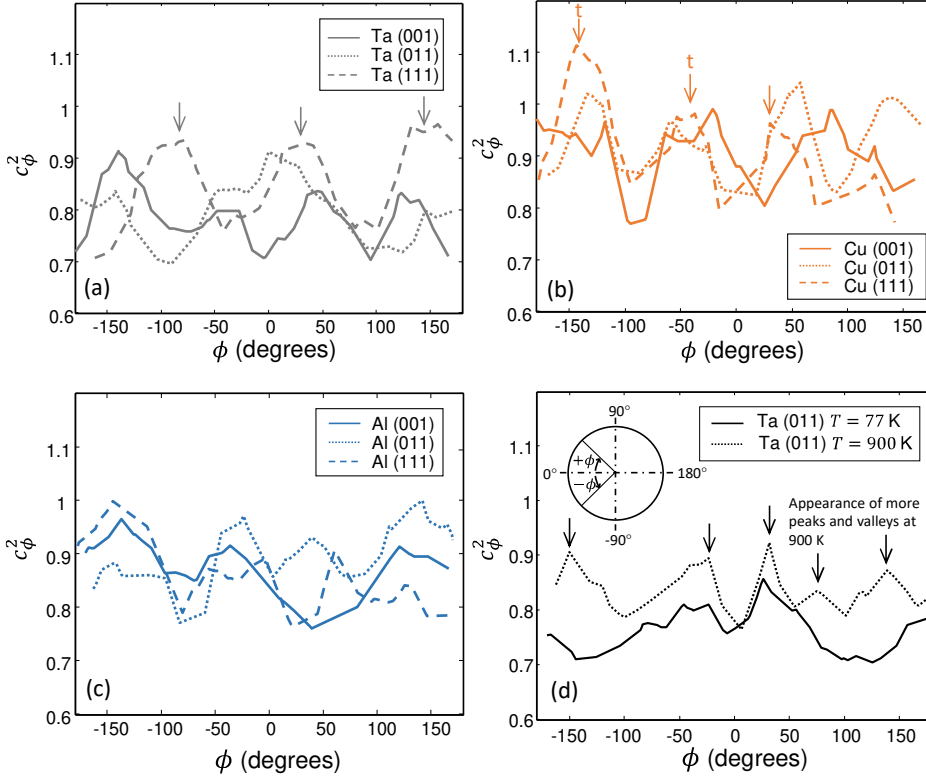
Figure 4.12. Circumferential pile-up parameter c_ϕ^2 around the contact boundary. The nanoindentations are performed with $D = 48$ nm at 4 m/s. (a)-(c): $c_\phi^2 - \phi$ curves for Ta ($T = 77$ K), Cu ($T = 77$ K), and Al ($T = 300$ K) surfaces at $h_s/D \approx 0.12$, respectively. (d) The effect of temperature in Ta (011) surfaces at distinct temperatures ($h_s/D \approx 0.12$). Circumferential angle ($+\phi$) increases in clockwise direction as depicted in the inset to (d).

In BCCs, the characteristic planar nucleation (Fig. 4.8(a)) at low temperatures governs the onset of both plastic hillocks ($r > a$) and material bulging ($r \approx a$). In accordance with the simulations, the growth direction of nucleated twins determines the preferential development of maximum pile-ups as the location of marked plastic bulging systematically coincides with the surface projections of the specific <111> twinning growth. In particular, the directions for the maximum material pile-ups at the contact boundary in the (111)-oriented Ta nanocontacts at 77 K (see the red regions in Fig. 4.13(c) characterized by peaks in the $c_\phi^2 - \phi$ curve, also see arrows in Fig. 4.12(a) for the (111) orientation) coincide with the growing directions of the three-fold twinning structure (Fig. 4.13(a)). Moreover, the attainment of the specific hillocks with **h1**, **h2**, and **h3** directions in Fig. 4.13(c) is associated with the slip clustering from the dislocation loops reaching the surface at these particular orientations, see Fig. 4.13(b). According to the results from Ta nanoindentation at 77 K, a significant amount of the emitted loops (marked "(3)" in Fig. 4.13(d)) stem from heterogeneous nucleation produced at the twin walls, see Fig. 4.13(d).
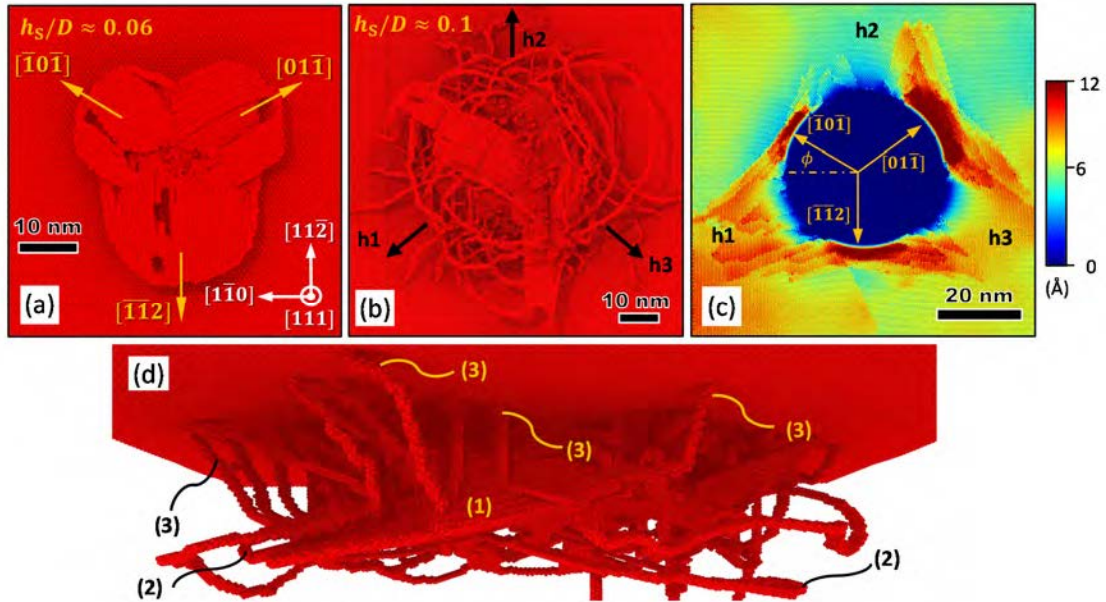
Figure 4.13. Nucleated twin structures and slip patterning in Ta. The results are for indentations on (111) surfaces at 77 K with $D = 48$ nm. (a) Nucleation of a three-fold nanotwin structure (in the bottom view). The nanotwin growth directions coincide with the locations of maximum material bulging around the contact boundary (red zones in (c)). (b) Emergence of heterogeneously-nucleated dislocation loops (growth directions marked with black arrows) which leads to the formation of the h1, h2 and h3 hillocks in (c). (c) Indented surface at $h_s/D \approx 0.12$. Colors denote surface elevations (red) and depressions (dark blue). (d) Defect network at $h_s/D \approx 0.1$, where "(1)" marks twinning, "(2)" detwinning and "(3)" heterogeneously-nucleated loops reaching the surface.

4.3.3. Collective mechanisms for plastic bulging

The indented FCC surfaces are distinguished by the onset of plastic vertexes (marked "v" in Fig. 4.14) that bound topographical depressions (dark blue regions) from the surrounding uplifted surface hillocks (red regions). Although these vertexes are encountered in all of the FCC nanocontacts with $D = 48$ nm (Fig. 4.14), the inception of nanotwins (Section 4.3.2) in conjunction with slip localization processes (Section 4.3.1) promotes prominent vertex development in the Cu nanoimprints, where the sharp edges are located in the regions with less marked material bulging, characterized by $c_\phi^2 \approx 0.75 - 0.85$, see Fig. 4.12(b).

The (001)- and (011)-oriented Ta surfaces indented at 77 K are distinguished by lower plastic levels of parameter $\overline{c^2}$ than those attained in all the FCC nanoindentations, see Fig. 4.10. In FCCs, the early development of prismatic loops (Fig. 4.4(c)) favors recurrent slip trace formation at the contact boundary, which promotes the onset of marked plastic bulging (material uplift) upon nucleation. By contrast, stationary planar networks underneath BCC nanocontacts essentially hinder recursive emissions of slip traces at the contact periphery (Fig. 4.8(b)). This explains why the $\overline{c^2}$ levels tend to become greater in the FCC simulations in comparison with the BCC counterparts (at low temperatures). In addition, the indented Al crystals at 300 K exhibit highly-mobile dislocation structures (Fig. 4.6(a)) that favor the injection of a vast amount of slip traces with increasing penetrations. Thus, the Al simulations feature the largest values of $\overline{c^2}$ obtained in all of the MD nanoindentations, see Fig. 4.10.

At elevated temperatures, the Ta and Fe surfaces also show the development of mobile dislocation networks, leading to the shift of the $\overline{c^2} - h_s/D$ evolutions towards greater values of $\overline{c^2}$ at deep indenter-tip penetrations. This is evidenced in the (011)-oriented Ta indentations, where the attainment of a full dislocation network with mobile screws (Fig. 4.8(f)) leads to greater $\overline{c^2}$ levels in the $\overline{c^2} - h_s/D$ curve at 900 K, see Fig. 4.10(d). Moreover, with increasing temperatures, the Ta (011) imprints develop surface decorations ($r > a$) comprised by closed slip terraces (compare Fig. 4.14(k) with 4.14(l)) as well as more markedly topographical pinnacles and depressions at $r \approx a$, see Fig. 4.12(d). By contrast, the $\overline{c^2}$ levels are apparently unaffected by temperature in the Cu nanoindentations, where the $\overline{c^2} - h_s/D$ evolutions in the (011)-oriented surface lead to the attainment of similar levels of $\overline{c^2}$ (for $h_s/D > 0.06$) at both 77 K and 400 K, see Fig. 4.10(d). In accordance with the discussion in Section 4.2.2, Cu indentations produce nanotwinning below the contact (Fig. 4.5(b)) whose presence ultimately hinders the emission of slip traces at the contact boundary.

4.3.4. Development of hillocks and rosettes

It is important to emphasize that plastic bulging and hillock development are two different plastic phenomena arising in the nano-indented surfaces. While the former stems from upward atomic displacements (Fig. 4.11(b)) in conjunction with a recurrent emergence of slip traces at the contact boundary ($r \approx a$), the latter is attained by slip trace patterning processes occurring at some distance away from the imprint ($r > a$). Thus, the quantification of hillock development by means of parameter c^2 is unfeasible (Section 4.3.1). In this context, the difference between the development of material bulging and plastic hillocks becomes manifest in the (011)-oriented Ta nanoindentations performed at 77 K. According to Figs. 4.9(a), the $\overline{c^2}$ levels increase from ≈ 0.50 to ≈ 0.85 with increasing penetrations, whereas the onset of hillock morphologies is globally lacking at the indented surface, see Fig. 4.14(k).

Hillock formation in FCCs involves slip trace patterning induced by (i) dislocation gliding outwards from the imprint along the preferential <110> and <112> slip directions (Fig. 4.5), (ii) cross-slip processes producing serrated terrace patterns (Section 4.2.3), and (iii) interceptions of surfaced dislocation segments leading to the production of terrace edges (Fig. 4.7(c)). With increasing temperatures, defect network intricacy is enhanced (cf. Figs. 4.6(b) and 4.6(c)), thus limiting long-range dislocation organization in favor of short-range interactions of mobile dislocations. This is evidenced in the (011)-oriented Cu indentations, where the development of hillock morphologies is promoted at 400 K (compare Figs. 4.14(b) and 4.14(c)). Moreover, the intricacy of terrace decorations in the FCC indentations increases in the Al surfaces as the recursive emission of serrated (cross-slipped) traces eventually leads to the appearance of more complex terrace shapes (compare Figs. 4.14(c) and 4.14(g)).
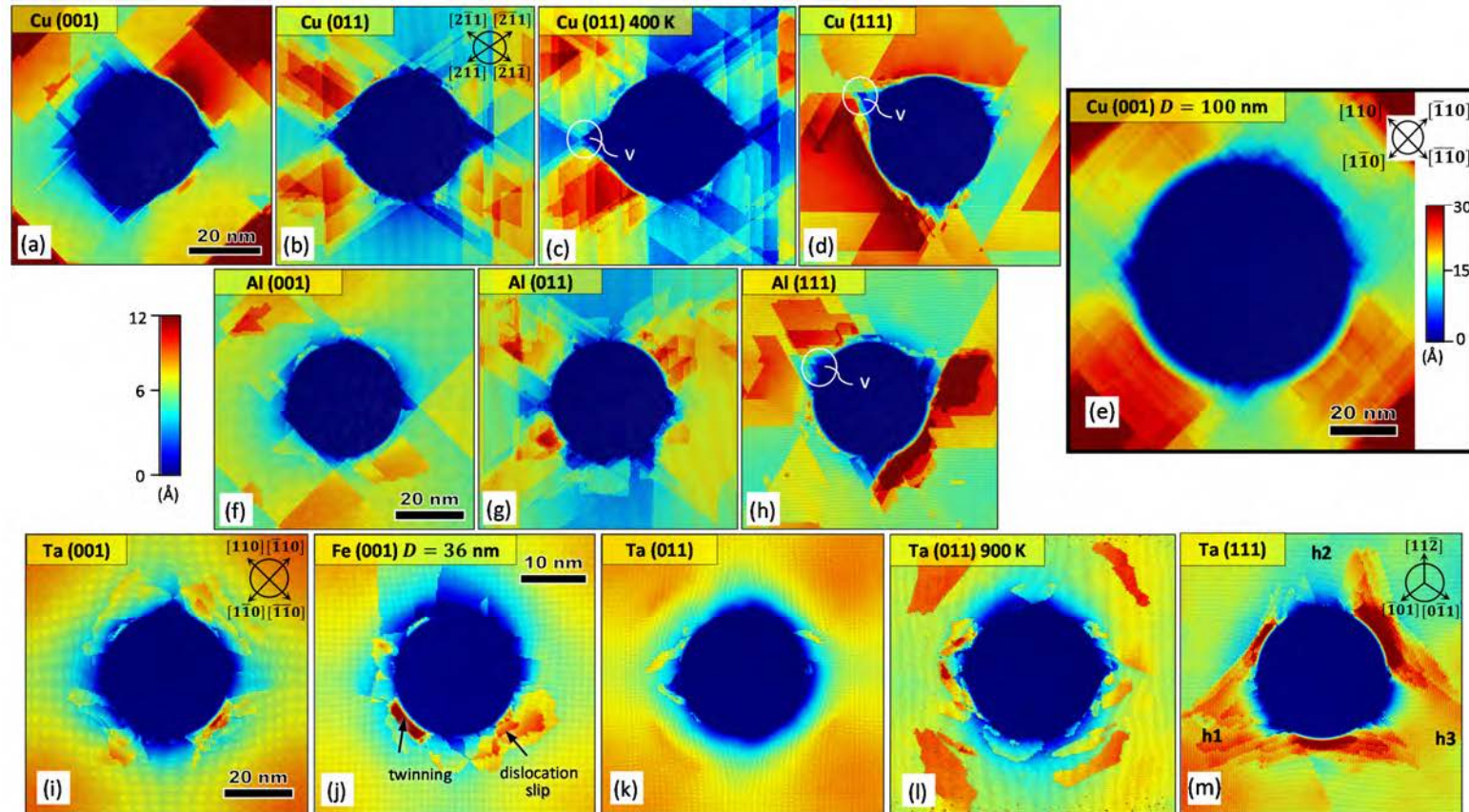
Figure 4.14. Pile-up topographies in the indented FCC and BCC surfaces. (a)-(h): FCC (Cu and Al) nanoindentations. Formation of four-fold rosette symmetries is illustrated in the (011) surfaces in (b) and (g), and in the (001) surface at $D = 100$ nm in (h). All the Cu surfaces are indented at $T = 77$ K except (c), which is indented at $T = 400$ K. The Al surfaces are indented at $T = 300$ K. (i)-(m): BCC (Ta and Fe) nanoindentations. Temperature is set at $T = 77$ K except in (l), which is set at $T = 900$ K. The onset of material bulging from twinning and dislocation slip is marked in (j). (k) and (l): The effect of temperature in the (011) surfaces of Ta, where dislocation loop emergence and terrace formation are promoted with increasing temperatures. (m) Development of a three-fold rosette arrangement comprised by the hillocks h1, h2, h3 in Ta (111). The color map indicates surface elevations (red) and depressions (dark blue). All of the indentations are performed at $D = 48$ nm (except (e) and (j)). The above pictures are obtained at maximum penetration depth ($h_s/D \approx 0.12$).

The Ta and Fe nanoindentations show that the surfaced screw segments gliding through kinking mechanisms lead to the development of plastic hillocks which are constituted by wavy terraces, see Figs. 4.14(i)-(m). Due to the reduced lateral expansion of the screw components emerging from twin annihilation at low temperatures (Fig. 4.8(c)), the onset of hillock morphologies and rosettes attain at surface projections of the preferential gliding direction of the edge components in the subsurface (Fig. 4.8(d)). In the (001)-oriented indentations, these projections correspond to the <110> directions in which the hillocks develop (cf. Figs. 4.14(i) and 4.14(j)). In addition, the Ta and Fe simulations reveal that the proximity of these plastic hillocks to the contact boundary is associated with the limited outward glide of the emitted loops (Fig. 4.8(b)). Interestingly, hillock development is lacking in the (011)-oriented Ta surface at 77 K (Fig. 4.14(k)) where the emitted loops propagate towards the indented plane. At elevated temperatures, the outward gliding of the surfaced dislocation segments is favored by kink-pair processes and by the complete annihilation of the planar core (Fig. 4.8(f)), which essentially promotes hillock development in the indented surface (Fig. 4.14(l)). Finally, the (111)-oriented Ta nanoindentation at 77 K exhibits a great lateral expansion in the emerging dislocation loops (Fig. 4.13(b)), which leads to a marked development of rosette arms lying at $\approx 45°$ from the surface projection of the nanotwin growth directions (Fig. 4.13(a)). This leads to the development of hillocks marked **h1**, **h2**, and **h3** in Fig. 4.13(c).

4.3.5. Size effects and comparison with experiments

The crystallographic slip features and preferential <110> and <112> trace directions obtained in the MD simulations are in a good agreement with experiments performed in Cu and Ni [69, 131], compare Figs. 4.2(i)-(j) with Fig. 4.5. Moreover, the rosette configurations encountered in the (MD) FCC crystals replicate the four-fold symmetries obtained from microindentation experiments in (011)-oriented surfaces [133, 134] (compare Figs. 4.2(b) and 4.2(e) with Fig. 4.14(b)). Although the experiments also show that a similar four-fold symmetry emerges in (001)-oriented FCC surfaces, this feature only becomes evident in the massive MD simulation performed with $D = 100$ nm (Fig. 4.14(e)). This result indicates that slip trace patterning may only be favored by the vast number defects introduced with greater indenter tips in larger material volumes. Furthermore, increasing tip diameter from $D = 24$ nm to $D = 100$ nm intensifies material bulging as evidenced in Fig. 4.10(b), where $\overline{c^2}$ shifts towards greater values with larger indenters. The simulations with $D = 48$ nm are not however conclusive when it comes to mimic the six-fold rotational symmetry of the rosettes in (111)-oriented FCC surfaces (see Fig. 4.2(c)), suggesting that indenter tips with $D > 100$ nm are still required so as to facilitate further development of surface deformation patterns.

The MD simulations of BCC crystals reproduce the hillock arrangements found in nanoindentation experiments performed in (001)- and (111)-oriented Ta surfaces [36]. In the case of the (001)-oriented surface, the four-fold rosette symmetry along the <110> directions (Fig. 4.14(i)) is in good accordance with the experimentally observed morphologies in Ta (compare Fig 4.3(b) and Fig. 4.14(i)). Moreover, the salient features at the surface that develop in nanoindentation experiments are analogous to those produced in the MD simulations (cf. Fig. 4.2(a) and Fig. 4.8(e)). This supports the presently found mechanisms for hillock development in BCCs, including the interplay between the surfaced edge and screw dislocation segments that leads to the formation of elongated terraces at the surface (Section 4.2.3). However, the experimentally observed rosette morphology in (111)-oriented Ta surfaces, which is found to exhibit a three-fold rotational symmetry [36], see Fig. 4.3(d)), is partially replicated in the MD simulations (Fig. 4.14(m)). While the location of two neighboring rosette arms is consistent

with that attained in the experiments, the development of the third arm (**h2** in Fig. 4.14(m)) is lacking at the-present indentation length scale.

Although increasing temperature promotes plastic bulging around the contact boundary in the (011)-oriented Ta nanoindentation (Fig. 4.12(d)), the simulations with an indenter tip of $D = 48$ nm at 77 K are unable to predict the experimentally observed six-fold rosettes [36] (compare Fig. 4.3(c) with Figs. 4.14(k) and 4.14(l)). According to these results, the use of greater tip diameters ($D > 100$ nm) would likely enhance slip trace recurrence and patterning so as to reproduce the missing features during the loading stage in indented FCC and BCC surfaces.

4.3.6. Material pile-up and surface patterning upon unloading

According to elastic contact mechanics, indenter tip removal readily produces a marked elastic rebound in the z-axis [9, 138] (Fig. 4.9) which at $r \approx a$ doubles the elastic recovery developed at the imprint center ($r = 0$) [138]. In this sense, it is recalled that the pressure levels induced in nanoindentation tests are much larger than those attained with greater indenter tips, so that the elastic rebound of the surface in macro and microindentations is consequently smaller [9]. The MD simulations of FCC and BCC nanocontacts systematically illustrate on the onset of such massive elastic rebounds (Figs. 4.15(b) and 4.15(f)).

Two different definitions for parameter $\overline{c^2}$ can be adopted to quantify the development of material pileup during the loading and unloading stages of the indentation cycle (Fig. 4.15); $\overline{c^2}_{\text{load}} = h_c/h_s$ (Eq. 4.1) and $\overline{c^2}_{\text{unload}} = h_c/h_f$, where h_f is the penetration depth remnant upon full indenter removal (i.e., the measured penetration depth from the $P - h_s$ curves at full unloading [6]). According to the simulations, indenter-tip unloading (at $h_s/D \approx 0.12$) produces a $\approx 10\%$ raise in the $\overline{c^2}$ levels as compared to those measured during the loading stage in both FCC and BCC nanoindentations (Table 4.1). Moreover, extreme local raises by an order of $\approx 50\%$ in parameter c^2 (Table 4.1) attain when considering the maximum bulging point at the contact boundary, characterized by $h_{c,\,\text{max}}$ (cf. Figs. 4.15(a) and 4.15(b)), where $c^2_{\text{max, unload}} = h_{c,\,\text{max}}/h_f$. This result indicates that the unloading stage leads to a very significant onset of localized material uplifts around the contact ($r \approx a$), leading to $c^2_{\text{max,unload}} \approx 1.3 - 1.5$. Table 4.1 shows the marked difference between the value $\overline{c^2}_{\text{loading}}$ (around which c^2_ϕ fluctuates, Fig. 4.12) and the levels of $c^2_{\text{max,unload}}$ obtained in the FCC and BCC surfaces (Fig. 4.16).

Figure 4.15 provides the contact profiles and the corresponding defect entanglements of loaded and unloaded imprints from the (011)-oriented Al and (111)-oriented Ta indentations. Notice the role that indenter removal plays in the development of the defect networks (Figs. 4.15(d) and 4.15(h)), where the elastic recovery favors (i) upward dislocation glide, (ii) dislocation surface annihilation, and (iii) the onset of further surface decorations (Fig. 4.16). Slip trace patterning and the development of rosette arms become more evident during unloading, as it leads to an enhancement of the topographical features that were not clear in the loading indentation. This is the case of the (111)-oriented Ta surface where the three-fold configuration [36] (and the missing **h2** hillock mentioned in Section 4.3.5) eventually upon during unloading. Moreover, note in Figs. 4.16(a) and 4.16(b) that indenter removal results in the development of more evident four-fold symmetries in (011)-oriented Cu and Al surfaces (compare Fig. 4.16(d) and Fig. 4.15(e)).
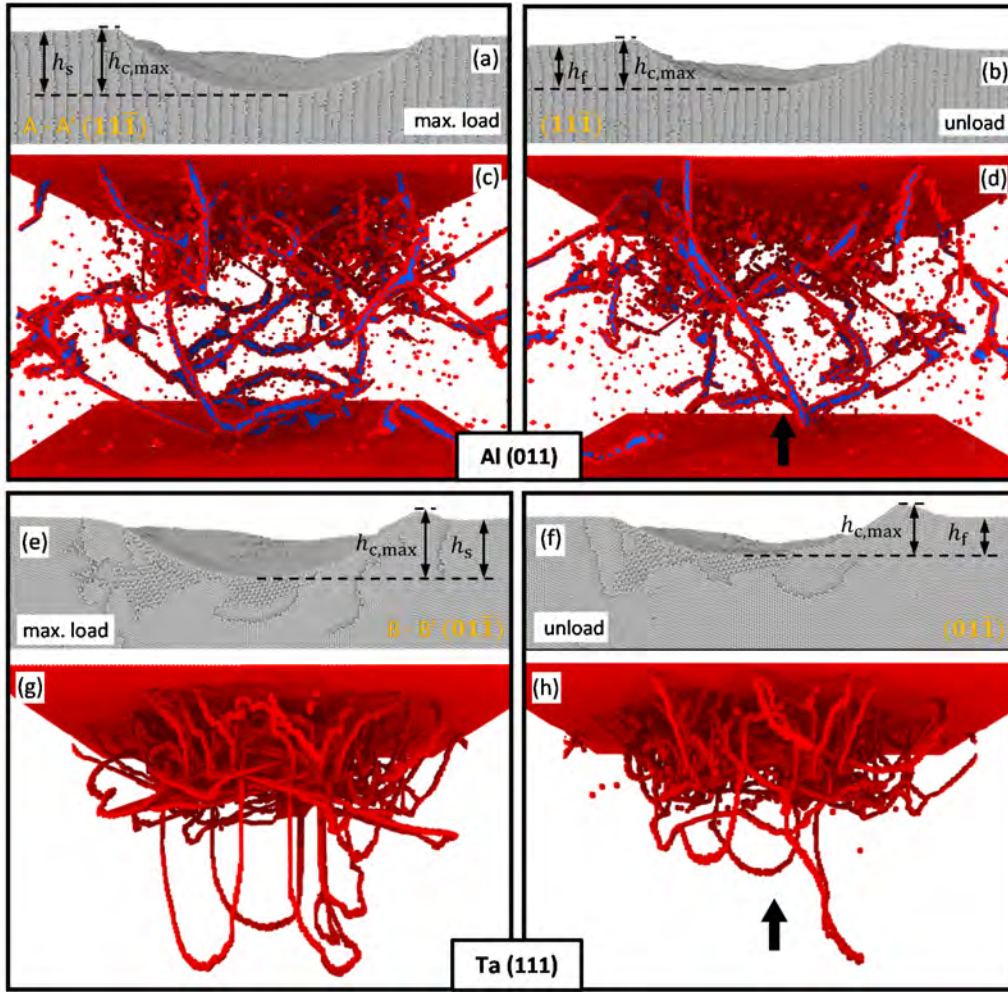
Figure 4.15. Loaded vs. unloaded contact profiles and defect networks in Al and Ta. The nanoindentations are performed with $D = 48$ nm at 4 m/s. Notice in (a) and (e) the marked material uplift upon elastic rebound. In the (111)-oriented Ta surface, indenter-tip removal leads to a significant reduction of the plastic zone and promotes the development of the h_1, h_2, h_3 plastic hillocks (cf. Figs. 4.14(m) and 4.16(c)). The A-A' (a) and B-B' (e) cross sectional cuts are respectively drawn in Figs. 4.16(e) and 4.16(f).

Table 4.1. Values of $\overline{c^2}$ and c^2_{max} under loading ($h_s/D \approx 0.12$) and upon indenter unloading.

Indented surface*	T (K)	$\overline{c^2}_{loading}$	$\overline{c^2}_{unload}$	$c^2_{max, load}$	$c^2_{max, unload}$
Ta (111)	77	$0.85 - 0.95$	$0.95 - 1.06$	$0.98 - 1.11$	$1.24 - 1.5$
Cu (011)	77	$0.9 - 0.98$	$1.02 - 1.1$	$1.12 - 1.16$	$1.28 - 1.46$
Al (011)	300	$0.91 - 0.99$	$1.02 - 1.15$	$1.06 - 1.2$	$1.25 - 1.5$

*The nanoindentations are performed with $D = 48$ nm at 4 m/s.
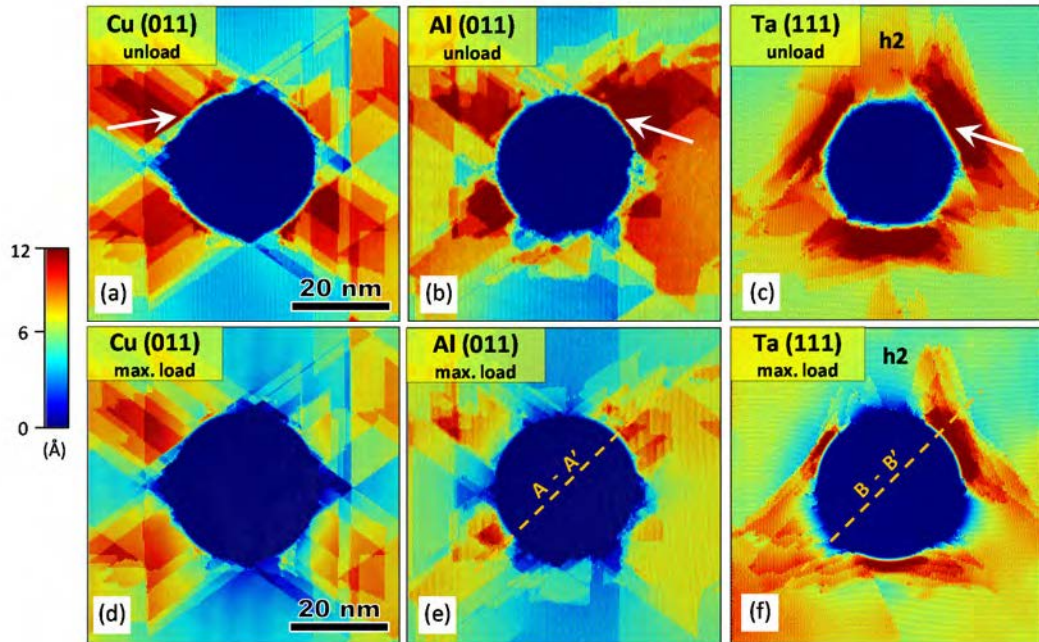
Figure 4.16. Pile-up topographies in loaded and unloaded FCC and BCC surfaces. The nanoindentations are performed with $D = 48$ nm at 4 m/s and maximum penetration of $h_s/D \approx 0.12$. The color map indicates surface elevations (red) and depressions (dark blue). (a)-(c): Indenter removal promotes the development of rosette morphologies (red zones marking material pile-up). (d)-(f): White arrows denote the location of the maximum plastic bulging around the contact boundary upon indenter-tip removal.

4.4. Conclusions

1. The MD simulations show that plastic deformation around FCC nanocontacts is governed by the emission of dislocations and nanotwins whose preferential glide along <110> directions produces <110> and <112> slip traces at the surface. The surfaced dislocation segments have predominantly screw character and originate from (i) prismatic loops emitted during early defect development; (ii) unzipping processes of dislocation junctions; and (iii) annihilation of SF-ribbons and nanotwins. Crystals with high stacking fault energy promote cross slip, leading to a more serrated configuration of slip traces. Cross slip is hindered by the straightening of the surfaced dislocation segments. Slip traces along non-crystallographic <001> directions emerge from the occasional glide of non-dissociated junction dislocations.

2. In BCCs, slip trace clustering and symmetric rosette-arms develop through the emission of dislocation loops to the surface. At low temperatures, homogeneously-nucleated twins lead to the emission of dislocation semi-loops through detwinning processes at the twin boundaries. At deeper penetrations, additional (heterogeneously-nucleated) dislocation loops are emitted. Loop expansion proceeds so that the edge regions glide towards the <111> direction while the screw components expand sideways through kinking processes. The edge segments gliding with net upward component intercept the surface and produce straight traces. The characteristic wavy traces detected in BCC surfaces are due to kinking mechanisms of the surface-truncated screw segments. With increasing temperature, the attainment of a highly-mobile dislocation network is

enhanced, which leads to a great amount of dislocation-loop emissions (without twin mediation) that favors marked outward spreading of slip traces and surface patterning development.

3. The plastic hillocks around FCC nanocontacts are comprised by planar atomistic terraces owing to the <110> and <112> crystallographic slip of surfaced dislocations. Cross-slip and dislocation interaction processes lead to the development of increasingly-serrated terrace morphologies. Slip trace patterning is favored in crystals with large stacking fault energy, which produces intricate hillock arrangements. With increasing temperatures, long-range dislocation organization is limited, which enhances formation of a less delineated morphology of plastic terraces. Although vast amounts of slip traces are introduced into the surface with increasing tip diameter, limited rosette development still occurs as compared to that found in greater (micrometer-sized) indentations. Extreme material pile-ups (material uplift) upon indenter unloading delineates hillocks topography, promoting further slip trace patterning and the development of the symmetric rosette configurations which are experimentally observed in greater (micrometer-sized) indentations.

4. The marked waviness of the hillocks in BCCs is due to kinking processes attaining in the surfaced screw segments of the emerging dislocation loops at the surface. At low temperatures, the hillocks are rather confined at the contact boundary in (001)-oriented surfaces, emerging along the surface projection of the preferential <111> gliding direction of the edge components of the dislocation loops. The hillocks are located further away from the contact boundary in the (111) indentation as the surfaced edge dislocation population pronouncedly glides outward from the imprint boundary. Increasing temperature in BCCs favors terrace and hillock development due to the onset of highly-mobile dislocation networks.

5. Plastic bulging of the surface around the indenter tip is strongly related to imprint formation processes. The mechanisms producing plastic bulging in FCC nanocontacts are: (i) recurrent slip trace emissions, which are favored in crystals with high stacking fault energy where highly mobile dislocation networks attain, and (ii) formation of imprint edges around the contact periphery due to slip trace localization. Plastic bulging in BCC nanocontacts at low temperatures is governed by nanotwin nucleations at specific locations around the imprint. In general, development of entangled defect networks that carry increasing dislocation slip favors material bulging in both FCC and BCC imprints. These features determine the atomic trajectories of surface atoms, leading to distinct material uplifts in nanocontact plasticity as a function of crystalline structure, orientation and temperature. Material bulging is characterized by an increase in parameter $\overline{c^2}$ with penetration from the elastic lower limit of $\overline{c^2} \approx 0.5$, where plastic $\overline{c^2}$ is predominantly greater in FCCs than in BCCs. Present simulations finally suggest that while the reported $\overline{c^2}$ is much smaller than the range of values measured in greater micro and macroscopic indentations, assessment of this parameter using the contact profile remnant upon indenter-tip unloading provides results that are more in agreement with those from greater indentation scales. This is an outcome of the marked surface rebounds attained during nanoindenter removal, which are indicative of the extreme contact pressures attained in nanocontact plasticity.

CHAPTER 5.

UNDERSTANDING NANOHARDNESS AND NANOIMPRINT FORMATION PROCESSES

5.1. What is the indentation hardness?

Material hardness is a widely employed parameter in indentation testing as its measurement provides a quantitative estimate of the *mean contact pressure* that leads to the formation of a permanent (plastic) imprint in the material [1, 6, 139, 140]. Hardness is consequently defined as [139]

$$p_\mathrm{m} = \frac{P}{A},$$
(5.1)

where *A* is the *projected* contact area as defined in Appendix A4.

In linear elastic contacts [138], the mean contact pressure is a function of the elastic properties of the sample and the corresponding indenter tip geometry [138]. With increasing penetrations, the onset of crystal plasticity leads to a complex phenomenology of dislocation propagation and interaction processes [10] occurring underneath indented metallic surfaces [16, 21, 31, 141]. Experiments conducted in macro and microscopic material length scales in conjunction with (bulk-like) continuum simulations have shown that plastic hardness measurements arguably follow certain correlations with intrinsic material properties (i.e. with the elastic modulus, the hardening exponent, and the yield stress [6, 7, 24, 90, 142]). With decreasingly indenter-tip dimensions, the onset of indentation size effects comes into play, affecting on the measured levels of contact pressure [12, 14] in accord with the framework in that "smaller is stronger" [143]. Although significant research efforts have been devoted to elucidate the correlations between the contact variables inferred through microindentation testing and the onset of geometrically necessary dislocations (GNDs) [10, 16, 21, 92], a clear understanding of the relationship between the hardness and the fundamental dislocation glide mechanisms developing as a function of crystal structure and temperature is essentially lacking in the open literature. Moreover, in spite of the pioneering research works [14, 36, 41, 62] that have demonstrated the dependency of the indentation pop-ins (marking the onset of plastic deformation in ultra-low load nanoindentation testing [14]) to the nature of the indented surface from room to elevated temperatures, the correlation between the hardness and the subsequent nanoindentation response at increasing tip penetrations is still a theme of intense debate [12, 16, 18, 21].

The central topic of this investigation is on the evaluation of the mechanisms that govern the formation of permanent nanoimprints in FCC and BCC metals as a function of surface orientation and temperature. In doing so, an extensive set of MD nanoindentation simulations is performed in distinct FCC and BCC crystals under a wide range of nanoindentation conditions, see Table 3.4. The attainment of the nanohardness evolutions with increasing indenter-tip penetration enables the evaluation of (i) the elastic response of the simulated FCC and BCC surfaces, (ii) the underlying crystalline mechanisms that lead to the formation of permanent imprints in nanoscale contacts, and (iii) the development of evolutionary defect networks with increasing tip penetration. In addition, it is investigated the role of the specific FCC and BCC defect nucleation phenomenology upon the material hardness and its transition towards *plateau* levels, a feature that is characterized by the periodic development of secondary pop-in excursions. Although the attainment of such hardness plateaus has been already reported in previous investigations [16, 21, 37, 119, 141, 144,], the discussion seeks to shed light on the mechanistic origin to their development, including the role of specific plastic processes. Overall, the discussion provides a fundamental background to explain why BCC surfaces are harder than FCC counterparts at the nanoscale.

5.2. Early elastic contact responses and the onset of plasticity

The elastic responses of the FCC and BCC nanocontacts match the predictions from linear elastic (Hertzian) contacts [138], where the contact pressure (or hardness) between the spherical tip and the flat surface adheres to the universal relationship

$$\frac{p_{\mathrm{m}}}{E} \approx \frac{0.8488}{(1 - v^2)} \frac{a}{D} \approx 0.9598 \frac{a}{D}, \tag{5.2}$$

where $v = 0.35$ is assumed [138]. Appendix A2 describes in detail the procedure employed to estimate the value of the effective elastic modulus, E, in the present MD simulations of nanocontacts. Figure 5.1 shows the evolution of p_{m}/E in terms of a/D. It is observed in this figure that all elastic responses fulfill Eq. (5.2) regardless of the crystalline structure, orientation or temperature.

Since the MD nanoindentations enable a direct assessment of the set of atoms that are effectively brought into contact with the indenter tip (Appendix A4), the simulations become powerful tools to investigate the contact conditions that lead to the onset of continuum-like elasticity in perfectly-flat surfaces. The present analysis yields a systematic examination of the $E - h_{\mathrm{s}}$ curves in conjunction with the number of in-contact atoms (N_{c}) that define the indentation response and its evolution with increasing penetration. In this context, a Hertzian contact is anticipated to follow the relationship [138],

$$E \approx \frac{1.2087 \, P}{h_{\mathrm{s}} \sqrt{D \, h_{\mathrm{s}}}} . \tag{5.3}$$

Figure 5.2(a) illustrates the $E - h_{\mathrm{s}}$ curves resulting in the (001)- and (011)-oriented Ta surfaces. It is found in this figure that the early development of an elastic contact attains with indenter-tip penetrations larger than, say, $h_{\mathrm{s \, (e)}} \approx 2.5 \, \text{Å}$. According to the simulations, the inception of elasticity in present nanoindentations is determined by about a few hundred atoms (Fig. 5.2(b)). The general outcome from this analysis is that a given elastic nanocontact satisfying the Hertzian contact (Eq. (5.3)) is necessarily defined by, at least, 100 atoms with indenter penetrations $\gtrsim 2.0 \, \text{Å}$, where $N_{\mathrm{c \, (e)}}$ may follow some exponential relationship with D, see Table 5.1.

With decreasingly indenter-tip sizes ($D < 30$ nm), present nanocontacts overestimate the magnitude of the elastic modulus, e.g., see in Table 5.1 the E value obtained in the indentations with $D = 24$ nm. This effect is associated with the fact that the response of a limited number of atoms cannot be coarse-grained through linear elastic continuum contact mechanics analyses. In this sense, it is noted that the present simulations clearly indicate that for $D > 30$ nm, reasonable accordance is reached between the values of E reported from nanoindentation experiments [36, 37, 62] and those inferred from the modeled nanocontacts. Furthermore, the MD simulations effectively capture the onset of anisotropic elasticity in the indented Cu surfaces, where the largest E values are encountered in the indentations of (111) planes while the lowest E values corresponds to the (001)-oriented surfaces, see Fig. 5.3. This result is in good agreement with the computational and theoretical works from Refs. [11, 37] (cf. Fig. 6 from Ref. [11]). By the same token, the nanoindentations also reproduce the moderate elastic isotropy that develops in the indented Ta and Al surfaces [37, 38, 145]. This is evidenced in the $p_{\mathrm{m}} - h_{\mathrm{s}}$ curves from Fig. 5.3 where the elastic responses follow similar trends regardless of the indented orientation.

Figure 5.1. $p_{\mathrm{m}}/E - a/D$ curves from the MD simulations of FCC and BCC nanoindentations. All of the indentations are carried out at 4 m/s. The indentations in (a),(c), and (d) are performed with indenter tips of $D = 48$ nm. The indentations marked "*prestr.*" (in parts (a),(c)-(d)) contain a preexisting defect network. See text for full details.

The onset of nanocontact plasticity attains at a critical load level and is characterized either by a marked discontinuity (pop-in) or by a sudden slope change in both the $p_{\mathrm{m}} - h_{\mathrm{s}}$ and $P - h_{\mathrm{s}}$ curves [21, 41, 68], see Figs. 5.3 and 5.4 (respectively). While sharp pop-ins are a signature of abrupt defect nucleations under large pressures (and penetrations) [37, 38], a more gradual transition to plasticity distinguished by milder load drops indicates the injection of crystalline defects at lower contact pressures [37, 38].The Cu and Al simulations show an analogous phenomenology of defect nucleation mechanisms attaining as a main function of the surface orientation characterized by development of specific pop-ins. It is encountered that the largest pop-ins are attributed to the (111)-oriented surfaces (see Fig. 5.4(c)) which correspond with the abrupt inception of prismatic loops. In contrast, the mildest pop-ins in FCCs develop in the (001) indentations (Fig. 5.4(a)) due to the nucleation of few dislocation lines (see that the corresponding dislocation densities burst in Figs. 5.5(a) and 5.5(b) at the first pop-in event). The interested reader is addressed to Fig. 4 from Ref. [37], where the nucleated defect geometries that arise as a function of surface orientation in FCC nanoindentations are shown.
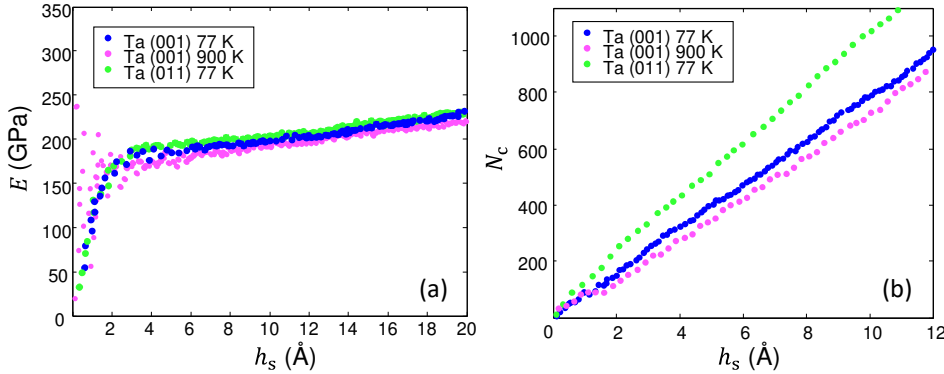
Figure 5.2. Onset of elastic contacts in Ta nanoindentations. The indenter tips have $D = 48$ nm while the penetration rate is set to 4 m/s. (a) $E - h_s$ curves in (001)- and (011)-oriented surfaces. Note that the use of Eq. (5.3) enables the computation of E at a given elastic loading state characterized by P and h_s. (b) The $N_c - h_s$ curves are indicative in that N_c linearly scales with h_s in a spherical elastic contact. Notice the role that surface orientation plays in the $N_c - h_s$ evolutions as the indentations performed on close packed planes (i.e. the (011)-oriented BCC surface, see Section 2.3) lead to steeper $N_c - h_s$ curves in elasticity. By contrast, elevated temperatures tend to reduce the slopes in the $N_c - h_s$ evolutions, compare 77 K vs. 900 K in the (001) indentation.

The dimensionless contact variables used in Eq. (5.2) can be employed to characterize the transition from the early linear elastic regime to the inception of a nanocontact instability (or first pop-in event) [146]. According to Table 5.1, different levels of the critical p_m/E, hereafter also referred to as $(p_m/E)_{(p)}$), marking the onset of such a pop-in event attain as a function of the indented FCC and BCC surfaces (note that these values are not particularly sensitive to the elastic properties and indenter-tip size). In this regard, the simulations show that the (001)-oriented FCC surfaces exhibit the lowest $(p_m/E)_{(p)}$ (≈ 0.1), while the (011) and (111) orientations are distinguished by larger $(p_m/E)_{(p)}$ values (≈ 0.125 and ≈ 0.14, respectively), see the arrows pointing to the different critical p_m/E levels in Figs. 5.1(c) and 5.1(d). Additionally, it is found that the indentations distinguished by a net hardness drop of more than $0.5p_{m\,(p)}$ at the first pop-in exhibit "extended" elastic regimes towards $(a/D)_{(p)} \approx 0.14$, see Fig. 5.1. Smaller p_m/E excursions attain for the smaller critical levels of a/D (< 0.14), which are generally associated with the onset of mild dislocation density bursts, cf. Figs. 5.1 and 5.5.

The specific defect inceptions in perfect BCC crystals are clearly influenced by temperature [38, 39, 41]. In this context, pop-ins developing at low temperatures ($T = 77$ K) are associated with twin-wall nucleations. The distinctive {112} twin-wall configurations attaining below indented BCC surfaces as a function of orientation govern the development of the pop-in event (see Fig. 2 from Ref. [38]). This is also captured in the $p_m/E - a/D$ curves of Figs. 5.1(a) and 5.1(b), where the $(p_m/E)_{(p)}$ levels in the (011)- and (111)-oriented surfaces exhibit $(p_m/E)_{(p)} \approx 0.12$ and ≈ 0.15, respectively, in both Ta and Fe nanoindentations. The BCC simulations reproduce the SF-wall nucleation in the (001)-oriented surfaces (reported elsewhere in Ref. [38]) which leads to the extreme value of $(p_m/E)_{(p)} \approx 0.21$. In the case of Ta surfaces indented at 77 K, this orientation exhibits the largest critical pressure ($p_{m\,(p)} \approx 42$ GPa) of all the indentations (with $D > 30$ nm), see Table 5.1. With increasingly temperatures, both $(p_m/E)_{(p)}$ and $(a/D)_{(p)}$ gradually shift to smaller values due to the enhancement of

detwinning and dislocation-loop emissions at the pop-in excursions. In particular, the (001)-oriented Fe surface exhibits a three-fold decrease in the $(p_\mathrm{m}/E)_{(\mathrm{p})}$ levels when temperature is raised from 77 K to 900 K, see Table 5.1. Following this trend, indented BCC surfaces could converge to a minimum value of $(p_\mathrm{m}/E)_{(\mathrm{p})} \approx 0.09$ in the (011) orientation, which arguably would correspond to a similar pop-in event (in terms of $(p_\mathrm{m}/E)_{(\mathrm{p})}$) to the easily-activated (001) orientation in the FCC counterpart.

Table 5.1. Contact parameters at the onset of coarse-grained elasticity and for the first plastic burst.

indented surface	D (nm)	T (K)	onset of elasticity			onset of plasticity		
			$h_{\mathrm{s\,(e)}}$ (Å)	$N_{\mathrm{c\,(e)}}$	E (GPa)*	$p_{\mathrm{m\,(p)}}$ (GPa)	$(p_\mathrm{m}/E)_{(\mathrm{p})}$	$(a/D)_{(\mathrm{p})}$
Ta (001) 36nm[†]	24	77	≈5.0	≈200	≈275	56.2	0.197	0.198
Ta (001) 70 nm	48	77	≈2.5	≈110	≈190	42.0	0.221	0.193
Ta (001) 70 nm	48	900	≈3.0	≈100	≈180	33.6	0.177	0.161
Ta (011) 70 nm	48	77	≈2.5	≈250	≈195	26.2	0.122	0.129
Ta (011) 70 nm	48	900	≈3.5	≈300	≈185	24.2	0.118	0.117
Ta (111) 70 nm	48	77	≈2.5	≈100	≈192	30.0	0.150	0.162
Ta (111) 70 nm prestr.	48	77	-	-	≈192	22.6	0.111	0.118
Ta (111) 70 nm	48	900	≈3.5	≈100	≈180	28.8	0.140	0.145
Fe (001) 50 nm	36	77	≈3.0	≈110	≈202	44.0	0.209	0.217
Fe (111) 50 nm	36	77	≈3.0	≈100	≈200	25.6	0.142	0.148
Fe (001) 50 nm	36	300	≈5.0	≈200	≈192	40.2	0.198	0.196
Fe (001) 50 nm prestr.	36	300	-	-	≈192	21.9	0.118	0.136
Fe (001) 50 nm	36	600	≈7.0	≈250	≈182	32.3	0.182	0.163
Fe (001) 50 nm	36	900	≈7.0	≈320	≈163	21.7	0.139	0.147
Fe (001) 70 nm	48	77	≈2.5	≈120	≈190	40.1	0.211	0.213
Fe (001) 70 nm	36	900	≈3.5	≈150	≈160	21.1	0.135	0.154
Cu (001) 36 nm	24	77	≈4.0	≈270	≈215	17.9	0.089	0.099
Cu (001) 70 nm	48	77	≈2.5	≈130	≈128	12.2	0.093	0.097
Cu (001) 105 nm**	100	77	≈2.0	≈150	≈120	11.9	0.091	0.098
Cu (011) 70 nm	48	77	≈2.0	≈210	≈155	20.0	0.126	0.130
Cu (011) 70 nm prestr.	48	77	-	-	≈155	9.9	0.065	0.073
Cu (011) 70 nm	48	400	≈3.5	≈150	≈140	17.1	0.112	0.119
Cu (011) 70 nm prestr.	48	400			≈140	7.8	0.060	0.069
Cu (111) 70 nm	48	77	≈2.0	≈95	≈170	23.7	0.140	0.143
Al (001) 70 nm	48	300	≈4.0	≈220	≈75	6.9	0.111	0.115
Al (001) 70 nm***	100	300	≈4.0	≈300	≈82	8.8	0.107	0.110
Al (011) 70 nm	48	300	≈4.0	≈250	≈100	12.7	0.121	0.124
Al (111) 70 nm	48	300	≈3.0	≈200	≈110	14.0	0.140	0.139
Al (111) 70 nm prestr.	48	300	-	-	≈110	9.0	0.088	0.850

Subscript (e) stands for elasticity in accordance with the contact state that leads to Hertzian-type predictions (Eq. (5.2)), while subscript (p) indicates the contact state at the onset of the first pop-in event. The indentations marked "*prestr.*" (pre-strained) are those containing a preexisting defect network prior to indentation.
The nanoindentations are performed at 4 m/s except **(30 m/s) and ***(0.2 m/s).
[†] refers to the indented surface and computational domain size, respectively (Table 3.2).
* the reported levels for E are computed in accordance with Appendix A2.

The above discussion indicates that the dimensionless parametrization of the contact in terms of the $p_\mathrm{m}/E - a/D$ evolutions tentatively captures the onset of the first nanocontact instability as a function of the specific defect nucleation processes attaining for different surface orientations, crystalline structures, and temperatures, thus adding to the detailed work by Ref. [146] on the possible mechanistic parameters governing the inception of plasticity in nanocontact loadings.
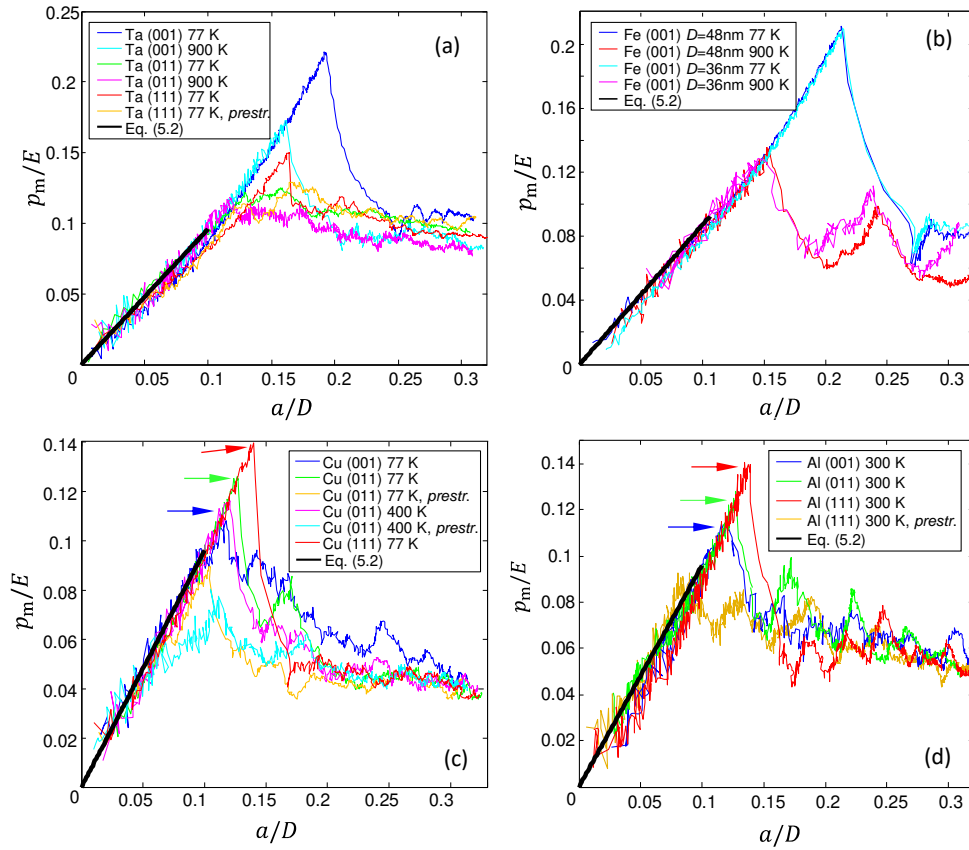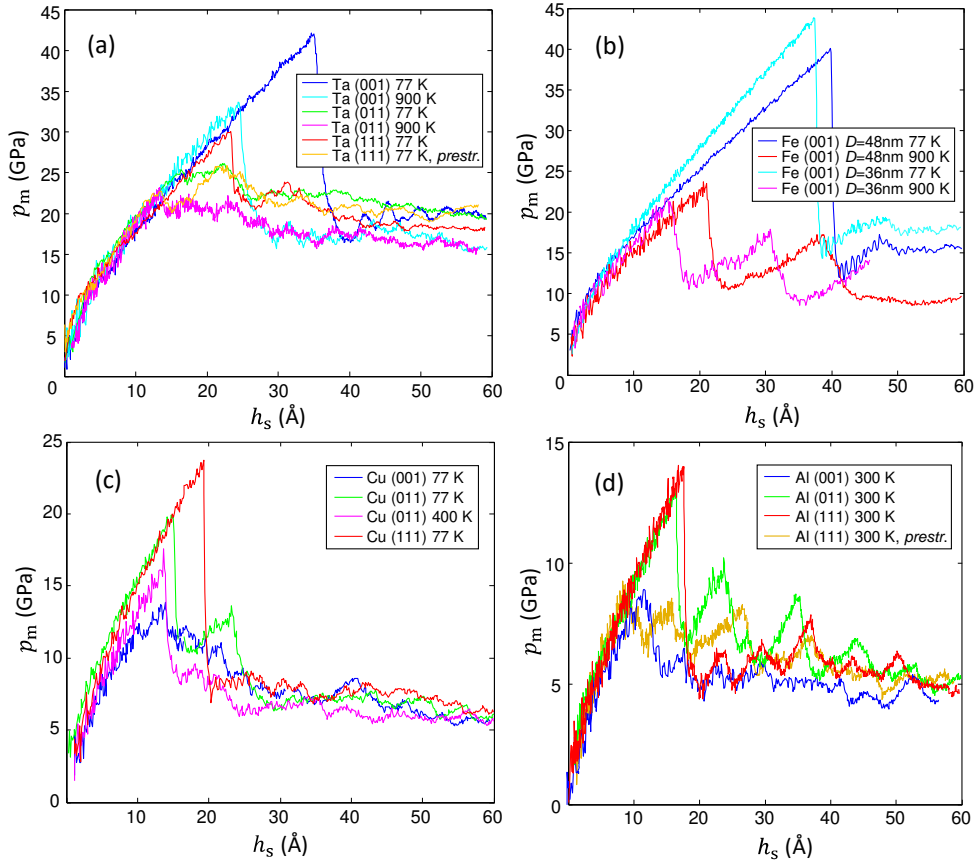
Figure 5.3. $p_m - h_s$ **curves from FCC and BCC nanoindentations. All of the indentations are carried out at 4 m/s. The indentations in (a), (c), and (d) are performed with indenter tips of $D = 48$ nm.**

The *pre-strained* computational domains that contain a preexisting (fully-developed) dislocation structure provide a special (but extremely pertinent) scenario to the inception of plasticity, where it is expected that the transition to plastic deformation is facilitated by the presence of such defect networks [21]. These defect configurations are constructed under the computational procedure described in Section 3.2.3. The subsequent indentations of pre-strained crystals are analogous to those used in the defect-free counterparts (Section 3.2.2). The onset of plasticity in the pre-strained simulations involves *heterogeneous* defect nucleation processes occurring in the (preexisting) defect network which lead to relatively low $p_{m\,(p)}$ levels (Fig. 5.3(d)) and fainting pop-in excursions (Fig. 5.4(c)). It is clear that the heterogeneous nucleation process in the indented crystals [28, 66, 147] requires smaller contact pressures that those typically obtained in the case of the homogenous defect nucleations in defect-free crystals [21, 62]. Along these lines, the MD nanoindentations thus show that the $(p_m/E)_{(p)}$ levels attained in pre-strained crystals are $\approx 30 - 40\%$ smaller than those encountered in defect-free crystals, see Figs. 5.1 and 5.6.
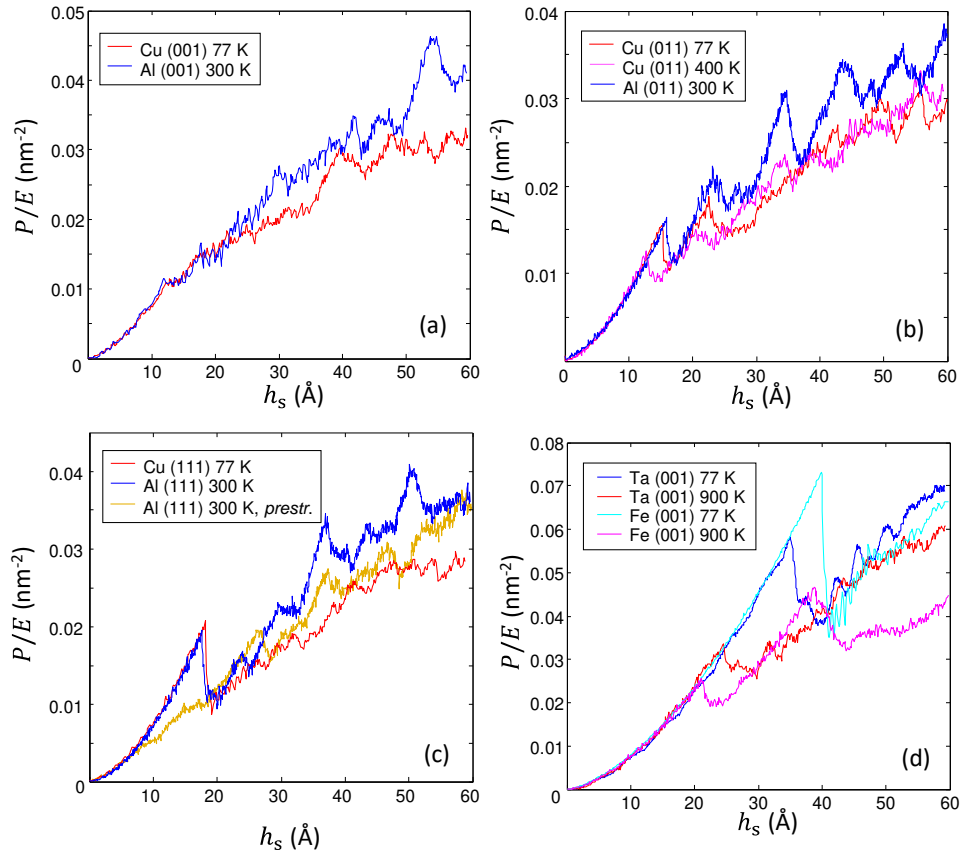
Figure 5.4. $P/E - h_s$ curves from FCC and BCC nanoindentations. All of the MD indentations are performed with indenter tips of $D = 48$ nm and an indentation rate of 4 m/s is imposed.

Although the above discussion describes the role that a preexisting (dense) dislocation entanglement plays in the onset of nanocontact plasticity, in reality, the likelihood of encountering a single (preexisting) dislocation below nanoindenter-tips is negligible [148]. Therefore, the onset of plasticity is commonly attributed to *homogeneous* nucleation processes [14]. Nanoindentation experiments have demonstrated [14, 21, 41, 79, 148] that defect inception follows stochastic laws as the process can be described under statistical distributions of both critical load and penetration. To evaluate the effect of such stochastically-occurring defect nucleation phenomena upon the $p_m - h_s$ curves at the first pop-in as well as for deeper indenter tip penetrations, a comprehensive set of Fe indentations at 300 K is performed for the (001) surface under identical testing conditions, where only the initial distribution of atomic velocities is varied. Thus, all such MD realizations concern statistically dissimilar initial conditions. Figure 5.6 illustrates that while the MD nanoindentations mimic a clear stochastic behavior at the pop-in level (see the insets to this figure), the influence of these stochastic processes on the overall $p_m - h_s$ response is inconsequential as all the realizations convergence towards similar levels of plastic hardness, see Fig. 5.6(b).
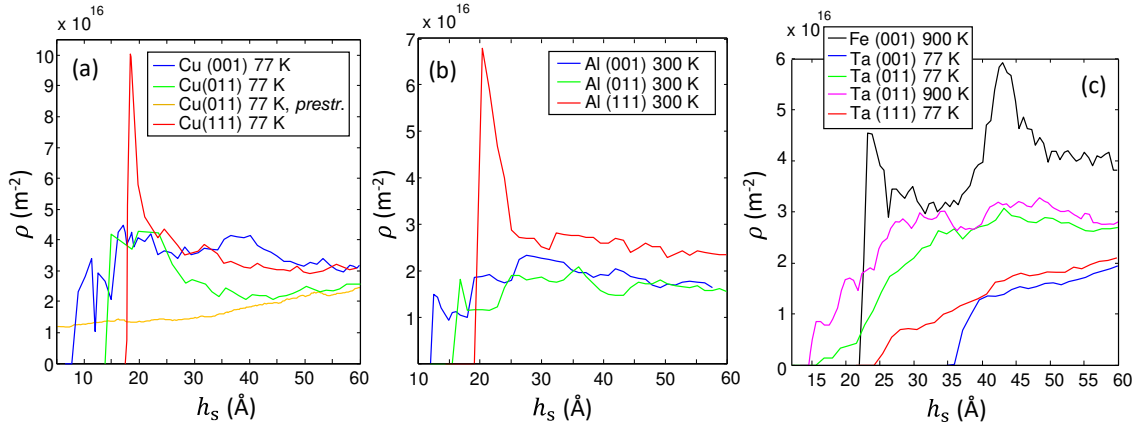
Figure 5.5. $\rho - h_s$ curves from FCC and BCC nanoindentations. All of the indentations are performed with indenter tips of $D = 48$ nm with an indentation rate 4 m/s. The ρ evolutions are computed in accordance with Appendix A8. V_{pl} in pre-strained crystals is defined as $V_{pl} = V - V_{ind}$ (see Eq. (A8.2) in Appendix A8). Note that the analysis of dislocation densities (Appendix A8) is unable to include BCC nanotwinning in the $\rho - h_s$ evolutions so that attainment of a steady-state defect network is lacking in the Ta (001) and (111) indentations at 77 K (part (c)).
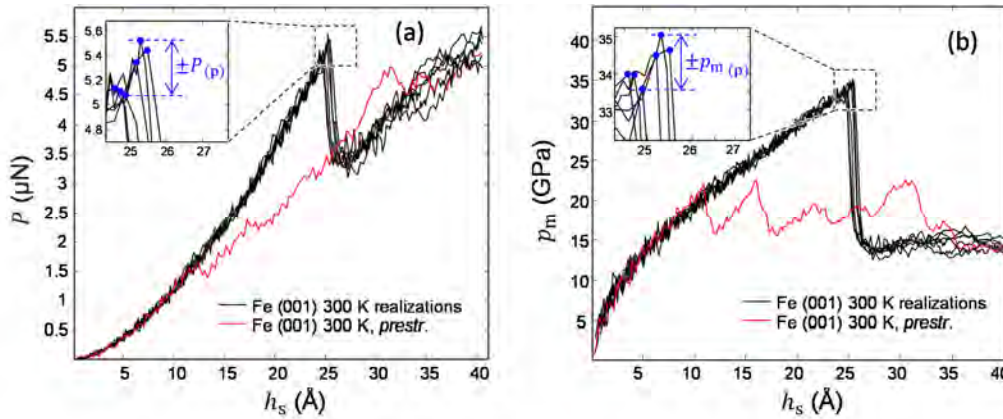
Figure 5.6. Distinct realizations of the Fe (001) nanoindentation. (a) $P - h_s$ and (b) $p_m - h_s$ curves obtained at $T = 300$ K with indenter tips of $D = 36$ nm. Under these conditions, the MD simulations show that the uncertainty [148] arising in critical load and critical hardness levels is characterized by $\pm P_{(p)} \approx \pm 0.5\ \mu N$ and $\pm p_{m\,(p)} \approx \pm 1.3$ GPa, respectively, see the insets to the above pictures. The exhibits contain 6 different realizations of a nominally identical indentation test.

Finally, special attention is given to investigate the role of the indentation rate (i.e., indenter-tip penetration velocity) in the onset of nanocontact instabilities. In consistency with the results reported in Ref. [38, 122] for BCC surfaces, the Al simulations corroborate that the defect mechanisms occurring at nucleation remain unaffected by the indentation loading rate (Appendix A5.1), while the critical load levels ($P_{(p)}$) exhibit a mild reduction with decreasing indentation velocities. According to Fig. 5.7, when the indentation rate is decreased by two orders of magnitude (i.e., from 4 m/s to 0.04 m/s) in the (001)-oriented Al surface, the value of $P_{(p)}$ shows a gradual decrease from 0.837 μN to 0.77 μN, which corresponds, in terms of $p_{m(p)}$, to a much milder decrease (i.e., from ≈ 8.9 GPa to ≈ 8.6 GPa), see the inset to this figure.
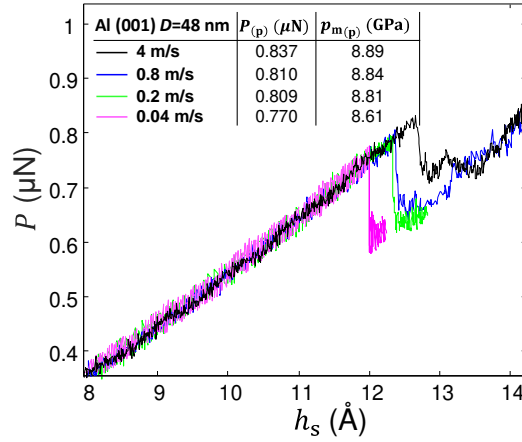
Figure 5.7. The effect of the indentation rate on the critical load levels. The results are for Al (001) nanoindentations with $D = 48$ nm at 300 K.

5.3. Contact mechanisms during nucleation pop-ins

The nucleation pop-ins involve a marked load drop in the $P - h_s$ curve (Fig. 5.4), which is a particular characteristic of nanoindentations performed under displacement control [38] [14, 38], where the elastic relaxation of the surfaces produced during defect nucleation leads to the onset of such load discontinuities. This process induces a sudden encasing of the indenter tip by the surrounding material due to the onset of pile-up effects, which lead to a market increase the contact area (Section 4.3.1). The development of nucleation pop-ins attain to a point where no additional sudden defect emissions occur underneath the nanoindenter.

Under the assumption that nanocontact plasticity is only due to dislocation slip, the advent of the first pop-in necessarily attains in such a way that the total slip produced by the nucleated dislocations results in a sudden expansion of the contact area. The model developed by Nix and Gao (NG) [10] then provides a simple representation for the development of the permanent imprint. According to this model, the GNDs which accommodate the plastic deformation produced by the indenter tip can be related to the indenter penetration [10, 143] as shown in Fig. 5.8(a). This model effectively captures the decrease in contact pressure with increasing penetrations and also provides a fundamental rationale to the onset of indentation size effects in indention testing with micrometer-sized indenters, where the injection of GNDs becomes consequential to imprint formation and strain hardening [10, 143]. According to Fig. 5.8(a), the total GND length is defined as $l_{\mathrm{GND}} \approx \pi h_s a / b$. Under the assumption that plasticity develops in a semi-hemispherical volume (V_{pl}) of radius a [10, 20], the GND density (ρ_G) injected under the indenter then follows the relation [10]

$$\rho_G^{\mathrm{NG}} = \frac{l_{\mathrm{GND}}}{V_{\mathrm{pl}}} \approx \frac{3 h_s}{2 b a^2} \, . \tag{5.4}$$

To verify whether *nucleated* GNDs can effectively account for early imprint formation during nanoindentation, a conceptual framework based on the NG model is tested here for the Al (111) indentation whose first pop-in event involves an abrupt nucleation of dislocation arrays with relatively short faulted planes (Section 4.2.2). The contact state for the analysis (Fig. 5.8(b)) is chosen so that a plastic imprint has been produced as if strict load-controlled conditions were imposed [14, 41], see Fig. 5.8(c). In this case, the imprint formation is assumed

65

to occur from h_1 to h_2 (Figs. 5.8(c) and 5.8(d)) and Eq. (5.4) provides $\rho_G^{NG} \approx 1.1 \times 10^{17}$ m^{-2}. By virtue of the results reported elsewhere in Ref. [119], the GND density encountered in MD nanoindentations follows $\rho_G^{MD} \approx 0.1\rho$ in FCC crystals. According to that, the Al simulation at h_2 exhibits a GND density of $\approx 2.8 \times 10^{15}$ m^{-2} (i.e., the $\approx 10\%$ of the density found in the $\rho - h_s$ curve from Fig. 5.5(b) at $h_s = h_2$). This indicates that the original NG model overestimates the value of ρ_G in the Al nanoindentation by two orders of magnitude.
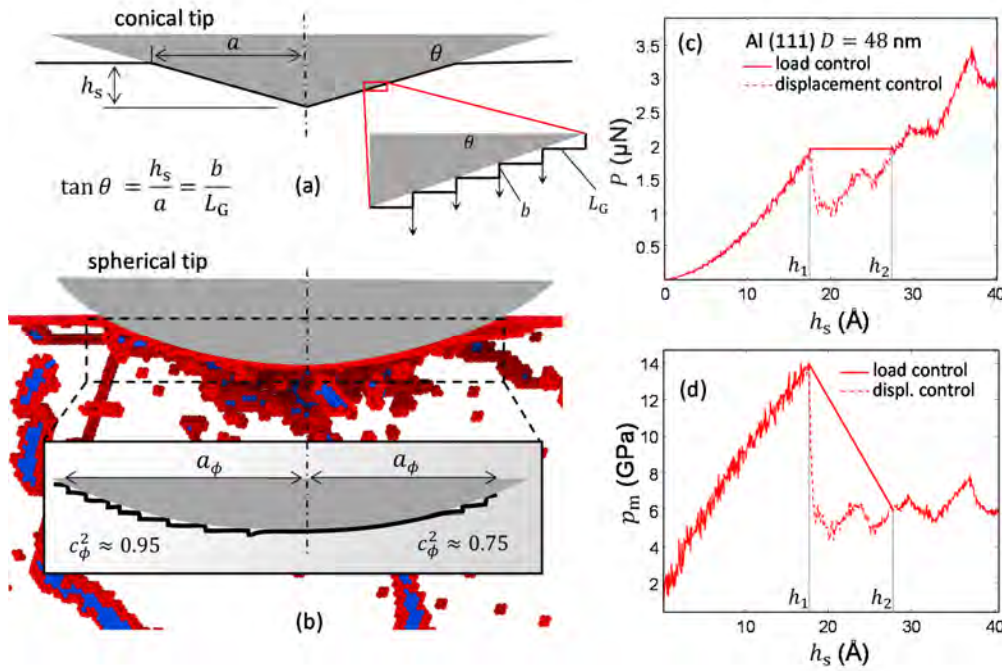
Figure 5.8. Imprint profiles and GNDs in the Al (111) nanoindentation. (a) Schematic representation of the NG contact. The inset to this picture displays the homogeneous distribution of GNDs, where the arrows point towards the evenly-spaced distribution of emitted GND loops characterized by the distance L_G. Since the GNDs conceptually produce steps of height b, the contact definition yields the equality $\theta = \tan^{-1}(b/L_G)$ [10]. (b) ($\bar{1}10$) cross-sectional cut in the Al indentation (300 K) at $h_s = h_2$ (see (c) and (d)). Notice in the inset to picture (b) that the marked slip features enhance the encasing of the indenter-tip by the surrounding material, favoring the onset of pile-up effects (with $c_\phi^2 \to 1$). (c) and (d): Load and hardness pop-ins (respectively) under load-controlled vs. displacement-controlled conditions in the Al nanoindentation.

The NG model fails in describing imprint formation with sub micrometer-sized indenters due to the following. (i) While any indenter tip is rounded to some extent at nanometer dimensions [16], the NG indenter is assumed to have a perfectly conical shape (Fig. 5.8(a)). (ii) The fact that the nucleated GNDs interact with each other results in a significant increase in dislocation density; so that most of the dislocations present in the subsurface are not GNDs [18]. (iii) Surface dislocation nucleation processes are not taken into account [20]. (iv) The onset of sink-in and pile-up effects around nanoindenters (Section 4.3.2) is not considered [18]. These issues have led to the conclusion [12, 16, 18, 143] that the use of nanometer-sized indenter tips produces much greater values of ρ_G ($\approx 10^{16}$ m^{-2} [18]) than those predicted in the original NG model.

When it comes to compare the GND distributions across the imprint profile, there is no possible comparison between the NG representation (Fig. 5.8(a)) and the actual results from the

MD simulations in Al (inset to Fig. 5.8(b)). In the latter, the advent of inhomogeneous surface step distributions at the contact leads to the detection of fluctuating values in the circumferential a_ϕ and c_ϕ^2 (Fig. 4.12(c)). It is noted that in all FCC and BCC nanoindentations, the $\overline{c^2}$ levels at h_2 are $\overline{c^2} \approx 0.65 - 0.85$ (Fig. 4.10). These values clearly evidence the important elastic component present in nanoimprint formation which cannot be possibly regarded as a fully plastic process. Furthermore, the dislocation distribution is not homogeneously distributed while both surface annihilation and interaction processes drastically affect the actual distribution of dislocation density underneath the nanoimprint.

5.4. Evolution of nanocontact plasticity

The attainment of serrated $P - h_s$ and $p_m - h_s$ curves is a characteristic feature of nanocontact plasticity (Figs. 5.3 and 5.4) [20, 38, 39], where the development of load (or hardness) drops stems from collective defect activities occurring bellow the indenter tip [39, 40]. According to the present nanoindentation simulations, the irregular expansion of the defect networks with increasing penetrations [39, 119] is distinguished by (i) dislocation emissions outwards and towards the contact surface, (ii) the gradual formation of short-range dislocation interactions, and (iii) dislocation annihilation resulting from segment truncation at the free surface. The strong role of the crystallographic orientation of the indented plane, crystalline structure and testing temperature upon the development of nanocontact plasticity becomes evident in Figs. 5.3 and 5.4, as each indentation (with 48-nm diameter tips) is found to produce specific plastic excursions in the $P - h_s$ and $p_m - h_s$ curves.

It is important to emphasize that although the dimensionless quantity p_m/E (referred hereafter to as the *normalized hardness*) enables the characterization of the pop-in instability in such a way that the elastic modulus is factored-out (see Eq. (5.2)), the p_m/E normalization is not strictly valid within nanocontact plasticity as the material hardness becomes a complex function of elastic and plastic parameters which cannot be simply deconvoluted through the ratio p_m/E. Note that the influence of the elastic properties upon the nanocontact response arises from the complex distribution of the elastic stress fields associated with the injected dislocations [3, 20, 21], which affect the p_m levels in a nontrivial manner. In this context, two indented surfaces showing identical mechanisms of nucleation and dislocation interactions but different elastic moduli would give rise to distinct values of p_m/E as a result of the different elastic fields generated by the "topologically identical" defect networks.

At deeper penetrations (say, $a/D > 0.2 - 0.25$), the simulations show the systematic attainment of a *stationary regime* in the $p_m - h_s$ and $p_m/E - a/D$ evolutions, where the specific plateau levels are found to attain irrespective of the crystalline orientation in all of the FCC and BCC nanoindentations, see Figs. 5.1 and 5.3. In consonance with the above discussion, it is believed that the elastic fields generated by the densely entangled dislocation arrangements ($\rho \approx 10^{16}$ m^{-2}) average out the elastic contributions on plastic imprint formation so that the p_m/E plateaus attain as a function of the distinctive defect structures and the corresponding dislocation density level. Within this framework, the attainment of the hardness plateau levels provides essential insight into FCC and BCC nanocontact plasticity.

Immediately upon the onset of the first pop-in event, the nanoindentations exhibit a mild decrease in hardness levels with increasing penetration (e.g., the (001)-oriented FCC surfaces in Figs. 5.3 and 5.5) which is due to the complex phenomenology associated with the development of the defect network and V_{pl} expansion [119, 149]. At larger penetrations, additional load drops (secondary pop-ins [14]) imply the onset of sporadic mobilization stages

of the defect network, which also lead to sudden increments in contact area and pile-up development at $r \approx a$, see the inset to Fig. 4.10(a). The hardness drops develop to a point where the active dislocations become arrested by the immobile defect entanglement. The nanocontact responses between adjacent pop-in events then involve *quasi-elastic* loading stages occurring
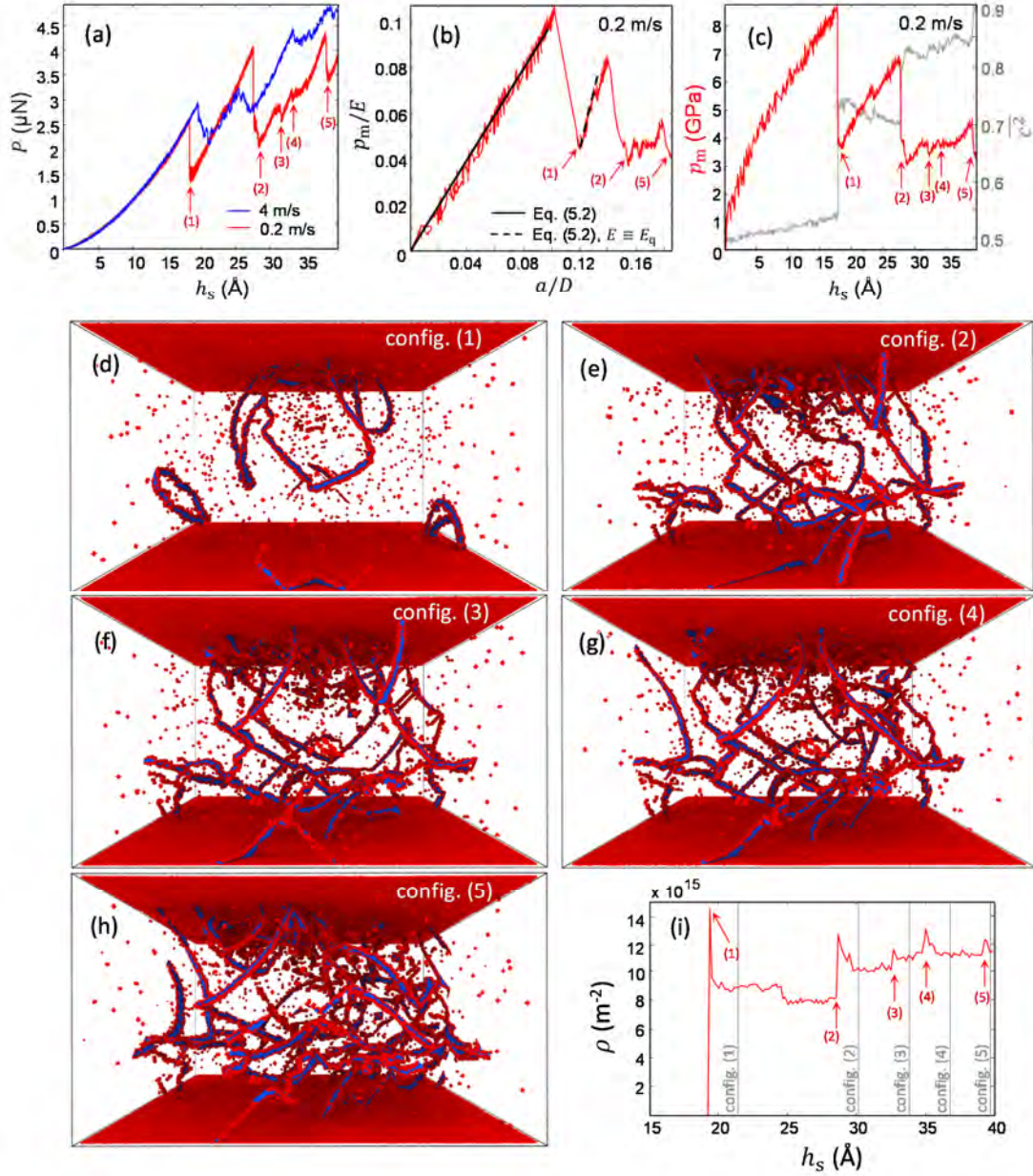
Figure 5.9. Intermittent development of the dislocation network in Al nanoindentation. The results are from the MD simulations of Al (001) indentations with $D = 100$ nm at 300 K with loading rates of 4 m/s and 0.2 m/s. (a) The $P - h_s$ curves evidence the onset of *intermittent* nanocontact plasticity at 0.2 m/s, where the plastic events (load drops) attain at fixed indentation depth. (b) $p_m/E - a/D$ curve at 0.2 m/s. The continuous and dashed lines in (b) respectively follow pure elastic and quasi-elastic stages (Eq. (5.2)). Note in the latter $E_q < E$ due to the onset of pile-up effects at $r \approx a$ [7]. (c) $p_m - h_s$ and $\overline{c^2} - h_s$ curves at 0.2 m/s. (d)-(h): Defect configurations detected during quasi-elastic loading characterized by $d\rho/dh_s \approx 0$ in the $\rho - h_s$ curve (picture (i)).

under a pinned defect configuration. The Al nanoindentation performed at 0.2 m/s serves as an exemplification of the above, where the development of a plastic nanoimprint strictly attains during secondary pop-ins so that every plastic event (intentionally marked "(1)", "(3)" and "(6)" in Fig. 5.9(b)) leads to a net increment in a/D. These plastic processes are additionally captured by the $\overline{c^2} - h_s$ curve (Fig. 5.9(c)) where (i) quasi-elastic loading attains at a constant value of $\overline{c^2}$, and (ii) secondary pop-ins are characterized by a net increment in $\overline{c^2}$. [Note that the associated Young's modulus in the quasi-elastic stages, E_q, takes a smaller value than in pure elastic contacts, see Figs. 5.9(b)] Figures 5.9(d)-(h) show the immobile (pinned) stages that develop during such quasi-elastic loadings, where $d\rho/dh_s \approx 0$ (see Fig. 5.9(i)) and $dp_m/dh_s > 0$, while p_m/E_q follows Eq. (5.2) as illustrated in Fig. 5.9(b).

At deeper penetrations (for, say, $a/D > 0.2 - 0.25$), the simulations show the systematic attainment of a *stationary regime* in the $p_m - h_s$ and $p_m/E - a/D$ curves, where the specific hardness plateau levels are not significantly affected by crystalline orientation in all of the modeled FCC and BCC nanoindentations, see Figs. 5.1 and 5.3. In the context of the above discussion, it is then believed that the elastic fields generated by the densely entangled dislocation arrangements ($\rho \approx 10^{16}$ m^{-2}) average out, thus yielding to an overall value of the material hardness which is not apparently dependent on the surface orientation. The p_m plateaus in Figs. 5.3(c) and 5.3(d) evidence that although Cu crystals (with $p_m \approx 6.0 \pm 0.2$ GPa) are essentially harder than Al surfaces ($p_m \approx 4.9 \pm 0.3$ GPa), this order is reversed when considering the plateaus of p_m/E, where the Al nanoindentations exhibit greater levels of p_m/E ($\approx 0.05 \pm 0.002$) than the Cu counterparts ($p_m/E \approx 0.039 \pm 0.0015$), see Figs. 5.1(c) and 5.1(d). The p_m/E analyses evidence the important elastic component present in nanocontact plasticity as the ("soft") Al surfaces with $E \approx 75 - 110$ GPa (Table 5.1) produce a stronger response in terms of p_m/E than the ("hard") Cu indentations ($E \approx 128 - 170$ GPa).

While the FCC nanocontacts show that the attainment of the p_m/E plateaus is not markedly affected by temperature (compare the (011) indentations at 77 K and 400 K in Figs. 5.1(c) and 5.3(c)), the opposite applies to BCC nanocontact plasticity as the mechanisms for defect nucleation and subsequent dislocation emissions are largely influenced by temperature (Section 4.2.3). Thus, at low temperatures (77 K), the plateaus attain for the largest hardness values of all of the modeled nanoindentations (i.e., $p_m \approx 19.5 \pm 1.0$ GPa and $p_m/E \approx 0.095 \pm 0.005$), see Figs. 5.1(a) and 5.3(a). The onset of stable nano-twin structures generates an important "back-stress" [38] preventing imprint formation, which then leads to an increase in the p_m level. [This particular phenomenology will be described in Section 5.5.2] Nevertheless, although the p_m plateaus in BCCs attain at (much) larger levels than those obtained in the indented FCC surfaces (Fig. 5.3), the difference in the magnitudes of the plateaus developing between FCCs and BCCs is reduced by a half when the variable p_m/E is at issue (Fig. 5.1). By increasing temperature to 900 K, where the indented Ta surfaces ($T/T_m \approx 0.3$) exhibit dislocation-loop emissions (Fig. 4.8(f)), it is found that the onset of the plateau stage attains at lower levels of both p_m and p_m/E (≈ 16 GPa and ≈ 0.08, respectively), see Figs. 5.1(a) and 5.3(a). This tendency reaches a lower limit in the Fe (001) indentation at 900 K ($T/T_m \approx 0.5$), where the highly mobile dislocation network promotes the attainment of a plateau level for a similar normalized hardness to that reached in Al nanocontacts ($p_m/E \approx 0.05$), see Fig. 5.1. According to these results, the development of BCC nanoimprints at elevated temperatures ($T/T_m > 0.3$) presumably reaches an analogous plateau stage to that encountered in FCC Al imprints under highly mobile (cross-slipped) dislocation networks (Fig. 4.6(d)).

The above discussion indicates that the normalized hardness, p_m/E , allows for an effective characterization of both the elastic nanocontact regime (*via* Eq. (5.2)) as well as the

pop-in instabilities (Section 5.2), which includes the underlying defect mechanisms associated with the development of plastic (permanent) nanoimprints at deep penetrations. These findings show that the plastic nanoimprint formation processes are essentially governed by the distinctive defect structures injected underneath the nanocontacts as a function of crystalline structure and temperature.

5.5. Strengthening properties of the simulated dislocation networks

An important concern in this investigation concerns the possible strengthening effects attaining in the simulated crystals, where the *dense* dislocation configurations ($\rho \approx 10^{16}$ m^{-2}) may lead to the extreme hardness levels obtained in the MD nanoindentations (Fig. 5.3). This is asserted by an additional group of uniaxial test simulations with periodic computational volumes that contain the fully-developed defect networks present underneath the indented surfaces. Uniaxial deformation is then imposed upon such material volumes under strict displacement controlled conditions with a stretching rate of ≈ 0.8 m/s ($\dot{\varepsilon} = 1.2 \times 10^7$ s^{-1}), see Table 3.5. The computational procedure employed in these simulations is described in Section 3.2.3.

By recourse to the Taylor's hardening model [3], where $\sigma = M\alpha Gb\sqrt{\rho}$ (see Section 2.1), it becomes possible to evaluate the strengthening coefficient α which provides an indication of the degree to which the injected dislocation networks have hardened the crystal [32, 75]. This model is invoked at the inception of plasticity, where the first stress burst in the $\sigma - \varepsilon$ curve (marking the σ_y level, see arrows in Figs. 5.10(f)-(h)) enables elucidation of the resolved critical shear stress, $\tau_c = M\sigma_y$, that leads to dislocation activation in the simulated periodic networks (see Figs. 5.10(a)-(e)). Within this framework, the inferred data from the FCC and BCC simulations are collected in Table 5.2. It is found that the Taylor's coefficient attains $\alpha \approx 0.34$ in the Al simulations, which is in good agreement with the reported values for bulk FCC crystals containing less entangled dislocation networks ($\rho \approx 10^8 - 10^{12}$ m^{-2}) [32, 76]. The simulated Cu crystals, however, exhibit lower values of α (≈ 0.26). This difference may be attributable to the long SF ribbons observed in the Cu simulations (compare Figs. 5.11(a) and 5.10(b)), where junction formation processes due to dislocation interactions become less evident. This issue is dramatically amplified with smaller MD cells (Fig. 5.10(c)) where the scarce number of dislocation arrays leads to $\alpha \approx 0.15$ (Table 5.2). The results from the Ta simulations capture the influence of temperature-assisted screw mobility over crystal strengthening as an increasingly mobile defect network (900 K) leads to a 20% decrease in α with respect to the value found at lower temperatures (300 K), see Table 5.2.

The above results support the concept in that the Taylor hardening model scales with dislocation density up to the presently injected extreme density levels. This is in agreement with the correspondence between the nanohardness and dislocation density levels present in the modeled nanocontacts, where the onset of a plateau stage (Fig. 5.3) is associated with the attainment of a stationary (fully-developed) dislocation network below the indenter tip (i.e., $d\rho/dh_s \approx 0$, see Fig. 5.5).
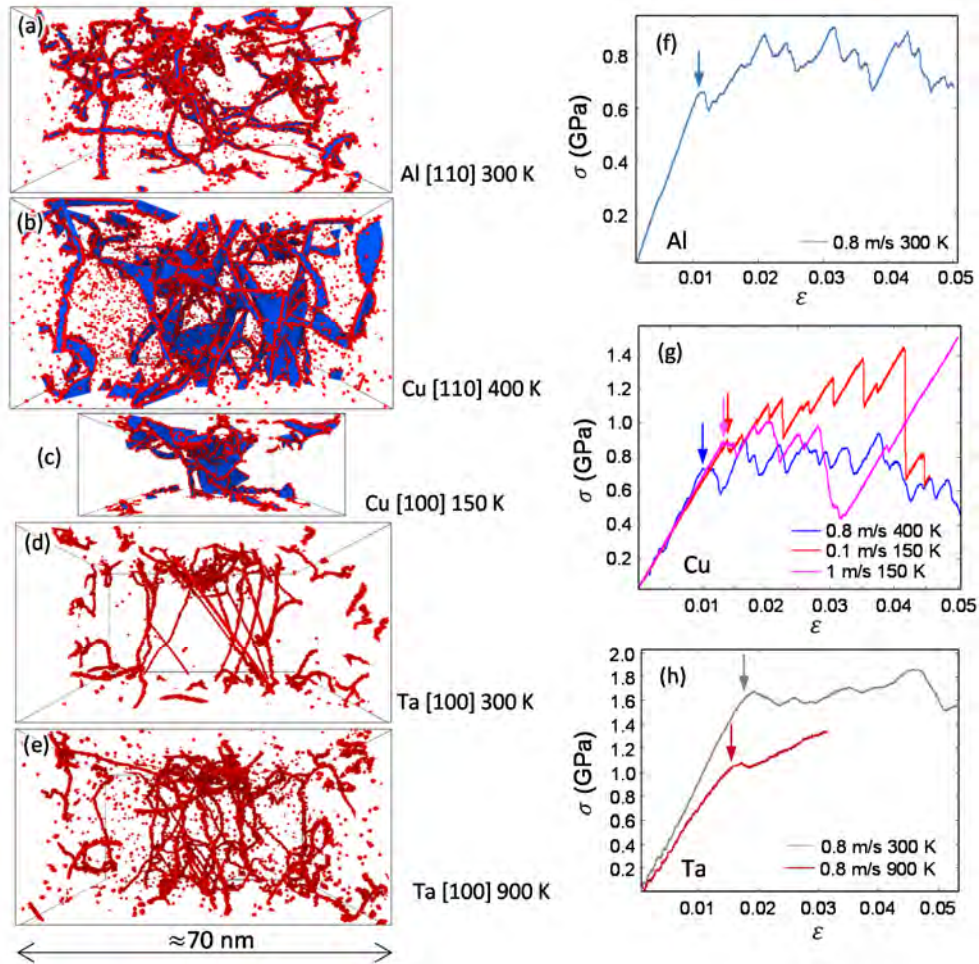
Figure 5.10. MD simulations of uniaxial tests in pre-strained FCC and BCC crystals. The left-hand side pictures show the preexisting dislocation configurations at the onset of plasticity (marked with arrow in the corresponding $\sigma - \varepsilon$ curves at the right-hand side).

It is emphasized that the underlying defect mechanisms governing nanoimprint formation are different than those associated with the development of dislocation networks under uniaxial straining. In the former, the gradual formation of a plastic nanoimprint occurs through recurrent processes of *heterogeneous dislocation* nucleation at extreme contact pressures [38], while in the latter the plastic response is governed by the local activation of dislocation segments within a short-range force landscape [22] leading to $d\rho/d\varepsilon > 0$ so that $d\sigma/d\varepsilon > 0$ (Eq. (2.2)). To probe the degree to which present nanoimprints are formed under classical strain hardening paradigms, the bulk-like Tabor's model is invoked [1, 24]. This model states that the elastic limit (uniaxial test) and material hardness (indentation) are correlated through $p_{\mathrm{m}}/\sigma_{\mathrm{y}} \approx 3$ [24]. Under this framework, present FCC and BCC simulations systematically indicate that the correlation between p_{m} and σ_{y} lacks all validity at nanoscale as it is found that $p_{\mathrm{m}}/\sigma_{\mathrm{y}} \approx 5 - 11$ in the present simulations (Table 5.2). In accord with the above discussion, note that both quantities (i.e., hardness and yield strength) are essentially obtained under the operation of two distinct plastic phenomenologies.

Table 5.2. Taylor's coefficient and Tabor's relation as inferred from the FCC and BCC simulations.

Crystal	T (K)	stretching rate (m/s)*	σ_y (GPa)	p_m plateau** (GPa)	ρ (m^{-2})***	α	p_m/σ_y
Ta (001) 70 nm	300	≈0.8	3.35	≈19.0	1.65×10^{16}	0.25	5.6
	900	≈0.8	2.20	≈16.0	1.46×10^{16}	0.20	7.3
Cu (011) 70 nm	400	≈0.8	0.80	≈6.5	1.22×10^{16}	0.26	7.5
Cu (001) 36 nm	150	≈1.0	0.95	≈10.5	3.41×10^{16}	0.17	11.0
	150	≈0.1	0.92	≈10.5	3.41×10^{16}	0.17	11.4
Al (011) 70 nm	300	≈0.8	0.65	≈4.5	1.08×10^{16}	0.34	10.8

*The stretching direction is imposed in accord with Fig. 3.4(c), see Section 3.2.3. The influence of the strain rate on the σ_y levels is shown in Appendix A5.2.

**see Fig. 5.3.

*** ρ characterizes the (preexisting) dislocation networks activating at σ_y (Fig. 5.10).

5.6. Nanoimprint formation processes

The imprint profiles obtained during the early elastic responses in both FCC and BCC MD nanoindentations are in good agreement with the radial pressure distributions, $p(r)$, predicted for Hertzian-type contacts, where [138]

$$p(r) = \frac{p_m(a^2 - r^2)^{1/2}}{a} .$$ (5.5)

Figure 5.11(a) illustrates the elastic contact of the (111)-oriented Cu surface (at penetration level marked "(a)" in Fig. 5.11(b)). While the central points ($r \approx 0$) exhibit the largest applied loads (Appendix A3), the load points (i.e. the in-contact atoms) tend to decrease in intensity (blue) with $\rightarrow a$, where the contact periphery is finally attained at $r \approx a$, $p(a) = 0$. The inset to Fig. 5.11(a) demonstrates that the discrete load distributions from the collection of in-contact atoms reproduces with a great accuracy a continuum elastic contact along r (Eq. (5.5)).

At the pop-in event, the nucleated defects promote a rapid expansion of the contact surface that results in an abrupt increment in the imprint size (see arrow in Fig. 5.11(a)). In this regard, a correlation is found between the nucleation phenomenology and the increment of parameter $\overline{c^2}$ at the onset of plasticity (hereafter referred to as $\Delta\overline{c^2}$). In particular, the (111)-oriented Al surface exhibits the largest $\Delta\overline{c^2}$ (≈ 0.35) of all nanoindentations (Fig. 4.10(c)), where the specific defect nucleation produces a rapid onset of slip traces throughout the imprint which in turn leads to the increase in contact surface as material pile-up is favored. However, although a similar nucleation mechanism is encountered in the Cu (111) indentation, the onset of slip traces is partly hindered due to the longer SFs developing in this material (cf. Fig. 4.6(a) and 4.6(b)), which leads to smaller $\Delta\overline{c^2}$ levels as compared to those attained in Al (Figs. 4.10(b) and 4.10(c)).

In BCCs, the values of $\Delta\overline{c^2}$ are not apparently affected by temperature, where it is noted that the low-temperature nucleation of nanotwin walls as well as the emission of highly-mobile dislocation arrangements at $T/T_m > 0.3$ leads to similar magnitudes of $\Delta\overline{c^2} \approx 0.3$. In addition, the surfaces with milder nucleations characterized by, say, $\Delta\overline{c^2} < 0.2$, (Fig. 4.10(a)) also exhibit the smaller p_m drops at the first pop-in (Section 5.2).
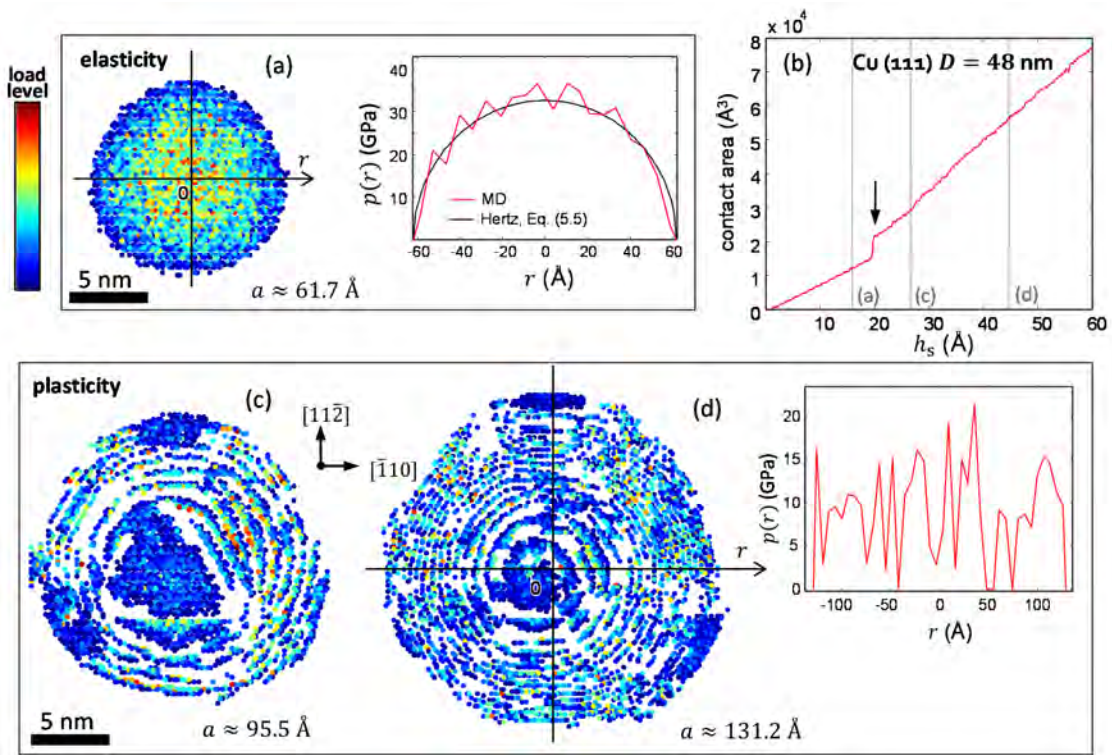
Figure 5.11. Imprint formation in (111)-oriented Cu. The indentation is performed with $D = 48$ nm and at 77 K. (a) The elastic contact (left-hand side) is in good agreement with the Hertzian radial function $p(r)$ (right-hand side). The coloring indicate the magnitude of the exerted force F_j to each of the in-contact atoms (see Appendix A3). (b) The $A - h_s$ curve captures the onset of elasticity and plasticity (see also Fig. A4.3 in Appendix A4). (c) and (d): Plastic nanoimprints lead to serrated $p(r)$ distributions due to the injected dislocations, where peaks and valleys in $p(r)$ evidence slip traces. A point in the $p(r) - r$ curve is defined by 4 neighbor atoms (where r is the center of the corresponding atomic region) so that a local area is conveniently defined for the contact pressure estimations, $p(r)$.

At larger indentation depths, the injection of dislocations results in slip trace emissions leading mild increments in both $\overline{c^2}$ (Fig. 4.10) and contact area (Fig. 5.11(a)) with increasing penetration. The analysis of the distributions of the atoms in contact (Figs. 5.11(c)-(d)) manifest the onset of slip traces around the imprint, which results in the development of loaded and unloaded regions, see Figs. 5.11(c)-(d). The inset to Fig. 5.11(d) provides the radial $p(r)$ distribution obtained for the Cu (111) indentation at a deep penetration. According to the simulations, the attainment of serrated $p(r)$ topographies is a signature of plastic nanoimprints, where sharp peaks and valleys denote imprint topographies with marked serrations (or slip traces).

5.6.1. Defect mechanisms for the development of plastic nanoimprints in FCCs

The Al simulations show that the emission of dislocations represents the dominant mechanism that leads to imprint formation, which is marked by the attainment of load excursions in the $P - h_s$ curves (Section 5.4). The incipient development of plastic (permanent) Al nanoimprints is characterized by the onset of loaded/unloaded regions (see the inset to Fig. 5.12(a)). To illustrate this process, Fig. 5.12(a) shows the early formation of the plastic imprint

in the (111) indentation. According to the Al simulations, the mechanisms associated with the dislocation injection and with the formation of permanent imprints are (i) the gliding of prismatic loops outwards from the contact, and (ii) dislocation emissions towards the surface during network development.

Notice that the orientation of the surface serrations or slip traces in the FCC nanoimprints is coincidental with the expected crystallographic character of plasticity (Fig. 4.5). With increasing penetration, further dislocation emissions originated from junction unzipping, heterogeneous nucleations, or the detachment of large SF ribbons (the latter mechanism is illustrated for Cu in Figs. 4.4(h)-(j)) conveniently directed towards the contact accounts for an effective source of slip trace emissions in Al nanoimprints. Note that the glide of dislocations leaves permanent traces (inset to Fig. 5.8(b)) that remain at the contact surface even upon indenter tip removal.
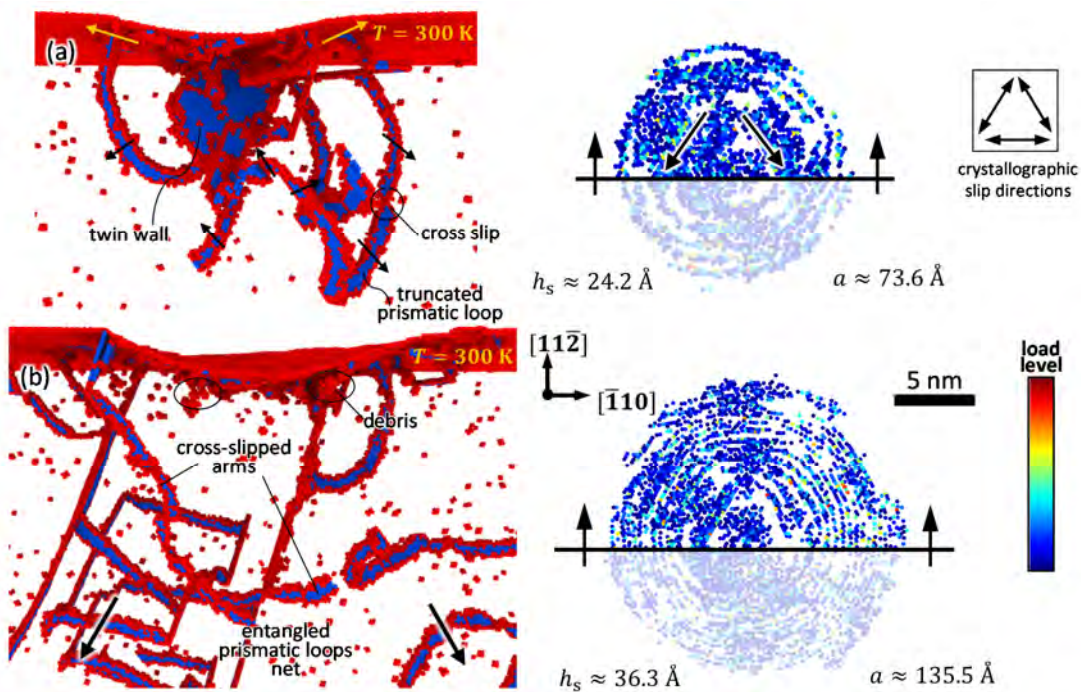
Figure 5.12. Mechanisms for plastic nanoimprint formation in FCC Al. The simulation features the (111) indentation at 300 K with an intender tip of $D = 48$ nm at 4 m/s. (a) $(11\bar{2})$ cross sectional cut of the early defect structure. Dislocation dissemination is further promoted by cross-slip processes, where cross-slipped segments obey the Friedel-Escaig model (Section 2.2.1). The inset to this picture illustrates the corresponding nanoimprint state. The brighter zone depicts the sectioned part in the main picture. The yellow arrows (or black arrows in the inset) mark dislocation slip. (b) Defect structure characterized by a general absence of dislocations below the contact during quasi-elastic loading. Dislocation debris (circles) and intricate slip distributions in the nanoimprint (inset) are a clear evidence of the spreading of the injected dislocations (arrows denote the gliding direction of the emitted prismatic loops).

In the Al nanocontacts, the role of cross slip becomes manifest in the gradual attainment of an intricate distribution of slip traces in the nanoimprints (see inset to Fig. 5.12(b)) due to the enhancement of dislocation network mobility (Fig. 5.12(b)). Although twin walls are occasionally encountered below the indenter tip (Fig. 5.12(a)) in the Al simulations, the total contribution of twinning dislocations to the total dislocation populations is rather small (about 1.5%). Cross-slip processes essentially promote the injection of slip traces in FCC nanocontacts

due to the dissemination of prismatic loops outwards from the nanocontact center (Fig. 5.12(b)). It is finally found that the quasi-elastic loading stages in the Al indentations mostly attain under the overall absence of a well-defined defect structure emerging throughout the imprint, see Fig. 5.12(b).
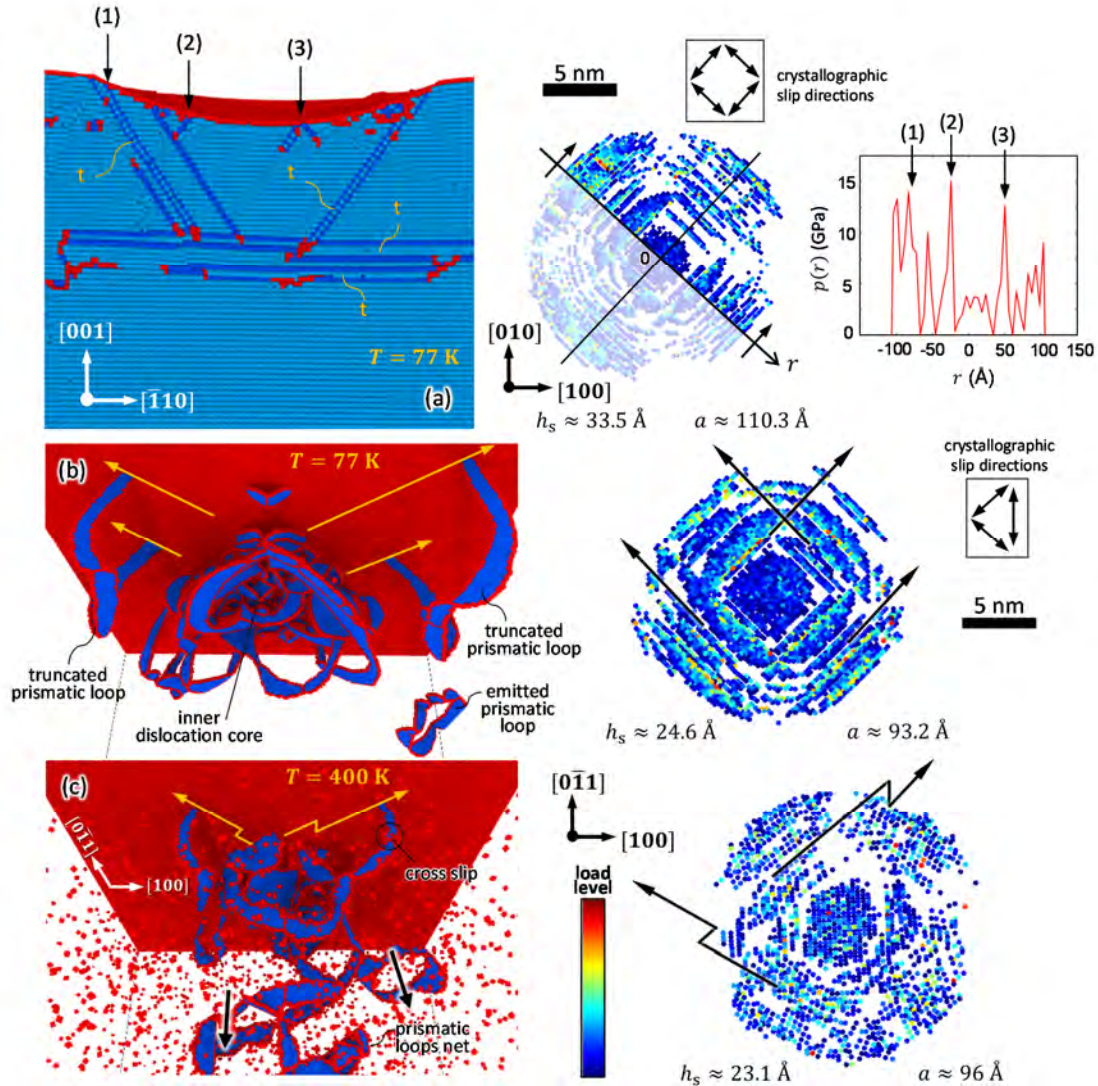
Figure 5.13. Mechanisms for plastic nanoimprint formation in FCC Cu. The indentations are performed with $D = 48$ nm at 4 m/s. (a) Nanotwinning in the (001) indentation at 77 K for a $(\overline{1}\overline{1}0)$ cross sectional cut ("t" denotes nanotwinned regions , see Section 4.2.1). The insets to this figure show the corresponding imprints (left-hand side) and $p(r)$ distributions (right-hand side). Marked peaks in the radial $p(r) - r$ topography evidence the presence of stable twin walls in Cu (see "(1)", "(2)" and "(3)"). (b) and (c): Defect configurations in the (011) indentation at 77 K and 400 K, respectively. With increasing temperatures, note that prismatic-loop mobility is promoted by thermally-enhanced cross-slip processes (see the serrated slip traces marked by yellow (picture) and black (inset) arrows).

By contrast, the Cu nanoindentations are distinguished by the presence of nanotwins (see the defect entanglement in Fig. 5.13(a)). The clustering of parallel crystallographic traces evidences the onset of nanotwinning (Section 4.2.1) in indented FCC surfaces, where the pronounced peaks detected in the radial $p(r)$ levels (right-hand inset to Fig. 5.13(a)) mark the

location of the SF walls. The MD simulations show that the marked development of nanotwinning underneath indented Cu surfaces (Figs. 4.4(c)) hinders the outward gliding of dislocations which remain trapped inside the twin entanglement (Fig. 5.13(a)). At higher temperatures, cross slip (Fig. 5.13(c)) enhances defect mobility and the attainment of a richer distribution of slip traces (compare the insets to Figs. 5.13(b) and 5.13(c)). However, the Cu simulations at 400 K indicate that nanotwin formation and development of dense dislocation networks with long SFs still dominate nanoimprint formation at large indentation depths (Fig. 4.6(c)). This leads to the attainment of similar levels of parameter $\overline{c^2}$ to those measured for lower temperatures (cf. the (011) indentations in Fig. 4.10(b)).

According to the above discussion, the inception of specific defect structures (dislocation glide vs. nanotwinning formation) plays a crucial role in the development of nanocontact plasticity of FCC crystals. In this context, the simulations show that the plastic responses from the indented Al crystals with mobile dislocation networks are characterized by the onset of marked plastic events that correspond with sharp drops in $p_\mathrm{m}/E - a/D$ curves (e.g., see the (011) indentation in Fig. 5.1(d)). As a result, the development of fluctuating $p_\mathrm{m}/E - a/D$ curves are a clear indication of heterogeneous nucleation and dislocation dissemination outward from the contact (Fig. 5.12(b)). By contrast, the Cu indentations produce milder fluctuations in the p_m/E levels (Fig. 5.1(c)) due to the emergence of a nanotwin sub-structure which hinders dislocation glide at the nanocontact. In the Cu simulations, the long SFs (Section 4.2.2) impede the expansion of the dislocation entanglements across the plastic volume, a feature that also hinders nanoimprint formation.

5.6.2. Defect mechanisms for the development of plastic nanoimprints in BCCs

At low temperature, the indented BCC crystals (77 K) exhibit nucleation of lenticular-shaped nanotwins (Fig. 4.8(a)) whose morphology is indicative of the crystalline orientation [38]. The resulting <111> growth direction of the {112} twins leads to the formation of crystalline nano-domains characterized by parent and twin orientations (marked in Fig. 5.14(a) as "p" and "t", respectively). With increasing penetrations, additional emissions of secondary (heterogeneously-nucleated) twins lead the production of an *intricate nanotwin structure* underneath the indenter (Fig. 5.14(a)). The Ta and Fe simulations evidence the great stability of such nanotwin structures, as they remain under the plastic impressions upon indenter removal (Fig. 4.15(h)). The upper inset to Fig. 5.14(a) is indicative in that the indented nano-domains (encased between twin walls) preserve the lattice configurations under the corresponding "p" or "t" orientations. The lack of dislocation slip throughout the imprint is attributable to the few atomic spacings ($\approx 5 - 15$) that exist between adjacent nano-domains (Fig. 5.14(b)), which hinders dislocation nucleation. The advent of such nanostructures restricts plastic imprint formation by dislocation slip, thus representing a small contribution to imprint formation in BCC plasticity at low temperatures. In accord with Fig. 5.14(b), dislocation slip is mostly limited to the small region contained between the periphery of the twin-induced nano-domains and the contact boundary ($r \approx a$). Notice in the radial $p(r)$ distribution from the Ta (011) indentation (inset to Fig. 5.14(c)) that the twinned nano-domains account for a considerable contribution to the mean contact pressure as the effective locations of twin-walls (see the "(1)"-"(4)" points) are characterized by prominent peaks in the $p(r)$ distributions.

Under these conditions, the gradual formation of plastic nanocontacts is then characterized (Fig. 5.14(b)) by (i) twinned domains accommodating the deformation by crystal rotation [119], (ii) inter-twinning elastic contacts (with, say, dislocation slip starvation), and (iii) dislocation slip outwards from the nanotwin structure that promotes pile-ups at the contact vicinity, see Section 4.2.3. In addition to the above mechanisms, the simulations show twin

band bending (see "bt" in Fig. 5.14(a)) occasionally attaining during the development of the complex nano-twin entanglement. It is believed that the latter mechanism further enhances the accommodation of large deformations in the zones where dislocation slip is restricted.
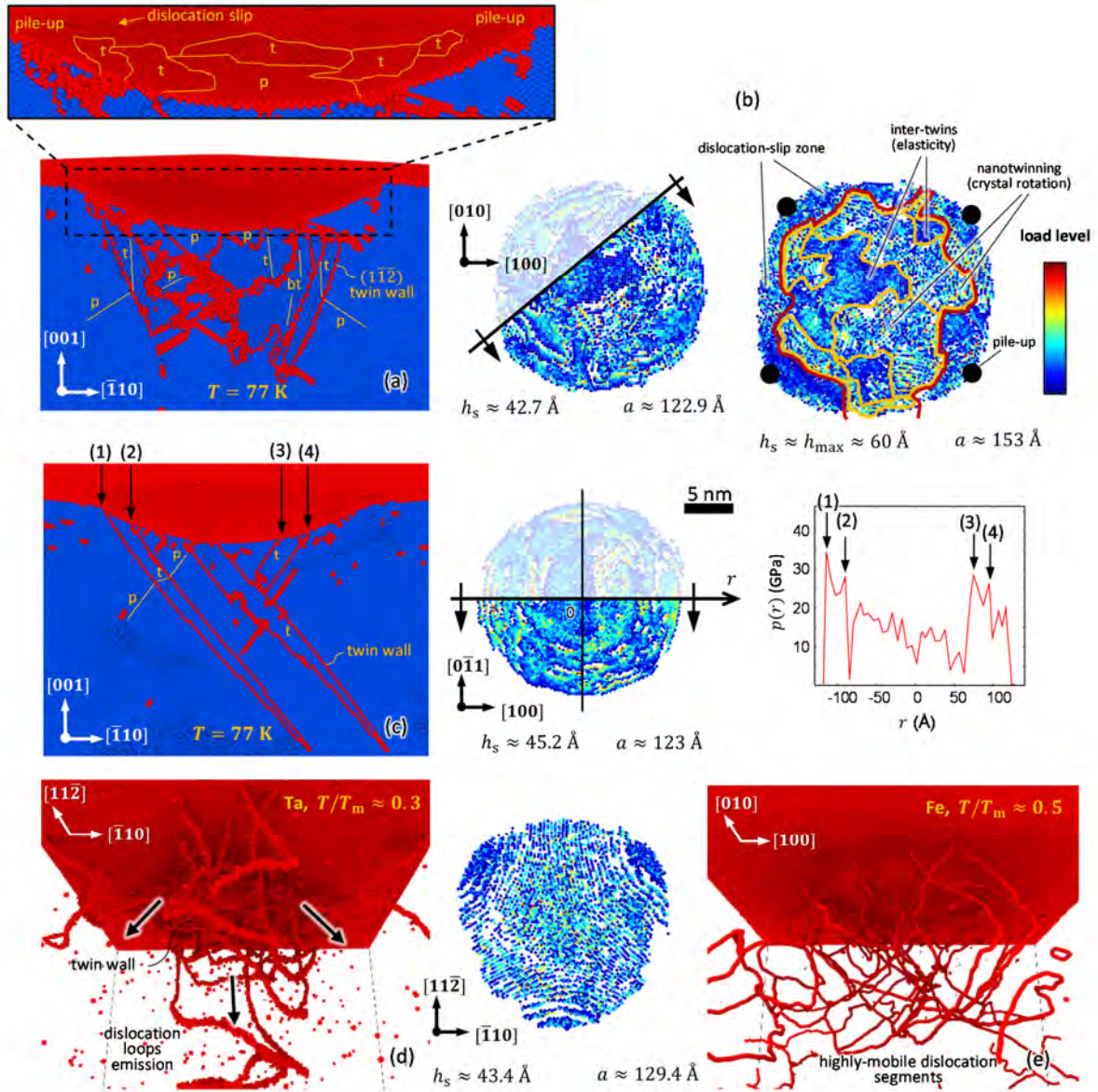
Figure 5.14. Mechanisms for plastic nanoimprint formation in BCC surfaces. The MD simulations comprise Ta and Fe nanoindentations with $D = 48$ nm at 4 m/s. (a) Twinning nano-structure in (001)-oriented Ta at 77 K under the $(1\bar{1}0)$ cross-sectional cut. The right-hand inset to this picture illustrates the corresponding nanoimprint. The upper inset displays the generation of "t" and "p" crystalline nano-domains in the inner imprint ($r \to 0$) whereas dislocation emissions are encountered as $r \to a$. (b) Mechanisms for BCC imprint formation at low temperature (77 K) where twin-wall truncation (marked in yellow) at the contact ultimately limits dislocation slip (which globally operates outside the red contour). Solid circles mark pile-up localization. (c) $(1\bar{1}0)$ cut in Ta (011) nanoindentation at 77 K. (d) Ta (111) indentation at 900 K ($T/T_m \approx 0.3$). (e) Attainment of a fully linear defect structure at elevated temperatures ($T/T_m \approx 0.5$) in (001)-oriented Fe at 900 K ($h_s \approx 45.8$ Å). The latter atomistic visualization of dislocation lines is performed in OVITO with DXA segmentation (Appendix A6).

Although the simulations additionally show that nanotwins may be also occasionally emitted at higher temperatures ($T/T_\mathrm{m} \approx 0.3$), BCC nanotwins are annihilated through detwinning processes with increasing penetrations (see Section 4.2.3) as the emission and propagation of full dislocation loops increasingly govern nanocontact plasticity, see Fig, 5.14(d). The thermally-enhanced mobility of the screw dislocations leads to the production of wavy traces at the contact surface so that plastic imprint formation is primarily due to dislocation slip emissions, see inset to Fig. 5.14(d). The gradual annihilation of nano-domains below the indenters is associated with a reduction in the plateau levels of normalized hardness. In this context, the Fe simulation at 900 K ($T/T_\mathrm{m} \approx 0.5$) suggests that a similar plastic evolution than that obtained in the indented Al surfaces at 300 K ($T/T_\mathrm{m} \approx 0.3$) arises as the plastic bursts attain through intermittent emissions of highly-mobile dislocation segments leading to p_m/E plateaus of ≈ 0.05, see Figs. 5.1(b) and 5.1(c).

5.7. Conclusions

1. The early elastic responses obtained in all of FCC and BCC nanocontacts are in good agreement with continuum predictions of the Hertzian contact. Within this framework, the MD simulations show that the mechanics of elastic nanocontacts is characterized by a linear relationship between the dimensionless ratios of p_m/E and a/D. In addition, the MD nanocontacts effectively reproduce the radial $p(r)$ Hertzian functions for the contact pressure.

2. The onset of plasticity is characterized by (i) a critical p_m/E level marking nanocontact instability and (ii) the magnitude of the hardness drop that attains at the first pop-in event, which is governed by specific defect nucleation mechanisms. The MD simulations reveal that the critical p_m/E level is a function of crystalline structure, surface orientation and temperature. In this context, the low-temperature inception of nanotwin walls in (001)-oriented Ta leads to the largest values of both the critical p_m/E value and the effective hardness drop at the first pop-in. With increasing temperatures, BCC surfaces exhibit the inception of mobile dislocation loops that results in a decrease in critical p_m/E levels. Defect nucleation in FCC (111) indentations are also characterized by relatively large values of the critical p_m/E as well as by sharp hardness drops because of the abrupt inception of prismatic loops during pop-in development. By contrast, the (001)-oriented FCC surfaces systematically exhibit the lowest critical p_m/E of all of the nanoindentations (with $D = 48$ nm), where the corresponding pop-in event results in the mildest hardness drops due to the inception of a small number of dislocation arrays. These findings suggest the attainment of a general pattern in the inception of nanocontact plasticity, where the sharper the hardness drop at pop-in, the larger the critical p_m/E (and vice versa).

3. The Al (111) indentation shows that the plastic accommodation to the indenter-induced displacements is due to the emission of dislocation slip during the early formation of the plastic nanoimprint. In this simulation, the associated GND density during the nucleation pop-in is found to be overestimated (by two orders of magnitude) in the continuum NG model. This finding emphasizes that the discrete dislocation nucleation and interaction events in conjunction with slip localization (pile-up) effects become the most relevant features during the incipient development of plastic nanoimprints which cannot be captured through NG-type models.

4. The nanocontact response past the first pop-in inception is dominated by serrated responses in the p_m levels, which is indicative of the intermittent evolution of the injected defect networks. The plastic $p_m - h_s$ responses involve brief quasi-elastic loading stages interrupted by the onset of plastic bursts, which stems from the combination of collective dislocation glide and heterogeneous defect nucleation. The simulations show that the amplitude of the fluctuations in p_m/E with increasing indentation depths is essentially associated to the mobility of the defect structures. At deep penetrations, nanocontact plasticity is characterized by the onset of a hardness plateau as a consequence of the attainment of stagnant dislocation density in the present FCC and BCC plastic volumes, where $d\rho/dh_s \approx 0$. Interestingly, these plateau levels are attained in all of the FCC and BCC nanoindentations regardless of the surface orientation and the underlying mechanism leading to defect nucleation. Although the BCC nanocontacts are generally much harder than the FCC counterparts, the difference between BCC and FCC surfaces notably decreases when the hardness plateau is examined using the p_m/E ratio. These findings indicate that nanoimprint formation occurs under an important elastic component, governed by the distinctive defect phenomenologies that occur below nanoindenter tips as a function of crystalline structure and temperature. This provides a mechanistic rationale to the explanation to why the (elastically stiffer) BCC crystals are much harder than FCC crystals at the nanoscale.

5. Additional MD simulations of the uniaxial test suggest that the densely-entangled dislocation networks characterizing the FCC and BCC hardness plateaus exhibit the strengthening properties anticipated from classical strain hardening models, where the applied stress scales with the square root of the (forest) dislocation density. This outcome supports the discussion on the attainment of a stationary hardness level as a result of the presence of a fully-developed dislocation network underneath the nanoindenter. This analysis additionally reveals a lack of continuity in the Tabor´s relation when the sample volume approaches nanometer dimensions, where the attainment of the yield stress (uniaxial test) and the material hardness (indentation) is fundamentally governed by two distinct plastic phenomenologies.

6. The gradual development of an inhomogeneous distribution of loaded and unloaded regions throughout the contact area is a distinctive feature of plastic nanoimprint formation. The process is characterized by ill-defined $p(r)$ distributions comprised by marked peaks which greatly contribute to the total p_m level. In indented FCC surfaces, the formation of a plastic nanoimprint is essentially governed by the competition of dislocation slip vs. nanotwinning formation. The Al indentations mostly exhibit the former due to the relatively high stacking fault energy of crystal, which hinders the inception of mechanical nanotwinning and enhances cross slip. Thus, the Al nanoimprints are distinguished by intricate distributions of crystallographic slip traces as a result of the effective dislocation dissemination during intermittent plastic bursting. By contrast, the moderately-low stacking fault energy Cu crystals show a marked development of nanotwin walls, leading to defect clustering into parallel planar arrays at $r \approx a$. These nanotwin structures globally impede nanoimprint development in the inner region ($r \to 0$) where the dissociated dislocations remain trapped within the twin entanglement. Low-temperature BCC surfaces undergo formation of a nanostructured polycrystalline aggregate comprised by twin boundaries, which effectively hinders dislocation slip with increasing penetrations. This phenomenology arguably raises the indentation nanohardness in BCCs due to the important elastic component associated to

the deformation of the nanotwin domains. At much higher temperatures, the onset of a highly mobile network of full dislocations leads to slip processes similar to those encountered in the Al nanoindentations during the formation of plastic nanoimprints.

CHAPTER 6.

DISLOCATION AVALANCHE EMISSIONS IN INTERMITTENT PLASTICITY

6.1. The onset of power-law dislocation avalanche distributions

The power-law scaling of avalanche size distributions provides a statistical framework to the investigation of intermittent responses that arise in dynamically-driven systems due to internal dissipation processes [48, 150]. The paper published by Bak, Tang, and Wiesenfeld (BTW) coined [53] the concept of *self-organized criticality* (SOC) in an attempt to generalize the ubiquitous "1/f" noise encountered in a significant number of dissipative physical phenomena [53, 151]. Interestingly, such a critical response is *not* set by any tuning parameter as SOC naturally evolves *through* critical points, or states, in a dynamically evolving system [53]. In other words, these critical points act as an *attractor* in the complex dynamics [152], which allows the system to dynamically evolve through scale-free self-arrangements [53, 152].

Although the BTW´s model has been probed to describe non-equilibrium (dissipative) processes with power-law avalanche distributions that span over a large range of sizes [45, 48, 150, 152], this line of thought has recently aroused some skepticism in the scientific community [150]. Nevertheless, the concept of SOC set the foundations for the study of dislocation-mediated plasticity [153] in the context of the intermittent evolution of dislocation networks attaining through sporadic bursts of activity, or avalanches, where the probability distribution of the fluctuating response could seemingly provide a fingerprint of the system criticality [47]. Early acoustic emission experiments in ice single crystals [47] and compression of metallic micropillars [42, 43] evidenced the attainment of power-law behavior in the measured plastic events. It was found that the power-law distributions of the plastic intermittences mirror those encountered in dissipative phenomena exhibiting crackling noise [42, 45], a universal (scale-free) response probed in many physical systems such as neuronal activities, fracture dynamics, magnetism, solar flares, or earthquakes [54, 152].

The development of dislocation networks in crystal plasticity is described under the analogy of a far-from-equilibrium slowly-driven dynamical system (similar to that described in Ref. [49]), where dissipation occurs much faster than external driving [46, 48] and subsequent pinning-depinning transitions systematically bring the system to a critical configuration [153]. Thus, the crystal resistance to deformation (e.g. positive slope in the stress-strain curve) arises during the pinning stages in the dislocation arrangement, while the onset of depinning leads to system instabilities manifested as plastic bursts [43, 47]. The mobilization of pinned dislocations therefore allows the system to evolve between critical (metastable) states [153, 154]. The collection of the dislocation activities operating during a plastic event is referred with the term "dislocation avalanche" [47].

Under this framework, a dislocation configuration is expected to evolve through a set of power-law distributed plastic bursts with the characteristic that the largest avalanche events are *exponentially* truncated [34, 51, 54, 154, 155]. This truncation [46] is associated with long-range dislocation interactions (leading to strain hardening [51, 156] in the context of dislocation jamming) as well as with the fact that the sample has finite sizes [34, 44, 51]. In crystals approaching submicrometer-sized dimensions, the reduced number of dislocation segments that are available in the sample leads to marked avalanche events at large stresses and to steeper power-law distributions [34, 44, 54, 72], which suggest the onset of stress-tuned criticality (STC) [44]. Recent micropillar experiments [50] clarify the interplay between the above self-organized and tuned criticality behaviors in the intermittent evolution of dislocation networks [50].

This investigation aims to shed new light on the underlying dislocation mechanisms that attain during self-organized (uncorrelated) and tuned (correlated) avalanche events in uniaxially stressed BCC and FCC crystals. To do so, massive periodic MD simulations of the uniaxial test

containing a preexisting dislocation entanglement are performed under displacement-controlled conditions (Section 3.2.3). The avalanche distributions obtained from the simulations are compared to those from the micropillar compression experiments published elsewhere in Refs. [34, 50]. The results from the simulations provide new insights into the dislocation avalanche behavior developing in Ta, Cu and Al crystals containing dense dislocation networks.

6.2. Dislocation avalanche distributions

Dislocation avalanche distributions are typically described by power-law functions of the form [42, 43]

$$P(S) \propto \frac{1}{S^\lambda},\tag{6.1}$$

where $P(S)$ is the probability density function (PDF) for the occurrence of an individual dislocation avalanche of size S, and λ is the critical exponent which takes the *universal* value of $\approx 1.5-1.7$ [34, 42, 43, 47, 52, 54, 152, 154, 155].

The magnitude of a plastic burst, can be effectively analyzed in terms of (i) the associated dissipated energy [46, 47], (ii) the stress (or strain) excursion sizes [44, 155, 157], or (iii) the slip carried by the avalanche [34, 50, 54]. It is important to remark that function $P(S)$ and exponent λ from Eq. (6.1) remain unaltered with the use of the above different measures of the avalanche size [48, 54, 150]. In this investigation, S is characterized by means of the slip size s carried during a dislocation avalanche event. Thus, the slip size distribution function follows

$$P(s) \propto s^{-\lambda},\tag{6.2}$$

where $P(s)$ is the PDF for the occurrence of a slip size s.

Under uniaxial straining, slip attains in the most favorable (slip) system with the largest Schmid factor M [34] (Section 2.1), see Fig. 6.1(a). In this context, the advent of an avalanche slip involves development of a net increment in sample strain of $\Delta\varepsilon = \Delta l/l = Ms/l$, where l is the sample length (Fig. 6.1(a)). In particular, displacement-controlled conditions (with quasi-static driving) lead to the onset of avalanche events distinguished by stress drops, $\Delta\sigma$, attaining at fixed strain, see the Appendix A7.1. Thus, slip s and the respective stress excursion detected in the stress (σ) – strain (ε) curve are related through [34]

$$s = \frac{\Delta\sigma \cdot l}{M \cdot E}.\tag{6.3}$$

Further details on the method employed for the evaluation of the avalanche events are given in Appendix A7.3.
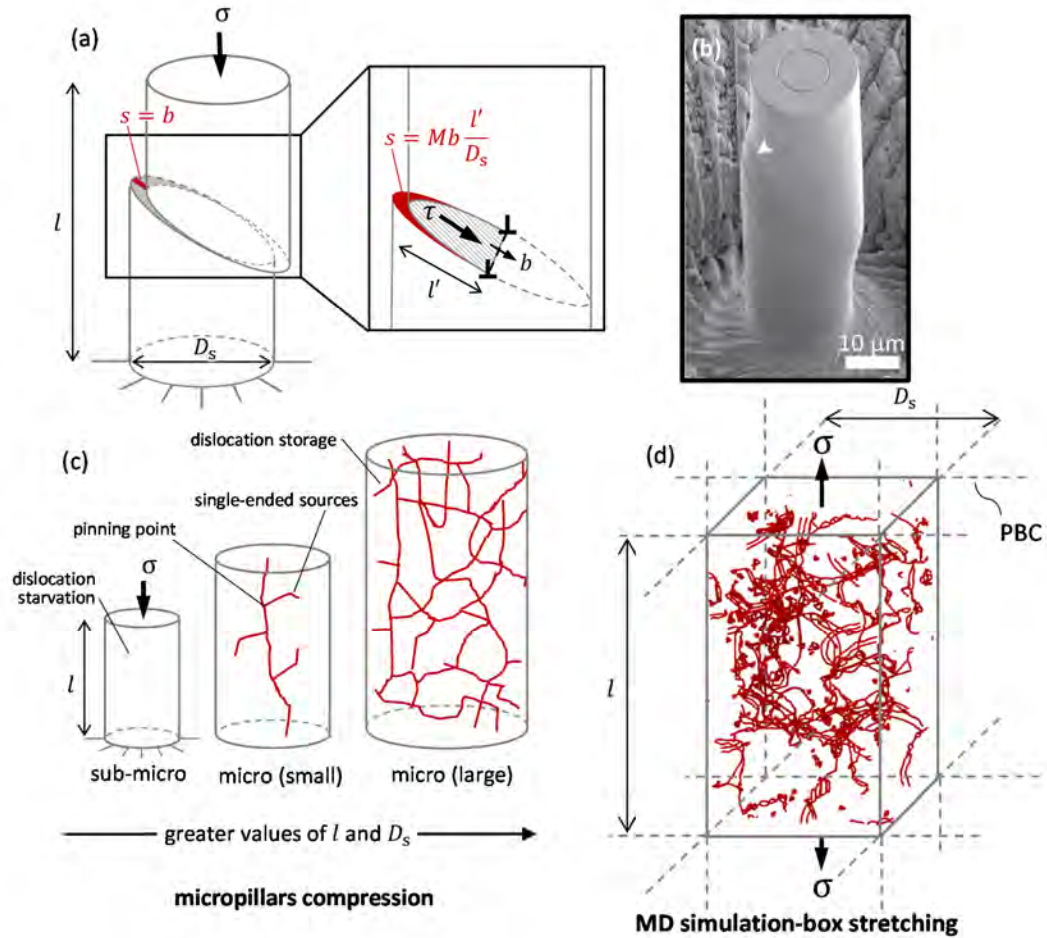
Figure 6.1. Avalanche slip in microcrystals with different sizes. (a) Production of a slip size ($s = b$) through the complete sweeping of a single dislocation across the sample. The inset to this figure depicts fractional slip ($s < b$) produced by an individual edge dislocation traveling across the crystal a distance l' ($< D_s/M$). (b) Dislocation slip (arrowhead) generated in a compressed Ni micropillar (from Ref. [42]). (c) Schematic of the (statistically) conceivable dislocation configurations in sub-micro and micrometer sized pillars characterized by a mean free path length L and effective sample diameter D_s. (d) Dislocation entanglement in the Al [110] MD (representative) periodic cell. Dislocation lines are obtained by means of DXA segmentation (Appendix A8).

Notice in Eq. (6.3) that a certain dislocation avalanche carrying a slip s leads to greater stress drops in samples with micrometer and sub-micrometer dimensions ($l \rightarrow 0$), see Fig. 6.1(b), than those producing the same value of s in much larger samples ($l \gg 0$) [35]. This emphasizes that although the inception of (intermittent) dislocation avalanches is a signature of crystal plasticity across scales [35, 45], such plastic bursts become mainly evident in micrometer- and submicrometer-sized samples [34].

The use of the mean-field parameter L (Section 2.1) enables a direct estimation of the number of dislocations, N_d, traveling across the sample during avalanche propagation [50], where

$$s = N_d\, b\, \frac{L}{D_s}, \tag{6.4}$$

see the inset to Fig. 6.1(a). In the above equation, note fundamental role of the effective sample diameter (D_s) and the mean free path length (L) traveled by the mobile dislocations upon the avalanche slip size (s). In this context, the attainment of a large slip size is physically limited by the L/D_s term, as the number of mobile dislocations N_d tentatively scales-with $\approx D_s^2$. On the other hand, small avalanches may also lead to the onset of fractional slips ($s < 1b$) due to the mobilization of an individual dislocation ($N_d = 1$) sweeping across the sample through a distance $L < D_s$. The inception of a fractional slip is conceivably attributed to the onset of avalanche events in dense dislocation networks with a small value of L [50].

6.3. Size effects in dislocation avalanches and the L/D_s ratio

In submicrometer-sized crystals ($l < 10^{-7}$ m), where a dislocation forest is absent [44], recurrent surface dislocation activity (or even surface dislocation nucleation [50]) govern the early development of crystal plasticity. This is the so-called dislocation starvation regime [158], see Fig. 6.1(c)), leading to the attainment of extreme levels of yield strength, σ_y (highlighted with a circle for $D_s \approx 0.6$ μm in Fig. 6.2), which could even approach the theoretical bonding strength of the crystal (Section 2.1). Since the mobile dislocations annihilate at the free surfaces, such small material volumes hinder dislocation storage as $L/D_s \approx 1$. The $\sigma - \varepsilon$ curves therefore evidence the onset of secondary (marked) avalanche events at large stresses (see $D_s \approx 0.6$ μm in Fig. 6.2), which indicates that additional homogeneous nucleations and surface annihilation/truncation of gliding dislocations occur in the crystal with increasing straining [116, 155].

In larger crystals ($10^{-7} < l < 10^{-5}$ m), a few dislocation segments become statistically available in the sample. The existing dislocations act as *single-ended sources* that revolve around pinning points [155, 159, 160], see Fig. 6.1(c), which provides an important source for the onset of plastic slip events in the sample as $L/D_s > 1$ [50]. Thus, the dislocation avalanches attain under smaller stress levels than those obtained through the above nucleations [50, 159-162], see the $\sigma - \varepsilon$ curves for FCC Cu $D_s \approx 2.5$ and $D_s \approx 3.5$ μm in Fig. 6.2. Although an evolutionary dislocation network exists in the crystal, the escape of dislocations at the surface hinders the onset of strain hardening ($d\sigma/d\varepsilon \approx 0$) [34, 162].

A completely different scenario arises as conventional strain hardening attains in microcrystals with sufficiently large volumes ($l > 10^{-5}$ m [34]), where surface dislocation annihilation eventually becomes inconsequential to the evolution of the dislocation network. Thus, *dislocation storage* dictates the development of generalized plasticity in microcrystals characterized by $L/D_s \to 0$, see Fig. 6.1(c) [35, 155, 156]. Development of the dislocation arrangement then entails formation of dislocation junctions where a dense distribution of forest dislocations intercept the mobile dislocations [22]. Although fluctuations in the applied stress and dislocation density levels are generally observed during a single dislocation avalanche, an overall increase in dislocation density prevails with increasing straining. This leads to the attainment of a positive slope in the stress-strain curve ($d\sigma/d\varepsilon > 0$) [163], see $D_s > 10$ μm in Fig. 6.2. It is important to remark that strain hardening operates in BCC crystals with smaller sample sizes than in FCCs, as the scarce mobility of screw dislocations facilitates dislocation storage at low temperatures ($T/T_m < 0.2$), e.g. $D_s \approx 5$ μm at 300 K in Fig. 6.3.

Figure 6.2. Stress-strain curves from uniaxial tests in FCC Cu crystals. The experimental data [34, 50] are reproduced with permission. The results from the Cu [110] MD simulation are displayed from $\varepsilon = 0$ to $\varepsilon \approx$ 0.055. The discontinuous (black) line denotes straining under $\approx$0.8 m/s to $\varepsilon \approx 0.03$ while the continuous line represents the slowly-driven dynamical results at $\approx$0.1 m/s (Appendix A5.2).

The periodic MD simulations with preexisting dislocation networks (that tentatively exhibit $L/D_s \approx 0.3 - 0.5$, see Fig. 6.1(d)) mimic a bulk material sample comprised by an array of (hypothetically infinite) connected domains whose identical dislocation networks simultaneously activate during the emission of dislocation avalanches. In this context, the criticality of the embodied (bulk) sample is assumed to remain size independent as a plastic slip is reproduced in all of the connected representative volumes. Note that this conception (Fig. 6.1(d)) transcends classical crystal plasticity [3] and multi-scale modeling of strain hardening in FCC crystals [23, 25, 94], where a positive slope in the stress-strain curve is attributed to two-part junction formations (see the constructions illustrated in Figs. 2.8(a)-(d) in Section 2.4.2) attaining under relatively long-range interactions characterized by a value of L which is about three orders of magnitude larger [26, 95] than that encountered in the periodic MD defect networks (Fig. 6.1(d)).
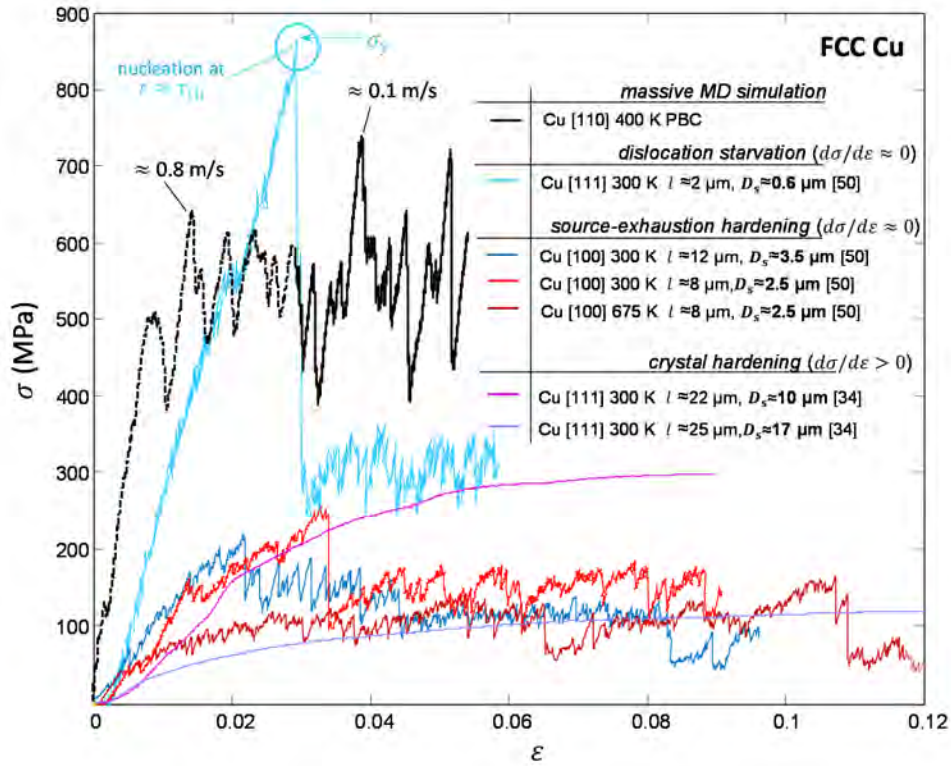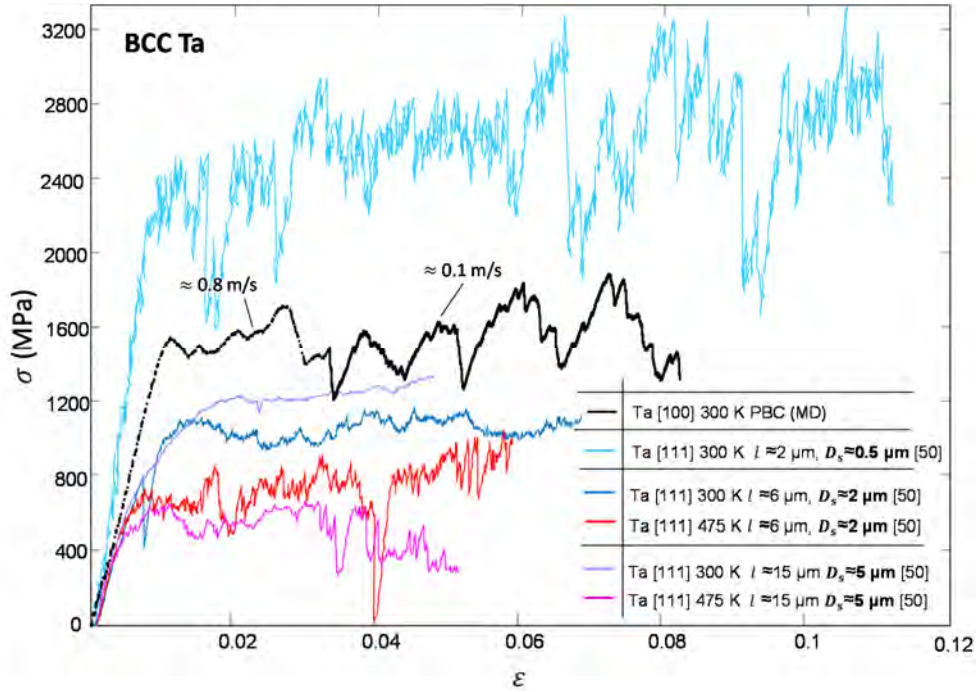
Figure 6.3. Stress-strain curves from uniaxial tests in BCC Ta crystals. The experimental data [34, 50] are reproduced with permission. Similarly to Fig. 6.2, the results from the Ta [100] MD simulation are displayed in the entire spectrum from $\varepsilon = 0$ to $\varepsilon \approx 0.08$. The discontinuous (black) line denotes straining to $\varepsilon \approx 0.03$ under a stretching velocity of ≈ 0.8 m/s while the continuous line represents the slowly-driven dynamical results at ≈ 0.1 m/s.

6.4. Stress-strain curves from the MD simulations

The MD simulations of the uniaxial stress—strain curves are obtained by means of the computational procedure discussed in Section 3.2.3 (see Fig. 3.4). The periodic domains are preliminarily deformed to $\varepsilon \approx 0.03$ under a stretching velocity of ≈ 0.8 m/s. This velocity stands for the rate at which the computational volume is uniaxially stretched (Fig. 3.4(c)), which in terms of the strain rate $\dot{\varepsilon}$ corresponds to 1.2×10^7 s^{-1}. The simulations show that, within this strain range, (i) the yield stress point is attained (Figs. 6.2 and 6.3), and (ii) the dislocation networks disseminate homogeneously throughout the periodic domain. Figure 6.4 shows the dislocation configurations obtained in the Ta, Al, and Cu simulations at $\varepsilon \approx 0.03$ ($l \approx 70$ nm), where the periodic domains enable modeling of a *representative volume* of a much bigger material sample. Notice in the dislocation networks of Fig. 6.4 that the mean-free path L is fully contained within each computational volume. Present simulations ensure that dislocations suddenly activating at the center of the simulation box can exit and reentry the computational domain at opposite locations of the boundary, interacting against different arrangements of immobile obstacles (see the purple dislocation segment in Fig 6.4(a)). This prevents the onset of unwanted recursive avalanche processes in present simulations.
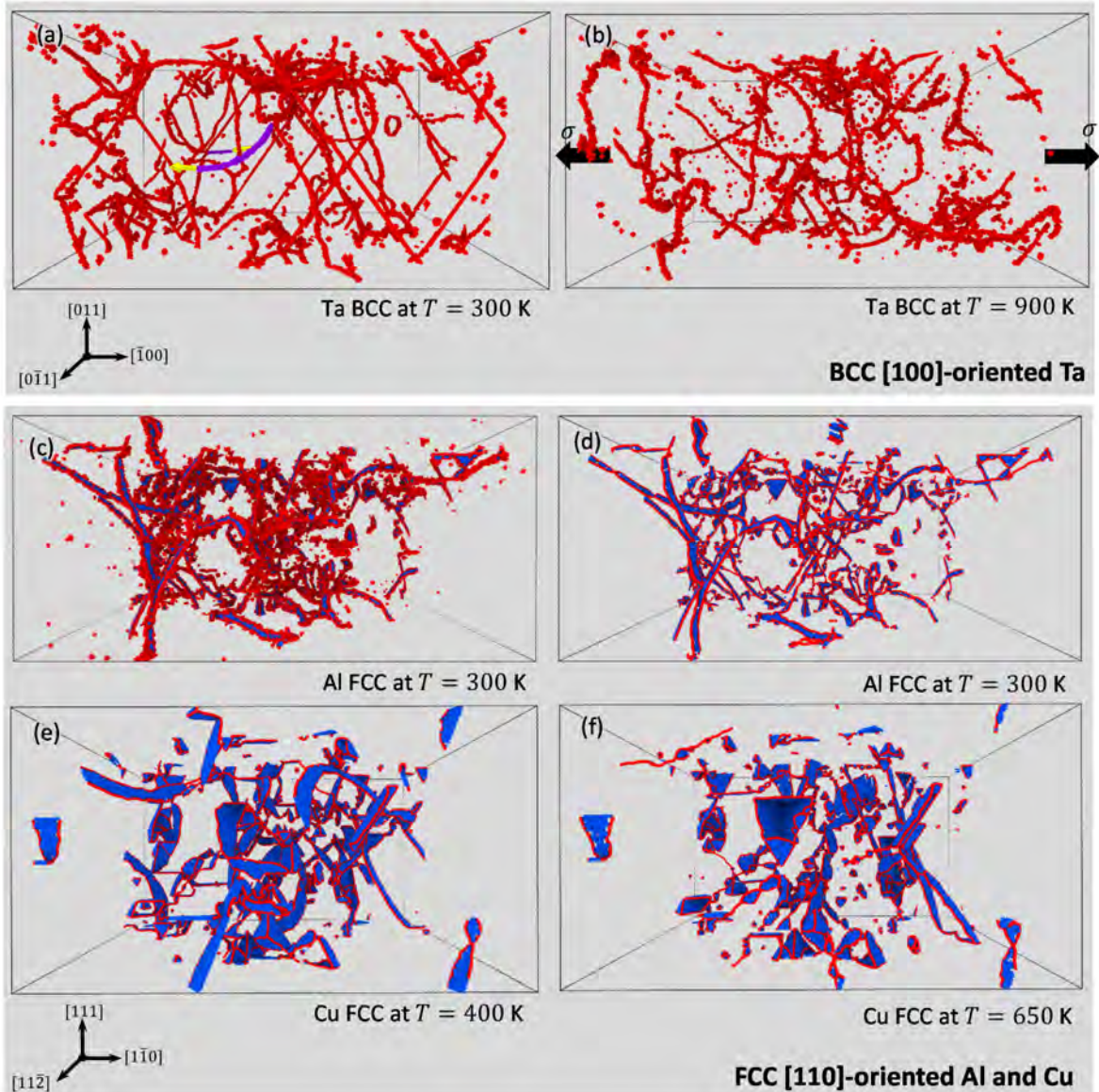
Figure 6.4. The initial dislocation configurations in the periodic MD simulations. (a)-(b): Ta [100] tensile test at $T = 300$ K and $T = 900$ K, respectively. The yellow arrows in picture (a) denote a dislocation segment exiting across a periodic side and entering at the opposite location of the boundary. Note that the imposed PBCs ensure the invariance of dislocation arrangements across an infinite three-dimensional network of identical connected cells. Atomistic visualization is performed with OVITO, see Appendix A6. (c) Dislocation network in the Al [110] tensile test at $T = 300$ K as visualized by OVITO. For the sake of clarity, DXA computations (Appendix A8) in (d) provide the topological network extracted from of the dislocations (red lines) in (c), where blue atoms denote SF planes. (e) and (f): Dislocation networks for the Cu [110] tensile tests at $T = 400$ K and $T = 650$ K respectively (under the aforementioned visualization scheme).

The periodic computational volumes (Fig. 6.4) are subjected to an additional $\Delta\varepsilon \approx 0.03 - 0.06$ at a stretching rate of ≈ 0.1 m/s ($\dot{\varepsilon} = 1.5 \times 10^6$ s^{-1}), where the dislocation networks from Fig 6.4 represent the *initial* pinning stages which lead to the intermittent plastic responses of Fig. 6.5. The novelty of these simulations stems in that generalized plasticity develops within a bulk volume of infinite size containing a dense dislocation arrangement

characterized by an extremely large dislocation density, $\rho \approx 10^{16}$ m^{-2}. Under these conditions, the simulations show the systematic emission of non-overlapped dislocation avalanches that exhibit power-law behavior (see Section 6.5), which suggests that the applied strain rate is fundamentally small when compared to the time scale that characterizes the intermittent process under study [43]. Appendix A5.2 provides a discussion on the effect of the strain rate on the intermittent plastic response and power-law behavior in present MD simulations.
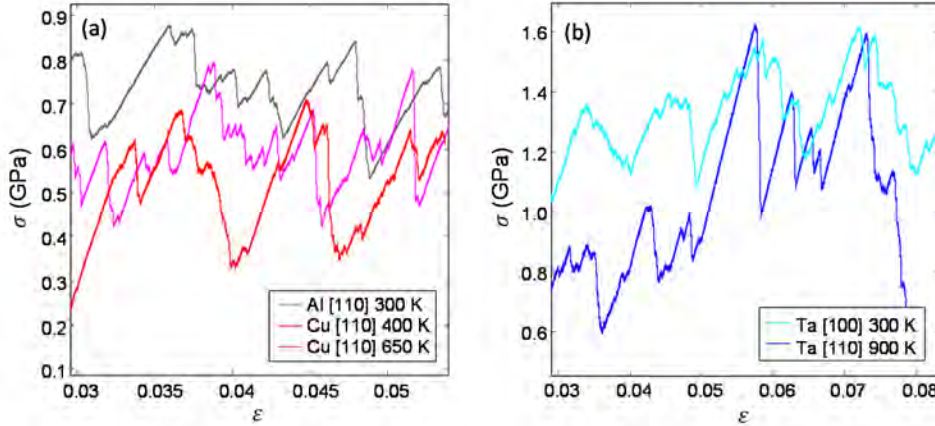
Figure 6.5. Stress–strain curves from the MD simulations of uniaxial tests at ≈ 0.1 m/s. It is noted that each stress drop is associated with the emission and propagation of a dislocation avalanche.

The periodic simulation domains are strained in the <110> crystalline direction in the FCC Cu and Al simulations, and in the <100> crystalline direction in the BCC Ta simulations, see Fig. 6.4. Although (mean-field) crystal plasticity predictions [23] indicate that the above <110> orientation exhibits smaller strain hardening rates in FCC crystals than the <111> or <001> orientations, the extreme dislocation densities modeled in the MD simulations (Section 5.5) may tentatively suppress such an orientation effect due to the large number of short-range interactions developing in the representative (modeled) volume element (Figs. 6.4(c)-(f)). In addition, the role of the stretching orientation upon the intermittent plastic response is neglected [50] in BCC crystals as the thermally-activated mobility of screw dislocations (Section 2.3) primarily governs the development of generalized plasticity [87]. While the applied stress leading to avalanche emission will depend on crystal orientation, the power-law distribution of avalanche slips may not be particularly sensitive to this issue [54].

6.5. The assessment of power-law avalanche distributions

In this work, the statistics of the slip events (Appendix A7.1) are investigated by means of the complementary cumulative distribution function (CCDF), $C(s)$. The CCDF provides the emission probability of a slip level $s \geq s_{\min}$,

$$C(s) = \int_s^\infty P(s)\, ds \,. \tag{6.5}$$

where, by definition, $C(s) \rightarrow 1$ as $s \rightarrow s_{\min}$ [34]. From the Eqs. (6.2) and (6.5), it then follows

$$C(s) \propto s^{-\kappa}, \tag{6.6}$$

where $\kappa = \lambda - 1$. This analytical scheme is pivotal in the estimation of the exponent κ (see Appendix A7.4), as it follows that $\kappa = \lambda - 1$ [34]. In Appendix A7.2, a detailed description on the derivation of Eqs. (6.5) and (6.6) is given as well as an appraisal to the use of empirical fits to the distribution function $P(s)$ from Eq. (6.2).

Although heavy-tailed probability distributions (such as the $C(s)$ distribution from the Al simulation shown in Fig. 6.6(a)) have long been modeled *via* power-laws [164], exponential functions [48, 165], or a mixture of both [46, 51], the present analysis of intermittent slip events is based on the statistical paradigm that includes the interplay between self-organized and tuned criticality during the development of dislocation networks [50]. This model provides fundamental background to the emission of uncorrelated and correlated dislocation avalanches [50], see Fig. 6.6(b), which features the bifurcation of a small slip regime with $\kappa \approx 0.5$ to one with larger slip events distinguished by $\kappa \approx 3.0$ at a critical slip size (s_c) [50], where both *power-law* regimes tentatively coexist (Fig. 6.6(b)). In this context, the power-law exponents κ_1 and κ_2 (Fig. 6.6(b)) from the $C(s) - s$ curves characterize the incipient slip and large avalanche slip regimes with $s < s_c$ and $s > s_c$, respectively. The associated critical exponents λ_1 and λ_2 are then calculated through $\lambda_1 = \kappa_1 + 1$ and $\lambda_2 = \kappa_2 + 1$.
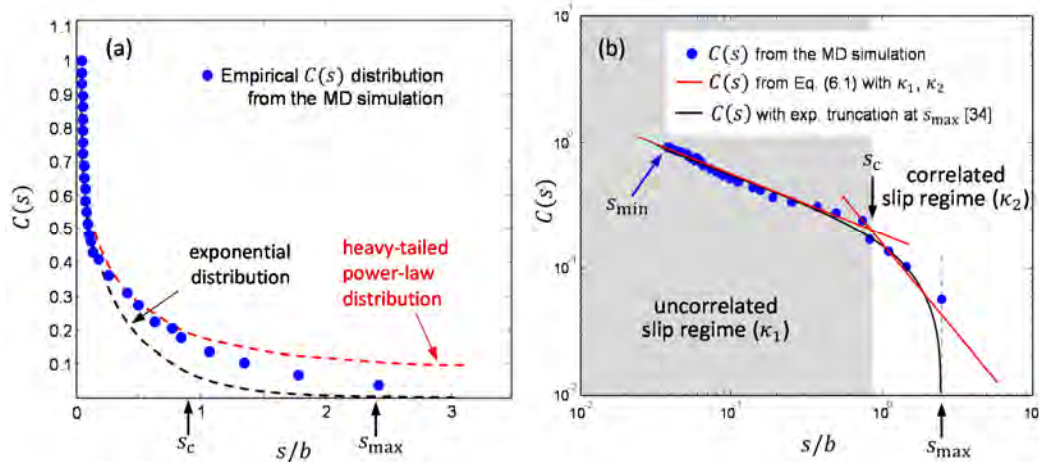
Figure 6.6. Heavy-tailed slip distribution from the Al [110] simulation. (a) $C(s) - s/b$ representation of the dataset. The probability distributions with thick ends or "tails" (heavy-tail) indicate likelihood for the attainment of a catastrophic (large size) event, which is a characteristic feature of power-law scaling [164]. (b) $C(s) - s/b$ logarithmic representation of the dataset. Note that the two $C(s)$ distributions model the crossover of uncorrelated and correlated slip events. The figure additionally shows the onset of a sharp (exponential) cut-off, a feature that is not observed in experiments [50]where the uncorrelated large slip regime is sensibly described through a power-law exponent κ_2, suggesting a linear response in the $\log(C(s)) - \log(s)$ curves [166].

6.5.1. Slip distributions in FCCs

Three master slip size distributions from experiments and simulations of FCC crystals are drawn in Fig. 6.7 (see Appendix A7.5). The distributions of the slip events detected in FCC crystals exhibit the attainment of an uncorrelated, incipient slip domain with $\kappa_1 \approx 0.4-0.7$ ($\lambda_1 \approx 1.4-1.7$) which cuts off at a critical slip size s_c leading to the onset of a correlated, large slip regime, characterized by $\kappa_2 \approx 3.0$ ($\lambda_2 \approx 4.0$) [50].

Dislocation avalanche emissions in submicrometer-sized Cu crystals are associated with the predominant onset of correlated (large slip) events as the sample becomes dislocation

starved ($L/D_s \approx 1$) [50, 162]. The typical extreme stress levels producing dislocation nucleations (see $D_s \approx 0.6$ μm in Fig. 6.2) facilitate the inception of large, correlated plastic events, which lead to $C(s)$ distributions with $\kappa_2 \approx 3.0$ [44, 50].

The avalanche distributions obtained in small micrometer-sized Cu pillars (*group 2* in Fig. 6.7) are characterized by large levels of the critical slip s_c as the operation of single-ended dislocations ($L/D_s > 1$) revolving around single pining points in the absence of a forest leads to large avalanche slips (Eq. (6.4)), see the $C(s)$ distribution at $T = 300$ K where $s_c \approx 7b$. With increasing temperatures, the slip distributions additionally shift to higher values due to thermally-enhanced cross-slip processes, as shown in the $C(s) - s/b$ curve at $T = 675$ K, where $s_c \approx 20b$.
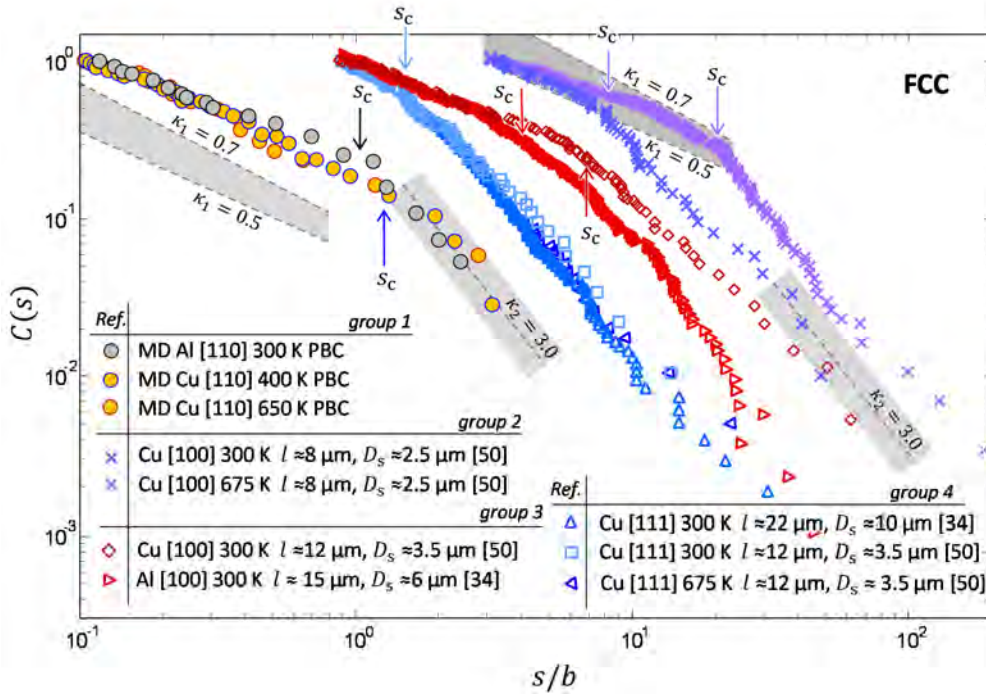
Figure 6.7. $C(s)$ **distributions from experiments and simulations in FCC crystals. The data from micropillar compression experiments [34, 50] are utilized with permission.** *Group 1* **concerns the avalanche distributions from present MD simulations.** *Group 2* **shows the effect of temperature upon the dislocation avalanche distributions in small [100]-oriented Cu microcrystals.** G*roup 3* **and** *group 4* **respectively display avalanche distributions under mild and intense dislocation interactions. Incipient slip and large slip domains are characterized by power-law exponents** $\kappa_1 \approx 0.4 - 0.7$ **and** $\kappa_2 \approx 3.0$ **in the** $C(s) - s$ **curves, respectively. Slip event** s_c **marks transition from the uncorrelated (small slip) to the correlated (large avalanche slip) domain. The grey bars are for visual guidance of the** κ **slopes. The goodness of the power-law fits is discussed in Appendix A7.4.**

In larger micropillars, where dislocations propagate through a dense dislocation forest with *strong* interactions (Section 2.4.2), strain hardening becomes manifest in the $\sigma - \varepsilon$ curves as $d\sigma/d\varepsilon > 0$, see the [111]-oriented Cu crystals with $D_s > 10$ μm in Fig. 6.2. By contrast, the development of strain hardening in (large) FCC microcrystals is hindered due to a predominant distribution of *mild* dislocation interactions, e.g. [100]-oriented FCC microcrystals with intrinsically weak strain-hardening [23, 50] (where $d\sigma/d\varepsilon \approx 0$, see Fig. 6.2). Although

dislocation avalanche events under both weak and strong interactions lead to the attainment of the two slip regimes with slopes κ_1 and κ_2, the master $C(s)$ functions in Fig. 6.7 that pertain to *group 3* (mild interactions) and *group 4* (intense interactions) evidence that the critical slip size increases from $s_c \approx 1.5b$ to $s_c \approx 4b$ as strain hardening processes become *inconsequential* to the plastic response in Cu crystals. This trend leads to avalanche distributions with $s_c \approx 7b$ when plasticity is confined into small Cu microcrystals (*group 2*). In light of the above, strong dislocation interactions promote the development of correlated (large) slip events, while mild interactions are associated with the inception of larger slip events with smaller emission probability of the critical slip size s_c ($C(s_c) \approx 0.2$), indicating a dominant onset of uncorrelated slip events in the context of SOC.

Present FCC simulations evidence the attainment of distinct topological features in the dislocation networks (Fig. 6.8) developing as a fundamental function of the SFE and temperature. In particular, the dislocation network obtained in the Al simulation at 300 K is comprised by Shockley segments with recurrent cross slip apparently through Friedel-Escaig mechanisms [115, 167], see Fig. 6.8(c). Although cross slip does not appear to be significant in the Cu simulation at 400 K, an increase in temperature (to 650 K) certainly enhances this mechanism (cf. Figs. 6.8(a) and 6.8(b)). In this regard, the effect of cross slip and temperature on defect mobility becomes manifest in the $C(s)$ distribuitions of *group 2* (Fig. 6.7), where it is found that the dislocation avalanches in Cu micropillars tend to carry larger slip events under thermally-enhanced cross slip (see the corresponding distribution at 675 K). By the same token, larger magnitudes of slip size s_c characterize the $C(s)$ functions of crystals with large SFE (where cross slip is promoted), see Al in *group 3* (Fig. 6.7).

Although the simulations reproduce the expected enhancement of cross slip as a function of temperature and SFE (Section 2.2.1), the Al and Cu simulations at $T/T_m \approx 0.3$ (Table 3.5) are inconclusive when it comes to mimic the effective role of cross slip in the $C(s)$ distributions, as s_c tentatively attains at a similar slip level ($s_c \approx 1b$) in both simulations, see *group 1* in Fig. 6.7. This is attributed to the extreme intricacy in the dislocation networks (Figs. 6.4(c)-(f)), where the development of dislocation avalanches is governed by short-range interactions with a small magnitude of L. In the present simulations, the forest dislocation configuration through which dislocation avalanches propagate is primarily comprised by sessile multi-junctions; a complex dislocation-arms structure with a heterogeneous topology of non-dissociated (full), dissociated (Shockley) and cross-slipped dislocations; and stacking fault tetrahedra (SFT), see Fig. 6.8(c), which essentially leads to $C(s)$ distributions with small slip events lying within the κ_1-domain, see Fig. 6.7
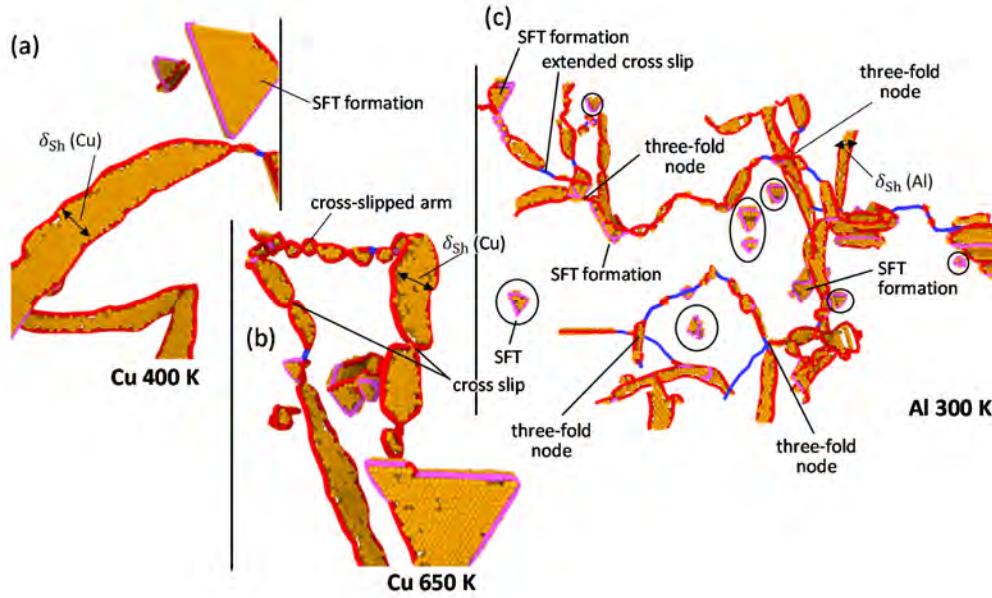
Figure 6.8. Dislocation segments in the simulated FCC crystals (MD). (a) The Cu simulation at $T = 400$ K shows development of a dislocation network with a predominant population of extended (non cross-slipped) segments. (b) The enhancement of cross slip plays an important role in the topological appearance of the dislocation networks in Cu, where a greater complexity attains in the dislocation entanglements that develop at 650 K. (c) Intricate defect network attained in the Al simulation. The extreme value of dislocation density ($\rho \approx 3 \times 10^{16}$ m^{-2}) is a clear indication of the onset of a dislocation configuration with strong interactions (which involves multi-junction development [96]). Orange atoms indicate SF planes. The atomic visualization is performed with OVITO and the dislocation segmentation is provided by DXA (Appendix A8). Segments in red, blue, and magenta correspond to full, Shockley, and stair-road dislocations, respectively. SFT are marked with circles.

6.5.2. Slip distributions in BCCs

The avalanche distributions from Fig. 6.9 evidence the systematic development of correlated and uncorrelated slip events in BCC crystals. In close agreement with the findings for FCC crystals (Fig. 6.7), the incipient slip and large size slip domains are respectively characterized by $\kappa_1 \approx 0.6$ ($\lambda_1 \approx 1.6$) and $\kappa_2 \approx 3.0$ ($\lambda_2 \approx 4.0$) [50]. While s_c shifts to larger values in the $C(s)$ distributions as cross-slip processes are enhanced in FCC micropillars (Fig. 6.7), a similar trend is observed in the slip distributions obtained in Ta crystals depending on the effective mobility of the screw segments. In this context, dislocation networks with mobile screw segments (elevated temperatures) lead to the onset of marked slip events as evidenced in the $C(s)$ distributions with large values of s_c, see Fig. 6.9.

In sub-micrometer sized BCC pillars, plasticity attains through single-ended source operation and recursive multiplication of screw segments [160] at stresses surpassing the Peierls barrier [85, 87]. This is shown in Fig. 6.3 for $D_s \approx 0.5$ μm where the onset of the plastic bursts is produced under large stresses ($\sigma \gtrsim 2000$ MPa) [50]. The combination of recurrent single-ended source activities and kinking mechanisms in sub-micrometer sized Ta crystals produces statistically larger L/D_s values, which promote the emission of correlated slip events characterized by avalanche distributions with a large s_c ($\approx 6b$), e.g. the $C(s)$ functions of Ta micropillars reported elsewhere in Ref. [50].

With increasing micropillar sizes ($D_s \gtrsim 1.5$ µm), dislocation loops are effectively accommodated within the sample volume, leading to dislocation storage in the crystal ($L/D_s < 1$) [39, 87]. The plastic intermittencies are then emitted under smaller stresses, which are associated with the activation of the edge sides of the loops ($\sigma < 1500$ MPa, see Fig. 6.3). This supports that the above single-ended source operation occurring in smaller microcrystal sizes may only attain when the Peierls barrier for the activation of the screw segments is reached (which necessarily develop as the sources revolve around their pinning points [50]) as the stress level required for the activation of the edge sides of the dislocation loops is smaller [85]. At low temperature ($T = 300$ K), the dislocation avalanches exhibit smaller values of s_c ($\approx 3b$) than at elevated temperatures, where the mobility of the screw dislocations is sharply enhanced so that the emission of statistically larger slip sizes is facilitated, see the $\sigma - \varepsilon$ curves at 475 K ($T/T_m \approx 0.22$) in Fig. 6.3. The onset of such large slip events is essentially captured in the $C(s)$ distributions as s_c shifts to greater values ($s_c \approx 10b$) at 475 K, see Fig. 6.9.
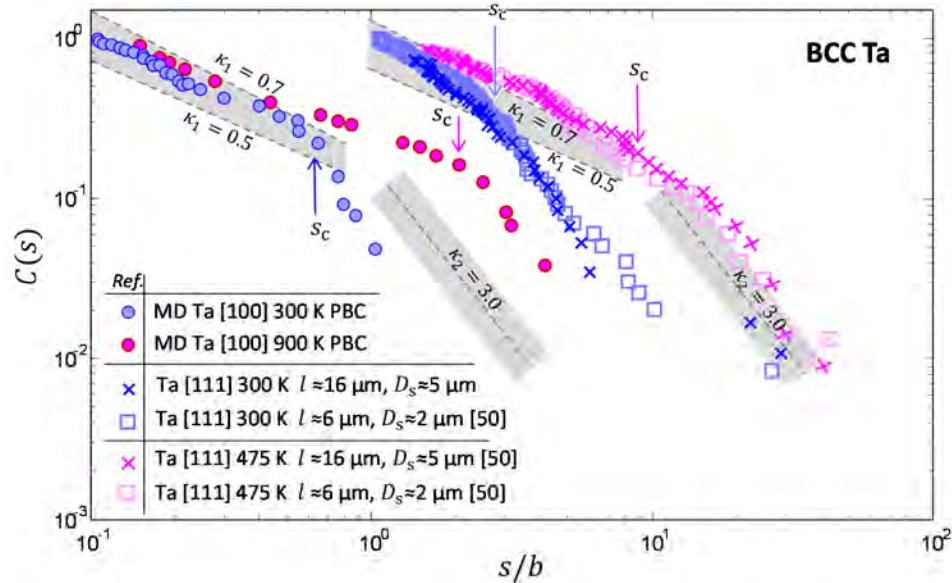
Figure 6.9. Master $C(s)$ distributions from experiments and simulations of Ta crystals. The data from micropillar compression experiments [34, 50] are utilized with permission. A reduction in micropillar diameter and temperature leads to a greater transitional slip s_c between the uncorrelated and correlated slip domains characterized by $\kappa_1 \approx 0.6$ and $\kappa_2 \approx 3.0$, respectively. The thermally-enhanced (and stress-activated) glide of screw dislocations essentially governs the shape of the $C(s)$ distributions through the parameter s_c. The points colored in magenta denote slip events occurring at high temperature ($T/T_m > 0.2$) while the blue points are from low temperature simulations ($T/T_m \approx 0.1$).

The role of the mobility of the screw dislocations upon the avalanche distributions becomes evident in the Ta simulations containing a highly dense dislocation network. The periodic Ta crystal at 300 K exhibits an immobile dislocation forest comprised by straight (screw) segments (Fig. 6.4(a)). Under these conditions, the intermittent plastic response (Fig. 6.5(b)) involves avalanche events that adhere to a $C(s)$ function with $s_c \approx 0.6b$ (Fig. 6.9). The wavy dislocation topology encountered in the simulation at 900 K (Fig. 6.4(b)) is indicative of the high mobility of the dislocation network comprised by thermally-activated screw segments, which enhances the onset of large avalanche events. This leads to a greater value of s_c ($\approx 2b$) in the $C(s)$ distribution at 900 K, see Fig. 6.9.

6.6. Dislocation activity during avalanche events in FCCs

According to the Al and Cu simulations, the slip events adhering to the incipient slip domain entail local activations of a small number of dislocations ($N_d = 1$ or occasionally $N_d = 2$) gliding $\approx 10-40$ atomic planes ($L < 20$ nm). Such a short-range glide suggests the attainment of fractional slips ($s < b$) within the κ_1-regime in the $C(s)$ distributions (Fig. 6.7). The minimum slip magnitude detected in the simulations ($s \approx 0.1b$) is produced by a sudden expansion of a dislocation arm across ≈ 10 atomic spacings. Since the simulations enable detection of such small slip events, the computational noise (periodic fluctuations in σ, see Appendix A7.3) is much smaller than the experimental fluctuations in the measured $\Delta\sigma$ levels, the κ_1-domain is therefore probed with smaller slip values than those obtained from the micropillar compression experiments [50]. In the Al [110] simulation (Fig. 6.7), the incipient slip domain tentatively spans from $s_{\min} \approx 0.1b$ to $s_c \approx b$, thus validating the power-law scaling of the incipient slip regime with $\kappa_1 \approx 0.5$, which in accord with Fig. 6.7, spans over ≈ 1.5 decades of slip sizes when Al experiments and simulations are brought together in a single $C(s)$ representation. Although a straight line in the $\log(C(s)) - \log(s)$ representations over less than two slip decades is not a solid proof of power-law behavior [164], assertion of a robust power-law scaling in the present $C(s)$ distributions would require measurement of plastic events that produce much smaller slip sizes than the above $s_{\min}$, which arguably surpasses the physical limit for the onset of plastic intermittencies.

Large slip events characterized by $s > s_c$ in the $C(s)$ distributions described through the exponent κ_2 (Fig. 6.7) are produced by the *collective* glide of dislocation segments. As elucidated in the periodic Cu and Al simulations, the motion of $3 \leq N_d \leq 6$ leads to the emission of large dislocation avalanches. Development of these avalanches implies depinning of the dislocation network, where the initially-activated dislocation segment triggers additional unzipping of further segments gliding a distance of $L \approx 10$ nm $- 40$ nm. The sequence of Figs 6.10(b)-(e) shows a dislocation avalanche in Al at 300 K carrying a slip size of $s \approx 2b$. The activation of dislocation "1" revolving around "j1" (Fig. 6.10(b)) mobilizes (i) three pinned segments in Fig. 6.10(d), and (ii) an additional dislocation in Fig. 6.10(e). The dense dislocation forest (Fig. 6.10(a)) secures the motion of the active dislocations (see the pinned dislocations (*) marked in cyan in Fig. 6.10(f)) as the dislocation configuration approaches a steady (subcritical) state, when the applied stress is lower than the critical stress [34, 44]. The strain evolution is drawn in Fig. 6.10(g) in terms of the effective σ and ρ. In this figure, it is observed that the sudden mobilization of the dislocation segments (unzipping and bowing) leads to discrete increases in density ($d\rho/d\varepsilon > 0$) during the avalanche development. The eventual avalanche arrest determines the initiation of a pinned stage in the dislocation network where the active segments are immobilized (see segment "5" in Figs. 6.10(e) and 6.10(f)). Although the dislocation segments may glide a few atomic distances within a pinned state [45], *quasi-elastic* periods (pinning) lying between two successive avalanche events entail $\Delta\sigma \approx E\Delta\varepsilon$ and an effective $\Delta\rho/\Delta\varepsilon \approx 0$, see Fig. 6.10(g).
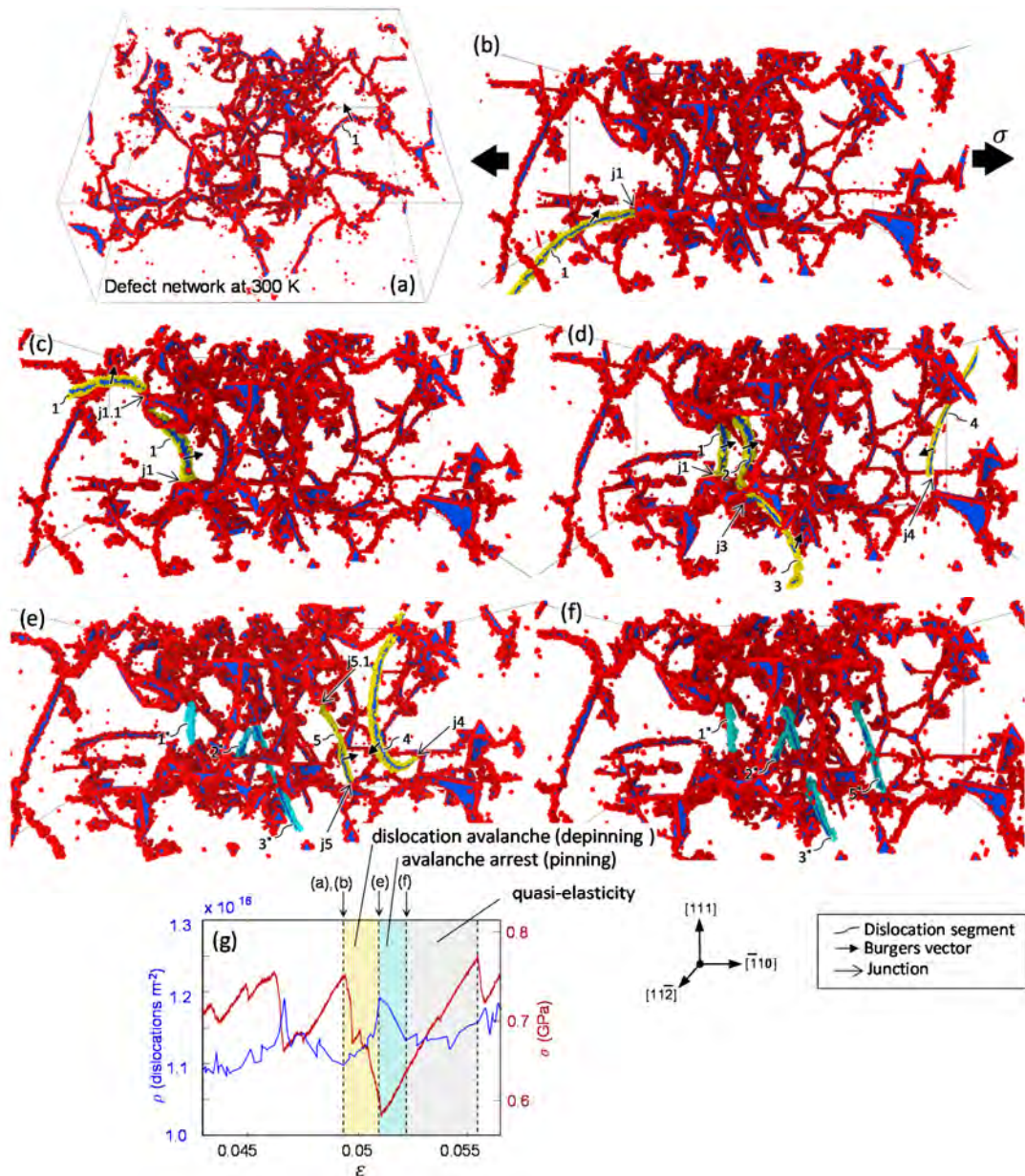
Figure 6.10. Large avalanche event in the Al [110] simulation at 300 K. (a) The periodic dislocation network ($\rho \approx 10^{16}$ m^{-2}) is mainly comprised by short-range multi-junctions of dislocations and SFT (see Fig. 6.8(c)). (b)-(f): Sequence of a dislocation avalanche carrying $s \approx 2b$. The avalanche involves sudden expansions of dislocation segments pinned at junctions "j". The mobile segments are marked in yellow while the arrested (*) dislocations are colored in cyan. Atoms are visualized with OVITO (Appendix A6). (g) Evolution of stress σ and dislocation density ρ as a function of strain during the avalanche event. Segment mobilization due to unzipping produces a net increment in ρ at the beginning of the avalanche (depinning). Avalanche termination (pinning) is characterized by a mild decrease in density due to eventual segment unbowing.

The $\rho - \varepsilon$ evolution from the Al simulation (Fig. 6.11(a)) indicates that increments in dislocation density (see the inset to Fig. 6.11(a)) are due to the proliferation of stair-rod segments in the dislocation network (pink line in Fig. 6.11(a)). Despite the fact that the emitted mobile dislocations predominantly exhibit the conventional Shockey partial dissociation (red

arrows in Fig. 6.11(a) mark the onset of large avalanche events), the Shockey density remains at a relatively constant level from $\varepsilon \approx 0.035$ to $\varepsilon \approx 0.07$, see Fig. 6.11(a). The simulation reveals that the increments in the stair-rod density are associated with the recurrent formation of SFTs [97], which produce intermittent slip events by means of specific unzipping processes which are illustrated in the sequence of Figs. 6.11(b)-(f), where the activation of segment "1" leads to junction formation with segment "2" (Fig. 6.11(c)) and "3" (Fig. 6.11(f)). Notice how the progressive SFT formation [97] that results from the interaction with segment "3" (Fig. 6.11(d)) leads to avalanche emission due to the unzipping of segments "2" and "3" in Fig. 6.11(e). Although the FCC simulations exhibit occasional formation of dual dislocation junctions during the emission of dislocation avalanches (e.g., the Lomer-Cottrell junction in Fig. 6.11(g) in the Al simulation (Fig. 2.8(a))), the above construction is found to evolve to one of the multi-segment type (Figs. 2.8(e)-(g)). In this regard, it is noted in the periodic simulations that the dense dislocation configurations favor multi-junction formation in FCCs (Fig. 6.8(c)) due to the small atomic distances between neighbor segments ($\approx$ 10–30 nm).
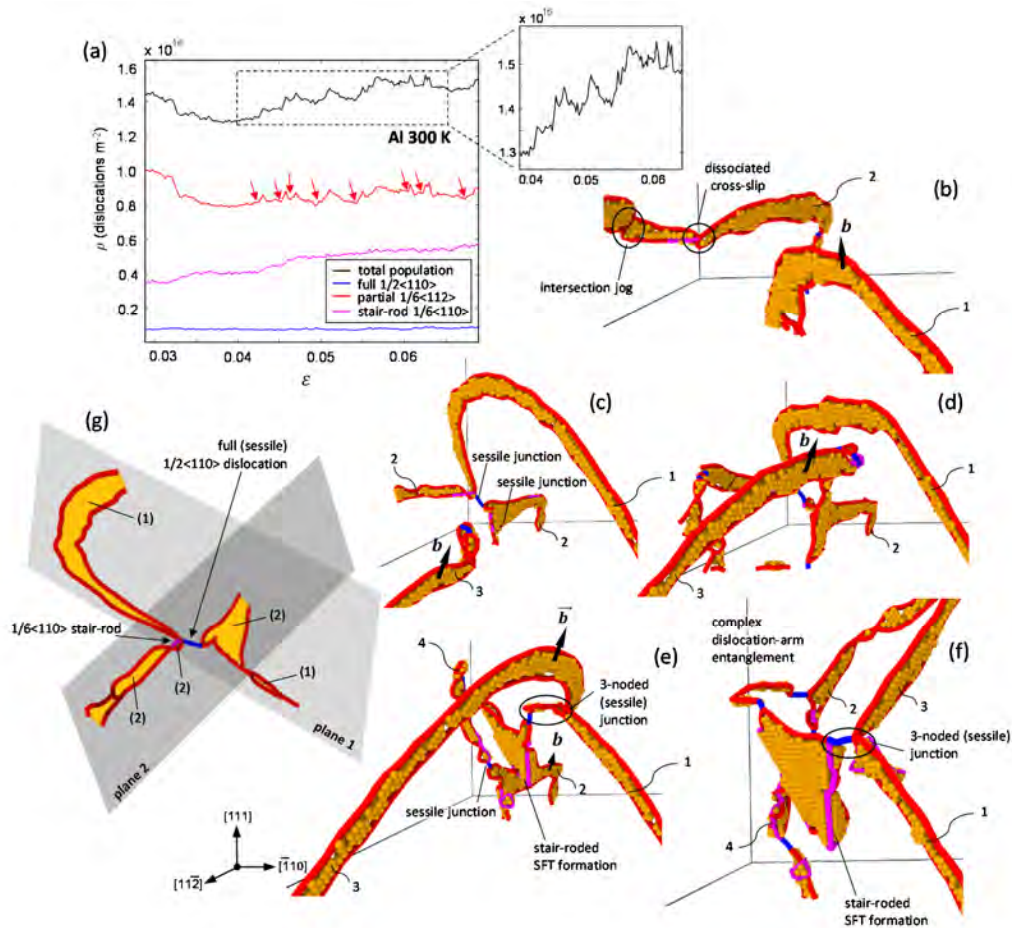
Figure 6.11. Development of dense dislocation network in the MD simulation of Al at 300 K. (a) Dislocation populations of 1/2<110> (full), 1/6<112> (Shockley) and 1/6<110> (stair-rod) segments during the simulation. (b)-(f): The interplay of segments "1", "2" and "3" leads to the formation of stair-rod arrangements which result in the onset of a SFT and a complex multi-junction. (g) Lomer-Cottrell junction detected in the MD simulation. The dislocations are labelled in accord with the corresponding slip plane. Segments in red, blue, and magenta correspond to full, Shockley, and stair-road dislocations, respectively. Orange atoms denote SF planes.

In the Cu simulation at 400 K, the depinning of dislocation segments from the network is also mediated through the aforementioned mechanisms involving SFT formation. The $\rho - \varepsilon$ evolutions in Fig. 6.12(b) show that the intermittent development of the dislocation entanglement is distinguished by (i) mild increases in the stair-rod populations (indicating SFT formation, see the circles in Fig. 6.12(a)) and (ii) a gradual reduction in Shockley density due to dislocation annihilation. At higher temperatures (e.g. at 650 K), the $\rho - \varepsilon$ curves from Fig. 6.12(d) show that the stair-rod density (pink curve) remains at a relatively fixed level during the simulation, indicating that SFT-mediated unzipping becomes inconsequential to the emission of the avalanches (red arrows in Fig. 6.12(b)). On the other hand, dislocation annihilation and cross-slip processes associated with Shockley partial dissociation play a much more important role in the development of the dislocation network (see red arrows in Fig. 6.12(d)). In this sense, it is noted that the enhancement of cross slip processes implies the arrangement of a defect configuration with much more intricate dislocation segments (cf. Figs. 6.8(a) and 6.8(b)). Finally, the greater δ_{Sh} of Shockley partials in Cu (compare Fig. 6.8(a) with 6.8(c)) arguably hinder dislocation dissemination across the periodic volumes, leading to the attainment of smaller dislocation densities in the periodic simulation cell at 650 K in comparison with that obtained in the Al simulation at 300 K (cf. Figs. 6.11(a) and 6.12(c)).
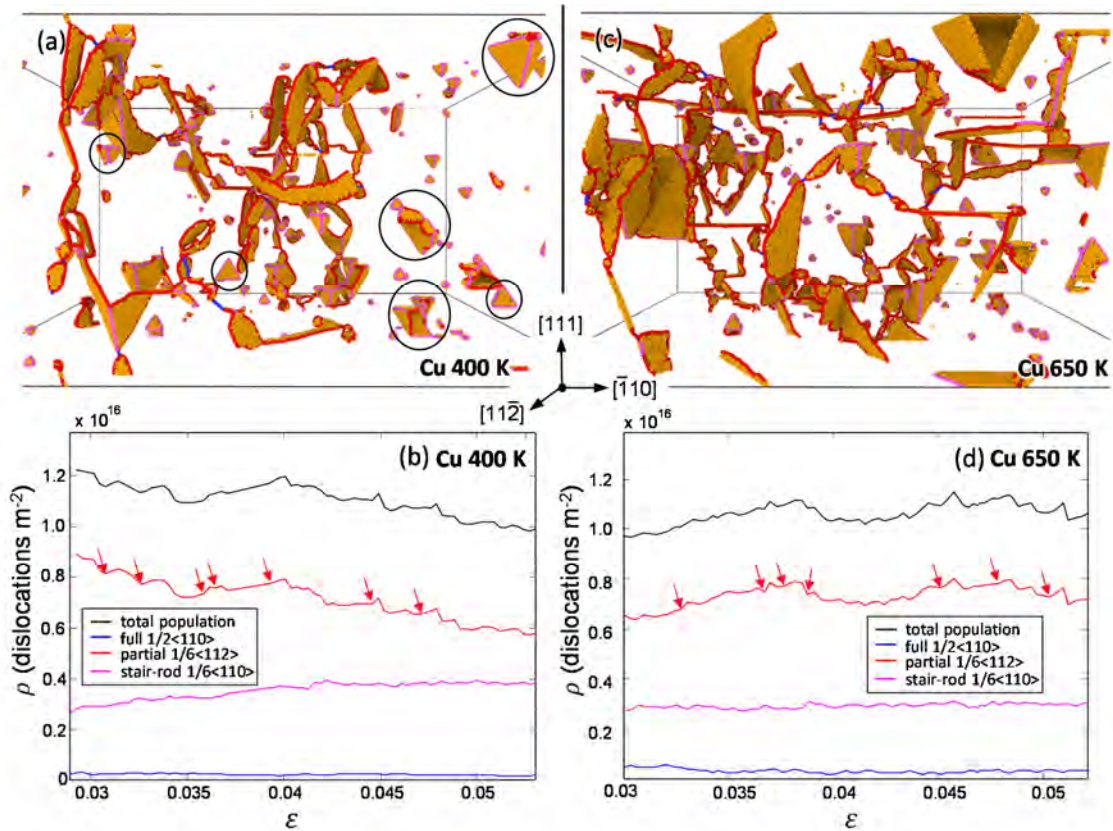
Figure 6.12. Development of the defect networks in the Cu simulations. Fully-fledged dislocation networks ($\varepsilon \approx 0.05$) at 400 K and 650 K are given in (a) and (c), respectively. Circles in (a) denote large-sized SFT arrangements. Segments in red, blue, and magenta correspond to full, Shockley, and stair-road dislocations, respectively. Orange atoms denote SF planes. The serrated evolution of the $\rho - \varepsilon$ curves from (b) and (d) are indicative of the intermittent development of the dislocation populations at 400 K and 650 K, respectively. Red arrows mark the onset of large avalanche events. See text for further details.

6.7. Dislocation activity during avalanche events in BCCs

The Ta simulations evidence that individual mobilizations of dislocation segments lead to the emission of dislocation avalanches within the incipient slip domain (κ_1) in the $C(s)$ distributions ($s < s_c$), see Fig. 6.9. The size of these slip events is essentially determined by the mobility of the screw dislocations. In this context, thermal-assisted kinking processes facilitate the dissemination of the mobile segments across the dense dislocation forest, while the limited screw mobility at low temperatures ($T/T_m < 0.2$ [85]) ultimately prevents the onset of large slip events. In the simulation at 300 K, where the periodic dislocation network is comprised by a significant number of (immobile) long screw segments (Fig. 6.4(a)), the inception of uncorrelated avalanche emissions is due to the mobilization of individual edge dislocations whose glide involves $\approx 8-20$ atomic spacings (3 nm $\lesssim L \lesssim 15$ nm). At 900 K, the enhanced-mobility of the dislocation network containing thermally-activated screws (Fig. 6.4(b)) leads to the emission of statistically larger (incipient) slip events (Fig. 6.9) as the glide of active segments exhibits 10 nm $\lesssim L \lesssim 40$ nm.
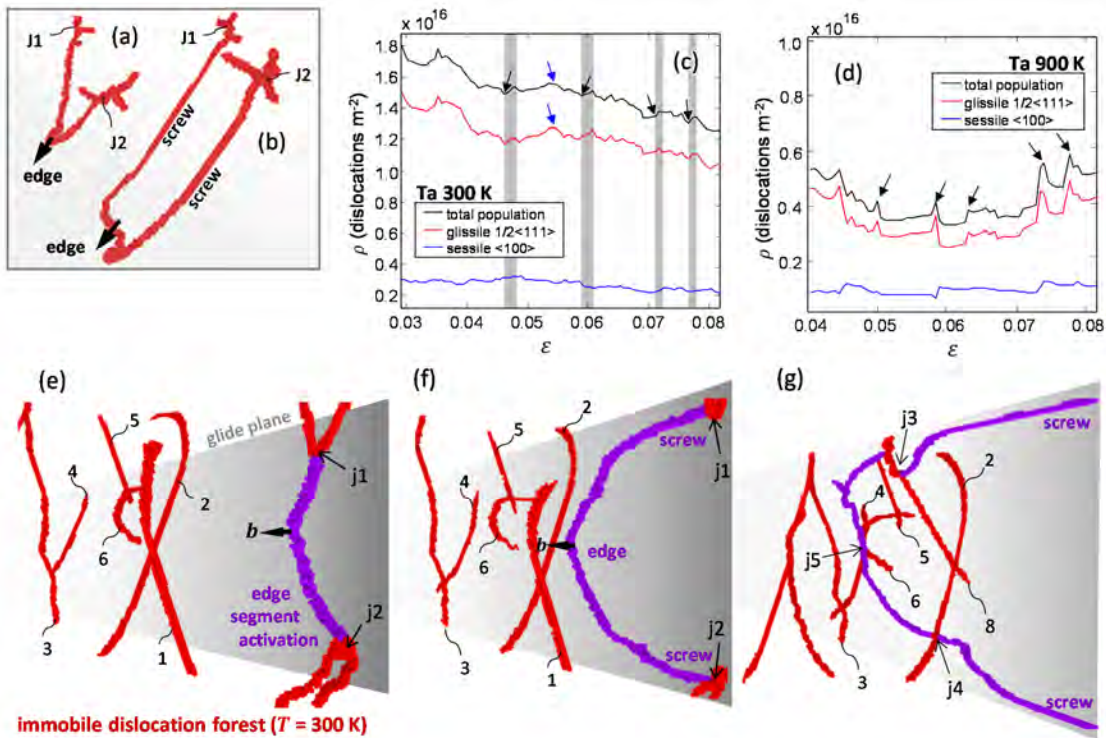
Figure6.13. Development of the defect networks in the Ta simulations. (a)-(b): Anisotropic loop expansion pinned at "J1" and "J2" at 300 K. (c) and (d): $\rho - \varepsilon$ curves of glissile 1/2<111> and sessile <100> segments during the Ta simulations at 300 K and at 900 K, respectively. As in the case of the FCC crystals, the onset of an avalanche leads to a sudden increase in the dislocation density while avalanche termination is associated with dislocation annihilation. Along these lines, it is noted that fluctuations in dislocation density at 900K are greater than at 300K because of the greater mobility of the networks with increasing temperature. (e)-(f): Expansion of an anisotropic loop (in violet) pinned at junctions " j1" and "j2" leads to the onset of a slip event characterized by $s \approx b$ at 300 K. The loop is arrested in (g) due to interaction with the steady dislocation forest network (in red) at points "j3"," j4" and "j5". Atoms are visualized through OVITO (see Appendix A6). See text for further details.

The present simulations reveal that the screw mobility also governs the inception of the large slip domain with ($s > s_c$) in the $C(s)$ distributions. In the Ta simulation at 300 K, the emission of large avalanches is due to the sudden activation of pinned dislocation arms that produces anisotropic loop expansions. The mobilization of the loop (Fig. 6.13(a)) requires the outward motion of the screw components along with the rapid propagation of the partner edge segment (Fig. 6.13(b)). The simulation shows that these loops (Figs. 6.13(e) and 6.13(f)) travel a distance $L \approx 10 - 30$ nm to the point where the loop expansion is arrested by the dense dislocation forest (Fig. 6.13(g)). These avalanche events are associated with abrupt increments in the dislocation density (marked with black arrows in Fig. 6.13(c)). The shaded areas in Fig. 6.13(c) mark the $\rho - \varepsilon$ evolution during the avalanche events that carry large slip sizes in Ta at 300 K. Notice in this figure that the local minima in the $\rho - \varepsilon$ curve indicate avalanche arrest and the onset of a pinning stage ($\Delta\sigma \approx E\Delta\varepsilon$). In addition, the $\rho - \varepsilon$ curve (Fig. 6.13(c)) shows an overall mild decrease in the global dislocation density with increasing straining, which is associated with dislocation annihilation processes mostly developing within the incipient slip domain where $s < s_c$. The sequence of Fig. 6.14 displays the partial annihilation of segment "2" due to the interaction with screw segment "1" as $\boldsymbol{b}_1 = -\boldsymbol{b}_2$. The ρ levels drawn in Fig. 6.13(c) finally suggest that the formation of sessile junctions is inconsequential to the development of the dense dislocation networks at 300 K (distinguished by long immobile screws). Thus, the overall density levels are reduced because of the decrease of mobile junctions as noted in the reduction of the <100> segment population (blue line) with increasing straining.
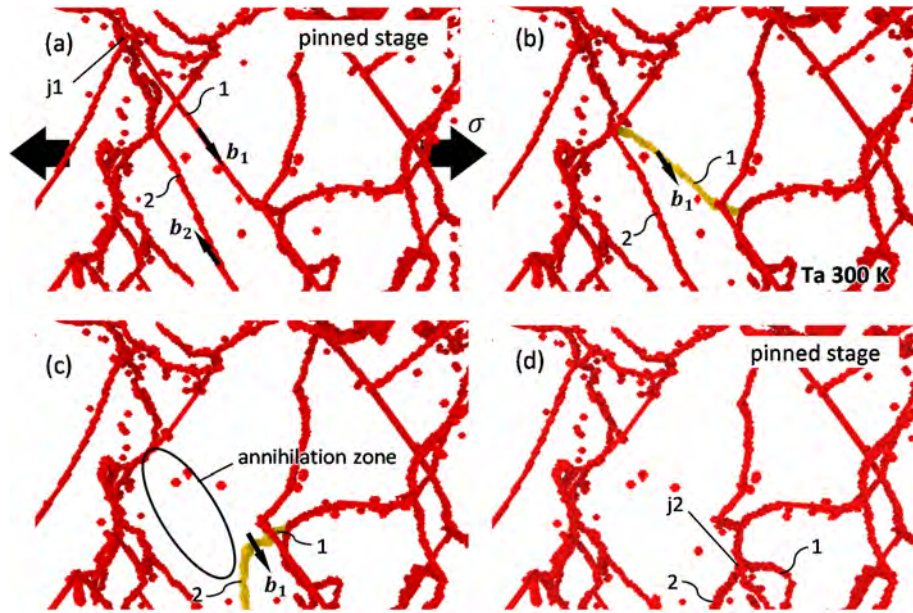
Figure 6.14. Sequence of a dislocation annihilation in Ta at $T = 300$ K. Unzipping of segment "1" initially pinned at "j1" in (a) leads to interaction with segment "2". Active segments are highlighted in yellow. Interaction between segments "1" and "2" results in the annihilation of both segments (in picture (c)) as $\boldsymbol{b}_1 = -\boldsymbol{b}_2$. The remnant segments "1" and "2" are finally arrested at junction "j2" in (d). The annihilation process reduces the dislocation density by $\Delta\rho \approx -5 \times 10^{14}$ m^{-2} (blue arrows in Fig. 6.13(c)).
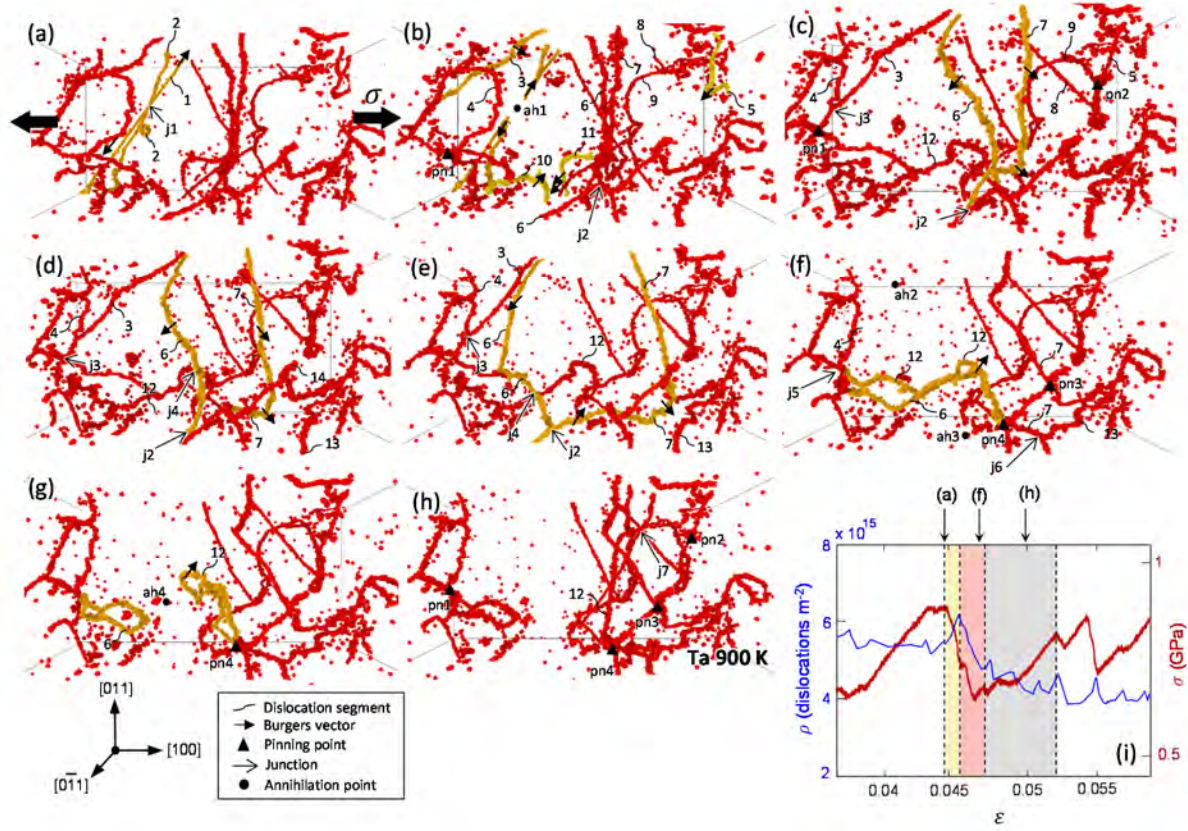
Figure 6.15. Sequence of a large avalanche event in Ta at 900 K where the active segments are marked in yellow. (a) Segments "1" and "2" interact at (unstable) "j1", which annihilates in (b) at the point "ah1". Segment "4" revolves around "pn1" in (b) and interacts with "3" producing stable "j3". Activation of segment "5" interacts with "8", producing a pinned structure ("pn2") composed of segments "5", "8" and "9" in (c), which remains immobile for the remaining avalanche. The mutually-attractive segments "10" and "11" produce segment "12" in (c). Additional mobilization of segment "6" in (c) results in: (i) formation of junction "j4" with segment "12", (ii) partial annihilation with segment "3" (marked "ah2" in (f)), (iii) additional junction formation "j5" with segment "4"; and, (iv) partial annihilation "ah4" (see the unzipping process of junction "j2" in (a)-(f)). The propagation of "7" ($L \approx$ 20 nm, from (c) to (f)) produces (i) pinning point "pn3", and (ii) junction "j6". Finally, unzipping of "j4" in (f) results in the formation of the pinning point "pn4" around which segment "12" revolves. This pivoting segment exhibits interaction and annihilation ("ah4") with segment "6". Segment "12" is finally pinned at "j7" in (h). Finally, part (i) provides the $\rho - \varepsilon$ evolution during the avalanche event. The yellow, red and grey regions denote dislocation multiplication (a), annihilation (f) and arrest followed by a quasi-elastic loading stage (h).

At higher temperatures ($T/T_\mathrm{m} > 0.2$), the dislocation networks in BCC crystals are characterized by highly-mobile segments whose glide spans over statistically larger distances ($L \gtrsim 35$ nm). In this context, the Ta simulation at 900 K shows that the emission of avalanches distinguished by $s > s_\mathrm{c}$ in the $C(s)$ distributions (Fig. 6.9) involves the activation (unzipping) of a precursory dislocation segment which gives way to the gliding of secondary dislocations, leading to the additional mobilization of a least 3 segments during the avalanche event. Figures 6.15(a)-(h) display the sequence of a dislocation avalanche in the simulation at 900 K, which carries a large slip size ($s \approx 4b$). This dislocation avalanche is constituted by the *collective* glide of 7 segments comprised by wavy mobile lines with kinked-screw and edge components (Fig. 6.4(b)). In accordance with the $\rho - \varepsilon$ curve in Fig. 6.13(d), the marked decrease in the density levels during avalanche arrest is a clear indication of the strong role that annihilation

processes (Fig. 6.14) play in the development of dense dislocation networks at elevated temperatures. These results differ from the above description for lower temperatures, where large avalanches (carrying $s > s_c$) lead to local raises in dislocation density, as large avalanches at elevated temperatures are always characterized by sharp reductions in density (see the black arrows in Fig. 6.13(d)).

6.8. Self-organized vs. tuned criticality

The extensive experimental and computational work analyzed in this investigation probes intermittent plasticity in the context of slip size distributions (Figs. 6.7 and 6.9) characterized by (i) an incipient slip domain ($s < s_c$) of *uncorrelated* slip processes, and (ii) a large avalanche size slip regime ($s > s_c$) of *correlated* events. The Pearson coefficient r and the p-value (both ranging from 0 to 1) enable assessment of the correlation level between the slip size and applied stress [50]. This standard procedure provides a formal support to the possible correlation (certain or accidental) between the two variables [168]. Under this framework, values of r approaching unity are indicative of an increasingly linear relationship between the two variables, while p-values close to 0 indicate that the likelihood for the possible correlation between the variables is high.

The outcomes from this analysis prove that the slip events detected in the incipient slip regime are not correlated with the applied stress τ. Figure 6.16 shows that this is indeed the case since for $< s_c$, as $r < 0.25$ and the p-value is much greater than 0 (> 0.30). These results are in good agreement with the slip events for $s < s_c$ obtained in micropillar compression experiments (see Ref. [50]), where the $s/b - \tau$ datasets exhibit $r \lesssim 0.15$ and p-value $\gtrsim 0.27$.
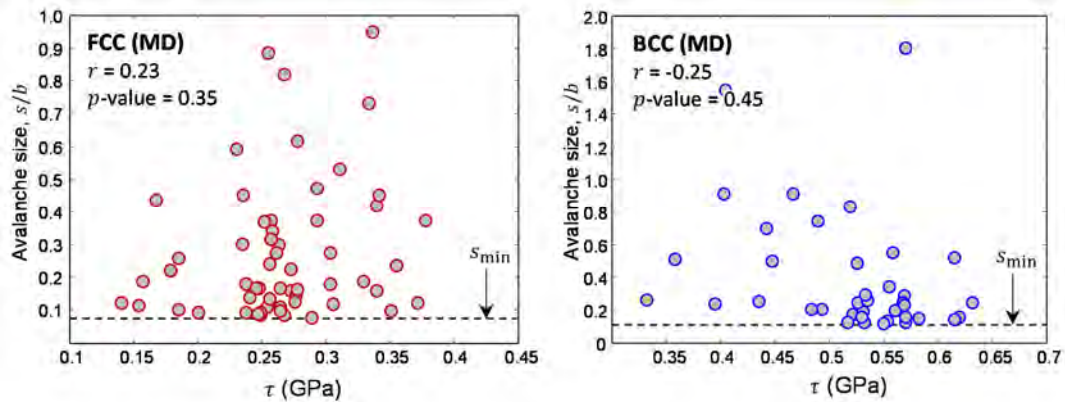
Figure 6.16. Scattered $s/b - \tau$ distributions of the avalanche events carrying $s < s_c$. Small values of Pearson coefficient ($r < 0.25$) with a relatively small confidence levels (p-value > 30%) indicate that the slip and stress are not correlated.

The few slip data available in the large slip size domains from present simulations do not allow the performance of a sound statistical analysis for the possible correlation between s and τ. [Note in Figs. 6.7 and 6.9 that the κ_2-regime in the $C(s)$ distributions only contains a few data points ($2 < n < 6$, see Appendix A7.2)]. Nonetheless, the much larger slip data obtained in micropillar compression experiments [50] reveal that within the large avalanche regime of strain hardening microcrystals ($s > s_c$) the slip sizes are not correlated with the applied stress, suggesting the onset of STC [44]. This becomes manifest in the greater linear

dependence of the $s/b - \tau$ datasets, where according to Ref. [50] $r > 0.4$ and $p \to 0$ in both FCC and BCC crystals. The greatest r values ($r > 0.5$) indicating a great linearity between slip and stress pertain to small microcrystals, distinguished by a predominance of dislocation starvation, which leads to the attainment of marked stress-binned $C(s, \tau)$ distributions [34, 44] for $s > s_{\mathrm{c}}$.

6.9. Conclusions

The extensive experimental and computational work analyzed in this investigation clearly shows the onset of two different slip regimes in the $C(s)$ distributions, where the critical slip size, s_{c}, marks transition between the incipient slip ($s < s_{\mathrm{c}}$) and large slip size ($s > s_{\mathrm{c}}$) domains characterized by power-law exponents κ_1 and κ_2, respectively. The results indicate that s_{c} acts as the essential material property that characterizes the intermittent response of dislocation-mediated plasticity in the context of the emissions of dislocation avalanches as a function of sample size, crystalline structure and temperature. These findings have deep implications in the understanding and characterization of dislocation glide processes governing the inception of intermitted avalanches in metal plasticity. The periodic FCC and BCC MD simulations provide new insights into the underlying dislocation mechanisms that become operative during intermittent slip processes. The following are the main conclusions drawn from this investigation.

1. The MD simulations indicate that the avalanche events carrying slip $s < s_{\mathrm{c}}$ are not binned by stress. The avalanche events attaining under a preexisting dislocation network with an extremely large density ($\rho \approx 1 \times 10^{16}\ \mathrm{m}^{-2}$) propagate through the periodic volume involving fractional slips ($s < 1b$). The resulting $C(s)$ distributions with power-law exponent κ_1 span about one entire logarithmic decade of (uncorrelated) fractional slip, extending the experimentally measured incipient slip domain towards the smallest possible slip value of $s_{\mathrm{min}} \approx 0.1b$. The large avalanche slip size domain ($s > s_{\mathrm{c}}$) emerges in the $C(s)$ distributions with κ_2 where correlated avalanche events attain.

2. In FCC metals, the onset of small s_{c} values is indicative of strong interactions between the mobile dislocations and the entangled dislocation forest, so that the slip distributions shift to smaller values as compared to the case of dislocation networks containing milder interactions. The enhancement of cross slip (which promotes dislocation mobility) results in the development of large s_{c} levels. The Cu simulations show that thermally-assisted cross-slip processes facilitate the dissemination of the mobile dislocations across the periodic cells, producing large slip events. In addition, dislocation annihilation dominates dislocation network development in the periodic Cu crystals, as $d\rho/d\varepsilon < 0$. In the Al simulation (with a large SFE), cross slip processes lead to a greater intricacy in the dislocation arrangements, which involve smaller statistical values of the mean free path length L. The simulations reveal that the development of SFT structures facilitates unzipping of the dislocation network, which leads to the inception of large avalanche events during the development of dense defect networks.

3. In BCC crystals, s_{c} is governed by the mobility of the screw dislocations, where thermally-assisted kinking processes render larger s_{c} values during the development of highly-mobile and wavy dislocation configurations. The Ta simulations capture the effective role of the screw mobility in the slip distributions, where the dislocation network at 900 K exhibits the onset of large slip events. The simulations additionally

show that intermittent plasticity progresses through a significant amount of dislocation annihilation processes which dominate the development of dense dislocation entanglements with relatively large values of L.

4. The Al and Cu simulations reveal that large avalanche events carrying correlated slip ($s > s_c$) are due to the collective glide of dislocations ($N_d \geq 3$) traveling across the intricate defect network. Unzipping of dislocation segments leads to mild increments in dislocation density during an avalanche. The mobile dislocations are arrested by the immobile forest, which leads to the onset of a quasi-elastic (pinning) regime, $\Delta\sigma \approx E\Delta\varepsilon$, characterized by stagnant density levels ($d\rho/d\varepsilon \approx 0$). Uncorrelated avalanche events are distinguished by the mobilization of individual dislocation segments ($N_d \leq 2$) that glide over a statistical distance L. The MD simulations show that the avalanche slip size is determined by L and N_d.

5. The underlying dislocation mechanisms associated with the development of large avalanche events in BCC crystals are also governed by the screw mobility. The Ta simulation at 300 K, where kinking of the screws is inhibited, shows that large slip events ($s > s_c$) are produced by anisotropic loop expansions comprised by a mobile edge segment and two partnering screws pinned in the immobile forest. Avalanche arrest attains as the immobile dislocation forest intercepts the expansion of the loops. With increasing temperature (900 K), a global enhancement in the screw mobility is encountered, which leads to the emission of large avalanches through the collective motion of dislocations ($N_d > 5$). The mobile segments produce an increment in dislocation density during the avalanche events, while a mild reduction in the ρ levels is associated with dislocation annihilation processes.

6. Although the results of the avalanches modeled through the MD simulations concern much larger strain rates than those imposed during conventional micropillar compression experiments ($\dot{\varepsilon} < 1 \times 10^{-3}$ s^{-1}) [34, 50, 163], the strain rate defined in the simulations ($\dot{\varepsilon} = 1.5 \times 10^{6}$ s^{-1}) prevents avalanche overlapping. Complementary MD simulations performed at much smaller strain rates ($\dot{\varepsilon} < 1 \times 10^{5}$ s^{-1}) are still required in order to assess the influence of the loading rate upon the emission and propagation of dislocation avalanches. These simulations lie beyond the current computational capacity [120].

APPENDIX A1. Statistical ensembles and the equations of motion in MD simulations

A1.1. Generalities

The classical formulation for molecular dynamics (MD) simulations [103] is based on the integration of the Newton's equations of motion (EOM) that strictly capture the time evolution of closed systems while system's energy remains constant (e.g., a particle system enclosed in a hermetic container) [103]. In statistical mechanics, this scheme corresponds to the *microcanonical* or *NVE* ensemble (constant *N*-number of atoms, *V*-volume, and *E*-energy) [108] whose EOM count with the robust Hamiltonian formulation [169]. Note that although every constituent particle is in motion due to the local force fields from the neighbor atoms, *NVE* systems do *not* statistically evolve over time as the system's energy is fixed to the same region in the Γ-space [108], which implies thermodynamic equilibrium [104].

Other statistical ensembles are available [103, 108], which are built by convenient reformulations of the Hamiltonian EOM [56, 103] that enable other quantities to fluctuate around a fixed value while the system's energy is *not* conserved. These approaches are framed in the class of non-equilibrium MD [108] described by non-Hamiltonian dynamics [105]. In particular, the *canonical NVT* and *NPT* ensembles [110] are a popular framework to run non-equilibrium MD simulations [108]. These EOM employ thermostat and barostat terms that respectively control the temperature and internal pressure of the system while the particles evolve in time matching the Boltzmann (canonical) distribution (Section 3.1). The thermostat term reproduces the effect of a heath bath (with constant temperature) acting on the system [105], whereas the barostat emulates the action of an arbitrary "*piston*" onto the system [108]. Nonetheless, these approaches are not exempt from subtleties [108]. The most obvious arises from the fact that while nature conserves system's energy due to particle collisions (momentum conservation [104]), *NVT* and *NPT* dynamics lead to the conservation of other energy-like quantities which lack physical meaning [103, 105].

In the following, Appendix A1.2 provides the formulation for MD simulations with Hamiltonian *NVE* dynamics using the velocity-Verlet algorithm described in Appendix A1.3 to integrate the EOM. Likewise, Appendixes A1.4 and A1.5 address the EOM of non-Hamiltonian *NVT* and *NPT* dynamics (respectively). These EOM are integrated by the r-RESPA algorithm reviewed in Appendix A1.6.

A1.2. *NVE* dynamics

The time evolution of the phase space $\Gamma\left(r_j, p_j\right)_{NVE}$ is described by the Hamiltonian EOM [57]

$$\dot{r}_j = \frac{p_j}{m_j}, \tag{A1.1a}$$

$$\dot{p}_j = m_j\ddot{r}_j = f_j, \tag{A1.1b}$$

where $\boldsymbol{f}_j$ is the force that drives particle j, see Section 3.1 for nomenclature. The particularity of the Hamiltonian EOM resides in the symmetries of the transformation [56, 169] which result in the conservation of the energy of the system,

$$\mathcal{H}(\boldsymbol{\Gamma}) = \sum_{j=1}^{N} \left[\frac{(\boldsymbol{p}_j(t))^2}{2m_j} + V\left(\boldsymbol{r}_j(t)\right) \right], \tag{A1.2}$$

as $\dot{\mathcal{H}}(\boldsymbol{\Gamma}) = 0$. In addition, Eqs. (A1.1a) and (A1.1b) satisfy the *symplectic* geometry [56, 169] which, apart from the above energy conservation, implies time invariance (or incompressibility) of the $\boldsymbol{\Gamma}$-space volume (Liouville theorem [104]) and time reversibility (deterministic dynamics [108]).

The probability distribution of an NVE system, φ_{NVE}, is defined as the inverse of the total number of microstates, W, occupying the *only possible* energy level $\mathcal{H}$,

$$\varphi_{NVE} = \frac{1}{W} = 1 / \int d\boldsymbol{\Gamma}_{NVE} \, \delta(\mathcal{H}(\boldsymbol{\Gamma}_{NVE}) - \mathcal{H}) \,, \tag{A1.3}$$

where $\delta(\dots)$ is the Dirac delta function. Notice in the above equation that every system state is invariably described by the same probability function φ_{NVE} as all microstates share the same probability irrespectively of the magnitude of $\mathcal{H}$.

A1.3. The velocity-Verlet algorithm

MD simulations under the microcanonical ensemble compute the motion of the constituent particles by integrating the Newton's second law [56],

$$\boldsymbol{a}_j = -\frac{1}{m} \frac{dV(\boldsymbol{r}_j)}{d\boldsymbol{r}_j}, \quad j = 1, \dots, N \,, \tag{A1.4}$$

where $\boldsymbol{a}_j$ is the acceleration vector of particle j. Note that $\boldsymbol{f}_j = dV(\boldsymbol{r}_j)/d\boldsymbol{r}_j$ (Eq. (A1.1b)). The Verlet algorithm is a simple (and widely employed [108]) time integrator of Eq. (A1.4) that satisfies the conservation laws of Hamiltonian dynamics [56]. The basic idea of this method resides in defining the Taylor expansion of function $\boldsymbol{r}_j(t + \Delta t)$ at t, where

$$\boldsymbol{r}_j(t + \Delta t) = \boldsymbol{r}_j(t) + \frac{\boldsymbol{p}_j(t)\Delta t}{m_j} + \frac{1}{2}\boldsymbol{a}_j(t)(\Delta t^2) + \mathcal{O}(\Delta t^3). \tag{A1.5}$$

The velocity-Verlet algorithm improves the accuracy of the original Verlet formulation (Eq. (A1.5)) through the addition of the Taylor expansions around $\boldsymbol{r}_j(t)$, i.e., $\boldsymbol{r}_j(t + \Delta t) + \boldsymbol{r}_j(t - \Delta t)$ [56, 108], where

$$\boldsymbol{r}_j(t + \Delta t) = 2\boldsymbol{r}_j(t) - \boldsymbol{r}_j(t - \Delta t) - \frac{1}{m_j}\frac{dV(\boldsymbol{r}_j)}{d\boldsymbol{r}_j}\Delta t^2 + \mathcal{O}(\Delta t^4) \,, \tag{A1.6a}$$

and by defining "mid-step" velocities [108],

$$\boldsymbol{v}_j\left(t + \frac{\Delta t}{2}\right) = \boldsymbol{v}_j(t) + \frac{1}{2}\boldsymbol{a}_j(t)\Delta t + \mathcal{O}(\Delta t^2) \,, \tag{A1.6b}$$

$$\boldsymbol{v}_j(t + \Delta t) = \boldsymbol{v}_j\left(t + \frac{\Delta t}{2}\right) + \frac{1}{2}\boldsymbol{a}_j(t + \Delta t) + \mathcal{O}(\Delta t^2). \tag{A1.6c}$$

Note that $v_j = dr_j/dt$ and $a_j = d^2r_j/dt^2$; and that $v_j(t + \Delta t)$ can only be computed once $r_j(t + \Delta t)$ is known [108].

The velocity-Verlet algorithm updates the particle positions at successive $t + \Delta t$ (Eq. (A1.6a)) by taking a numerical error of $\mathcal{O}(\Delta t^4)$, which is an order of magnitude smaller than the numerical error of the original Verlet algorithm (Eq. (A1.5)) [108]. In addition, the update of particle velocities leads to a larger numerical error ($\mathcal{O}(\Delta t^2)$) through a time increment $t + \Delta t$. Nonetheless, the velocity-Verlet scheme reduces by a half this numerical error by the above mid-stepping of the velocities (i.e., dividing $t + \Delta t$ into two parts), see Eqs. (A1.6b) and (A1.6c). This splitting corresponds to the Liouville-operator breakup of $i\mathcal{L} = i\mathcal{L}_p/2 + i\mathcal{L}_r + i\mathcal{L}_p/2$, which yields the time propagator (Trotter factorization) $e^{i\mathcal{L}\Delta t} \approx e^{i\mathcal{L}_p\Delta t/2}e^{i\mathcal{L}_r\Delta t}e^{i\mathcal{L}_p\Delta t/2}$ (Section 3.1) with additionally results in a numerical error of $\mathcal{O}(\Delta t^2)$ [56, 108], see Eq. (A1.6d). See the action of the above Trotter breakup [105] in Fig. A1.1, where it is illustrated the operation of the velocity-Verlet time integrator algorithm in terms of the discrete time evolution of a harmonic-oscillator in the Γ-space [108].
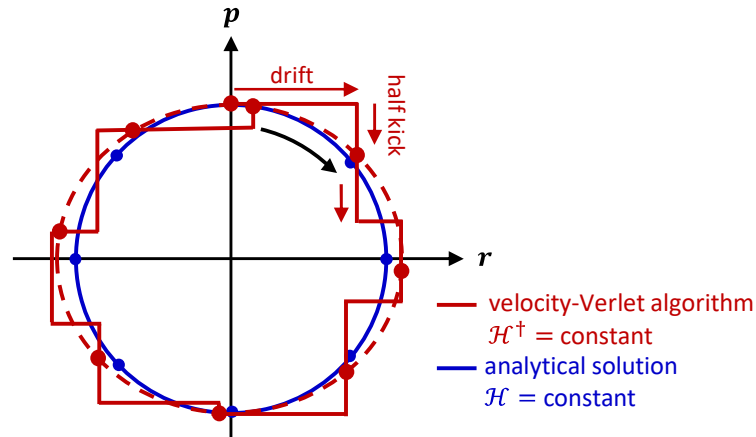
Figure A1.1. Illustration of the harmonic-oscillator phase portrait [108]. The red line depicts the Liouville operator splitting ($i\mathcal{L} = i\mathcal{L}_p/2 + i\mathcal{L}_r + i\mathcal{L}_p/2$) acting between successive red points. In the context of the velocity-Verlet algorithm, this implies solving $r_j(t + \Delta t)$ and $v_j(t + \Delta t)$ (Eqs. (A1.6)) by the action of (i) a half kick (half integration of the p-term, $\mathcal{L}_p/2$, at fixed r), followed by (ii) a drift (integration of the r-term, $i\mathcal{L}_r$, at fixed v), and finally followed by (iii) a half kick. Formally, the algorithm presents a long-term conservation of the quantity $\mathcal{H}^\dagger = \mathcal{H} + \mathcal{O}(\Delta t/2)^2$ [108].The blue line illustrates the analytical solution which strictly conserves $\mathcal{H}$ (Eq. (A1.2)).

A1.4. *NVT* dynamics

The present *NVT* simulations employ the Nosé-Hoover chains (NHC) [110] that introduce k additional degrees of freedom ξ_k in the $6N$-dimensional Γ-space to mimic the heat transfer from a (large) reservoir at T_{ext}. The time evolution of the phase space, $\Gamma(r_j, p_j, \xi_1, ..., \xi_M, p_{\xi_1}, ..., p_{\xi_M})_{NVT}$, implies non-Hamiltonian dynamics [106] described by the following EOM,

$$\dot{r}_j = \frac{p_j}{m_j} \qquad j = 1, ..., N, \qquad (A1.7a)$$

$$\dot{\boldsymbol{p}}_j = \boldsymbol{f}_j - \frac{p_{\xi_1}}{Q_1}\,\boldsymbol{p}_j\,, \tag{A1.7b}$$

$$\dot{\xi}_k = \frac{p_{\xi_k}}{Q_k} \quad k = 1, \dots, M\,, \tag{A1.7c}$$

$$\dot{p}_{\xi_1} = \sum_{j=1}^{N} \frac{\boldsymbol{p}_j^2}{m_j} - (N_\mathrm{f} + d^2)\mathrm{k_B}T_\mathrm{ext} - p_{\xi_1}\frac{p_{\xi_2}}{Q_2}\,, \tag{A1.7d}$$

$$\dot{p}_{\xi_k} = \left(\frac{p_{\xi_{k-1}}}{Q_{k-1}} - \mathrm{k_B}T_\mathrm{ext}\right) - p_{\xi_k}\frac{p_{\xi_{k+1}}}{Q_{k+1}} \quad \text{for} \quad k = 2, \dots, M-1\,, \tag{A1.7e}$$

which conserve the following quantity

$$H'_{NVT} = \sum_{j=1}^{N} \frac{\boldsymbol{p}_j^2}{2m_j} + \sum_{k=1}^{M} \frac{p_k^2}{2Q_k} + V(\boldsymbol{r}_j) + (N_\mathrm{f} + d^2)\mathrm{k_B}T_\mathrm{ext}\xi_1 + \sum_{k=2}^{M} \mathrm{k_B}T_\mathrm{ext}\xi_k\,. \tag{A1.8}$$

Here, m_j is the mass of particle j, Q_k is the "mass" of the kth thermostat that tunes the frequency with which temperature T fluctuates [105], N_f is the number of DF ($=3N$), d the system's dimension, M the number of NHC, $\mathrm{k_B}$ is the Boltzmann's constant, and ξ_k and p_k are , respectively, the thermostat variable (extra M degrees of freedom) and conjugate momentum of the kth thermostat. Equation (A1.8) reads as an energy-like relationship $H'_{NVT}(\boldsymbol{\Gamma}_{NVT})$, where the first and second terms of the right-hand side stand for the kinetic energy of the N-atom (real) system and the ξ_M thermostats, respectively; and the successive third and remaining terms account for the potential energy of real system and $(k-1)$ thermostats, respectively [106]. Note that T is not a strictly conserved quantity in the dynamics but, rather, it is a quantity numerically controlled by an external body (i.e., the heat bath modeled by imposing the above DF) which fluctuates around the imposed value to T_ext (Eqs. (A1.7d) and (A1.8)).

It is demonstrated elsewhere in Ref. [105] that the thermostat masses Q_k should satisfy $Q_1 = N_\mathrm{f}\mathrm{k_B}T_\mathrm{ext}/\omega_\mathrm{p}^2$ and $Q_k = \mathrm{k_B}T_\mathrm{ext}/\omega_\mathrm{p}^2$ (for $k = 2, \dots, M-1$), where ω_p is the frequency at which the particles are thermostated. Figure A1.2 displays the system's energy and temperature fluctuations during NVT dynamics under a wide range of thermostat frequencies ω_p. It is observed that low frequencies ($\omega_\mathrm{p} < 10\Delta t$) lead to wild fluctuations in temperature and energy, while large frequencies ($\omega_\mathrm{p} > 10000\Delta t$) result in constant-energy dynamics due to the poor contribution of the thermostat into the dynamics. In the present NVT simulations, ω_p is set to $100\,\Delta t$ [118].

The physical intuition for the action of the thermostat onto the $\{\boldsymbol{r}_j, \boldsymbol{p}_j\}$ system is revelead *via* the scaling of the velocities of the particles, i.e. $\boldsymbol{v}_j = \xi\,\dot{\boldsymbol{r}}_j$ [Nosé1983], where $\boldsymbol{v}_i$ is the real velocity of atom j. This can be interpreted as an exchange of heat between the real system and the external system (heat reservoir) [Nosé1983]. In this context, note that the first multiplier ξ_1 thermostats the particle momenta $\boldsymbol{p}_j$, the second multiplier ξ_2 thermostats ξ_1, a third ξ_3 acts on ξ_2, and so on [110]. It is remarked to mention that the introduction of extra M degrees of freedom to the system appears to be arbitrary as it lacks of a solid statistical mechanics base [110].

The Jacobian $\boldsymbol{J}$ that accounts for the weight associated with the phase space $\boldsymbol{\Gamma}\left(\boldsymbol{r}_j, \boldsymbol{p}_j, \xi_1, \dots, \xi_M, p_{\xi_1}, \dots, p_{\xi_M}\right)_{NVT}$ is [106]

$$\boldsymbol{J} = e^{\left[(N_\mathrm{f}+d^2)\xi_1 + \Sigma_{k=2}^{M}\,\xi_k\right]}\,. \tag{A1.9}$$

Since the EOM sample the canonical ensemble, the Jacobian $\boldsymbol{J}$ is constrained to unity ($\boldsymbol{J} = 1$) in order to meet the *incompressibility* condition of $\boldsymbol{\Gamma}_{NVT}$ [104, 105], where the particle distribution function satisfies $\varphi_{NVT}(\boldsymbol{\Gamma}_{NVT}) = 1/Z_{NVT}(e^{-\beta H''_{NVT}})$ [104]. This leads to the partition function [105, 106]

$$Z_{NVT} = \int d\boldsymbol{\Gamma}_{NVT}\, e^{-\beta H''_{NVT}},\tag{A1.10}$$

where

$$H''_{NVT} = \sum_{j=1}^{N} \frac{\boldsymbol{p}_j^2}{2m_j} + \sum_{k=1}^{M} \frac{p_k^2}{2Q_k} + V(\boldsymbol{r}_j).\tag{A1.11}$$

A1.5. *NPT* dynamics

The *NPT* simulations use a barostat [110] which employs the (fully flexible) cell $\boldsymbol{h}$ of Cartesian parameters (with an invariant form of the moment [105, 106]) so that the internal pressure tensor $\boldsymbol{P}$ is controlled while the system is thermostated by the previous NHC formulation (Eq. (A1.7)). Under this framework, the EOM are described by [106]

$$\dot{\boldsymbol{r}}_j = \frac{\boldsymbol{p}_j}{m_j} + \frac{\boldsymbol{p}_g}{W_g}\boldsymbol{r}_j,\tag{A1.12a}$$

$$\dot{\boldsymbol{p}}_j = \boldsymbol{f}_j - \frac{1}{N_f}\frac{\mathrm{Tr}[\boldsymbol{p}_g]}{W_g}\boldsymbol{p}_j - \frac{p_{\xi_1}}{Q_1}\,\boldsymbol{p}_j,\tag{A1.12b}$$

$$\dot{\boldsymbol{h}} = \frac{\boldsymbol{p}_g}{W_g}\boldsymbol{h},\tag{A1.12c}$$

$$\dot{\boldsymbol{p}}_g = V(\boldsymbol{P} - I P_{\text{ext}}) - \boldsymbol{h}\boldsymbol{\Sigma}\boldsymbol{h}^t + \left(\frac{1}{N_f}\sum_{j=1}^{N}\frac{\boldsymbol{p}_j^2}{m_j}\right)\boldsymbol{I} - \frac{p_{\xi_1}}{Q_1}\boldsymbol{p}_g,\tag{A1.12d}$$

$$\dot{\xi}_k = \frac{p_\xi}{Q_k}\quad k = 1, \dots, M,\tag{A1.12e}$$

$$\dot{p}_{\xi_1} = \sum_{j=1}^{N}\frac{\boldsymbol{p}_j^2}{m_j} + \frac{1}{W_g}\mathrm{Tr}[\boldsymbol{p}_g^t\,\boldsymbol{p}_g] - (N_f + d^2)\mathrm{k_B}T_{\text{ext}} - p_{\xi_1}\frac{p_{\xi_2}}{Q_2},\tag{A1.12f}$$

$$\dot{p}_{\xi_k} = \left(\frac{p_{\xi_{k-1}}}{Q_{k-1}} - \mathrm{k_B}T_{\text{ext}}\right) - p_{\xi_k}\frac{p_{\xi_{k+1}}}{Q_{k+1}}\quad\text{for}\quad k = 2, \dots, M-1,\tag{A1.12g}$$

where $\boldsymbol{\Sigma}$ and $\boldsymbol{P}$ are defined as

$$\boldsymbol{\Sigma} = \boldsymbol{h}_0^{-1}(\boldsymbol{t} - I P_{\text{ext}})\boldsymbol{h}_0^{t-1},\tag{A1.13}$$

$$\boldsymbol{P} = \frac{1}{V}\left\{\frac{(\boldsymbol{p}_g)_\alpha (\boldsymbol{p}_g)_\beta}{m_j} + (\boldsymbol{f}_j)_\alpha (\boldsymbol{f}_j)_\beta - (V'\boldsymbol{h}^t)_{\alpha\beta}\right\},\tag{A1.14}$$

being $V' = \partial V(r_j, h)/\partial(h)_{\alpha\beta}$, t is the stress applied to the system [106], and I is the identity matrix. The above equations lead to non-Hamiltonian dynamics whose conserved quantity is [106]

$$H'_{NPT} = \sum_{j=1}^{N} \frac{p_j^2}{2m_j} + \frac{1}{W_g}\text{Tr}[p_g^t\, p_g] + \sum_{k=1}^{M} \frac{p_k^2}{2Q_k}$$

$$+P_{\text{ext}}\det[h] + \frac{1}{2}\text{Tr}[h_0^{-1}(t - IP_{\text{ext}})h_0^{t-1}G]$$

$$+V(r_j, h) + (N_f + d^2)k_B T_{\text{ext}}\xi_1 + \sum_{k=2}^{M} k_B T_{\text{ext}}\xi_k. \qquad (A1.15)$$

Here, W_g is the "piston mass" of the barostat [108, 110] that controls P, p_g is the modularly invariant form of the momenta of the cell α–by-β matrix h [106] (where the system's volume $V = \det[h]$ [105]), and $G = h^t\, h$ is the metric tensor. Note that the sixth term in the right-hand side of Eq. (A1.15) represents the elastic energy due to the external stress [106]. To eliminate the rotation of the cell matrix h [105] (i) the off-diagonal elements of the barostat cell momenta p_g should fulfill $(p_g)_{\alpha\beta} = (p_g)_{\beta\alpha}$, and (ii) the associated kinetic energy for the barostat $\{(p_g)_{\alpha\beta} + (p_g)_{\beta\alpha}\}^2/2W_g$ should be $k_B T_{\text{ext}}/2$ (not $k_B T_{\text{ext}}$) [106, 110]. The mass of the barostat should satisfy $W_g = (N_f + d)k_B T_{\text{ext}}/d\omega_g^2$ [105], where ω_g is the frequency at which atoms are barostated. In the present NPT simulations, ω_g is set to $1000\,\Delta t$ [105, 118].

The Jacobian J of the associated phase space, $\Gamma(r_j, p_j, \xi_1, \dots, \xi_M, p_{\xi_1}, \dots, p_{\xi_M}, h, p_g)_{NPT}$, is defined as [106]

$$J = \det[h]^{1-d}\, e^{[(N_f+d^2)\xi_1 + \sum_{k=2}^{M} \xi_k]}. \qquad (A1.16)$$

The EOM satisfy the canonical particle distribution as $J = 1$ [106]. This leads to the partition function [106]

$$Z_{NPT} \propto \int dh\, e^{-\beta H''_{NPT}} \det[h]^{1-d}, \qquad (A1.17)$$

where

$$H''_{NPT} = \sum_{j=1}^{N} \frac{p_j^2}{2m_j} + \frac{1}{2W_g}\text{Tr}[p_g^t\, p_g] + \sum_{k=1}^{M} \frac{p_k^2}{2Q_k} + V(r_j, h)$$

$$+P_{\text{ext}}\det[h] + \frac{1}{2}\text{Tr}[h_0^{-1}(t - IP_{\text{ext}})h_0^{t-1}G]. \qquad (A1.18)$$

A1.6. r-RESPA algorithm

The time-reversible operator $e^{i\mathcal{L}\Delta t}$ from Eq. (3.3) is integrated by means of the (reversible) *reference system propagator algorithm* (r-RESPA) [105]. Although there are available several choices for the factorization of $e^{i\mathcal{L}\Delta t}$ [105, 106], the present NVT and NPT simulations use the Trotter factorization of the Liouville operator defined by $i\mathcal{L} = i\mathcal{L}_1 + i\mathcal{L}_2 + i\mathcal{L}_{\text{bath}}$ [106]. Thus,

$$e^{i\mathcal{L}\Delta t} \approx e^{i\mathcal{L}_{\text{bath}}\frac{\Delta t}{2}}e^{i\mathcal{L}_2\frac{\Delta t}{2}}e^{i\mathcal{L}_1\Delta t}e^{i\mathcal{L}_2\frac{\Delta t}{2}}e^{i\mathcal{L}_{\text{bath}}\frac{\Delta t}{2}}, \tag{A1.19}$$

where

$$i\mathcal{L}_1 = \sum_{j=1}^{N}\left[\boldsymbol{v}_j + \boldsymbol{v}_{\text{g}}\boldsymbol{r}_j\right]\cdot\boldsymbol{\nabla}_{\boldsymbol{r}_j} + \sum_{\alpha,\beta}\left(\boldsymbol{v}_{\text{g}}\right)_{\alpha\beta}\frac{\partial}{\partial(\boldsymbol{h})_{\alpha\beta}}, \tag{A1.20a}$$

$$i\mathcal{L}_2 = \sum_{j=1}^{N}\left[\frac{\boldsymbol{f}_j}{m_j}\right]\cdot\boldsymbol{\nabla}_{\boldsymbol{v}_j}, \tag{A1.20b}$$

$$i\mathcal{L}_{\text{bath}} = \sum_{j=1}^{N}\left[-\left\{\boldsymbol{v}_{\text{g}} + \left(\frac{1}{N_{\text{f}}}\right)\text{Tr}\left[\boldsymbol{v}_{\text{g}}\right] + v_{\xi_1}\right\}\boldsymbol{v}_j\right]\cdot\boldsymbol{\nabla}_{\boldsymbol{v}_j}$$

$$+ \sum_{\alpha,\beta}\left\{\frac{1}{W_{\text{g}}}\left[\sum_{j=1}^{N}m_j\left(\boldsymbol{v}_j\right)_\alpha\left(\boldsymbol{v}_j\right)_\beta + \sum_{j=1}^{N}\left(\boldsymbol{f}_j\right)_\alpha\left(\boldsymbol{r}_j\right)_\beta - (V'\boldsymbol{h}^{\text{t}})_{\alpha\beta}\right.\right.$$

$$\left.+ \left(\frac{1}{N_f}\sum_{j=1}^{N}m_j\boldsymbol{v}_j^2 - P_{\text{ext}}V\right)\delta_{\alpha\beta} - [\boldsymbol{h}\boldsymbol{h}_0^{-1}(\boldsymbol{t} - \boldsymbol{I}P_{\text{ext}})\boldsymbol{h}_0^{t-1}\boldsymbol{h}^t]_{\alpha\beta}\right]$$

$$\left.- \boldsymbol{v}_{\xi_1}\left(\boldsymbol{v}_{\text{g}}\right)_{\alpha\beta}\right\}\frac{\partial}{\partial\left(\boldsymbol{v}_{\text{g}}\right)_{\alpha\beta}} + \sum_{k=1}^{M}v_{\xi_k}\frac{\partial}{\partial\xi_k}$$

$$+ \left[\frac{1}{Q_1}\left(\sum_{j=1}^{N}m_j\boldsymbol{v}_j^2 + W_{\text{g}}\text{Tr}\left[\boldsymbol{v}_{\text{g}}^t\boldsymbol{v}_{\text{g}}\right] - (N_{\text{f}} + d^2)\text{k}_{\text{B}}T_{\text{ext}}\right) - v_{\xi_1}v_{\xi_2}\right]\frac{\partial}{\partial v_{\xi_1}}$$

$$+ \sum_{k=2}^{M-1}\left[\frac{1}{Q_k}\left(Q_{k-1}v_{\xi_{k-1}} - \text{k}_{\text{B}}T_{\text{ext}}\right) - v_{\xi_k}v_{\xi_{k+1}}\right]\frac{\partial}{\partial v_{\xi_k}}$$

$$+ \frac{1}{Q_M}\left(Q_{M-1}v_{\xi_{M-1}}^2\right.$$

$$\left.- kT_{\text{ext}}\right)\frac{\partial}{\partial v_{\xi_M}}, \tag{A1.21c}$$

and $\boldsymbol{v}_j = \boldsymbol{p}_j/m_j \neq \boldsymbol{r}_j$, $\boldsymbol{v}_{\text{g}} = \boldsymbol{p}_{\text{g}}/W_{\text{g}}$, $v_{\xi_k} = p_{\xi_k}/Q_k$ [106]. Eq. (A1.19) carries the numerical error $\mathcal{O}(\Delta t^3)$ [105]. In the case of performing NVT dynamics, note that all the barostat terms in Eqs. (A1.21) vanish.
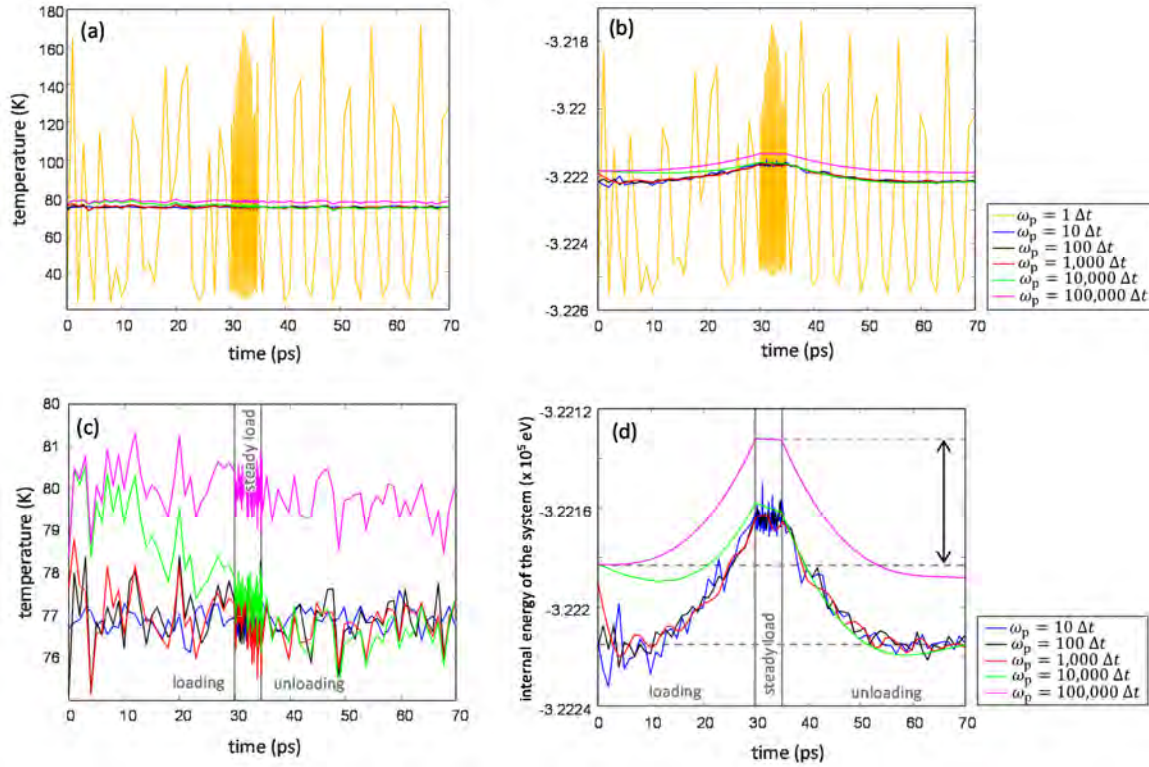
Figure A1.2. System's temperature (left-hand side pictures) and internal energy (right-hand side pictures) fluctuations during *NVT* molecular dynamics with different values of thermostat frequency ω_p. The above MD simulations comprise a 40,000-particle system subjected to loading, steady load, and (complete) unloading of an external force $F(x_j)$ similar to that from Eq. (A3.2) in Appendix A3. Timestep is set to 3 fs and thermostat temperature is $T_{ext} = 77$ K. The loading (and unloading) rate is set to 10 m/s. Double-headed arrow in (d) denotes the action of $F(x_j)$ into the system's energy during loading with $\omega_p = 100,000\,\Delta t$. Note that extremely large frequencies ($\omega_p = 100,000\,\Delta t$) lead to *NVE* dynamics due to a poor contribution from the thermostat. Fluctuations in both temperature and energy accentuate by decreasing ω_p. Low thermostat frequencies ($\omega_p < 10\,\Delta t$) lead to unrealistic dynamics with wild fluctuations around T_{ext} and system's internal energy, see the MD simulations with $\omega_p = 1\Delta t$ in (a) and (b).

APPENDIX A2. The statistical ensemble in the simulations of nanoindentation

Although MD simulations have been long used in the assessment and characterization of the inception and development of crystalline defects in metals subjected to nanoindentation testing [14, 37-39, 59, 102, 149, 170], it is apparently unclear in the open literature which type of particle ensemble [108] accounts for the most accurate statistical representation of indented crystals. Within this framework, the most widely employed statistical ensembles are the microcanonical NVE [37, 60, 102, 121, 171, 172], the canonical NVT [38, 117, 170], and the (canonical) isothermal-isobaric NPT ensembles [124, 173]. The above schemes ultimately describe distinct time evolutions of the system in the $\mathbf{\Gamma}$-space, which conceivably carries deep implications in the outcome of the MD simulations.

In order to shed light on this issue, a group of MD simulations is systematically carried out under the NVE, NVT and NPT statistical ensembles. To this end, the computational domains of size 70 nm (Table 3.1) constructed for both (001)-oriented Ta at 77 K and (111)-oriented Al at 300 K are indented with $D = 48$ nm at 4 m/s. The Hamiltonian EOM of the NVE ensemble (Appendix A1.3) are integrated by means of the velocity-Verlet algorithm described in Appendix A1.3, while the r-RESPA method (Appendix A1.6) is employed to integrate the non-Hamiltonian EOM of the NVT and NPT ensembles (Appendixes A1.4 and A1.5). In the following, a comparative study is presented on the effect of the statistical ensembles upon (i) the thermalization of the particle system, (ii) the elastic and plastic response, and (iii) the underlying mechanisms that govern defect nucleation and (later) incipient plasticity in the modeled nanoindentations. It is finally discussed that the most appropriate statistical approach for the time evolution of the indented crystals is the canonical NVT ensemble (over the NVE and NPT schemes).

The MD crystals are constructed in such a way that the constituent particles cover the computational volume according to their corresponding spatial distribution at ground state (Section 3.2.1). It could seem obvious that system's thermalization (Section 3.2.1) at finite temperature ($T > 0$ K) leads to unwanted built-up pressures on the periodic sides in the simulations (Fig. 3.3) with preserving-volume ensembles (i.e. NVT and NVE) as these conditions strictly restrict thermal expansion of the crystal [108]. In the context of the present nanoindentations, these ensembles may conceivably produce tougher indented surfaces due to these constriction effects. To investigate the magnitude of this possible computational artifact, a group of MD thermalization runs in (001)-oriented Ta boxes are performed at 300 K ($\approx 0.1 T_{\mathrm{m}}$) under the canonical NVT ensemble. These simulations evidence the onset of built-up pressures in the normal directions to the periodic sides which roughly match the pressures predicted by the linear model of thermal expansion, where $P = E \alpha_{\mathrm{T}} \Delta T$ [4] (α_{T} is the expansion coefficient and $\Delta T = T - 0$). However, it is noted that these pressures obtained due to the thermal expansion restriction in the present nanoindentations are much smaller ($< 2\%$) that those generated during nanoindentation loading.

The elastic response from the indented surfaces is analyzed by means of the Hertzian spherical contact which provides the analytical solution for the applied load, P, in terms of the penetration depth of the indenter tip, h_{s}, as [138]

$$P = \frac{4}{3} E^* \left(\frac{D}{2}\right)^{1/2} h_{\mathrm{s}}^{3/2}, \tag{A2.1}$$

where

$$\frac{1}{E^*} = \frac{1 - \nu^2}{E} + \frac{1 - \nu_{\text{ind}}^2}{E_{\text{ind}}}, \qquad\qquad (A2.2)$$

E^* stands for the *effective* indentation modulus [6], E and E_{ind} are respectively the elastic moduli for the sample and indenter, and ν and ν_{ind} are the Poisson's ratios for the sample and indenter, respectively. In this analysis, $E_{\text{ind}} = \infty$ and $\nu = 0.35$ are assumed.

The elastic $P - h_s$ curves obtained in the (001)-oriented Ta simulations under distinct statistical ensembles are given in Fig. A2.1(a). In the range of small deformations (i.e., $a/D \lesssim$ 0.1 [174]), the $P - h_s$ responses obtained in the MD simulations under the three ensembles are in good agreement with the predictions from complementary (anisotropic coarse-grained) finite element analyses (FEA) mimicking the present Ta nanocontact. At larger penetrations, the *NPT* simulations exhibit a mild softening in $P - h_s$ elastic response as compared to the $P - h_s$ curves from the *NVE* and *NVT* nanoindentations (Fig. A2.1(a)). This is a particular effect from the barostat defined in the *NPT* simulation, where the P_{xx} and P_{yy} components of the (internal) pressure tensor $\boldsymbol{P}$ (Eq. (3.9)) fluctuate around 0. As *NPT* simulations maintain pressure along the periodic boundaries of the cell, the atoms at the indented surface undergo "pressure relaxation" towards the periodic sides. This apparently leads to softer elastic contacts (with smaller E levels, see Fig. A2.2) than those obtained in non-barostated (*NVE* and *NVT*) indented crystals, see Fig. A2.1(b).

The simulations systematically show a mild increase in the Young's modulus, E, with increasing penetrations. This effect is denominated *pressure hardening* [37] and manifests the onset of non-linear elasticity. According to Fig. A2.2, pressure hardening issues are further enhanced under constant-V conditions as the present *NVE* and *NVT* indented domains depict an infinite group of attached identical crystals being concurrently indented. The effective value for E elucidated from the nanoindentations (Table 5.1) is systematically determined in the limit of small deformations (i.e., at $a/D \approx 0.1$ [174]), where the simulated nanocontacts with non-barostated (*NVT* and *NVE*) dynamics exhibit a reasonable elastic modulus (in comparison with the E obtained in Ta experiments [36, 38, 175].

While the onset of defect nucleation attains at similar critical load irrespective of the statistical ensemble in present Ta and Al simulations, differences are observed between the defects configurations developed in the subsequent nanocontact plasticity. In particular, the Ta indentations with the *NPT* and the *NVE* ensembles exhibit significant twin propagation thus hindering dislocation-loop emissions through detwinning processes [38]. A similar trend is found in the Al simulations. Although twin formation is limited in Al crystals limit due to their low stacking fault energy (Section 4.3.2), the Al indentations with the *NPT* ensemble exhibits marked twinning underneath the contact, see Fig. A2.4.

Figure A2.5 provides the evolution of temperature in the Ta indentations with thermostated (*NVT* and *NPT*) vs. non-thermostated (*NVE*) ensembles. It is systematically observed that the *NVE* simulations produce temperature increases in the onset of (irreversible) plastic events due the inception of crystalline defects. By contrast, the system temperature is controlled by the thermostat (Appendix A1.4) in *NVT* and *NPT* dynamics, which effectively reproduce the evolution of particle systems embedded inside a large reservoir at finite temperature (in the case of the Ta simulations of Fig. A2.5, at $T = 77$ K).

In accord with the above results, it is assumed here that the canonical *NVT* ensemble represents the most adequate statistical scheme for the present simulations of nanoindentation, as this approach provides realistic outcomes during nanocontact plasticity. In this context, the Hamiltonian NVE ensemble leads to arguably excessive crystal twinning during defect network development (Fig. A2.3). Moreover, the abrupt increases in temperature during plasticity (Fig.

A2.5) lead to the reduction in contact pressure with increasing penetration (see inset to Fig. A2.1(b)). On the other hand, the use of a barostat (Appendix A1.5) in the present indentations results in nanocontact softening (Fig. A2.1(a)), also favoring the onset of twinning processes (Figs. A2.3 and A2.4). It is finally noted that while the thermalization and subsequent indentation loading stages can be performed under different ensembles, the present computations are carried out under a fixed ensemble definition throughout the entire simulation.
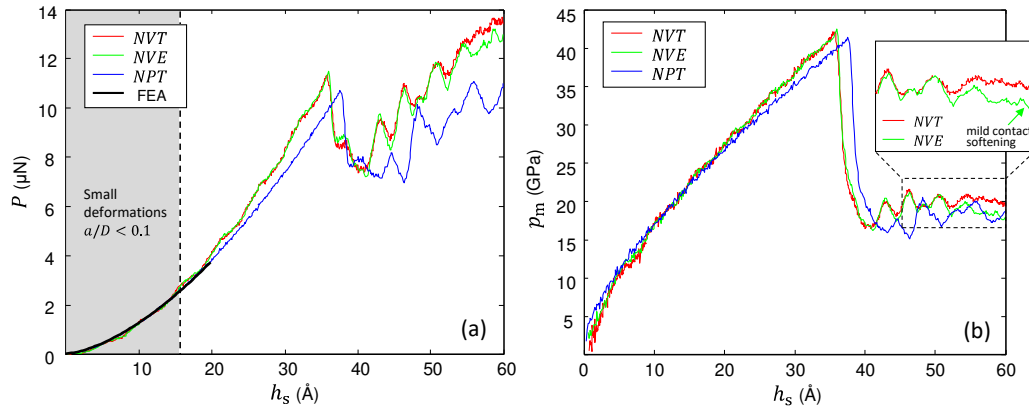

Figure A2.1. The Ta simulations under the *NVE*, *NVT* and *NPT* ensembles. (a) $P - h_s$ curves. (b) $p_m - h_s$ curves.
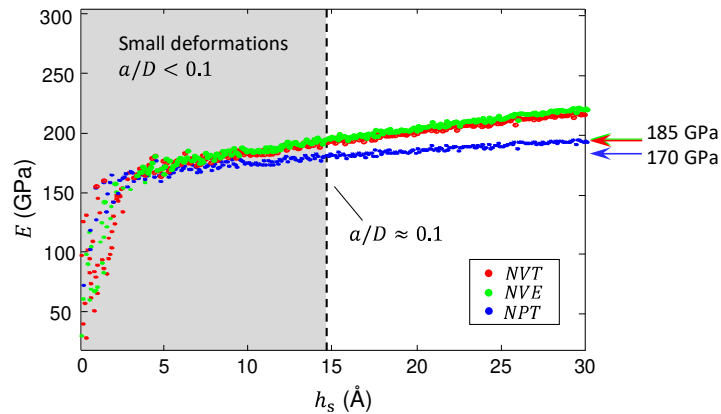
Figure A2.2. $E - h_s$ curves in the Ta simulations under the *NVE*, *NVT* and *NPT* ensembles. Computation of E at a given (P, h_s) point is performed by means of the Hertzian contact (Eq. (A2.1)).

117
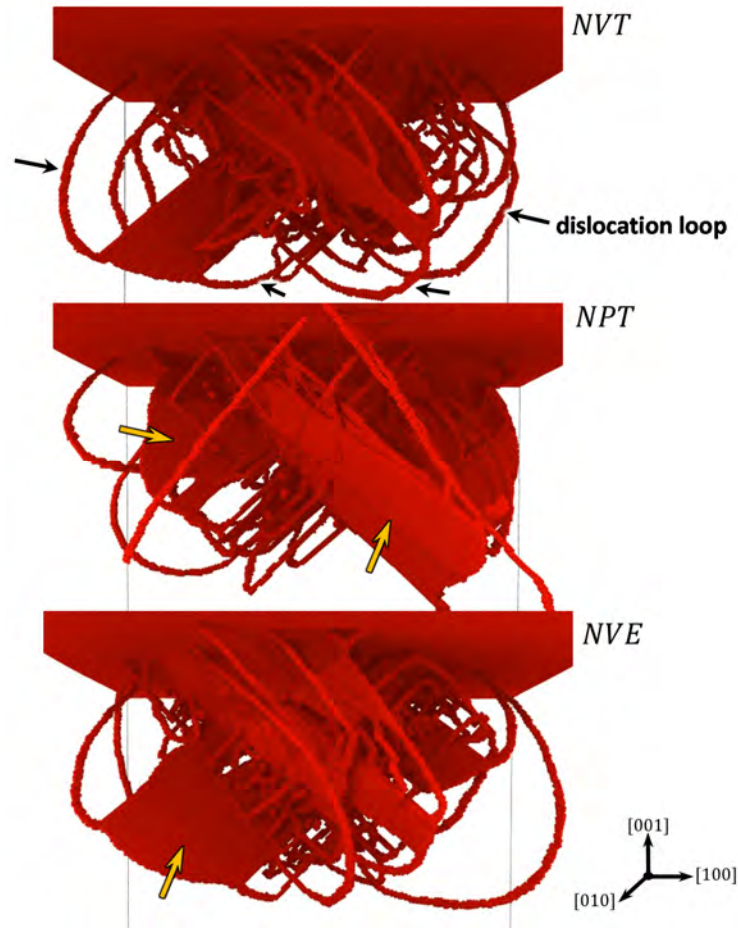
Figure A2.3. Defect structures in the Ta indentations with *NVE*, *NVT* and *NPT* ensembles. Black arrows mark detwinning loops [38] with the *NVT* ensemble. Yellow arrows denote twin-walls expansion under the *NPT* and *NVE* simulations. The above defect networks are obtained at maximum indenter penetration, $h_s \approx 60$ Å. Atomistic visualization is performed in OVITO, see Appendix A6.
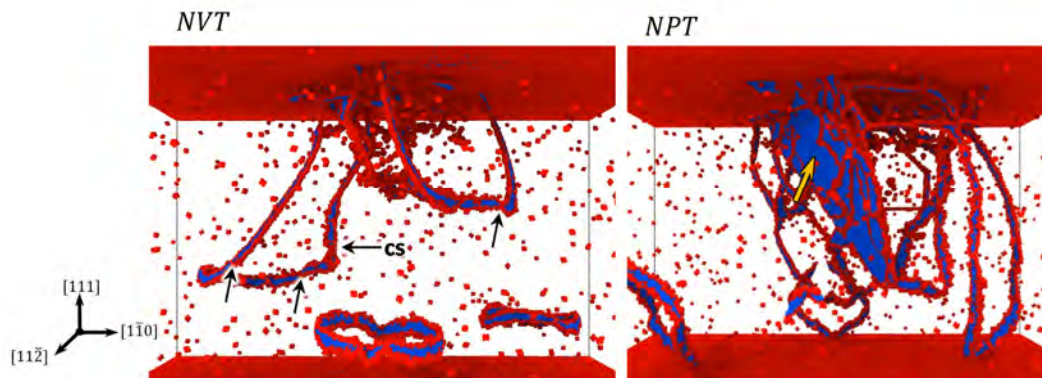
Figure A2.4. Defect structures in the Al simulations under the *NVT* and *NPT* ensembles. Cross-slip is marked "cs" (black arrows). The yellow arrow denotes twinning in the *NPT* simulation. The defect networks are obtained at indenter penetrations of $h_s \approx 30$ Å. Atomistic visualization is performed in OVITO, see Appendix A6.
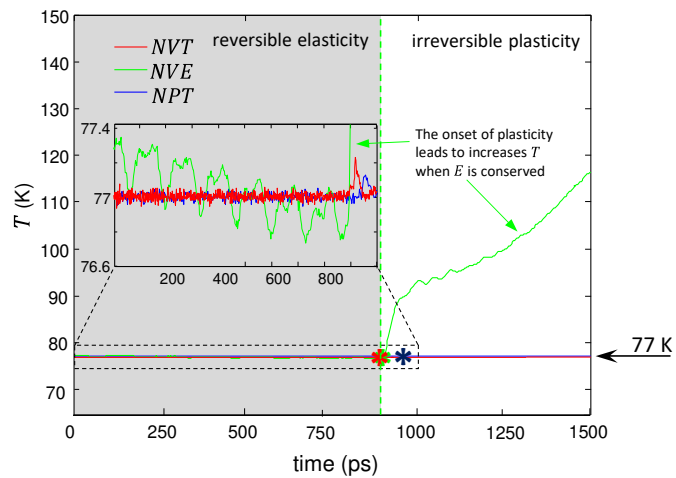
Figure A2.5. Temperature-time evolution in the Ta simulations with *NVE*, *NVT* and *NPT* ensembles. Temperature is computed by means of the equipartition theorem [118] where N is assumed to be large [104], so that the kinetic energy $K = 3/2(N k_B T)$ is computed as $K = \sum_{j=1}^{N}(p_j^2/2m_j)$ [57]. Stars (*) indicate the onset of plasticity. The inset illustrates the evolution of temperature during elasticity with non-thermostated (*NVE*) vs. thermostated (*NVT* and *NPT*) dynamics. Elasticity and plasticity are marked for the *NVE* simulation (green line).

APPENDIX A3. Model for the indenter

The repulsive spherical indenter is modeled with the potential

$$V(x_j) = \frac{K}{3} x_j^3 , \tag{A3.1}$$

where K is the indenter stiffness, $x_j = (D/2 - \delta_j)$ represents the effective penetration of atom j inside the spherical potential $V(x_j)$, D is the indenter diameter, and $\delta_j = r_j - r_c$ is the distance from atom j (described by $r_j = (x_j, y_j, z_j)$) to the center of the repulsive sphere ($r_c = (x_c, y_c, z_c)$), see Fig. A3.1(a).

Atoms that fulfill $\delta_j < D/2$ (then $V(x_j) > 0$) are taken to become *in-contact*. In accord with Ref. [59], the use of the above potential leads to realistic displacement fields generated by a spherical indenter tip against a (free) surface. The force applied to each surface atom j satisfying $\delta_j < D/2$ is defined as $F_j(x_j) = -dV(x_j)/dx_j$, where

$$F_j = -K \left(\frac{D}{2} - \delta_j \right)^2 . \tag{A3.2}$$

Note in the above equation that F_j is directed from the center of the repulsive sphere (that is the direction of δ_j, see Fig. A3.1(a)). To illustrate the action of $V(x_j)$ on in-contact atoms j, it is drawn in Fig. A3.1(a) the trajectory of one atom which happens to enter into a *steady* repulsive potential (Eq. (A3.1)). The atom trajectory inside the potential is curved by the additional contribution of force F_j repelling atom j. According to Fig. A3.1(a), the utmost penetration of atom j inside the potential, h_j, can be defined as $h_j \propto f K^{-1}$, where f is a function of $f(m_j, \alpha_j^{(i)}, v_j^{(i)}, D, \beta_j^{(t)})$. Notice in this figure that the system's energy is strictly conserved upon the complete repulsion of atom j due to momentum conservation $(d(\sum p_j)/dt = 0)$ as $v_j^{(i)} = v_j^{(f)}$. By contrast, the action of the *mobile* repulsive potential against the surface (such is the case of indenter loading) essentially produces an increase in the internal energy (Fig. A3.2(b)) as positive work is done onto the system (note that $v_j^{(i)} < v_j^{(f)}$ and therefore $d(\sum p_j)/dt \neq 0$, see Fig. A3.1(b)).

An adequate choice of parameter K is crucial in the computation of realistic displacements for the in-contact atoms during indentation loading. In this context, large values of K may give rise to unrealistic atom trajectories characterized by a small magnitude of h_j (Fig. A3.2(a)), while low values of K may produce a poor effect from the potential as in-contact atoms spend excessive time inside the indenter due to mild repulsion forces. Figure A3.2(a) shows the early elastic responses produced by a wide range of K values, where the (001)-oriented Ta surface is probed with $K = 0.1 - 100,000$ eV/Å^3. It is noticed in Fig. A3.2(a) that the physically realistic range of K values is broad as all the elastic responses with $K = 10$ eV/Å$^3 - 1,000$ eV/Å^3 are in good agreement with the $P - h_s$ curve from complementary coarse-grained finite element analyses (FEA). Increasing computational fluctuations in the $P - h_s$ curve arise with values of $K > 1,000$ eV/Å^3, while soft elastic responses attain with $K < 10$ eV/Å^3 where the magnitude of the Young's modulus is underestimated.

In light of the above results, parameter K is set to 100 eV/Å^3 in all of the MD nanoindentations (Section 3.2.2). Moreover, the contribution from the potential $V(x_j)$ (Eq.

(A3.1)) is included in the internal energy (Fig. A3.2(b)). This adds function $V(x_j)$ function to the quantity being conserved during the dynamics, see Appendix A1.
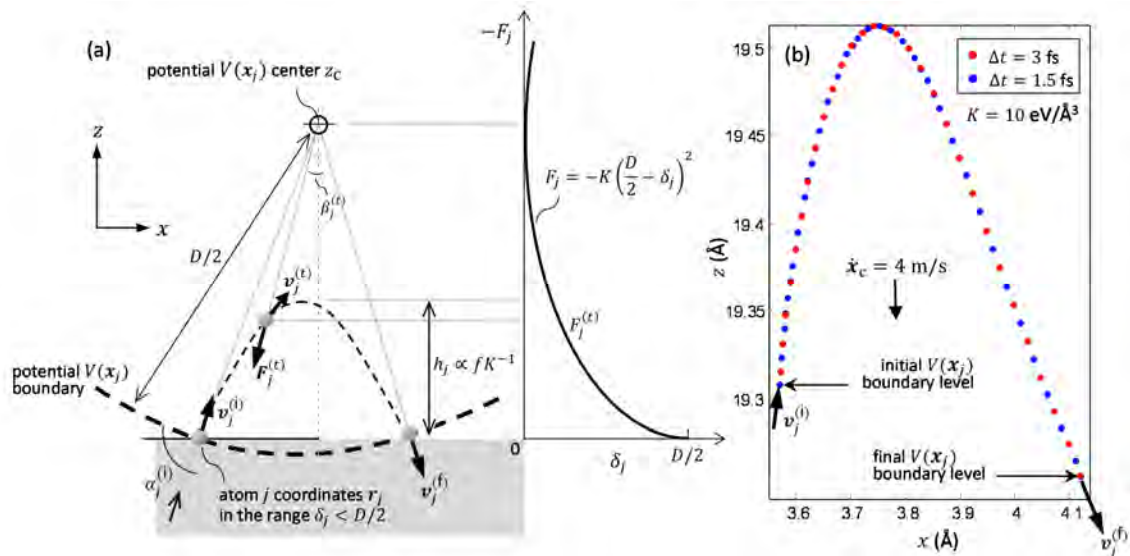
Figure A3.1. Trajectory of in-contact atoms inside the repulsive potential $V(x_j)$. (a) Illustration of the trajectory that atom j describes inside steady potential $V(x_j)$. The right-hand inset displays the exerted force magnitude ($F_j(x_j) = -dV(x_j)/dx_j$) to atom j as a function of δ_j. (b) The computed trajectories inside a mobile $V(x_j)$ show an affordable convergence for $\Delta t < 5$ fs (for the sake of visualization, it is only drawn the trajectories obtained with $\Delta t = 3$ fs and $\Delta t = 1.5$ fs). These results emphasize that the employed timestep in the present nanoindentations (i.e., $\Delta t = 3$ fs, see Section 3.2.2) leads to a realistic discretization of the atom-indenter interaction.
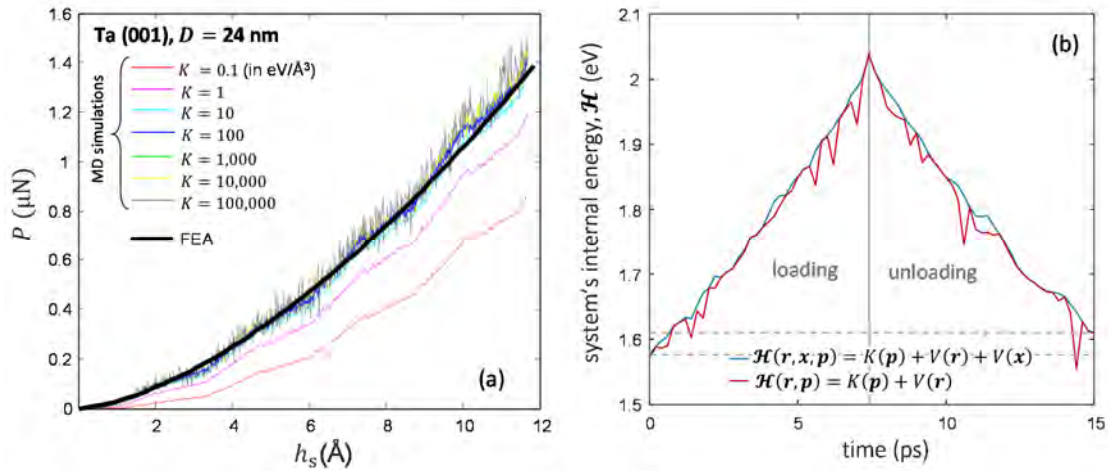
Figure A3.2. (a) $P - h_s$ responses in early elasticity from Ta (001) indentations (Section 3.2.2) with $D = 24$ nm under a wide range of K values. (b) The variation of the internal energy ($\mathcal{H}$) during a loading/unloading cycle with a repulsive indenter of $D = 0.5$ nm. The computational domain comprises a small NVT system of $\approx$100 atoms. It is observed that by including the potential $V(x)$ on the system's energy [118], so that $\mathcal{H}(r, x, p) = K(p) + V(r) + V(x)$, fluctuations in $\mathcal{H}$ are reduced, where $K(p) = p^2/2m$ is the kinetic energy and $V(r)$ is the potential energy from the interatomic potential (Section 3.2.1).

APPENDIX A4. Contact area computations

An important part of the analysis performed in this investigation relies on a correct estimation of the *projected* contact area $A = \pi a^2$ during indenter-tip loading, where a is the contact radius (Figs. A4.1(a) and A4.1(b)). In particular, the contact parameter $\overline{c^2}$ (from Section 4.3.1) defined by the ratio between the contact depth h_c and indenter-tip depth h_s, $\overline{c^2} = h_c/h_s$, is given by

$$c^2 = \frac{1}{h_s}\left(\frac{D}{2} - \left(\frac{D^2}{4} - a^2\right)^{\frac{1}{2}}\right). \tag{A4.1}$$

where D the indenter-tip diameter. In addition, the center of the discussion in Chapter 5 concerns the evaluation of the hardness levels, $p_m = P/A$, obtained in the MD nanoindentations, where P is the applied force by the indenter tip. It is thus clear that good estimations of the contact area, A, become crucial for the accuracy of the results reported from the MD nanoindentations.
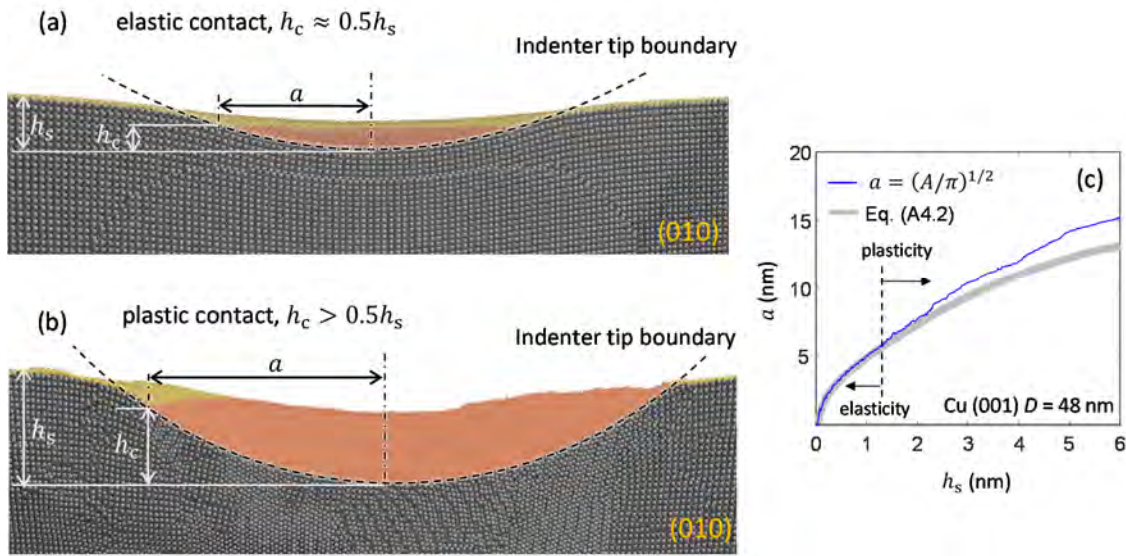
Figure A4.1. (a) and (b) display the elastic and plastic nanocontacts (respectively) in a (001)-oriented Ta at $h_s \approx 15$ Å and $h_s \approx 45$ Å, respectively. The indenter has $D = 48$ nm and both pictures are taken for a (010)-cross sectional cut located at the contact center. The colored atoms (in red and yellow) mark surface atoms, where the reddish atoms denote the in-contact atoms with the indenter tip (Appendix A3). (c) $a - h_s$ curve from the Cu (001) indentation with $D = 48$ nm. Note that the values of a obtained from the DT computations ($a = \sqrt{A/\pi}$) differ from those determined by Eq. (A4.2) during the plastic contact, where an analytical solution for a as a function of h_s is unavailable.

In accord with elastic contact mechanics [138], where $h_c/h_s = 0.5$ and a is defined as $a = (D\,h_c - h_c^2)^{1/2}$, the contact radius follows

$$a = \frac{h_s}{2}\left(\frac{2D}{h_s} - 1\right)^{1/2}. \tag{A4.2}$$

Figure A4.1(c) displays the $a - h_s$ evolution in the Cu (001) indentation with $D = 48$ nm. Note in this figure that the analytical solution for a of Eq. (A4.2) fails in reproduction the contact response beyond the elastic limit due to the onset of pile-up effects [9] (where $h_c/h_s > 0.5$), compare Fig. A4.1(a) with Fig. A4.1(b).

In this work, an in-house algorithm is used, which computes the set of the in-contact atom coordinates that define the contact area, see Figs. A4.1(a) and A4.1(b), where the particles colored in red represent the *in-contact* atoms. The criterion that enables detection of in-contact atoms is described in Appendix A3. In order to transform the in-contact atom coordinates into the effective value of A, the (two-dimensional) Delaunay triangulation (DT) algorithm is employed [176]. The DT identifies among all possible triangulations of a given set of 2-D points, the triangulation which maximizes the *minimum* angle [176], see Fig. A4.2(a). Thus, the DT of the set of in-contact atoms partitionates the projected contact area into little Delaunay triangles satisfying the Delaunay criterion (Fig. A4.3(a)) [176]. The value of A is the sum of all the areas of the above Delaunay triangles. Figures A4.2(b)-(d) show the set of the detected 2-D points (*in-contact* atoms coordinates) in Ta and Cu nanoindentations with $D = 48$ nm.
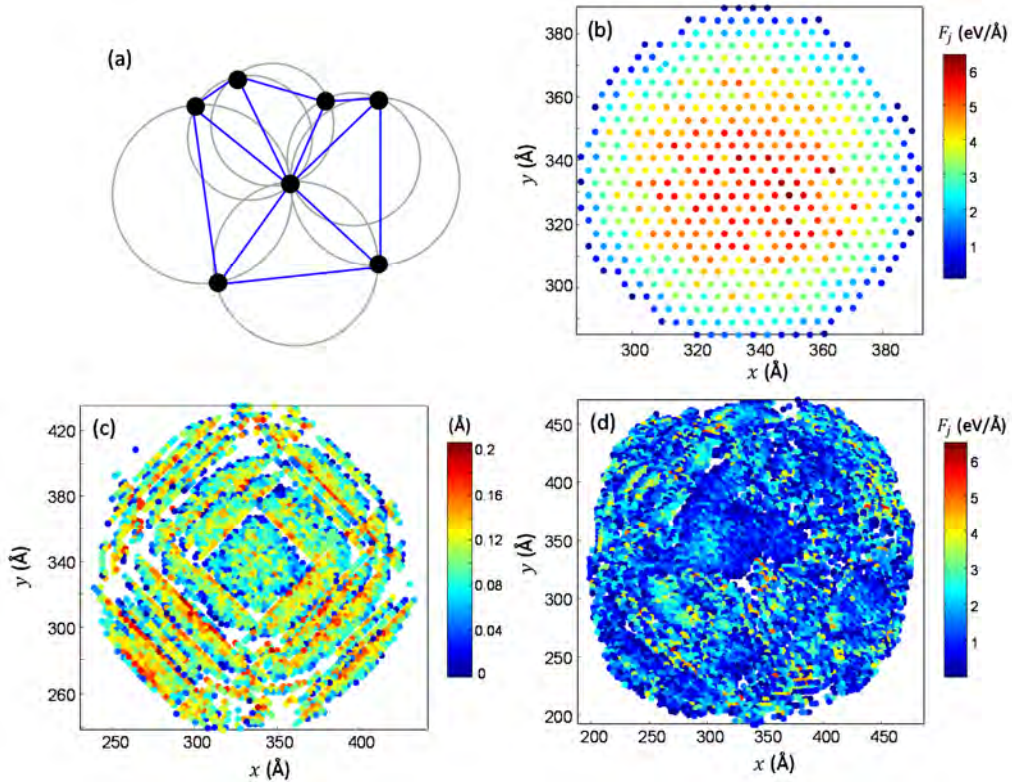
Figure A4.2. (a) DT of the black points. Such a triangulation (in blue) ensures that the circumcircle associated with each circle (in grey) contains the tree points forming the Delaunay triangles for all the given set of points (Delaunay criterion [176]). The in-contact atom coordinates that define the contact area in the indented Ta surfaces from Figs. A4.1(a) and A4.1(b) are given in (b) and (d), respectively. The colors express the magnitude of the exerted force F_j to every in-contact atom j (see Appendix A3). (c) In-contact atoms describing the contact area in the Cu (001) indentation ($D = 48$ nm, 77 K) at $h_s \approx 22$ Å . The colors show the value of the penetration level of the in-contact atoms.

Finally, Fig. A4.3 illustrates the evolutions of the projected contact area with increasing penetration in Ta and Cu indentations with $D = 48$ nm. Note that the contact area calculations using the above algorithm generate $A - h_s$ curves that effectively capture the transition from elasticity to plasticity, where abrupt increases in A are a clear indication of the defect nucleation at the pop-in event. Moreover, note that the onset of different slopes in both elasticity (m_{el}) and plasticity (m_{pl}), where $m_{pl} > m_{el}$ (Fig. A4.3).
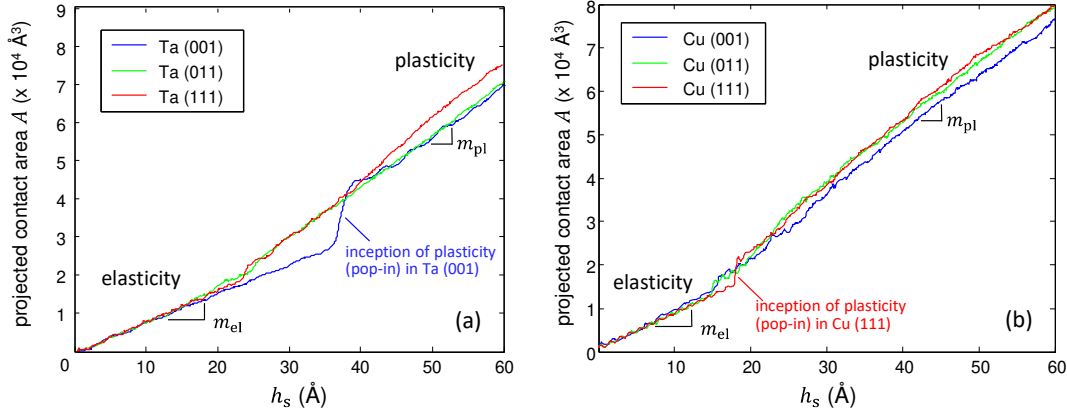
Figure A4.3. $A - h_s$ evolutions obtained in the Ta and Cu indentations with $D = 48$ nm at 77 K.

APPENDIX A5. The effect of the driving rate in the MD simulations

A5.1. Loading-rate sensitivity in the simulations of indentation

To study the effect of the indentation rate on the contact response, a group of identical Ta nanoindentations at 77 K is carried out under a wide range of loading rates (i.e., from 4 m/s to 1,000 m/s). The computational domain consists of a repulsive spherical indenter with $D = 6$ nm (Appendix A3), and a (001)-oriented $1.8D \times 1.8D \times D$ cuboid that contains $\approx 40,000$ atoms (Section 3.2.2). The Ta surface is systematically subjected to a full loading/unloading cycle (with constant loading/unloading rate) characterized by a maximum indenter penetration of $\approx$ 2.5 Å. It is assumed that this contact regime, distinguished by such small penetrations ($a/D <$ 0.1 [174]), ensures the onset of *continuum-like* elasticity following Eq. (A2.1).

The results reveal that the Ta nanoindentations performed under extreme loading rates (say > 100 m/s) exhibit the onset of undulations in the applied load (P)- indenter-tip penetration (h_s) curves, see Fig. A5.1(a). The simulations indicate that such $P - h_s$ curves describe an *impact* process rather than a *quasi-static* elastic contact [138]. Figure A5.2 illustrates the (numerical) origin of these findings at extreme loading rates. Consider a surface atom j (Fig A5.2(a)) entering the repulsive potential that models the indenter (Appendix A3). In successive computations of the trajectory of central atom j inside the indenter, this atom undergoes an increasingly marked repulsion (characterized by F_j, see Figs. A5.2(b) and A5.2(c)) due to the large penetration velocity of the indenter, so that the contact surface (denoted by the vertical component (z_j) of highest atom j in Figs. A5.2(a)-(d)) develops an abrupt upward displacement due to the repelled (or propelled) atom j (Fig. A5.2(e)). The response of the repelled/bouncing atoms from/into the penetrating indenter leads to these undulations in the $P - h_s$ curves (Fig. A5.1(a)), where the inflexion points (marked in black in Fig. A5.2(h)) arguably capture the above bouncing effect.

Finally, an elastic response is attained at slower indentation loading (say < 50 m/s). Although the numerical fluctuations encountered in the MD simulations lead to wavy $P - h_s$ evolutions (Fig. A5.2(b)), the in-contact atoms produce a $P - h_s$ response that fully satisfies the Hertzian spherical contact model (Eq. (A2.1)) [138]. The onset of elasticity becomes manifest in the *reversibility* of the $P - h_s$ curves [138] as the nanocontacts systematically follow identical $P - h_s$ paths during both loading and unloading, see the inset to Fig. A5.1(b). The simulations show a crossover of impact and elastic responses in the nanoindentations performed at 50 m/s, where although some undulations are certainly present in the $P - h_s$ curves, the overall contact response tentatively adheres to linear elastic contact mechanics analyses, see Fig. A5.1(b).

As a final remark, MD simulations of nanoindentation are usually performed with loading rates (in m/s) [21, 37, 38, 122] that are of some orders of magnitude larger than those normally employed in nanoindentation experiments (in μm/s) [122]. While such experimental indentation rates are ultimately unfeasible with MD simulations under the current computational power, the MD results reported elsewhere in Refs. [21, 38, 122] in conjunction with the present nanoindentations (Section 5.2) reveal that the *mechanisms* at the inception of plasticity (defect nucleation) in cubic crystals remain unaffected with loading rates varying from ≈ 0.04 m/s to ≈ 30 m/s.
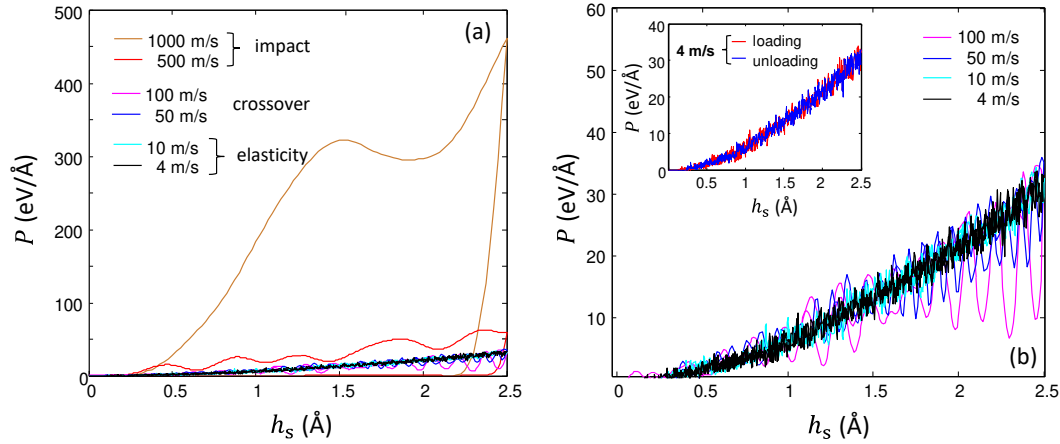
Figure A5.1. $P - h_s$ curves from the Ta (001) indentations with $D = 6$ nm under different loading rates.
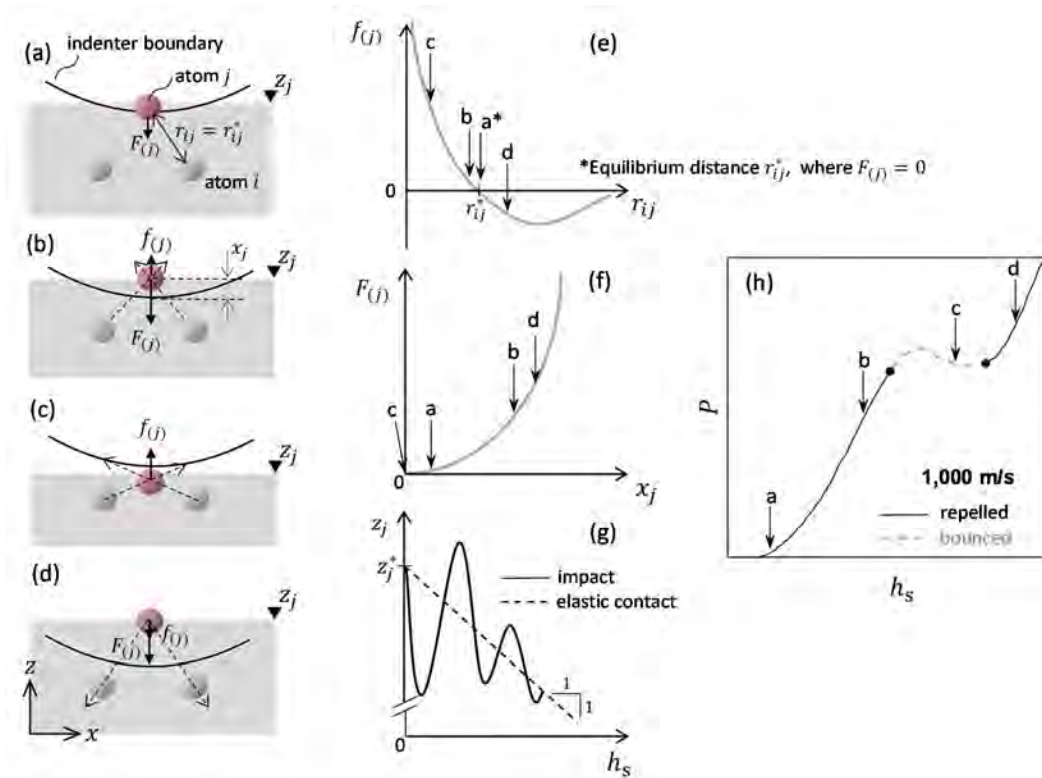
Figure A5.2. Illustration of the origin of loading rate effects on the $P - h_s$ curves in present MD simulations. (a)-(d): Schematic of the dynamics of atom j interacting with a penetrating indenter with large loading velocity. (e) The force field from the ij interaction (interatomic potential, Section 3.2.1) acting in atom j, where $f_j = -dV_j(r_{ij})/dr_{ij}$. (f) The exerted force on atom j from the indenter, $F_j = -Kx_j^2$ (Appendix A3). (g) Evolution of the surface level z_j (of central atom j) with increasing penetration h_s, where z_j^* is the surface level prior indentation. Note that undulated $z_j - h_s$ curves mark the onset of the bouncing effect of the impacted surface in present MD simulations. (h) The wavy $P - h_s$ curve obtained at $1,000$ m/s illustrates the onset of an impact curve characterized by extreme values of applied load due to the repelled/bouncing of atoms. See the text for further details.

126

A5.2. Strain-rate sensitivity in the simulations of uniaxial test

In this work, the MD simulations of the tensile test aim to reproduce the emissions of dislocation avalanche events attained in micropillar compression experiments [34, 42, 54]. The computational procedure employed in these simulations is described in Section 3.2.3. To investigate the effect of the loading rate (in this case, the strain rate) upon the plastic response in terms of the stress-strain curves, uniaxial stretching is performed along the [011] orientation (Fig. 3.4(c)) in a periodic Al crystal containing a largely-entangled dislocation network (Fig. A5.3(a)) throughout a wide range of stretching rates (i.e., from $\approx$100 m/s to $\approx$0.1 m/s) see Table 3.5.

The simulations carried out for stretching rates < 10 m/s (or, equivalently, at $\dot{\varepsilon} < 1.5 \times 10^8$ s^{-1}) lead to serrated stress-strain curves (Fig. A5.4), evidencing intermittent behavior of plasticity as the dislocation network essentially develops through (discrete) avalanche events, see the inset (c.1) in Fig. A5.3. With sufficiently slow deformation rates, slow driving [47, 54] is attained for ≈ 0.1 m/s ($\dot{\varepsilon} = 1.5 \times 10^6$ s^{-1}) in present MD simulations, where the inception of dislocation avalanches is finally characterized by stress drops $\Delta\sigma$ at fixed strain [50, 166] so that the plastic burst are not overlapped [43], see the inset to Fig. A5.4. It is remarked that the strain rate employed in the present simulations ($\dot{\varepsilon} = 1.5 \times 10^6$ s^{-1}), Section 6.4, is about two orders of magnitude smaller than that those recently reported in similar MD studies [125, 157, 177, 178].

Interestingly, the Al simulations under larger stretching rates (>10 m/s) evidence the onset of a completely different plastic behavior distinguished in that the dislocation network develops homogeneously with increasing straining (note in the inset (b.1) in Fig. A5.3 that $d\rho/d\varepsilon > 0$), which hinders the above emission of avalanche events [125, 177]. This is particularly clear in the Al simulation with ≈ 100 m/s, where recursive (non-discrete) heterogeneous defect nucleations govern the plastic deformation (beyond σ_y), see Fig. A5.3(b). This specific plastic response attains as the dislocation configuration (Fig. A5.3(a)) is arguably unable to adjust to the rapid deformation of the computational domain through the onset of intermittent avalanche processes.

Thus, the Al simulations show that the fundamental intermittent character of crystal plasticity (characterized by the inception of collective dislocation glide processes, in the form of avalanches [42, 43]) is observed when $\dot{\varepsilon} < 1.5 \times 10^8$ s^{-1}. The size of the distinctive $\Delta\sigma$ associated with such avalanches in the stress-strain curves (Fig. A5.4) rapidly decreases with increasing strain rate to a point where plasticity becomes a continuous phenomenon as the onset of quiescent periods between avalanches is hindered. These simulations also mark the attainment of a transition in dislocation-mediated plasticity from "quasi-stastic" loading to impact loading conditions.
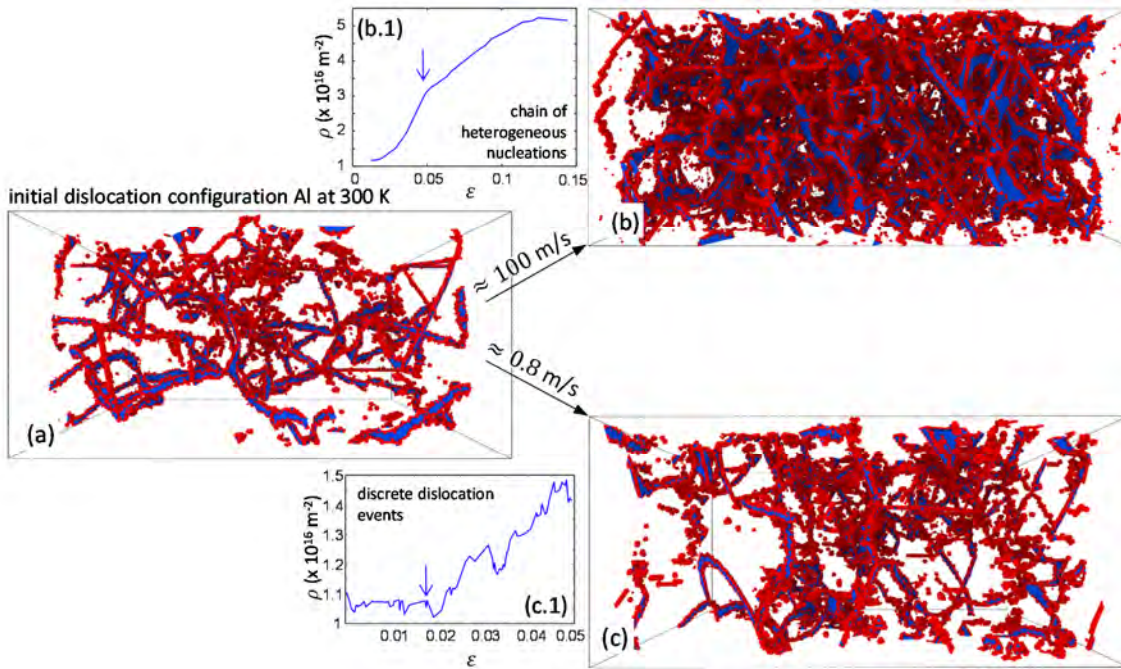
Figure A5.3. Development of the dislocation network in Al [011] as a function of the stretching rate. (a) The initial dislocation configuration characterized by $\rho \approx 1.1 \times 10^{16}$ m^{-2}. (b) Dislocation arrangement obtained at $\varepsilon \approx 0.1$ under ≈ 100 m/s. The inset (c.1) shows the corresponding $\rho - \varepsilon$ evolution at ≈ 100 m/s, where heterogeneous defect nucleations govern plasticity. (c) Dislocation arrangement obtained at $\varepsilon \approx 0.04$ under ≈ 0.8 m/s. The inset (c.1) shows the corresponding $\rho - \varepsilon$ evolution at ≈ 0.8 m/s, where discrete plastic events (avalanches) govern the development of intermittent plasticity. The blue arrow in the $\rho - \varepsilon$ curves marks inception of plasticity.
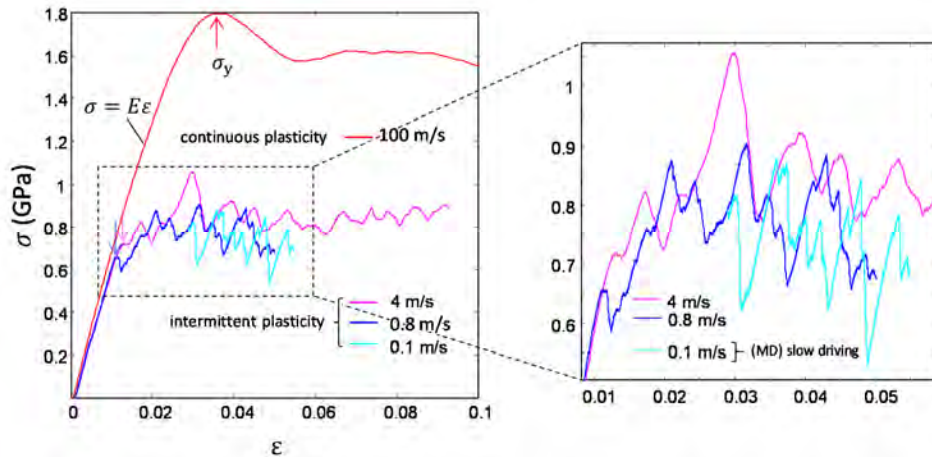
Figure A5.4. $\sigma - \varepsilon$ curves for tensile tests in Al [011] at 300 K under different stretching rates. The onset of intermittent plasticity tentatively emerges at stretching rates < 10 m/s, while larger stretching rates produce a continuous (non-discrete) development of plasticity. Arrows in the left-hand side figure mark the inception of plasticity passed the yield stress, σ_y.

APPENDIX A6. The atomistic visualization of the MD simulations

An MD simulation of 10×10^6 atoms may produce over 500×10^6 bytes of output data (coordinates and velocities of constituent atoms) at every computational step [56]. In one million timesteps, the total amount of data can exceed 5×10^{14} bytes (500 terabytes) [56]. This enormous amount of data is quite useless in such a raw form, therefore dumping atom positions at every simulation step is unusual. Processing and reduction of the raw data [56]) are necessary to make the MD simulation less time consuming [108]. Therefore, in the MD simulations performed in this investigation, file dumping is performed every 1,000-10,000 computational steps.

In present simulations, it is also required to find crystalline defects and how atoms are arranged around them, where atoms away from defects are usually much less interesting [56]. For this purpose, the common neighbor analysis (CNA) [129] is employed to calculate the local crystalline structure around the constituent atoms [56]. This algorithm is based on nearest-neighbor computations that encodes the bond connectivity between a given central atom with its closest atoms [129, 179]. The cut-off radius parameter r_{coff} then classifies atom pairs so that particles closer to each other than r_{coff} are considered to be bonded [56]. Under this framework, the CNA computation specifies the type of crystalline coordination (BCC, FCC, HCP, or "unknown") by using the following cut-off distances [118];

$$r_{coff}^{FCC} = \frac{1}{2}\left(\frac{\sqrt{2}}{2} + 1\right)a_o \approx 0.8536 a_o \,, \tag{A6.1a}$$

$$r_{coff}^{BCC} = \frac{1}{2}\left(\sqrt{2} + 1\right)a_o \approx 1.207 a_o \,, \tag{A6.1b}$$

$$r_{coff}^{HCP} = \frac{1}{2}\left(1 + \sqrt{\frac{4 + 2x_o^2}{3}}\right)a_o \,, \tag{A6.1c}$$

where a_o is the lattice constant for BCC and FCC crystals, a_o and c_o are the shortest and longest lattice constants for HCP crystals respectively, and $x_o = c_o/1.633 a_o$. The CNA algorithm usually classifies the atoms around crystalline defects with "unknown" coordination as the associated r_{coff} does not correspond to any of those from above.

In this investigation, atomistic visualization is performed by means of the Open Visualization Tool (OVITO) software [179] which enables the representation of single-point particles (atoms) whose positions are given in the dumped (output) files from the simulations. The OVITO package contains an extensive list of advanced atomistic analyses such as the CNA and dislocation analyses (by DXA [180], see Appendix A8). Figures A6.1(a) and A6.1(b) provide two snapshots obtained from the Ta (001) nanoindentation at 77 K. The visualization scheme is based on the coloring of the CNA computation (Eqs. (A6.1)) for every atom. In the case of the BCC simulations, coordinated (BCC) atoms are colored in blue (or are made invisible Fig. A6.1(a)) and uncoordinated atoms are colored in red. Likewise, Figs. A6.1(c) and A6.1(d) show a snapshot from the nanoindentation of (001)-oriented Cu. In the FCC simulations, the pale-blue atoms have the FCC coordination (invisible in Fig. A6.1(c)), the red atoms are uncoordinated, and the blue atoms have HCP coordination.
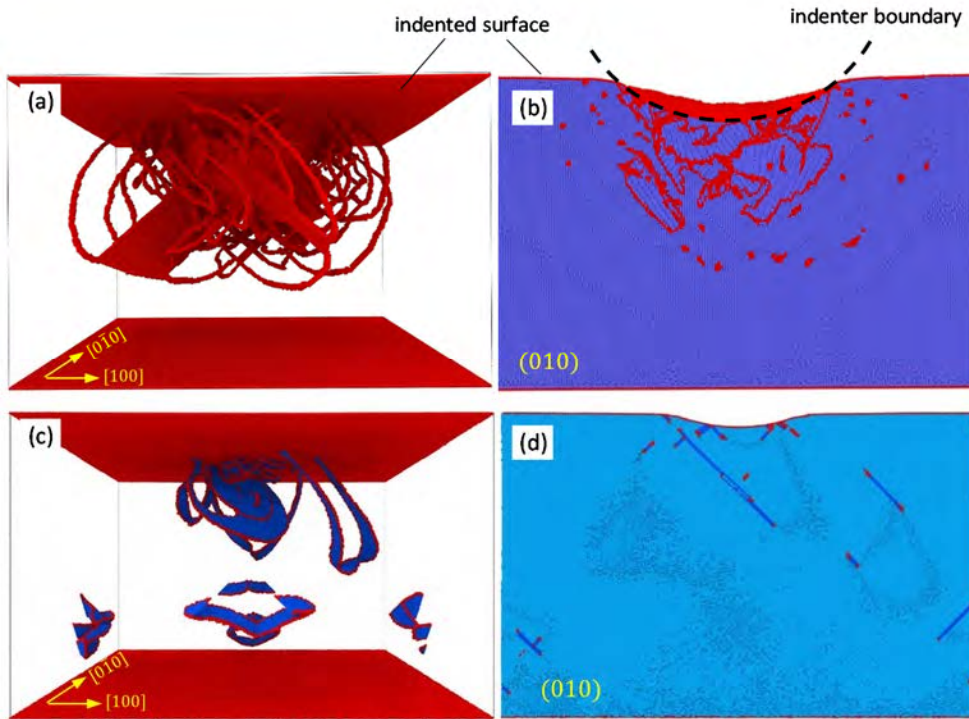
Figure A6.1. Snapshots from the (001) indentations with $D = 48$ nm at 77 K as visualized in OVITO [179]. (a)-(b): Ta at $h_s \approx 40$ Å, (c)-(d): Cu at $h_s \approx 18$ Å. The left-hand side figures show the inception of crystalline defects below the indenters, where coordinated atoms are made invisible. The right-hand side figures display the computational domains with a (010) cross-sectional cut located at the contact center.

APPENDIX A7. Dislocation avalanche analysis

A7.1. Assessment of the slip magnitures during avalanching

The emission of dislocation avalanches is detected through the stress drops in the stress (σ)−strain (ε) curves (Figs. A7.1(a) and A7.1(b)), where a single stress drop, $\Delta\sigma$, is given by $\Delta\sigma = \sigma_{max} - \sigma_{min}$, see inset to Fig. A7.1(a). When a stress drop $\Delta\sigma$ attains at relatively $\Delta\varepsilon \approx 0$, the accumulated uniaxial *plastic* strain due to avalanche slip (Fig. 6.1(a)) becomes equal to the elastic strain relaxed in the sample as the crystals unloads from $\sigma = \sigma_{max}$ to $= \sigma_{min}$ [166]. Under the assumption that the uniaxial displacement $\Delta u = s \cdot M$, where M is the Schmid factor and s is the slip size which equals the *elastic relaxation* of the sample [34, 50], Δu is related with the corresponding stress drop $\Delta\sigma$ through [34, 50]

$$\frac{\Delta\sigma}{E} = \Delta\varepsilon = \frac{\Delta u}{l} = \frac{s \cdot M}{l} \ , \tag{A7.1}$$

where l is the sample length, see Fig. 6.1(a). Thus, the avalanche slip size follows

$$s = \frac{\Delta\sigma \cdot l}{M \cdot E} \ , \tag{A7.2}$$

as defined in Eq. (6.2).

Since avalanche propagation develops over a certain time interval [50], the externally applied strain rate is assumed to be sufficiently small so as to neglect attainment of any additional uniaxial strain $\Delta\varepsilon$ (see Fig. A7.1(a)) during the avalanche events, which satisfies the conditions of slow driving [34, 54]. The effect of the applied strain rate on the onset of specific plastic responses in present MD simulations are discussed in Appendix A5.2.

A7.2. Avalanche size probability distributions

The probability density function (PDF) describing the slip size distributions, $P(s)$, follows a power-law relation of the form $P(s) \propto 1/s^\lambda$ [47, 154], formally

$$P(s) = \frac{1}{A} s^{-\lambda} \ . \tag{A7.3}$$

Here, A is the factor that normalizes $P(s)$ as $\int_{s_{min}}^{\infty} P(s)ds = 1$ [107], hence

$$A = \int_{s_{min}}^{\infty} s^{-\lambda}ds \ . \tag{A7.4}$$

Note that s_{min} is the minimum slip size that the avalanche events (measured in the stress-strain curve) carry [166].

The (continuous) function $P(s)$ cannot be defined by sets of discrete points (i.e., the collection of slip sizes) [107]. In this investigation, the use of the *empirical* distribution function (EDF) of the n-detected avalanches producing the corresponding slip size s in accord with Eq. (A7.4) enables elucidation of the shape of $P(s)$ and the value of exponent λ (Eq. (A7.3)). The EDF of a given slip s is defined as [107, 181]

$$\tilde{F}_n(s) = \frac{\text{number of avalanches with slip} \leq s}{n} = \frac{1}{n} \sum_{i=1}^{n} \mathbf{1}_{s_i \leq s}, \qquad (A7.5a)$$

where

$$\mathbf{1}_{s_i < s} \begin{cases} 1 & \text{if} \quad s_i \leq s \\ \\ 0 & \text{if} \quad s_i > s \end{cases}. \qquad (A7.5b)$$

$\mathbf{1}_E$ is the indicator of event i [181].

For a large n $((n+1)/n \to 1)$, $\tilde{F}_n(s) \to F(s)$ [181], where $F(s)$ is the (continuous) cumulative distribution function (CDF) of slip size s. $F(s)$ is correlated with $P(s)$ through [181]

$$F(s) = \int_{s_{\min}}^{s} P(s)ds. \qquad (A7.6)$$

With the use of the complementary cumulative distribution function (CCDF) of s defined as [107],

$$C(s) = 1 - F(s) = 1 - \int_{s_{\min}}^{s} P(s)ds = \int_{s}^{\infty} P(s)ds, \qquad (A7.7)$$

estimations of the critical exponent λ become available from the $C(s) - s$ data. Note that $P(s) = dC(s)/ds$, which leads to $C(s) \propto s^{-\kappa}$, where $\kappa = \lambda - 1$.

A7.3. Avalanche detection through stress-strain curve analyses

The analysis of the serrated stress-strain curves (Section 6.1) is systematically performed by an in-house code that extracts (avalanche) slip sizes by means of Eq. (A7.2). Throughout a given stress-strain curve, the algorithm searches for local maxima that indicates the onset of an individual avalanche event (Section 6.2). The inset to Fig. A7.1(a) illustrates the criterion employed to identify local minima and maxima, $\sigma_{\min}$ and $\sigma_{\max}$ respectively, through the $\sigma - \varepsilon$ curve. In the present simulations, the numerical fluctuations lead to an uncertainty of $\Delta\sigma_{\text{noise}} \approx 10$ MPa in the $\sigma - \varepsilon$ curves (inset to Fig. A7.1(a)), which essentially restrict the detection of avalanche slips to those plastic events characterized by stress drops $\Delta\sigma > \Delta\sigma_{\text{noise}}$ (Fig. A7.1(b)). According to Eq. (A7.2), the existence of $\Delta\sigma_{\text{noise}}$ in the $\sigma - \varepsilon$ curves from the simulations limits the magnitude of the minimum measurable slip to $s_{\min} \approx 0.03b$.

Figure A7.1(b) shows the $\sigma - \varepsilon$ curve obtained in the MD simulation of the Cu [011] uniaxial test at 400 K (≈ 0.1 m/s, see Appendix A5.2), where the detected avalanche events characterized by a sharp $\Delta\sigma$ are marked in red. The analysis of the EDF (Eq. (A7.5)) of the measured set of the slip events (Eq. (A7.2)) enables the attainment of the $C(s)$ function (Eqs. (A7.6) and (A7.7)). Figure A7.1(d) tentatively exhibits the attainment of two different power-law regimes in the $\log(C(s)) - \log(s)$ representation; i.e., $C(s) \propto s^{-0.5}$ for $s < s_c$; and $C(s) \propto s^{-3.0}$ for $s > s_c$. It is remarked that the $C(s)$ distributions change from power-law to Gaussian-like functions when avalanche identification is reliable down to events smaller than the above $\Delta\sigma_{\text{noise}}$ [44].

The $C(s)$ distributions shift as a function of the imposed minimum slip $s_{\min}$ with $C(s_{\min}) = 1$ [166]. In this context, a reduction in slip resolution (implying an increase in $s_{\min}$)

decreases n while the number of avalanches with slip $\leq s$ is maintained for all $s > s_{\min}$, see Eq. (A7.5). This implies that the shape of the present $C(s)$ functions remains unaffected by changes in the $s_{\min}$ level as illustrated in Fig. A7.2.

A7.4. $C(s)$ distributions from present MD simulations and comparison with available data

The $C(s)$ distributions are determined by assuming that the n-detected avalanches are sufficient so that $\tilde{F}_n(s) \rightarrow F(s)$, see Eqs. (A7.5) and (A7.6). Within this context, it is noted that the analysis of the slip distributions (and exponent κ) obtained in the massive MD simulations lacks of statistical robustness due to the relatively small number of avalanche events captured in the stress-strain curves (Fig. 6.5), where $18 < n < 35$. In this regard, the current computational power restricts the analysis of MD simulations (Section 3.2.3) with smaller strain rates [120] which would conceivably lead to a larger number of avalanche events within the same strain range ($\Delta \varepsilon \approx 0.03$). Nonetheless, the slip distributions obtained in the present simulations (Figs. 6.7 and 6.9) are supported by the extensive statistical work reported in Refs. [34, 43, 54, 50] that verifies the attainment power-law behavior over several decades of slip size [50].

Since visual fitting using log-log representations underestimates the magnitude of power-law exponents [43], the κ exponents from the $C(s) - s$ data are determined by the alternative approach described in Ref. [164] which provides better estimations of these exponents. Moreover, the use of bootstrapping methods enables assessment of the statistical fluctuation in the power-law exponents [43]. In this sense, it is proven in Ref. [43] that the estimations of the λ_1 exponent contains a small error of ± 0.02. Equally, it is also reported in Ref. [50] that exponent κ_1 exhibits an estimation error of ± 0.03 to ± 0.06. Although data sets with large-exponent power-laws can be equally fitted into exponential or log-normal distributions [165], it is formally proven elsewhere in Ref. [166] that the large slip size domain (with $s > s_c$) in the $C(s)$ distributions (Fig. A7.1(c)) systematically exhibits power-law behavior ($\kappa_2 \approx 3.0$) without exponential cut-off, where κ_2 takes a statistical error from ± 0.3 to ± 0.6.

A7.5. Master $C(s)$ distributions from simulations and experiments

The master $C(s)$ distributions of Fig. 6.7 and 6.9 are obtained by conveniently referring the slip data from different $\sigma - \varepsilon$ curves to the same $s_{\min}$ level. This can be simply accomplished by shifting individual distributions along the vertical logarithmic axis as illustrated in Fig. A7.2 [50]. Notice that this scaling cannot affect the fundamental analysis of the intermittent responses (i.e., the κ exponents and s_c level) as the minimum measurable slip is an experimental variable rather than a material-related property. In this context, individual probability values of slip cannot provide any specific physical meaning as the $C(s)$ distributions can be arbitrarily shifted along the vertical axis depending on the selected $s_{\min}$ level.

Four groups of master $C(s)$ distributions are drawn in the slip distributions obtained in FCC crystals, where the above scaling is conveniently applied to the detected avalanches from experiments [34, 50] and MD simulations. In doing so, the master curves are found to share a common initial slip domain ($\kappa_1 \approx 0.5 - 0.7$) marked by a straight line in the $C(s) - s$ logarithmic representations, see Fig. 6.7. The effect of temperature in small Cu micropillars of

$D_s = 2.5$ µm [50], (labelled as *group 2* in Fig. 6.7) is analyzed by imposing $s_{min} \approx 3b$. Additionally, the slip distributions of *group 4* contain dislocation avalanches produced under severe interactions (marked strain hardening along the [111] orientation [23]) in samples with diameters ranging from $D_s = 3.5$ to $D_s = 10$ µm under, where s_{min} is set to $\approx 0.8b$ (Fig. 6.7). Further master $C(s)$ distributions are obtained with avalanches propagating under weak interactions (*group 3*) in soft [100] crystallographic directions [23] with $s_{min} \approx 0.9b$. Since the MD simulations provide a greater slip resolution as compared with the slip sizes obtained in the experiments (Sections 6.6 and 6.7), the slip distributions from the Al and Cu simulations (*group 1*) are all determined under $s_{min} \approx 0.1b$.

Finally, the slip distributions obtained in Ta BCC crystals are represented in terms of two master $C(s)$ distributions (Fig. 6.9), where the slip resolution is imposed to $s_{min} \approx 1b$ and $\approx 0.1b$ for the avalanche events detected in the experiments [50] and the simulations, respectively.
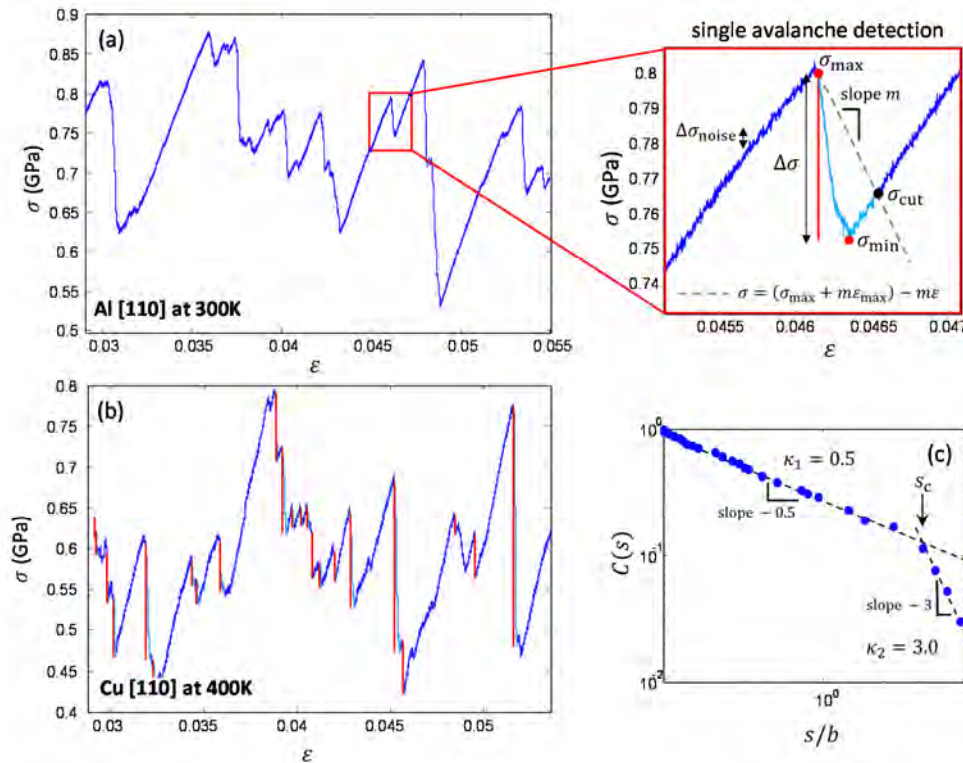
Figure A7.1. Avalanche analysis using the $\sigma - \varepsilon$ curves. (a) The $\sigma - \varepsilon$ curve from the Al [011] simulation at 300 K (≈ 0.1 m/s). The inset illustrates the procedure for the detection of an individual avalanche event characterized by $\Delta\sigma$, where the dotted line (with arbitrary slope m) fixed at $(\sigma_{max}, \varepsilon_{max})$ marks the range (in pale blue) covering from the local maximum $(\sigma_{max}, \varepsilon_{max})$ to the intersection point $(\sigma_{cut}, \varepsilon_{cut})$ of the line with the $\sigma - \varepsilon$ curve. Note that σ_{min} is necessarily the minimum stress level between σ_{max} and σ_{cut}. Following this criterion, individual local maxima are systematically detected as a given σ point leads to intersection with the $\sigma - \varepsilon$ curve so that $\Delta\sigma > \Delta\sigma_{noise}$. (b) The $\sigma - \varepsilon$ curve from the Cu [110] simulation at 400 K. (c) The Cu simulation exhibits two different power-law regimes in the $C(s)$ distributions characterized by $\kappa_1 \approx 0.5$ and $\kappa_2 \approx 3.0$.
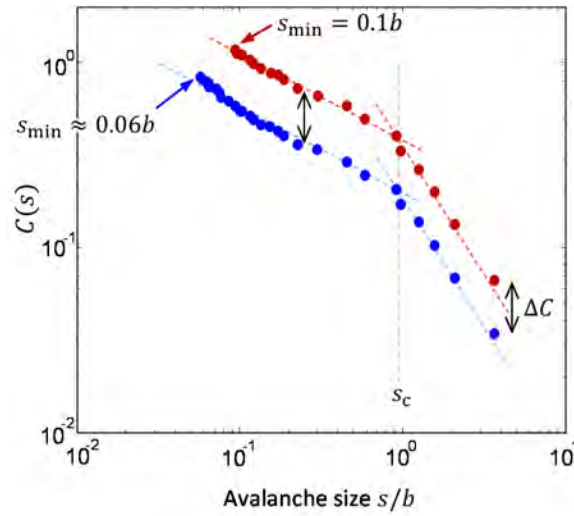
Figure A7.2. Slip distributions obtained in the Al [110] simulation at 300 K (≈ 0.1 m/s) under the assumption of different levels of slip resolution s_{min}. Note that by changing s_{min} the entire slip distribution shifts in the vertical axis a constant value of ΔC, where the exponents κ_1 and κ_2 as well as the critical slip size s_c remain unaltered by s_{min}.

APPENDIX A8. Dislocation density computations

In this investigation, the use of the Dislocation Extraction Algorithm (DXA) [180] (which is implemented in OVITO, see Appendix A6) allows one to convert the dislocation network detected in the raw data produced by present MD simulations (Fig. A8.1(a)) into a three-dimensional mesh of discretized dislocation lines (Fig. A8.1(b)). The DXA method effectively constructs a segment mesh from the uncoordinated (dislocation) atoms, where the identification of these atoms is performed by the CNA calculations described in Appendix A6.

This algorithm also identifies the Burgers vector for each dislocation segment [180] so that a direct characterization of the dislocation type (Section 2.1) is additionally available, see Figs. A8.1(c) and A8.1(d) The application of the DXA with the raw data of atom-point coordinates implies that the total length of the dislocation segments l_{disloc} becomes an accessible quantity [180]. These computations enable the estimation of the dislocation density, ρ, in present simulations, where

$$\rho = \frac{l_{\mathrm{disloc}}}{V_{\mathrm{pl}}} \ . \tag{A8.1}$$

Here, V_{pl} is the plastic volume (or the volume of the *process zone* [148]) in which plasticity develops, see Fig. A8.2(a). The dislocation density ρ expresses the number of available dislocations per crystal unit volume (units in dislocations/m^{-2}). It is remarked to mention that, in the particular case of FCC dislocation networks, DXA computations of l_{disloc} overestimate Eq. (A8.1) by a factor of ≈ 2 due to the characteristic dislocation splitting where a single full dislocation dissociates into two partnering Shockley partials (Section 2.2). This is illustrated in the dislocation segment marked in Fig. A8.1(a) whose length is $\approx$ ("Shockey 1" length + "Shockey 2" length)/2, where the corresponding Shockley partials are marked with arrows in Fig. A8.1(b). In this regard, the analyses of the dislocation densities in FCCs involves computation of Eq. (A8.1) with a correction factor of 0.5.

In nanocontact plasticity, the analysis of the evolutionary V_{pl} becomes a complex task as crystalline defects emanate from a single point at the nucleation (Fig. A8.2(b)) and expand inhomogeneously with indenter-tip penetration [119, 122]. Recent investigations [20, 182] indicate that V_{pl} can be estimated in nanoindentation of metals through the relation [182]

$$V_{\mathrm{pl}} \approx \frac{2\pi}{3} r_{\mathrm{pl}}^3 - \pi h_{\mathrm{s}}^2 \left(\frac{D}{2} - \frac{h_{\mathrm{s}}}{3} \right), \tag{A8.2}$$

where, $r_{\mathrm{pl}} \approx fa$ is the plastic radius and f is the process-zone size factor [119, 122]. Note in Eq. (A8.2) that the plastic volume is described as a hemisphere of radius r_{pl} (cubic term) [20], where the second term of the right-hand side subtracts the volume of the penetrating indenter, V_{ind}, modeled by a spherical cap of height h_{s} assuming $h_{\mathrm{c}} \approx h_{\mathrm{s}}$. Since the latter term is much lower than the cubic term, one can get the idea that V_{pl} essentially scales with the cube of the contact radius a [122, 138, 148]. Thus, the plastic volume V_{pl} attained in the MD nanoindentations with cuboidal domains is modeled using the relationship

$$V_{\mathrm{pl}} = 32a^3 - V_{\mathrm{ind}} \ . \tag{A8.3}$$

In the context of the above definition of plastic radius r_{pl}, Eq. (A8.3) assumes a process-zone size factor $f \approx 2.5$. The rationale underlying Eq. (A8.3) is illustrated in Fig. A8.2(a), where the process zone continuously develops in the computational domain under a $4a \times 4a \times 2a$ cuboidal volume (Figs. A8.2(b)-(d)). This approach ensures that at maximum tip

penetration, (i) $V_{pl} \approx 0.75\,V$ (where V is the simulation-box volume) and that (ii) the top (indented) surface of the simulation cell is of $\approx 4a \times 4a$ (Fig. A8.2(d)). The inset to Fig. A8.2(e) indicates that the V_{pl} from Eq. (A8.3) matches the relationship for V_{pl} elucidated in experiments and simulations [182]. In the context of Eq. (A8.2)), the proposed V_{pl} for the MD nanoindentations leads to $f \approx 2.5$, which is also in good agreement with the evolutionary development of the process zone in both FCC and BCC nanoindentations (as reported elsewhere in Refs. [119, 122]), where f spans from ≈ 2 to ≈ 3.
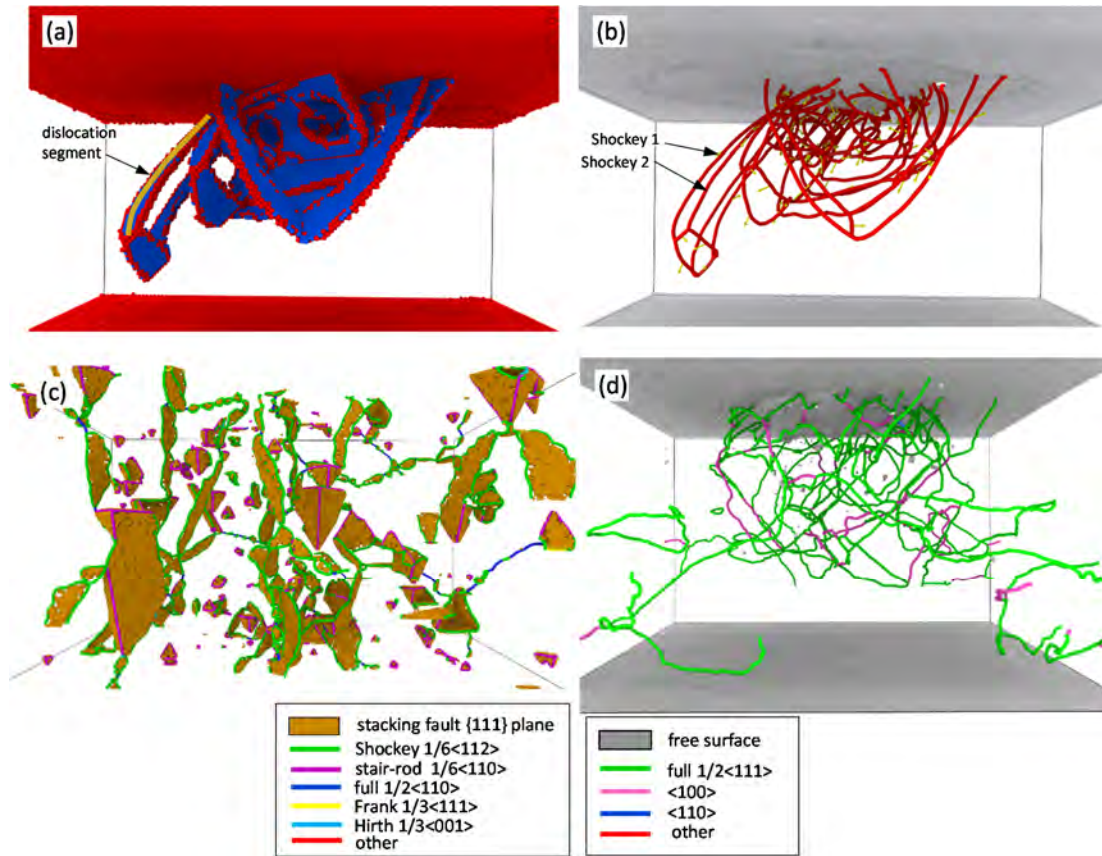
Figure A8.1. DXA computations in presents MD simulations. (a)-(b): Snapshot from the Cu (001) indentation with $D = 24$ nm at 77 K. The DXA converts the discrete points of uncoordinated atoms in (a) (Appendix A6) into the dislocation-segment net in (b). The DXA computation provides a complete analysis of the dislocation network, where Burgers vectors (yellow arrows) and dislocation-line magnitude for every single dislocation are available [180]. DXA computations additionally provide the dislocation segment type as shown in the dislocation networks obtained from the (FCC) Cu [110] tensile test at 650 K ($\varepsilon \approx 0.03$) and the (BCC) Fe (001) indentation with $D = 48$ nm at 900 K.

Figure A8.3 shows the $\rho - h_s$ evolutions obtained in the Cu nanoindentations at 77 K ($D = 48$ nm) using two different approaches for the computation of V_{pl} in Eq. (A8.1). The $\rho - h_s$ evolutions employing the V_{pl} from Eq. (A8.3) are given in Fig. A8.3(a), while the $\rho - h_s$ curves in Fig. A8.3(b) are obtained assuming a constant $V_{pl} = V$. The evolution of ρ against time t can be modeled with simple phenomenological relationships of the class $\dot{\rho} = \alpha\rho - \beta\rho^2$, where $\dot{\rho} = d\rho/dt$ [183, 184]. The first term ($\alpha\rho$) leads to an exponential growth in dislocation

populations with time, and the negative term $(-\beta\rho^2)$ is associated to annihilation processes leading to a net reduction in the ρ levels. α and β account for the fitting parameters of the model [184]. The associated $\dot{\rho} - \rho$ evolution exhibits a fixed point ($\dot{\rho} = 0$) at $\rho^* = \alpha/\beta$ which captures the natural saturation point (ρ^*) of dislocation systems [183, 184], see inset to Fig. A8.3(a). In this context, it is believed that a reasonable $\rho - h_s$ evolution in the Cu simulations attains under the definition for V_{pl} given in Eq. (A8.3) as the dislocation populations eventually exhibit a saturation point with increasing penetration [119], see arrow marked "f.p." (fixed point) in Fig. A8.3(a). The inset to this figure shows the $\dot{\rho} - \rho$ evolution for the (001)-oriented indentation, where ρ saturates at $\rho^*_{(001)} \approx 3 \times 10^{16}$ m^{-2}. By contrast, the constant-V_{pl} approach fails in describing such $\rho - t$ evolutions [26] as ρ levels globally increase with increasing penetration, see Fig A8.3(b).

In simulations of the tensile test (Section 3.2.3), as a well-distributed dislocation network is present in the crystal prior deformation (Fig. 3.4(b)), the computation of dislocation densities by means of Eq. (A8.1) assumes V_{pl} as the total volume of the (periodic) simulation cell.
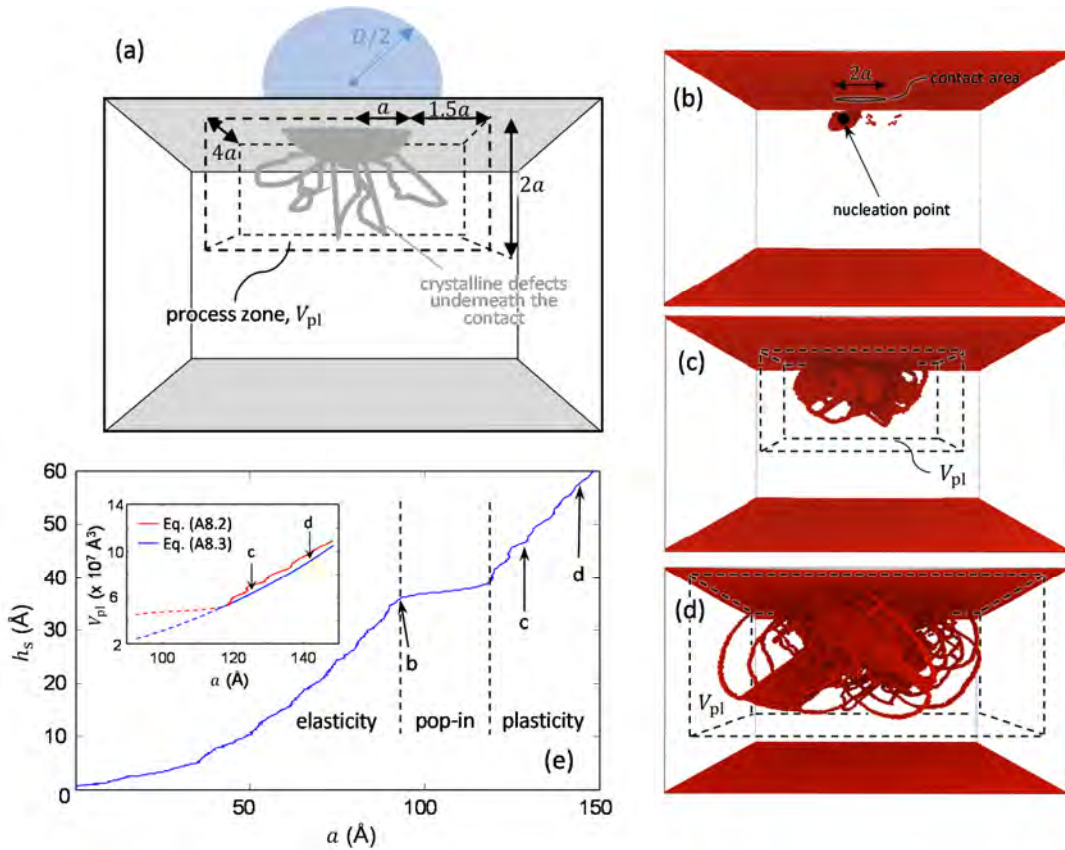
Figure A8.2. (a) Schematic representation of the geometry defining the plastic volume V_{pl} (Eq. A8.3) in present nanoindentations. (b)-(d) Evolution of V_{pl} in the Ta (001) indentation with $D = 48$ nm at 77 K. (e) $h_s - a$ and $V_{pl} - a$ curves for the above indentation, where in the latter the dashed lines denote the increments in a during the pop-in event. See text for further details.
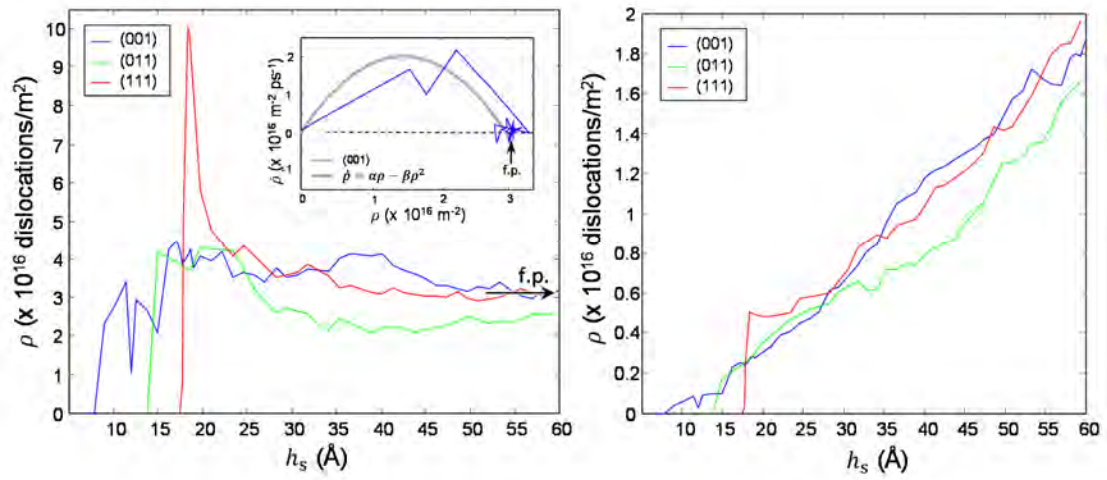
Figure A8.3. $\rho - h_s$ curves from the Cu indentations with $D = 48$ nm (at 77 K). The ρ evolutions in (a) employ the V_{pl} defined in Eq. (A8.3), while $V_{pl} = V$ is assumed in (b).

References

[1]   D. Tabor, The Hardness of Metals, Clarendon Press, Ed., 1951.

[2]   G. Dieter, Mechanical Metallurgy, McGraw-Hill, Ed., 1986.

[3]   D. Hull and D. J. Bacon, Introduction to Dislocations, Fith edition, Fourth Edition ed., D. Hull and D. J. Bacon, Eds., Oxford: Butterworth-Heinemann, 2011, pp. 42-61.

[4]   W. D. Callister and D. G. Rethwisch, Fundamentals of materials science and engineering: An integrated approach., John Wiley & Sons, Inc Hoboken, NJ, Ed., 2008.

[5]   P. Rodriguez, "Sixty years of dislocations," *Bulletin of Materials Science,* vol. 19, pp. 857-872, 1996.

[6]   W. C. Oliver and G. M. Pharr, "An improved technique for determining hardness and elastic modulus using load and displacement sensing indentation experiments," *Journal of Materials Research,* vol. 7, no. 6, pp. 1564-1583, 1992.

[7]   W. C. Oliver and G. M. Pharr, "Measurement of hardness and elastic modulus by instrumented indentation: Advances in understanding and refinements to methodology," *Journal of Materials Research,* vol. 19, pp. 3-20, 2004.

[8]   J. Alcalá, A. E. Giannakopoulos and S. Suresh, "Continuous measurements of load-penetration curves with spherical microindenters and the estimation of mechanical properties," *Journal of Materials Research,* vol. 13, no. 5, pp. 1390-1400, 1998.

[9]   J. Alcalá, A. C. Barone and M. Anglada, "The influence of plastic hardening on surface deformation modes around Vickers and spherical indents," *Acta Materialia,* vol. 48, pp. 3451-3464, 2000.

[10]   W. D. Nix and H. Gao, "Indentation size effects in crystalline materials: A law for strain gradient plasticity," *Journal of the Mechanics and Physics of Solids ,* vol. 46, pp. 411-425, 1998.

[11]   J. J. Vlassak, M. Ciavarella, J. R. Barber and X. Wang, "The indentation modulus of elastically anisotropic materials for indenters of arbitrary shape," *Journal of the Mechanics and Physics of Solids ,* vol. 51, pp. 1701-1721, 2003.

[12]   Z. G. Voyiadjis and M. Yaghoobi, "Review of Nanoindentation Size Effect: Experiments and Atomistic Simulation," *Crystals,* vol. 7, 2017.

[13]   M. F. Horstemeyer, M. I. Baskes and S. J. Plimpton, "Length scale and time scale effects on the plastic flow of fcc metals," *Acta Materialia,* vol. 49, pp. 4363-4374, 2001.

[14]   C. A. Schuh, "Nanoindentation studies of materials," *Materials Today ,* vol. 9, pp. 32-40, 2006.

[15]   H.-J. Chang, M. Fivel, D. Rodney and M. Verdier, "Multiscale modelling of indentation in FCC metals: From atomic to continuum," *Comptes Rendus Physique,* vol. 11, pp. 285-292, 2010.

[16]   Z. Zong, J. Lou, O. O. Adewoye, A. A. Elmustafa, F. Hammad and W. O. Soboyejo, "Indentation size effects in the nano- and micro-hardness of fcc single crystal metals," *Materials Science and Engineering: A,* vol. 434, pp. 178-187, 2006.

[17]   P. M. Derlet and R. Maaß, "A probabilistic explanation for the size-effect in crystal plasticity," *Philosophical Magazine,* vol. 95, pp. 1829-1844, 2015.

[18]   Y. Huang, F. Zhang, K. C. Hwang, W. D. Nix, G. M. Pharr and G. Feng, "A model of size effects in nano-indentation," *Journal of the Mechanics and Physics of Solids,* vol. 54, pp. 1668-1686, 2006.

[19]   J. Alcalá, D. Esqué-de los Ojos and J. Očenášek, "Extracting uniaxial responses of single crystals from sharp and spherical hardness measurements," *Mechanics of Materials ,* vol. 84, pp. 100-113, 2015.

[20]   K. Durst, B. Backes and M. Göken, "Indentation size effect in metallic materials: Correcting for the size of the plastic zone," *Scripta Materialia,* vol. 52, pp. 1093-1097, 2005.

[21] M. A. Lodes, A. Hartmaier, M. Gaken and K. Durst, "Influence of dislocation density on the pop-in behavior and indentation size effect in CaF2 single crystals: Experiments and molecular dynamics simulations," *Acta Materialia ,* vol. 59, pp. 4264-4273, 2011.

[22] L.P. Kubin and G.R. Caniva, "The modelling of dislocation patterns," *Scripta Metall.,* vol. 27, pp. 957-962, 1992.

[23] J. Alcalá, Esqué-de los Ojos and J. Očenášek, "Continuum crystal plasticity analyses of the plastic flow features underneath single-crystal indentations," *Philosophical Magazine,* vol. 91, pp. 1050-1069, 2011.

[24] J. Alcalá and Esqué-de los Ojos, "Reassessing spherical indentation: Contact regimes and mechanical property extractions," *International Journal of Solids and Structures ,* vol. 47, pp. 2714-2732, 2010.

[25] L. P. Kubin, R. Madec and B. Devincre, "Dislocation Intersections and Reactions in FCC and BCC Crystals," *Laboratoire d'Etude des microstructures*, CNRS-ONERA, Chatillon Cedex, France, 2003.

[26] U. F. Kocks and H. Mecking, Physics and phenomenology of strain hardening: the FCC case, Oxford; New York: Pergamon, pp. 171-273, 2003.

[27] S. Ciliberto, A. Guarino and R. Scorretti, "The effect of disorder on the fracture nucleation process," *Physica D: Nonlinear Phenomena,* vol. 158, pp. 83-104, 2001.

[28] H. M. Zbib, T. D. de la Rubia, M. Rhee and J. P. Hirth, "3D dislocation dynamics: stress–strain behavior and hardening mechanisms in fcc and bcc metals," *Journal of Nuclear Materials,* vol. 276, pp. 154-165, 2000.

[29] N. Verdhan and R. Kapoor, "Comparison of the Strength of Binary Dislocation Junctions in fcc Crystals," *Indian Journal of Materials Science,* vol. 5, p. 5, 2014.

[30] J. Alcalá, O. Casals and J. Očenášek, "Micromechanics of pyramidal indentation in fcc metals: Single crystal plasticity finite element analysis," *Journal of the Mechanics and Physics of Solids,* vol. 56, pp. 3277-3303, 2008.

[31] Y.-T. Cheng and C.-M. Cheng, "What is indentation hardness?," *Surface and Coatings Technology,* vol. 133, pp. 417-424, 2000.

[32] M. E. Kassner, "Taylor hardening in five-power-law creep of metals and Class M alloys," *Acta Materialia,* vol. 52, pp. 1-9, 2004.

[33] D. R. Steinmetz, T. Japel, B. Wietbrock, P. Eisenlohr, I. Gutierrez-Urrutia, A. Saeed-Akbari, T. Hickel, F. Roters and D. Raabe, "Revealing the strain-hardening behavior of twinning-induced plasticity steels: Theory, simulations, experiments," *Acta Materialia,* vol. 61, pp. 494-510, 2013.

[34] J. Alcalá, J. Očenášek, K. Nowag, D. Esqué-de los Ojos, R. Ghisleni and J. Michler, "Strain hardening and dislocation avalanches in micrometer-sized dimensions," *Acta Materialia ,* vol. 91, pp. 255-266, 2015.

[35] J. A. El-Awady, "Unravelling the physics of size-dependent dislocation-mediated plasticity," *Nature Communications,* vol. 6, p. 5926, 2015.

[36] M. Biener, J. Biener, A. Hodge and A. Hamza, "Dislocation nucleation in bcc Ta single crystals studied by nanoindentation," *Physical Review B,* vol. 76, p. 165422, 2007.

[37] G. Ziegenhain, H. M. Urbassek and A. Hartmaier, "Influence of crystal anisotropy on elastic deformation and onset of plasticity in nanoindentation: A simulational study," *Journal of Applied Physics,* vol. 107, 2010.

[38] J. Alcalá, R. Dalmau, O. Franke, M. Biener, J. Biener and A. Hodge, "Planar Defect Nucleation and Annihilation Mechanisms in Nanocontact Plasticity of Metal Surfaces," *Phys. Rev. Lett.,* vol. 109, no. 7, p. 075502, 2012.

[39] T. P. Remington, C. J. Ruestes, E. M. Bringa, B. A. Remington, C. H. Lu, B. Kad and M. A. Meyers, "Plastic deformation in nanoindentation of tantalum: A new mechanism for prismatic loop formation," *Acta Materialia,* vol. 78, pp. 378-393, 2014.

[40] R. Kositski and D. Mordehai, "Depinning-controlled plastic deformation during nanoindentation of BCC iron thin films and nanoparticles," *Acta Materialia ,* vol. 90, pp. 370-379, 2015.

[41] O. Franke, J. Alcalá, R. Dalmau, Z. C. Duan, J. Biener, M. M. Biener and A. M. Hodge, "Incipient plasticity of single-crystal tantalum as a function of temperature and orientation," *Philosophical Magazine,* vol. 0, pp. 1-12, 2014.

[42] M.-C. Miguel and S. Zapperi, "Fluctuations in Plasticity at the Microscale," *Science,* vol. 312, pp. 1151-1152, 2006.

[43] D. M. Dimiduk, C. Woodward, R. LeSar and M. D. Uchic, "Scale-Free Intermittent Flow in Crystal Plasticity," *Science,* vol. 312, pp. 1188-1190, 2006.

[44] N. Friedman, A. T. Jennings, G. Tsekenis, J.-Y. Kim, M. Tao, J. T. Uhl, J. R. Greer and K. A. Dahmen, "Statistics of Dislocation Slip Avalanches in Nanosized Single Crystals Show Tuned Critical Behavior Predicted by a Simple Mean Field Model," *Phys. Rev. Lett.,* vol. 109, no. 9, p. 095507, 2012.

[45] R. Maaß and P. M. Derlet, "Micro-plasticity and recent insights from intermittent and small-scale plasticity," *Acta Materialia,* vol. 143, pp. 338-363, 2018.

[46] M. Zaiser and P. Moretti, "Fluctuation phenomena in crystal plasticity—a continuum model," *Journal of Statistical Mechanics: Theory and Experiment,* vol. 2005, p. P08004, 2005.

[47] M.-C. Miguel, A. Vespignani, S. Zapperi, J. Weiss and J.-R. Grasso, "Intermittent dislocation flow in viscoplastic deformation," *Nature,* vol. 410, p. 667, 2001.

[48] D. Marković and C. Gros, "Power laws and self-organized criticality in theory and nature," *Physics Reports,* vol. 536, pp. 41-74, 2014.

[49] F.-J. Pérez-Reche, L. Truskinovsky and G. Zanzotto, "Driving-Induced Crossover: From Classical Criticality to Self-Organized Criticality," *Phys. Rev. Lett.,* vol. 101, no. 23, p. 230601, 2008.

[50] J. Alcalá, J. Očenášek, J. Varillas, J. El-Awady, J. M. Wheeler, and J. Michler, "A statistical pathway to characterizing dislocation avalanches spanning crystal structures, temperatures, and sample sizes," *(in revision),* 2019.

[51] F. F. Csikor, C. Motz, D. Weygand, M. Zaiser and S. Zapperi, "Dislocation Avalanches, Strain Bursts, and the Problem of Plastic Forming at the Micrometer Scale," *Science,* vol. 318, pp. 251-254, 2007.

[52] P. D. Ispánovity, L. Laurson, M. Zaiser, I. Groma, S. Zapperi and M. J. Alava, "Avalanches in 2D Dislocation Systems: Plastic Yielding Is Not Depinning," *Phys. Rev. Lett.,* vol. 112, no. 23, p. 235501, 2014.

[53] P. Bak, C. Tang and K. Wiesenfeld, "Self-organized criticality: An explanation of the 1/f noise," *Phys. Rev. Lett.,* vol. 59, no. 4, pp. 381-384, Jul 1987.

[54] R. Maaß, M. Wraith, J. T. Uhl, J. R. Greer and K. A. Dahmen, "Slip statistics of dislocation avalanches under different loading modes," *Phys. Rev. E,* vol. 91, no. 4, p. 042403, 2015.

[55] J. Li, "Basic Molecular Dynamics," in *Handbook of Materials Modeling*, S. Yip, Ed., Springer Netherlands, pp. 565-588, 2005.

[56] V. V. Bulatov and W. Cai, Computer Simulations of Dislocations, Oxford University Press, Ed., 2006.

[57] W. Cai, J. Li and S. Yip, "1.09 - Molecular Dynamics," in *Comprehensive Nuclear Materials ,* R. J. M. Konings, Ed., Oxford: Elsevier, pp. 249-265, 2012.

[58] M. S. Daw and M. I. Baskes, "Embedded-atom method: Derivation and application to impurities, surfaces, and other defects in metals," *Phys. Rev. B,* vol. 29, no. 12, pp. 6443-6453, 1984.

[59] C. L. Kelchner, S. J. Plimpton and J. C. Hamilton, "Dislocation nucleation and defect structure during surface indentation," *Phys. Rev. B,* vol. 58, no. 17, pp. 11085-11088, 1998.

[60] G. Ziegenhain, A. Hartmaier and H. M. Urbassek, "Pair vs many-body potentials: Influence on elastic and plastic behavior in nanoindentation of fcc metals," *Journal of the Mechanics and Physics of Solids ,* vol. 57, pp. 1514-1526, 2009.

[61] B. Hess, B. J. Thijsse and E. Van der Giessen, "Molecular dynamics study of dislocation nucleation from a crack tip," *Phys. Rev. B,* vol. 71, no. 5, p. 054111, 2005.

[62] I. Salehinia, S. K. Lawrence and D. F. Bahr, "The effect of crystal orientation on the stochastic behavior of dislocation nucleation and multiplication during nanoindentation," *Acta Materialia ,* vol. 61, pp. 1421-1431, 2013.

[63] P. A. Gordon, T. Neeraj, Y. Li and J. Li, "Screw dislocation mobility in BCC metals: the role of the compact core on double-kink nucleation," *Modelling and Simulation in Materials Science and Engineering,* vol. 18, p. 085008, 2010.

[64] C. J. Ruestes, A. Stukowski, Y. Tang, D. R. Tramontina, P. Erhart, B. A. Remington, H. M. Urbassek, M. A. Meyers and E. M. Bringa, "Atomistic simulation of tantalum nanoindentation: Effects of indenter diameter, penetration velocity, and interatomic potentials on defect mechanisms and evolution," *Materials Science and Engineering: A,* vol. 613, pp. 390-403, 2014.

[65] X. Nie, R. Wang, Y. Ye, Y. Zhou and D. Wang, "Calculations of stacking fault energy for fcc metals and their alloys based on an improved embedded-atom method," *Solid State Communications,* vol. 96, pp. 729-734, 1995.

[66] A. Ukwatta and A. Achuthan, "A molecular dynamics (MD) simulation study to investigate the role of existing dislocations on the incipient plasticity under nanoindentation," *Computational Materials Science ,* vol. 91, pp. 329-338, 2014.

[67] P. Peralta, R. Ledoux, M. Hakik, R. Dickerson and P. Dickerson, "Characterization of surface deformation around vickers indents in monocrystalline materials," *Metallurgical and Materials Transactions A,* vol. 35, pp. 2247-2255, 2004.

[68] S. Pathak, J. L. Riesterer, S. R. Kalidindi and J. Michler, "Understanding pop-ins in spherical nanoindentation," *Applied Physics Letters,* vol. 105, 2014.

[69] K. A. Nibur and D. F. Bahr, "Identifying slip systems around indentations in FCC metals," *Scripta Materialia ,* vol. 49, pp. 1055-1060, 2003.

[70] S. Harvey, H. Huang, S. Venkataraman and W. W. Gerberich, "Microscopy and microindentation mechanics of single crystal Fe 3 wt. % Si: Part I. Atomic force microscopy of a small indentation," *Journal of Materials Research,* vol. 8, no. 6, pp. 1291-1299, 1993.

[71] O. Casals and J. Alcalá, "The duality in mechanical property extractions from Vickers and Berkovich instrumented indentation experiments," *Acta Materialia ,* vol. 53, pp. 3545-3561, 2005.

[72] J. Weiss, W. B. Rhouma, T. Richeton, S. Dechanel, F. Louchet and L. Truskinovsky, "From Mild to Wild Fluctuations in Crystal Plasticity," *Phys. Rev. Lett.,* vol. 114, no. 10, p. 105504, 2015.

[73] J. P. Hirth, "A brief history of dislocation theory," *Metallurgical Transactions A,* vol. 16, pp. 2085-2090, 1985.

[74] E. Schmid and W. Boas, Kristallplastizität: Mit Besonderer Berücksichtigung der Metalle, Springer, 1935.

[75] G. I. Taylor, "The Mechanism of Plastic Deformation of Crystals. Part I. Theoretical," *Proceedings of the Royal Society of London A: Mathematical, Physical and Engineering Sciences,* vol. 145, pp. 362-387, 1934.

[76] F. F. Lavrentev, "The type of dislocation interaction as the factor determining work hardening," *Materials Science and Engineering,* vol. 46, pp. 191-208, 1980.

[77] J. J. Gilman, "Dislocation Sources in Crystals," *Journal of Applied Physics,* vol. 30, pp. 1584-1594, 1959.

[78] H. Van Swygenhoven, P. M. Derlet and A. G. Froseth, "Stacking fault energies and slip in nanocrystalline metals," *Nat Mater,* vol. 3, pp. 399-403, 2004.

[79] D. Wu and T. G. Nieh, "Incipient plasticity and dislocation nucleation in body-centered cubic chromium," *Materials Science and Engineering: A ,* vol. 609, pp. 110-115, 2014.

[80] P. R. Thornton, T. E. Mitchell and P. B. Hirsch, "The dependence of cross-slip on stacking-fault energy in face-centred cubic metals and alloys," *The Philosophical Magazine: A Journal of Theoretical Experimental and Applied Physics,* vol. 7, pp. 1349-1369, 1962.

[81] K. Kang, J. Yin and W. Cai, "Stress dependence of cross slip energy barrier for face-centered cubic nickel," *Journal of the Mechanics and Physics of Solids,* vol. 62, pp. 181-193, 2014.

[82] W. Püschl and G. Schoeck, "Calculation of cross-slip parameters in f.c.c. crystals," *Materials Science and Engineering: A,* vol. 164, pp. 286-289, 1993.

[83] A. M. Hussein, S. I. Rao, M. D. Uchic, D. M. Dimiduk and J. A. El-Awady, "Microstructurally based cross-slip mechanisms and their effects on dislocation microstructure evolution in fcc crystals," *Acta Materialia,* vol. 85, pp. 180-190, 2015.

[84] C. R. Weinberger, B. L. Boyce and C. C. Battaile, "Slip planes in BCC transition metals," *International Materials Review,* 2012.

[85] W. Cai, V. Bulatov, J. Chang, J. Li, S. Yip and J.-P. Chang, "Dislocation core effects on mobility," vol. 12, pp. 1-80, 01 2004.

[86] L. Dezerald, D. Rodney, E. Clouet, L. Ventelon and F. Willaime, "Plastic anisotropy and dislocation trajectory in BCC metals," *Nature Communications,* vol. 7, pp. 11695, 2016.

[87] K. Kang, V. V. Bulatov and W. Cai, "Singular orientations and faceted motion of dislocations in body-centered cubic crystals," *Proceedings of the National Academy of Sciences,* vol. 109, pp. 15174-15178, 2012.

[88] L. H. Yang and J. A. Moriarty, "Kink-pair mechanisms for a/2 111 screw dislocation motion in bcc tantalum," *Materials Science and Engineering: A ,* vol. 319-321, pp. 124-129, 2001.

[89] J. Chaussidon, M. Fivel and D. Rodney, "The glide of screw dislocations in bcc Fe: Atomistic static and dynamic simulations," *Acta Materialia ,* vol. 54, pp. 3407-3416, 2006.

[90] J. Chang, W. Cai, V. V. Bulatov and S. Yip, "Dislocation motion in BCC metals by molecular dynamics," *Materials Science and Engineering: A,* Vols. 309 - 310, pp. 160-163, 2001.

[91] A. Stukowski, D. Cereceda, T. D. Swinburne and J. Marian, "Thermally-activated non-Schmid glide of screw dislocations in W using atomistically-informed kinetic Monte Carlo simulations," *International Journal of Plasticity ,* vol. 65, pp. 108-130, 2015.

[92] J. Huang, K. Xu, Y. M. Fan, J. F. Wang, J. C. Zhang and G. Q. Ren, "Dislocation luminescence in GaN single crystals under nanoindentation," *Nanoscale Research Letters,* vol. 9, pp. 649-649, 2014.

[93] R. Madec, B. Devincre, L. Kubin, T. Hoc and D. Rodney, "The role of collinear interaction in dislocation-induced hardening," *Science Mag,* 2003.

[94] D. Rodney and R. Phillips, "Structure and Strength of Dislocation Junctions: An Atomic Level Analysis," *Physical Review Letters,* vol. 82, no. 8, pp. 1704-1707, 1999.

[95] L. Kubin, B. Devincre and T. Hoc, "Modeling dislocation storage rates and mean free paths in face-centered cubic crystals," *Acta Materialia ,* vol. 56, pp. 6040-6049, 2008.

[96] V. V. Bulatov, L. L. Hsiung, M. Tang, A. Arsenlis, M. C. Bartelt, W. Cai, J. N. Florando, M. Hiratani, M. Rhee, G. Hommes, T. G. Pierce and T. Díaz-de la Rubia, "Dislocation multi-junctions and strain hardening," *Nature,* no. 440, p. 1174–1178, 2006.

[97] Q. Liu, L. Deng, X. Wang and J. Li, "Formation of stacking fault tetrahedron in single-crystal Cu during nanoindentation investigated by molecular dynamics," *Computational Materials Science,* vol. 131, pp. 44-47, 2017.

[98] Y. T. Zhu, X. Z. Liao and X. L. Wu, "Deformation twinning in nanocrystalline materials," *Progress in Materials Science,* vol. 57, pp. 1-62, 2012.

[99] A. Machová, G. E. Beltz and M. Chang, "Atomistic simulation of stacking fault formation in bcc iron," *Modelling and Simulation in Materials Science and Engineering,* vol. 7, p. 949, 1999.

[100] A. Ojha and H. Sehitoglu, "Twinning stress prediction in bcc metals and alloys," *Philosophical Magazine Letters,* vol. 94, 2014.

[101] Y. F. Wen and J. Sun, "Generalized planar fault energies and mechanical twinning in gamma Ti-Al alloys," *Scripta Materialia,* vol. 68, pp. 759-762, 2013.

[102] S. Goel, B. Beake, C.-W. Chan, N. H. Faisal and N. Dunne, "Twinning anisotropy of tantalum during nanoindentation," *Materials Science and Engineering: A*, 2014.

[103] D. Frenkel and B. Smit, Understanding Molecular Simulation - From Algorithms to Applications, N. Academic Press, Ed., 2002.

[104] D. J. Evans and G. Morris, Statistical Mechanics of Nonequilibrium Liquids, Second Edition. Cambridge University Press, Ed., 2008.

[105] G. J. Martyna, M. E. Tuckerman, D. J. Tobias and M. L. Klein, "Explicit reversible integrators for extended systems dynamics," *Molecular Physics,* vol. 87, pp. 1117-1157, 1996.

[106] W. Shinoda, M. Shiga and M. Mikami, "Rapid estimation of elastic constants by molecular dynamics simulation under constant stress," *Phys. Rev. B,* vol. 69, no. 13, p. 134103, 2004.

[107] C. Walck, "Hand-book on statistical distributions for experimentalists," 1996.

[108] M. P. Allen and D. J. Tildesley, Computer Simulation of Liquids, 2nd Edition, Oxford University Press, Ed., 2017.

[109] S. Plimpton, "Fast Parallel Algorithms for Short-Range Molecular Dynamics," *J Comp Phys,* pp. 1-19, 1995.

[110] W. G. Hoover, "Canonical dynamics: Equilibrium phase-space distributions," *Phys. Rev. A,* vol. 31, no. 3, pp. 1695-1697, 1985.

[111] J. A. Harrison, J. D. Schall, S. Maskey, P. T. Mikulski, M. T. Knippenberg and B. H. Morrow, "Review of force fields and intermolecular potentials used in atomistic computational materials research," *Applied Physics Reviews,* vol. 5, p. 031104, 2018.

[112] M. I. Mendelev, S. Han, D. J. Srolovitz, G. J. Ackland, D. Y. Sun and M. Asta, "Development of new interatomic potentials appropriate for crystalline and liquid iron," *Philosophical Magazine,* vol. 83, pp. 3977-3994, 2003.

[113] Y. Li, D. J. Siegel, J. B. Adams and X.-Y. Liu, "Embedded-atom-method tantalum potential developed by the force-matching method," *Phys. Rev. B,* vol. 67, no. 12, p. 125101, 2003.

[114] Y. Mishin, D. Farkas, M. J. Mehl and D. A. Papaconstantopoulos, "Interatomic potentials for monoatomic metals from experimental data and ab initio calculations," *Phys. Rev. B,* vol. 59, no. 5, pp. 3393-3407, 1999.

[115] E. Oren, E. Yahel and G. Makov, "Kinetics of dislocation cross-slip: A molecular dynamics study," *Computational Materials Science,* vol. 138, pp. 246-254, 2017.

[116] C. R. Weinberger and G. J. Tucker, "Atomistic simulations of dislocation pinning points in pure face-centered-cubic nanopillars," *Modelling and Simulation in Materials Science and Engineering,* vol. 20, p. 075001, 2012.

[117] G. B. Sushko, A. V. Verkhovtsev, A. V. Yakubovich and A. V. Solov'yov, "Molecular dynamics simulation of nanoindentation of nickel-titanium crystal," *Journal of Physics: Conference Series,* vol. 438, p. 012021, 2013.

[118] S. Plimpton, A. Thomson, P. Crozier, A. Kohlmeyer, "LAMMPS massive-parallel atomistic simulator manual. Available: https://lammps.sandia.gov/doc/Manual.html," lammps.sandia.gov, [10-1-2019].

[119] C. Begau, J. Hua and A. Hartmaier, "A novel approach to study dislocation density tensors and lattice rotation patterns in atomistic simulations," *Journal of the Mechanics and Physics of Solids,* vol. 60, pp. 711-722, 2012.

[120] L. A. Zepeda-Ruiz, A. Stukowski, T. Oppelstrup and V. V. Bulatov, "Probing the limits of metal plasticity with molecular dynamics simulations," *Nature,* vol. 550, p. 492, 2017.

[121] X. Du, H. Zhao, L. Zhang, Y. Yang, H. Xu, H. Fu and L. Li, "Molecular dynamics investigations of mechanical behaviours in monocrystalline silicon due to nanoindentation at cryogenic temperatures and room temperature," *Scientific Reports,* vol. 5, p. 16275, 2015.

[122] Y. Gao, C. J. Ruestes, D. R. Tramontina and H. M. Urbassek, "Comparative simulation study of the structure of the plastic zone produced by nanoindentation," *Journal of the Mechanics and Physics of Solids ,* vol. 75, pp. 58-75, 2015.

[123] S. J. A. Koh and H. P. Lee, "Molecular dynamics simulation of size and strain rate dependent mechanical response of FCC metallic nanowires," *Nanotechnology,* vol. 17, p. 3451, 2006.

[124] D. A. Kilymis, J.-M. Delaye and S. Ispas, "Nanoindentation of the pristine and irradiated forms of a sodium borosilicate glass: Insights from molecular dynamics simulations," *The Journal of Chemical Physics,* vol. 145, p. 044505, 2016.

[125] B. Tang and R. Yang, Molecular dynamics study of uniaxial deformation in perfect and defective aluminum, vol. 53, pp. 1-13, 2015.

[126] T. Tsuru and Y. Shibutani, "Atomistic simulations of elastic deformation and dislocation nucleation in Al under indentation-induced stress distribution," *Modelling and Simulation in Materials Science and Engineering,* vol. 14, p. S55, 2006.

[127] E. Polak, and G. Ribiere, "Note sur la convergence de méthodes de directions conjuguées," *ESAIM: Mathematical Modelling and Numerical Analysis - Modélisation Mathématique et Analyse Numérique,* vol. 3, pp. 35-43, 1969.

[128] A. P. Thompson, S. J. Plimpton and W. Mattson, "General formulation of pressure and stress tensor for arbitrary many-body interaction potentials under periodic boundary conditions," *The Journal of Chemical Physics,* no. 131, 2009.

[129] J. D. Honeycutt and H. C. Andersen, "Molecular dynamics study of melting and freezing of small Lennard-Jones clusters," *The Journal of Physical Chemistry,* vol. 91, pp. 4950-4963, 1987.

[130] L. Yang, D. J. Srolovitz and A. F. Yee, "Extended ensemble molecular dynamics method for constant strain rate uniaxial deformation of polymer systems," *The Journal of Chemical Physics,* vol. 107, pp. 4396-4407, 1997.

[131] E. Renner, Y. Gaillard, F. Richard, F. Amiot and P. Delobelle, "Sensitivity of the residual topography to single crystal plasticity parameters in Berkovich nanoindentation on FCC nickel," *International Journal of Plasticity ,* vol. 77, pp. 118-140, 2016.

[132] G. K. Baranova, "Etching of dislocations in niobium single crystals," *Scripta Metallurgica,* vol. 11, pp. 827-830, 1977.

[133] Y. Wang, D. Raabe, C. Kluber and F. Roters, "Orientation dependence of nanoindentation pile-up patterns and of nanoindentation microtextures in copper single crystals," *Acta Materialia ,* vol. 52, pp. 2229-2238, 2004.

[134] Y. Liu, S. Varghese, J. Ma, M. Yoshino, H. Lu and R. Komanduri, "Orientation effects in nanoindentation of single crystal copper," *International Journal of Plasticity ,* vol. 24, pp. 1990-2015, 2008.

[135] Y. Z. Xia, H. Bei, Y. F. Gao, D. Catoor and E. P. George, "Synthesis, characterization, and nanoindentation response of single crystal Fe-Ni alloys with FCC and BCC structures," *Materials Science and Engineering: A ,* vol. 611, pp. 177-187, 2014.

[136] S. E. Kadijk and A. B. V. Groenou, "Cross-slip patterns by sphere indentations on single crystal MnZn ferrite," *Acta Metallurgica,* vol. 37, pp. 2625-2634, 1989.

[137] R. A. Mirshams, Z. Zhao and Z. Wang, "Experimental analysis and computational modeling of pile-up formation in nanoindentation," *Mexican Journal of Materials Science and Engineering,* vol. 1, pp. 1-11, 2014.

[138] K. L. Johnson, Contact Mechanics, Cambridge University Press, Ed., 1985.

[139] D. Tabor, "A Simple Theory of Static and Dynamic Hardness," *Proceedings of the Royal Society of London A: Mathematical, Physical and Engineering Sciences,* vol. 192, pp. 247-274, 1948.

[140] M. F. Doerner and W. D. Nix, "A method for interpreting the data from depth-sensing indentation instruments," *Journal of Materials Research,* vol. 1, no. 04, pp. 601-609, 1986.

[141] H. Zbib, "Introduction to Discrete Dislocation Dynamics," in *Generalized Continua and Dislocation Theory*, vol. 537, C. Sansour and S. Skatulla, Eds., Springer Vienna, pp. 289-317, 2012.

[142] N. Panich and S. Yong, "Improved method to determine the hardness and the elastic moduli using nano-indentation," *KMITL Sci. J.,* vol. 5, pp. 483-492, 2005.

[143] H. Gao and Y. Huang, "Geometrically necessary dislocation and size-dependent plasticity," *Scripta Materialia,* vol. 48, pp. 113-118, 2003.

[144] H. Somekawa, T. Tsuru, A. Singh, S. Miura and C. A. Schuh, "Effect of crystal orientation on incipient plasticity during nanoindentation of magnesium," *Acta Materialia,* vol. 139, pp. 21-29, 2017.

[145] A. Garg and C. E. Maloney, "Universal scaling laws for homogeneous dislocation nucleation during nano-indentation," *Journal of the Mechanics and Physics of Solids,* vol. 95, pp. 742-754, 2016.

[146] A. Garg and C. E. Maloney, "Mechanical Instabilities in Perfect Crystals: From Dislocation Nucleation to Bucklinglike Modes," *Journal of Applied Mechanics,* vol. 83, pp. 121006-121009, 2016.

[147] K. Kolluri, M. R. Gungor and D. Maroudas, "Molecular-dynamics Simulations of Stacking-fault-induced Dislocation Annihilation in Pre-strained Ultrathin Single-crystalline Copper Films," *Physics Department Faculty Publication Series. University of Massachusetts, Amherst,* 2009.

[148] J. K. Mason, A. C. Lund and C. A. Schuh, "Determining the activation energy and volume for the onset of plasticity during nanoindentation," *Phys. Rev. B,* vol. 73, no. 5, p. 054102, 2006.

[149] T. Zhu, J. Li, K. J. Van Vliet, S. Ogata, S. Yip and S. Suresh, "Predictive modeling of nanoindentation-induced homogeneous dislocation nucleation in copper," *Journal of the Mechanics and Physics of Solids,* vol. 52, pp. 691-724, 2004.

[150] N. W. Watkins, G. Pruessner, S. C. Chapman, N. B. Crosby and H. J. Jensen, "25 Years of Self-organized Criticality: Concepts and Controversies," *Space Science Reviews,* vol. 198, pp. 3-44, 2016.

[151] P. Bak and K. Chen, "The physics of fractals," *Physica D: Nonlinear Phenomena,* vol. 38, pp. 5-12, 1989.

[152] J. P. Sethna, K. A. Dahmen and C. R. Myers, "Crackling noise," *Nature,* vol. 410, p. 242, 2001.

[153] M.-C. Miguel, A. Vespignani, S. Zapperi, J. Weiss and J.-R. Grasso, "Complexity in dislocation dynamics: model," *Materials Science and Engineering: A,* vol. 309, pp. 324-327, 2001.

[154] S. Papanikolaou, Y. Cui and N. Ghoniem, "Avalanches and plastic flow in crystal plasticity: an overview," *Modelling and Simulation in Materials Science and Engineering,* vol. 26, p. 013001, 2018.

[155] Y. Cui, G. Po and N. Ghoniem, "Controlling Strain Bursts and Avalanches at the Nano- to Micrometer Scale," *Phys. Rev. Lett.,* vol. 117, no. 15, p. 155502, 2016.

[156] B. Devincre, T. Hoc and L. Kubin, "Dislocation Mean Free Paths and Strain Hardening of Crystals," *Science,* vol. 320, pp. 1745-1748, 2008.

[157] T. Niiyama and T. Shimokawa, "Atomistic mechanisms of intermittent plasticity in metals: Dislocation avalanches and defect cluster pinning," *Phys. Rev. E,* vol. 91, no. 2, p. 022401, 2015.

[158] J. R. Greer and W. D. Nix, "Nanoscale gold pillars strengthened through dislocation starvation," *Phys. Rev. B,* vol. 73, no. 24, p. 245410, 2006.

[159] J. A. El-Awady, M. Wen and N. M. Ghoniem, "The role of the weakest-link mechanism in controlling the plasticity of micropillars," *Journal of the Mechanics and Physics of Solids,* vol. 57, pp. 32-50, 2009.

[160] I. Ryu, W. D. Nix and W. Cai, "Plasticity of bcc micropillars controlled by competition between dislocation multiplication and depletion," *Acta Materialia,* vol. 61, pp. 3233-3241, 2013.

[161] F. Sansoz, "Atomistic processes controlling flow stress scaling during compression of nanoscale face-centered-cubic crystals," *Acta Materialia,* vol. 59, pp. 3364-3372, 2011.

[162] A. A. Benzerga, "An analysis of exhaustion hardening in micron-scale plasticity," *International Journal of Plasticity,* vol. 24, pp. 1128-1157, 2008.

[163] J. M. Wheeler, C. Kirchlechner, J.-S. Micha, J. Michler and D. Kiener, "The effect of size on the strength of FCC metals at elevated temperatures: annealed copper," *Philosophical Magazine (Abingdon, England),* vol. 96, pp. 3379-3395, 2016.

[164] M. E. J. Newman, "Power Laws, Pareto Distributions and Zipf's Law," vol. 46, 2004.

[165] A. Clauset, C. Shalizi and M. Newman, "Power-Law Distributions in Empirical Data," *SIAM Review,* vol. 51, pp. 661-703, 2009.

[166] J. Alcalá, J. Očenášek, J. Varillas, J. El-Awady, J. M. Wheeler, and J. Michler, "A statistical pathway to characterizing dislocation avalanches spanning crystal structures, temperatures and sample sizes. Supplementary Material.," *(in revision),* 2019.

[167] W. Puschl, "Reactions between glide dislocations and forest dislocations in anisotropie B.C.C. metals," *physica status solidi (a),* vol. 90, pp. 181-189, 1985.

[168] Mathworks, "Computation of the correlation coefficients," Available: https://www.mathworks.com/help/matlab/ref/corrcoef.html [21-6-2018.].

[169] A. van der Schaft, "Symmetries and conservation laws for Hamiltonian systems with inputs and outputs: A generalization of Noether's theorem," *Systems & Control Letters,* vol. 1, pp. 108-115, 1981.

[170] S.-W. Liang, R.-Z. Qiu and T.-H. Fang, "Molecular dynamics simulations of nanoindentation and scratch in Cu grain boundaries," *Beilstein J. Nanotechnol.,* vol. 8, p. 2283–2295, 2017.

[171] S. Chen and F. Ke, "MD simulation of the effect of contact area and tip radius on nanoindentation," *Science in China Series G: Physics, Mechanics and Astronomy,* vol. 47, pp. 101-112, 2004.

[172] M. J. Buehler, A. Hartmaier, H. Gao, M. Duchaineau and F. F. Abraham, "Atomic plasticity: description and analysis of a one-billion atom simulation of ductile materials failure," *Computer Methods in Applied Mechanics and Engineering ,* vol. 193, pp. 5257-5282, 2004.

[173] M. Yaghoobi and G. Z. Voyiadjis, "Effect of boundary conditions on the MD simulation of nanoindentation," *Computational Materials Science,* vol. 95, pp. 626-636, 2014.

[174] E. H. Yoffe, "Modified Hertz theory for spherical indentation," *Philosophical Magazine A,* vol. 50, pp. 813-828, 1984.

[175] Z.-L. Liu, X.-F. Li, L.-C. Cai and F.-Q. Jing, "FP-LAPW calculations of structural and elastic properties of tantalum under high pressure," *physica status solidi (b),* vol. 248, pp. 175-180, 2011.

[176] A. Okabe, B. Boots, K. Sugihara and S. Chiu, Spatial Tessellations: Concepts and Applications of Voronoi Diagrams, vol. 43, 2000.

[177] N. Q. Vo, R. S. Averback, P. Bellon, S. Odunuga and A. Caro, "Quantitative description of plastic deformation in nanocrystalline Cu: Dislocation glide versus grain boundary sliding," *Phys. Rev. B,* vol. 77, no. 13, p. 134108, 2008.

[178] S. Hocker, M. Hummel, P. Binkele, H. Lipp and S. Schmauder, "Molecular dynamics simulations of tensile tests of Ni-, Cu-, Mg- and Ti-alloyed aluminium nanopolycrystals," *Computational Materials Science,* vol. 116, pp. 32-43, 2016.

[179] A. Stukowski, "Visualization and analysis of atomistic simulation data with OVITO the Open Visualization Tool," *Modelling and Simulation in Materials Science and Engineering,* vol. 18, p. 015012, 2010.

[180] A. Stukowski and K. Albe, "Extracting dislocations and non-dislocation crystal defects from atomistic simulation data," *Modelling and Simulation in Materials Science and Engineering,* vol. 18, p. 085001, 2010.

[181] A. W. van der Vaart, Asymptotic Statistics, Cambridge University Press, Ed., 2000.

[182] J. Hua and A. Hartmaier, "Determining Burgers vectors and geometrically necessary dislocation densities from atomistic data," *Modelling and Simulation in Materials Science and Engineering,* vol. 18, p. 045007, 2010.

[183] U. F. Kocks, "Laws for Work-Hardening and Low-Temperature Creep," *Journal of Engineering Materials and Technology,* vol. 98, pp. 76-85, 1976.

[184] B. A. Senior, "Constitutive relationships for the time-dependent deformation of precipitation-hardened metals," *Materials Science and Engineering: A,* vol. 124, pp. 159-169, 1990.

Publications from this thesis

J. Varillas, J. Očenášek, J. Torner, and J. Alcalá. *Unraveling deformation mechanisms around FCC and BCC nanocontacts through slip trace and pileup topography analyses.* Acta Materialia (2017).

J. Alcalá, J. Očenášek, **J. Varillas**, J. El-Awady, J. M. Wheeler, and J. Michler. *A statistical pathway to characterizing dislocation avalanches spanning crystal structures, temperatures and sample sizes* (in revision).

J. Varillas, J. Očenášek, J. Torner, and J. Alcalá. *Understanding hardness and imprint formation processes in FCC and BCC nanocontacts: An interplay between dislocation slip, nanotwinning and the onset of nanostructured crystals* (in preparation)